RELIABILITY−BASED TOPOLOGY OPTIMIZATION FRAMEWORKS FOR THE DESIGN OF STRUCTURES SUBJECTED TO RANDOM EXCITATIONS

BY

JUNHO CHUN

DISSERTATION

Submitted in partial fulfilment of the requirements
for the degree of Doctor of Philosophy in Civil Engineering
in the Graduate College of the
University of Illinois at Urbana-Champaign, 2016

Urbana, Illinois

Doctoral Committee:

Professor Glaucio H. Paulino, Chair and Director of research
Professor Junho Song, Seoul National University
Professor Ivan F. M. Menezes, Pontifícia Universidade Católica do Rio de Janeiro
Professor Ahmed E. Elbanna
Professor Andrés Tovar, Indiana University-Purdue University Indianapolis
William F. Baker, Skidmore, Owings & Merrill LLP

Abstract

Structural optimization aims to provide structural designs that allow for the best performance while satisfying given design constraints. Among various applications of structural optimization, topology optimization based on mathematical programming and finite element analysis has recently gained great attention in research community as well as in applied structural engineering fields. One of the most fundamental requirements for building structures is to withstand various uncertain loads such as earthquake ground motions, wind loads and ocean waves. The design of structures, therefore, needs to ensure safe and reliable operations of structures over a prolonged period of time during which they may be exposed to various randomness of excitations caused by hazardous events. As such, significant amount of time and financial resources are invested to control the dynamic response of a structure under random vibrations caused by natural hazards or operations of non-structural components. In this regard, topology optimization of structures with stochastic response constraints is of great importance and consideration in industrial applications. This thesis discusses the development of structural optimization frameworks for a wide spectrum of deterministic and probabilistic constraints in engineering and investigate numerical applications.

First, the efficient optimization framework for statics and dynamics problems is investigated. In many incidences, expensive computational cost and labor hours are so prohibitive that optimization processes become impractical or inapplicable. To alleviate the computational burden in dynamic topology optimization, the multiresolution topology optimization approach is adopted. Based on the polygonal finite element method and multiresolution topology optimization techniques, a method of polygonal multiresolution topology optimization for statics and dynamics

problems is developed. This development provides methods to discretize complicated geometries and reduce computational cost to obtain topology results of high-resolutions.

Despite rapid technological advances, incorporating stochastic response of structures into topology optimization is considered a relatively new field of research mainly due to computational challenges. In order to overcome such technical challenges in this field, a new method is introduced for incorporating random vibration theories into topology optimization using a discrete representation method for stochastic processes. Furthermore, a novel formulation is developed for sensitivity analysis of stochastic responses to use gradient-based optimization algorithms for the proposed topology optimization employing the discrete representation method.

To assess the reliability of a structure subjected to random excitations, the probability of the occurrence of at least one failure event over a time interval, i.e. the first-passage probability, often needs to be evaluated. In this thesis, a new method is proposed to incorporate probabilistic constraints on the first-passage probability into structural design and topology optimization. To obtain the first-passage probability effectively during each iteration, the failure event is described as a series system event consisting of failure events defined at discrete time points, and the system failure probability is obtained with the sequential compounding method. A new sensitivity formulation is developed employing the sequential compounding method to facilitate the use of gradient-based optimizers for the proposed method.

Finally, the conventional filter effects are investigated in reliability-based topology optimization using the elastic formulation of the ground structure method. In addition, an optimization scheme employing the discrete filter is proposed to ensure that optimized solutions satisfy the probabilistic constraints and global equilibrium. Moreover, the single-loop approach is incorporated to enhance the computational efficiency of the proposed RBTO method.

To my parents, Myong Hee & Sun Hee.

Acknowledgments

This dissertation would not have been possible without the help and support from my family, friends and colleagues. First of all, I would like to express my deepest gratitude to my advisers Dr. Glaucio H. Paulino and Dr. Junho Song for the encouragement and guidance throughout my graduate career. Their advice and support allowed me to explore and expand my research areas. Additionally, I would like to thank my committee members, Professor Ivan Menezes, Professor Ahmed E. Elbanna, Professor Andres Tovar, and William Baker for their valuable contributions and comments.

I am very grateful for my friends who shared many memories in Champaign-Urbana. I would especially like to thank Joon Han Kim and Eun Hyun Park for making graduate school more enjoyable, and for their support through my difficult moments. It has been a great pleasure working with the colleagues, many of whom have become great friends. It would be impossible to name them all, but I would like to acknowledge Professor Song's Structural System Reliability Group: Tam Hong Nguyen, Won Hee Kang, Young Joo Lee, Hyun-woo Lim, Derya Deniz, Nolan Kurtz. I would also like to thank all my colleagues in Professor Paulino's Computational Mechanics Group: Arun L. Gain, Evgueni Filipov, Heng Chi, Tomas Zegard, Oliver Giraldo-Londono, Cameron Talischi, Lauren Beghini, Xiaojia (Shelly) Zhang, Ke (Chris) Liu, Tuo Zhao, Emily Daniels, Yang Jiang, Ludimar Lima de Aguiar, Marco Alfano, Luis Arnaldo, Peng Wei, Helio Emmendoerfer Jr., Rejane Canha, and Leonardo Duarte. Memories I shared with all of you will be cherished for very long time. I would like to give special thanks to Koh Eun Narm for her unconditional support, patience and inspiration.

I gratefully recognize the financial support from the National Science Foundation through projects CMMI 1234243 and CMMI 1559594 (formerly CMMI 1335160). I would like to thank all of the departmental faculty and staff for welcoming me into the program and allowing me to pursue my academic and professional goals. Finally, I would like to thank my parents, Myong Hee Chun, Sun Hee Kim and my sister Chae Young Chun for their support, patience, prayers, and unconditional love they have given me throughout my life.

Table of Contents

List of Figures

List of Tables

Chapter 1

Introduction

Building structures are explicitly exposed to uncertain conditions induced by natural and man-made hazards. The uncertainty of such conditions may exist in applied loading conditions, material properties of structural members, force magnitude and directions, or future realization of earthquakes in a seismic region. The uncertainty of building components also can coexist and interact with conditional uncertainties, and cause undesirable effects on performances of building systems and operations. In the field of structural engineering, various methods of design optimization have emerged over the past few decades to consider the conditional and material uncertainties and their implications in structure design. Structural design optimization is commonly performed in a deterministic manner, whereas reliability based design optimization focuses on finding optimal solutions that account for the existence of various uncertainties such as loads and material properties. Although theories and numerical frameworks of structural design and topology optimization for statics problems in both deterministic and probabilistic approach have been well developed, optimization for structural dynamics problems as well as the practical application of these developments in the broad field need further research and development. Optimization of dynamics problems is mainly categorized into the frequency minimization, the band gab maximization, and dynamic compliances minimization in the literature. However, only limited literature is available for addressing the incorporation of dynamic characteristics in time or frequency domain with broader and significant properties into optimization. That is primarily due to expensive computational cost and lack of efficient framework which adds to the complexity of sensitivity analysis for gradient-based optimization algorithms. In order to design structures

with safety criteria governed by natural hazards, a new optimization framework is needed, so optimal solutions under stochastic process representing extreme events rather than conventional formulations of deterministic and probabilistic design optimization can be provided.

1.1. Motivation

Engineering design and analysis of structures subjected to environmental hazards, such as earthquake and wind loading, are fundamental aspects of structural engineering. These forces, known as stochastic excitations, directly influence the building safety and affect the robustness of building performances. Thus, structure engineers strive to optimally design structures that are safe and reliable in operations that can withstand the random excitations repeatedly induced by natural hazards over time. Due to the randomness of the natural disaster, uncertainties invariably exist and cannot be avoided. Accordingly, the performance of the structural system can be best expressed in a probabilistic setting so that the inherent uncertainties in loading conditions to which structures are exposed can be considered appropriately. The main focus of the present work is identifying the optimal structure and structural system that satisfies the given reliability under stochastic excitations caused by earthquake ground motions. The present work focuses on developing accurate predictions of stochastic responses of a structure to natural hazards or operations and providing efficient and robust optimization frameworks for discrete and continuum structures. In addition, this dissertation investigates and explores the sensitivity analysis of the system failure probability defined in the high-dimension and time domain to employ gradient-based optimization methods.

This chapter includes a brief introductory background on deterministic and probabilistic optimization frameworks and discusses discrete- and continuum-based optimization. At the conclusion of this chapter, the outline, and scope of the current work as well as the organization of the topics in each of the remaining chapters are summarized.

1.2. Optimization

It is difficult to provide structural design solutions through building and testing prototypes due to limited time and resources, and prohibitive financial cost. As an alternative method, mathematical modeling is developed to perform simulations of the behavior of structures and predict operations under various conditions. From the simulation results, the final structural components or structural system are decided, and the prototype of those designs are built to validate the expected performance and results. If predicted performance does not satisfy the design criteria, however, the mathematical model is modified, and the aforementioned design process is repeated until an optimal solution is achieved.

The classical structural optimization can be mainly categorized into size, shape and topology optimization (Bendsøe and Sigmund 2003). In size optimization (Figure 1.1 (a)), commonly considered design variables are thicknesses or cross sectional areas of structural elements and are to be determined. An alternative technique, shape optimization, considers the boundary $\partial\Omega$ of the shape Ω as the design variable. The shape optimization can reshape boundaries to obtain optimal solutions with fixed topology (e.g. the number of holes) of the design domain (Figure 1.1 (b)). Topology optimization is optimizing a shape by acting on its topology (Figure 1.1 (c)), where the design variable is a material density in the continuum setting or a cross sectional size in the discrete setting. Therefore, topology optimization determines the optimal physical size, shape and connectivity and generates material layouts. The continuum-based and discrete-based topology optimization will be discussed in the following section.

1.3. Discrete – continuum topology optimization

Topology optimization is a mathematical tool that has been utilized to explore solutions for various engineering problems. Topology optimization of continuum structures seeks for optimal material layouts and connectivities in a design domain (Bendsøe and Sigmund 2003). In continuum based

topology optimization, the design domain is discretized with finite elements (see Figure 1.2 (a)), each of which is assigned as void or solid material through the iterative optimization procedure (see Rozvany (2009) and Deaton and Grandhi (2014) for a state-of-the-art review of topology optimization). In the field of structural engineering, continuum-based topology optimization has been applied to design lateral-load resisting systems (Mijar et al. 1998; Stromberg et al. 2012; Bobby et al. 2014; Chun et al. 2016).

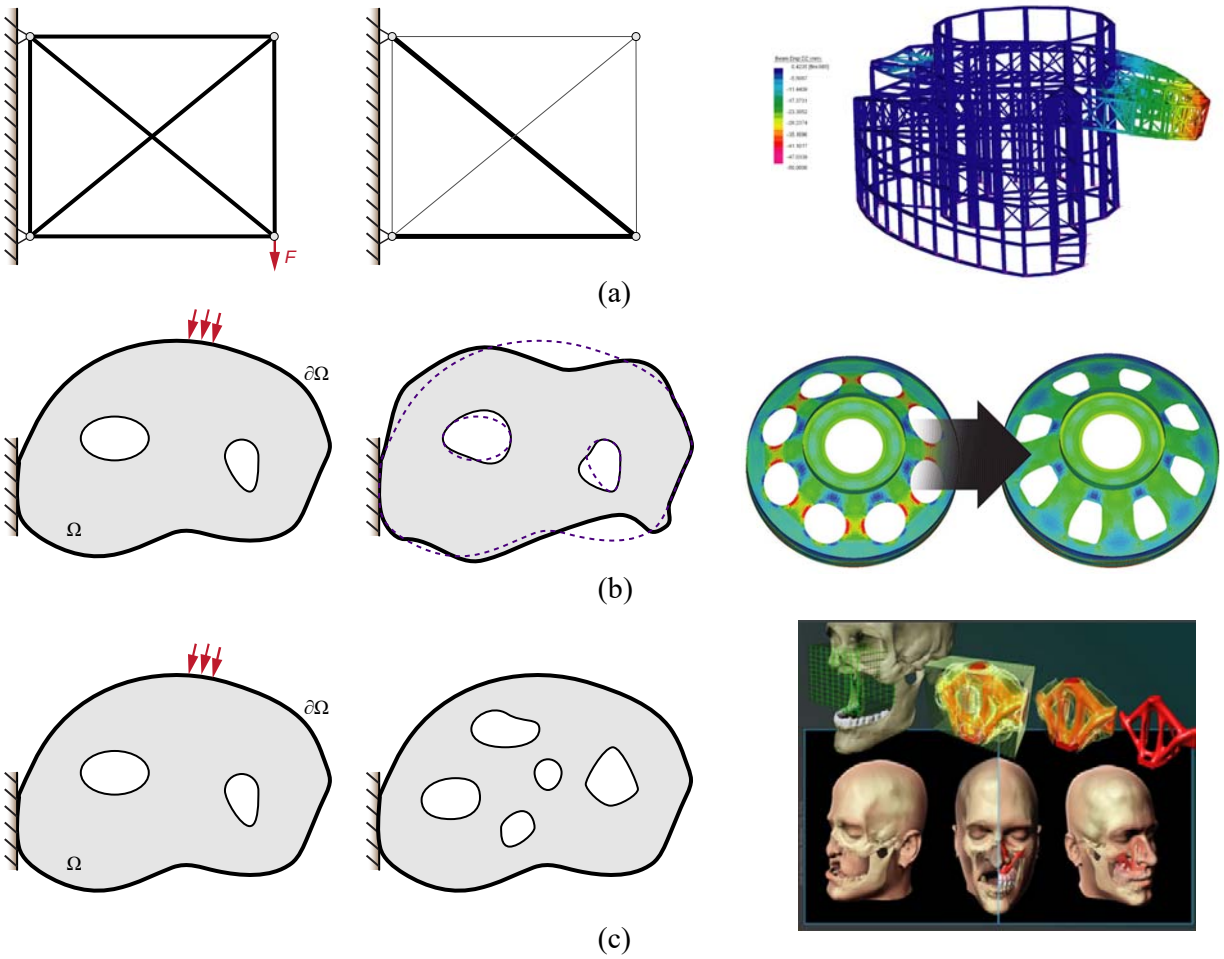

Figure 1.1: Structural optimization and application: (a) size optimization, (b) shape optimization (figure on the right: http://altairenlighten.com), and (c) topology optimization (figure on the right: Sutradhar et al. 2010, PNAS).

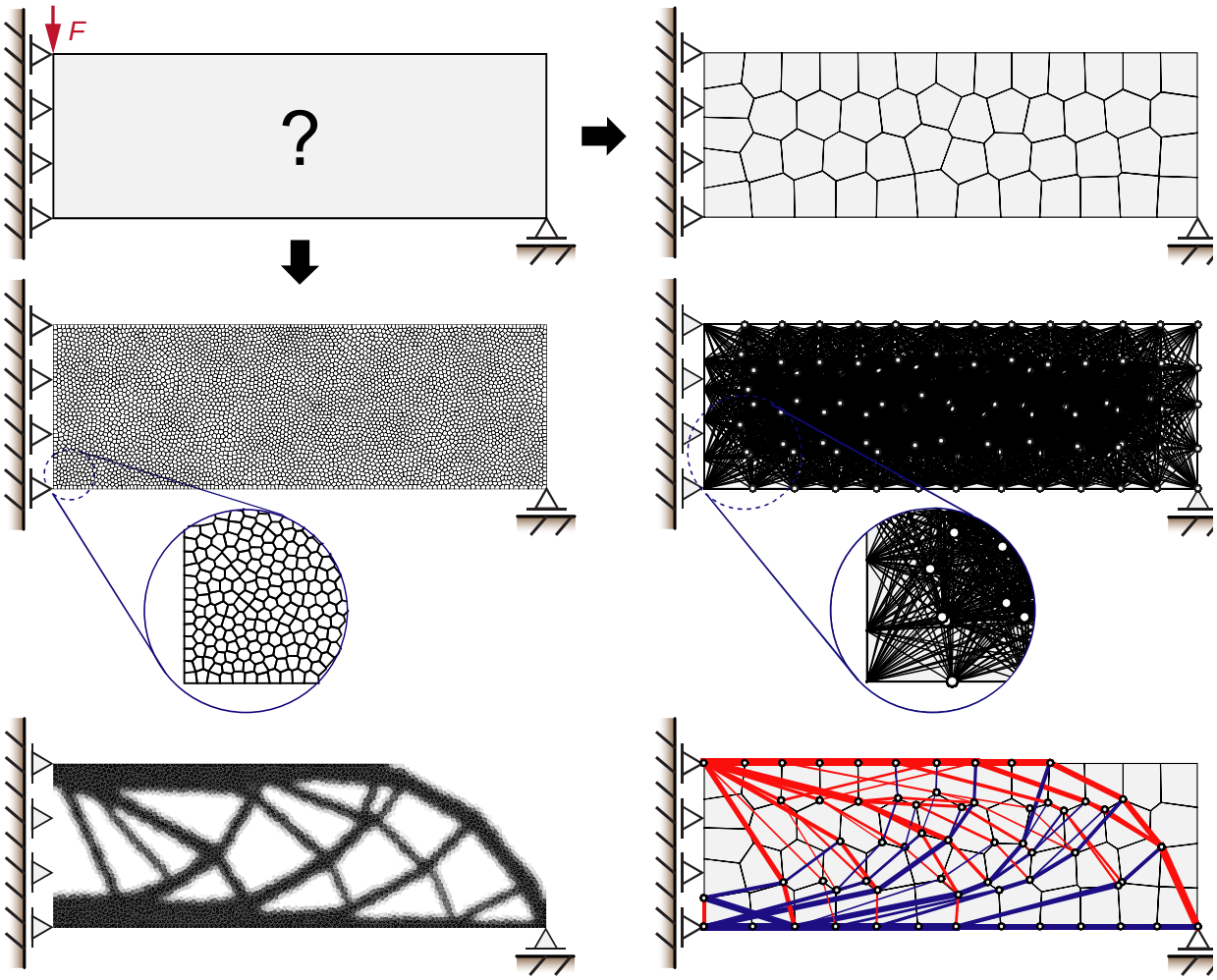

Figure 1.2: (a) Continuum-based topology optimization, and (b) discrete-based topology optimization.

Topology optimization of discrete structures such as trusses and frames is applied to find optimal connectivity of the nodes by the structural elements (see Figure 1.2 (b)). This approach commonly implements the ground structure method (Bendsøe and Sigmund 2003; Ohsaki 2010), in which the design domain is discretized with spatial nodes and highly interconnected by truss or frame elements. Topology optimization is performed on the generated ground structure to minimize an objective function while satisfying constraints, and the size of elements and connectivities are subsequently determined.

1.4. Reliability-based design optimization

Deterministic optimization (DO) for both the continuum and discrete topology optimization considers all design parameters such as material properties, loadings, and geometry, as deterministic in optimization. However, consideration of uncertainties in loads and material properties is also an important aspect of structural engineering as they aid in preventing unexpected structural failures that may result in catastrophic damage and/or loss of life. Therefore, optimization processes associated with the treatment of uncertainties should be utilized to obtain engineering solutions to achieve a satisfactory level of reliability. This approach commonly referred to as RBDO, reliability-based design optimization (Frangopol and Maute 2005; Tsompanakis et al. 2008). RBDO aims to achieve the optimal design under given probabilistic constraints, arising from uncertainties in material properties or loads. For example, Component Reliability Based Design Optimization (CRBDO) seeks to satisfy the probabilistic constraint for each failure mode. This component-based approach, however, may lead to an overly conservative or unsafe design when the failure event in the probabilistic constraint needs to be modeled as a system event. The failure probability often needs to be evaluated at a system level because the system may fail its operation when a combination of component failure events occur. To address this issue, System Reliability Based Design Optimization (SRBDO) methods was developed by Nguyen et al. (2010).

1.5. Robust design optimization

The variation of parameters and input design variable in the optimization process causes the corresponding alterations of the performance of design structures. Ben-Tal and Nemirovski (2000) show that solutions to optimization problems can be extremely sensitive to perturbations of the parameters. Those sensitivities may result in infeasible solutions. In robust design optimization, optimal solutions are commonly obtained by minimizing the performance variance so that the

robustness of a design objective is achieved. That is, finding the most insensitive solutions to problems is the goal of the robust design optimization. There are many established and proposed methods of robust design optimization in the literature. Sigmund (2009) proposed a morphology-based filter scheme in topology optimization considering manufacturing errors of micro-structures so that manufacturing robust optimal topologies can be obtained. Schevenels et al. (2011) extended the Sigmund's method to address non-uniform manufacturing errors with spatially varying magnitude. In addition, a robust shape and topology optimization method considering material uncertainties was proposed by Chen et al. (2010). Recently, a bi-level formulation for robust topology optimization that accounts for the uncertainty of boundary variations was proposed by Guo et al. (2013).

1.6. Thesis scope and organization

The objective of this dissertation is to provide efficient optimization schemes for deterministic statics and dynamics problems and develop novel methods and frameworks to advance structural optimization of discrete and continuum structures considering uncertainty caused by natural hazards, especially earthquake ground motions. The reminder of the dissertation is organized as follows. Chapter 2 presents a polygonal multiresolution topology optimization scheme. The efficient topology optimization framework for statics and dynamics problems developed by the author is discussed in detail. This development enables obtaining of high-resolution topologies while maintaining relatively low computational cost, particularly related to the finite element analysis. In Chapter 3, the discrete representation of random vibrations and its statistical quantities are discussed. The development of a systematic framework for incorporating random vibration theories and reliability analysis into structural optimization is discussed, whose solutions can withstand the presence of uncertainty induced by earthquake events. In Chapter 4, the parameter sensitivity analysis of system failure probability consisting of a large number of components is explored. Adaptation of the sequential compounding method to develop the efficient algorithm for

sensitivity analysis is also included. Chapter 5 discusses the first-passage probability and its significance in engineering and optimization. It also includes the development of the computational framework for stochastic topology and design optimization under first-passage probability of practical engineering constraints such as stress, inter-drift ratios, and maximum displacement. Chapter 6 explains the implementation of the discrete filtering approach in reliability-based topology optimization for truss structures. Finally, the summary and principal conclusions of the present work and future directions are described in Chapter 7.

Chapter 2

Polygonal multiresolution topology optimization for structural dynamics

Topology optimization method of distribution of a given amount of materials in a design domain satisfying loads and boundary conditions has been well-developed and researched. Although extensive applications and various theories of topology optimization are rapidly expanding for static problems, dynamic problems have received relatively less attention. One of the important issues related to optimization in dynamics is the expensive computational costs of finite element (FE) analysis and optimization procedure. The resolution of optimal topologies is proportionally linked to the mesh size used in FE analysis in a conventional approach to topology optimization. Finer meshes in dynamic optimization problems increase computing resources. Another shortcoming of a conventional framework is that fixed discretized FE meshes lead to mesh-oriented results. To obtain a higher resolution with relatively low computational cost, a multiresolution topology optimization (MTOP) technique that separately introduces different meshes for FE analysis and density / design variable meshes has been developed. In this chapter, polygonal finite elements are adopted to reduce the influence of the fixed discretization. Unstructured meshes with polygonal elements provide ways to resolve the issue in topology optimization. Moreover, irregular polygonal meshes help to overcome difficulties in discretizing complicated geometries. Based on the polygonal finite element method and the multiresolution topology optimization technique, a method of polygonal multiresolution topology optimization (PolyMTOP) is developed for static and dynamic problems. This research addresses ways to improve the vibration characteristic of structures subjected to periodic loading by incorporating a new method into topology optimization.

2.1. Introduction

In recent times topology optimization has been used in the design of aircraft (Maute and Allen 2004; Sleesongsom and Bureerat 2013), cars (Yang and Chahande 1995), buildings (Mijar et al. 1998; Stromberg et al. 2011), and even human bones (Sutradhar et al. 2010). The use of topology optimization has increased over the past few decades in part due to improving capabilities of computational modeling, but also due to improved understanding of the continuum optimization problem. Recent advances such as the solid isotropic material with penalization (SIMP) material interpolation model (Bendsøe 1989; Rozvany et al. 1992) has allowed for effective discretization of continuum domains, and filtering methods (e.g. Sigmund and Petersson 1998; Petersson and Sigmund 1998; Guest et al. 2004; Almeida et al. 2009) have allowed for mesh independent solutions. Structural dynamic modeling has similarly evolved in the past years and can include modal, time history, or transformed problem analysis. Topology optimization for freely vibrating systems has included the design of beams, trusses, plates and other systems (Olhoff 1976; Du and Olhoff 2007; Olhoff et al. 2012; Zhou 2013). Typically these systems are designed such that the natural frequencies of the structure are changed from the initial configuration. Recent research (Yoon 2010a, b; Huang et al. 2010) has introduced dynamic optimization for nonlinear structures. Alternatively, Tsai and Cheng (2013) have developed a method for optimizing dynamic structures and fixing a specific mode shape. Optimization can also be performed for forced vibration systems where a system is designed such that the maximum response (dynamic displacement) for a given input frequency is optimized. Recent research has shown that the structural response for resonating structures can be maximized (Tcherniak 2002) or, more typically, minimized (Ma et al. 1995; Jog 2002; Dahl et al. 2007; Jensen 2007; Larsen et al. 2008) for a set of design frequencies.

Recent advances in finite element (FE) modeling (e.g. Sukumar 2004; Sukumar and Malsch 2006; Ghosh 2011) have allowed for the use of polygonal elements in continuum modeling. A significant benefit of these elements is that they are well suited for modeling of complex domains and can be used to easily create areas of high and low mesh refinement. In topology optimization these

elements have been shown to significantly reduce instabilities associated with checkerboard and islanding effects, and have been shown to be stable and accurate (Jog and Haber 1996; Talischi et al. 2009a, b). Recent educational codes (Talischi et al. 2012a, b) provide a polygonal element mesher and a package for efficient topology optimization, and these codes are used as the basis for the work presented herein. Furthermore, recent advances in multiresolution modeling have allowed for high resolution results with relatively low computational costs. Nguyen et al. (2009, 2012), introduce Multiresolution Topology Optimization (MTOP), and use different overlying meshes for FE analysis and for the density/design variables, to harvest the higher order accuracy of the displacement solution in obtaining higher resolution solutions. Such mesh refinements and adaptivity techniques can provide significant improvements in computational speed and solution resolution. Other methods have taken advantage of higher-order finite elements to improve the speed and quality of topology optimization. For example Parvizian et al. (2011) use a finite cell method to separate geometry and FE analysis, while Nguyen et al. (2013) use high-order elements to enhance the MTOP approach.

In this study, the existing polygonal finite element codes (Talischi et al. 2012a, b), with higher resolution density and design discretizations to obtain high fidelity multiresolution designs (Nguyen et al. 2009) for structural dynamic problems are adapted. This combined modeling approach (PolyMTOP), provides adaptable, high resolution structural optimization techniques that can be used to tailor the dynamic performance of buildings, vehicles, and other systems. This chapter is organized as follows: Section 2.2 provides an overview of the multiresolution approach and introduces the formulation for non-matching multiresolution discretizations and polygonal finite element; Section 2.3 presents the topology optimization framework for static and dynamic problems; Section 2.4 discusses sensitivity analysis of optimization problems and PolyMTOP scheme; Section 2.5 provides the projection scheme associated with the proposed method; Section 2.6 discusses the numerical applications of the proposed method. It shows the approach used in

the optimization of static compliance problems and forced vibration problems, and Section 2.7 presents concluding remarks.

2.2. Multiresolution approach for polygonal elements

2.2.1. Non-matching sub-discretizations

In the multiresolution approach, the *design variables* in the optimization framework are material densities for a predefined portion of the mesh. Subsequently, a projection filter (Section 2.5) is used to obtain a mesh independent solution of *density variables* that are used to represent the actual material distribution and to compute stiffness and mass matrices. There are various ways in which the design variable can be positioned such that it does not overlap with the FE mesh, for example, nodal approaches (Guest et al. 2004; Rahmatalla and Swan 2004; Matsui and Terada 2004) use design variables that are placed on individual nodes, or alternatively design variables can be placed between nodes such as in Paulino and Le (2008). Alternatively, the multiresolution scheme introduced in Nguyen et al. (2009) uses coarser meshes for FE analysis and finer mesh discretizations for optimization and design. This generates a high-resolution result without a significant increase in computational cost. Furthermore, the same authors showed that by using alternative design and density variable placement, and an adaptive multiresolution approach they could obtain higher efficiency (Nguyen et al. 2012). Expanding the multiresolution approach to polygonal elements, there are various ways in which a polygonal element can be divided such that the design mesh is finer than the FE mesh. In this section, several cases are considered where elements are divided into non-matching sub-discretizations, however, in all cases, the design variables are at the same location as the density variables. For example, Figure 2.1 shows the superposition of design and density variables for an eleven sided polygonal element. For non-matching sub-discretizations, the finite element is divided into convex, Centroidal Voronoi Tessellations (CVTs). Figure 2.2 shows the proposed approach, where the naming P5/n7 and

P5/n18 respectively are used to indicate the number of edges of the polygon (P) and the number of design variables (n) placed inside. This approaches can easily be applied to any type of polygon in the FE mesh. This approach uses the same number of sub-discretizations based on randomly placed seeds within each element. As shown in Figure 2.3, these seeds are moved using a Lloyd algorithm to create CVTs that consist of regularized convex elements (Talischi et al. 2009b). Note that the Lloyd algorithm allows the sub-discretizations to be relatively uniform with similar areas within each element.

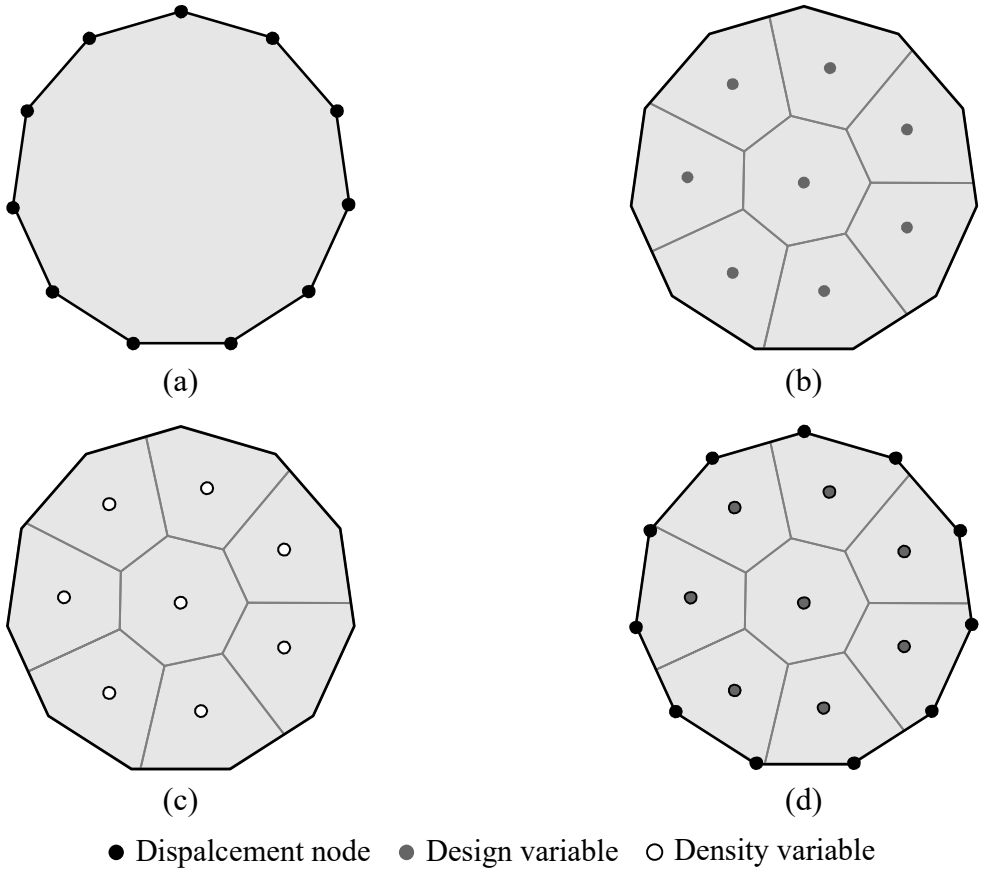

Figure 2.1: Eleven sided polygon element: (a) Finite element (displacement based), (b) Design variable mesh, (c) Density variable mesh, and (d) Superposed meshes.

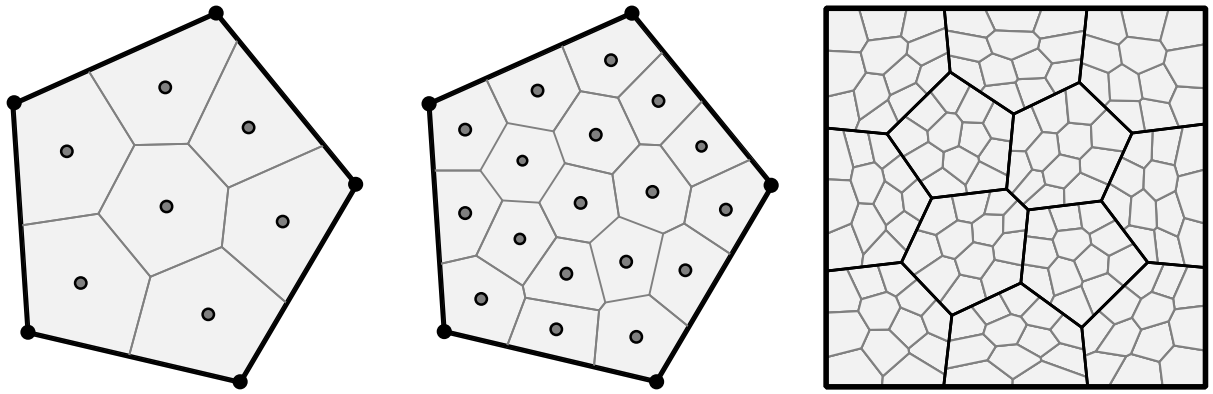

Figure 2.2: Sub-discretizations for five sided polygon element: (a) P5/n7, (b) P5/n18, and (c) Mesh of Pn/n12 elements.

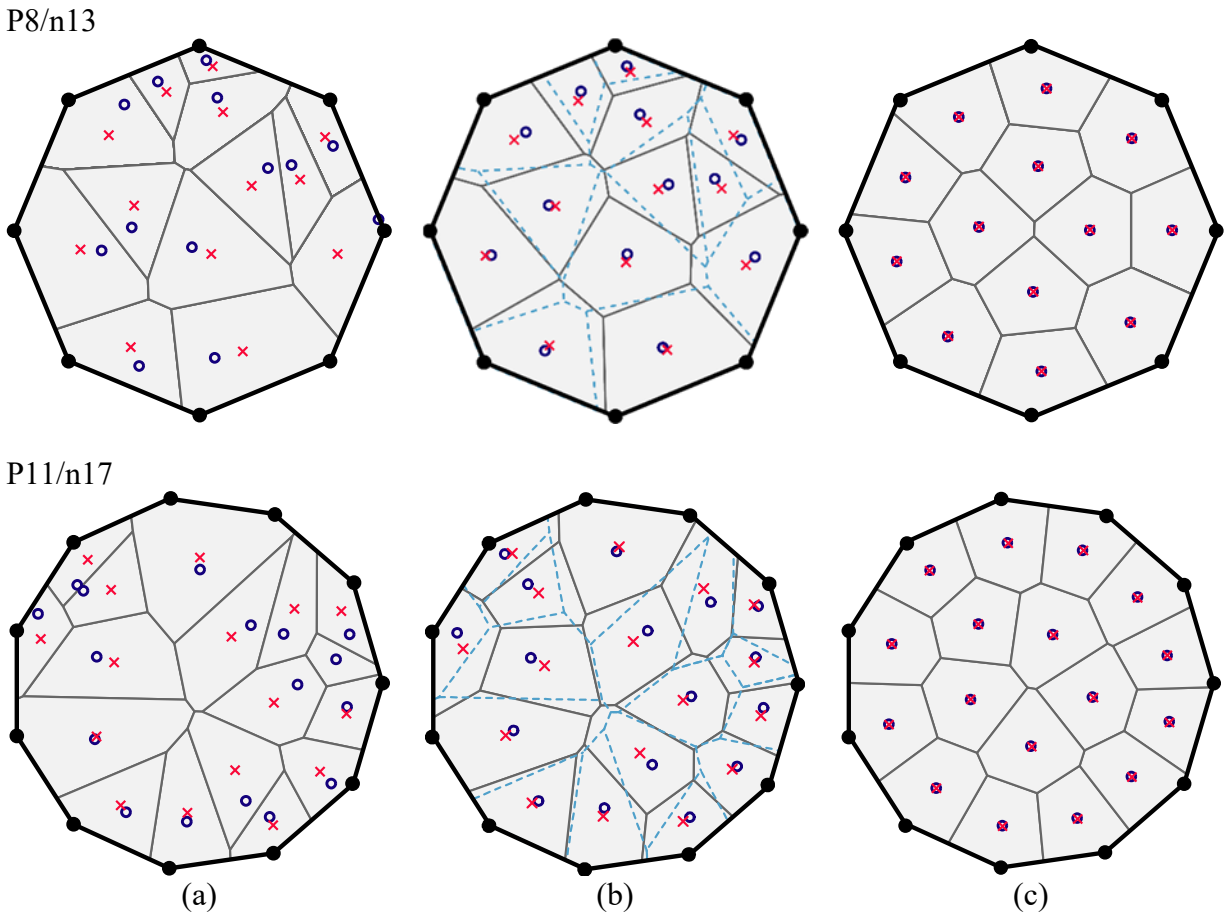

Figure 2.3: Illustration of Lloyd's algorithm optimizing the sub-discretizations of a P8/n13, and a P11/n17 element: (a) initial distribution of seeds (*circles*), the corresponding Voronoi diagram, and the centroid of the Voronoi cells (*crosses*), (b) the Voronoi diagram after one iteration, and (c) the Voronoi diagram after 50 iterations.

2.2.2. Shape functions for polygonal elements and numerical integration

The Wachspress shape functions (Sukumar and Tabarraei 2004) are adopted on a reference element with coordinate $\boldsymbol{\xi} = (\xi_1,\xi_2)$ as a polygonal interpolant as:

$$N_i(\boldsymbol{\xi}) = \frac{\alpha_i(\boldsymbol{\xi})}{\sum_{k=1}^{n} \alpha_k(\boldsymbol{\xi})} \tag{2.1}$$

And the interpolants $\alpha_i(\boldsymbol{\xi})$ are of the following form:

$$\alpha_i(\boldsymbol{\xi}) = \frac{A(\mathbf{p}_{i-1},\mathbf{p}_i,\mathbf{p}_{i+1})}{A(\mathbf{p}_{i-1},\mathbf{p}_i,\boldsymbol{\xi})A(\mathbf{p}_i,\mathbf{p}_{i+1},\boldsymbol{\xi})} \tag{2.2}$$

where A represents the area of the triangle defined with the points in its arguments (see Figure 2.4).

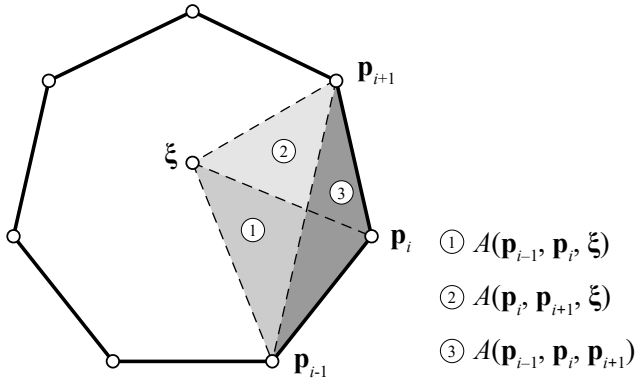

Figure 2.4: Triangular areas used to the interpolants, α_i.

By considering a regular polygon in the reference domain, $A(\mathbf{p}_{i-1}, \mathbf{p}_i, \mathbf{p}_{i+1})$ can be factored out of Equation 2.2. The simplified expression (Talischi et al. 2012b) for the interpolants can be obtained by adopting the notation $A_i(\boldsymbol{\xi}) := A(\mathbf{p}_{i-1}, \mathbf{p}_i, \boldsymbol{\xi})$:

$$\alpha_i(\boldsymbol{\xi}) = \frac{1}{A_i(\boldsymbol{\xi})A_{i+1}(\boldsymbol{\xi})} \tag{2.3}$$

The shape function gradients are computed as:

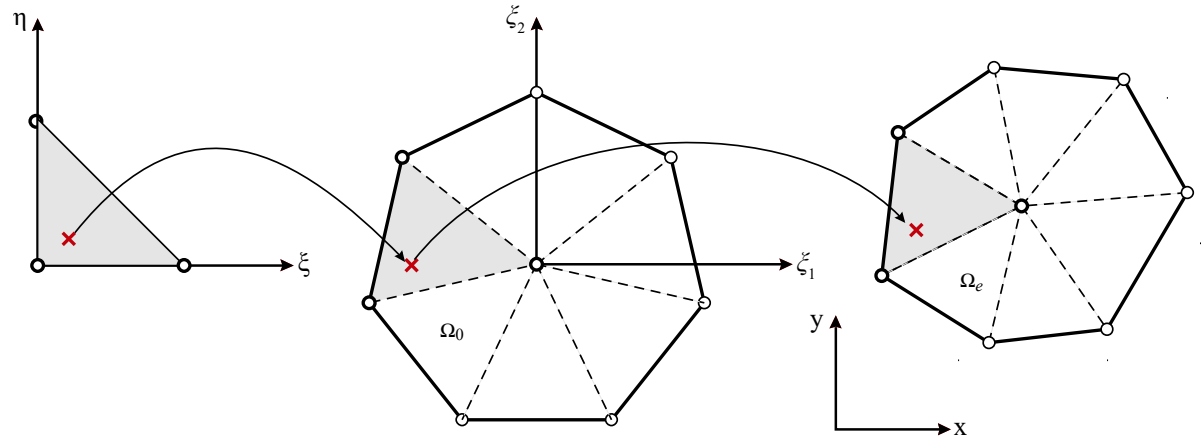

Figure 2.5: Numerical integration scheme based on the partition of the sub-divided element.

$$\frac{\partial N_i}{\partial \xi_j} = \frac{1}{\sum_{k=1}^{n} \alpha_k} \left(\frac{\partial \alpha_i}{\partial \xi_j} - N_i \sum_{k=1}^{n} \frac{\partial \alpha_k}{\partial \xi_j} \right), \quad j = 1, 2 \tag{2.4}$$

where

$$\frac{\partial \alpha_i}{\partial \xi_j} = -\alpha_i \left(\frac{1}{A_i} \frac{\partial A_i}{\partial \xi_j} + \frac{1}{A_{i+1}} \frac{\partial A_{i+1}}{\partial \xi_j} \right), \quad j = 1, 2 \tag{2.5}$$

Numerical integration is performed by sub-dividing the physical or reference element into triangles and then using numerical quadrature rules. In this work, 3-point quadrature rules are used on each subdivided triangle from the reference n-gon as shown in Figure 2.5. Alternatively, other numerical schemes for a polygonal element can be found in (Mousavi et al. 2009; Natarajan et al. 2009).

2.2.3. Stiffness and mass matrix computing

For a discretized finite element mesh, the global stiffness matrix can be calculated as:

$$\mathbf{K} = \sum_{e=1}^{N_{el}} \mathbf{K}_e = \sum_{e=1}^{N_{el}} \int_{\Omega_e} \mathbf{B}^{\mathrm{T}} \mathbf{D} \mathbf{B} d\Omega \tag{2.6}$$

where N_{el} is the number of elements, **B** is the strain displacement matrix of shape function derivatives, and **D** is the constitutive matrix. The constitutive matrix is calculated for a plane stress case (Cook et al. 2007) and Young's modulus is calculated as a function of the density ρ at position **x** on the multiresolution mesh, as

$$E(\mathbf{x}) = \rho(\mathbf{x})^p E_0 \tag{2.7}$$

In Equation 2.7, E_0 is Young's modulus of the solid material and the objective in topology optimization is to determine the distribution of material in the domain to satisfy a set of objectives. To achieve this, a SIMP model is used to penalize locations of intermediate densities. Alternatively, the Rational Approximation of Material Properties (RAMP) scheme (Stolpe and Svanberg 2001) can be implemented as:

$$E(\mathbf{x}) = \frac{\rho(\mathbf{x})}{1 + s(1 - \rho(\mathbf{x}))} E_0 \tag{2.8}$$

where s is the penalization. The value of the density $\rho(\mathbf{x})$ can be between $\rho_{\min} = 10^{-3}$ and 1, and the penalization parameter p is chosen to be more than 1 (typically 3 or 4) and can be used in an incremental, iterative fashion. This type of model serves to transform the discrete formulation into a continuous solvable problem that can be treated numerically. Since the stiffness matrix is linearly dependent on the elastic modulus, the penalized density terms ($\rho(\mathbf{x})^p$) are taken out from the integration of the stiffness matrix, as shown in Equation 2.7. Each polygonal element includes sub-discretized elements having densities in the multi-resolution approach as illustrated in Figure 2.6. The element stiffness matrix is constructed by assembling stiffness contributions from sub-divided elements in a polygon. Thus, the element stiffness matrix is approximated as:

$$\mathbf{K}_e = \int_{\Omega_e} \mathbf{B}^{\mathrm{T}}\mathbf{D}\mathbf{B} d\Omega \cong \sum_{i=1}^{Nn} \left(\mathbf{B}^{\mathrm{T}}\mathbf{D}\mathbf{B} \right)\Big|_i A_i = \sum_{i=1}^{Nn} \left(\rho_i \right)^p \mathbf{I}_i \tag{2.9}$$

where

$$\mathbf{I}_i = \left(\mathbf{B}^{\mathrm{T}}\mathbf{D}_0\mathbf{B} \right)\Big|_i A_i \tag{2.10}$$

and Nn is the number of integration points in each polygonal element, and ρ_i represents the density at each non-conforming element. $\mathbf{D}(\rho_i)$ is the constitutive matrix which is dependent on the density. For example, the constitutive matrix for plane stress in 2-D is as the following:

$$\mathbf{D}(\rho_i) = \frac{\rho_i^{\,p} \cdot E_0}{1-\nu^2} \cdot \begin{bmatrix} 1 & \nu & 0 \\ \nu & 1 & 0 \\ 0 & 0 & (1-\nu)/2 \end{bmatrix} = \rho_i^{\,p} \mathbf{D}_0 \tag{2.11}$$

The global mass matrix can similarly be calculated by integrating over the domain as:

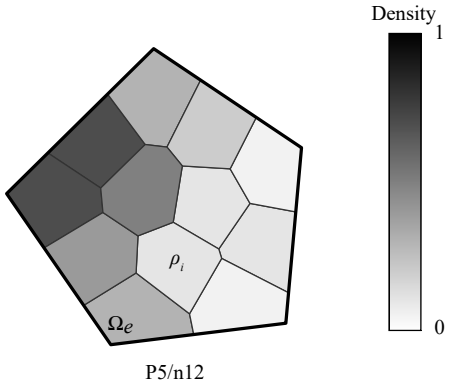

Figure 2.6: Polygonal element (P5/n12) with sub-discretizations and densities.

$$\mathbf{M} = \sum_{e=1}^{N_{el}} \mathbf{M}_e = \sum_{e=1}^{N_{el}} \int_{\Omega_e} \rho_m \mathbf{N}^{\mathrm{T}} \mathbf{N} d\Omega \tag{2.12}$$

where $\mathbf{N}$ denote the element shape functions and ρ_m represents the mass density of material. The element mass matrix ($\mathbf{M}_e$) can furthermore be approximated by

$$\mathbf{M}_e = \int_{\Omega_e} \rho_m \mathbf{N}^{\mathrm{T}} \mathbf{N} d\Omega \cong \sum_{i=1}^{Nn} (\rho_i)^q \, \rho_m \left(\mathbf{N}^{\mathrm{T}} \mathbf{N} \right)\Big|_i A_i = \sum_{i=1}^{Nn} (\rho_i)^q \, \mathbf{H}_i \tag{2.13}$$

where q is the penalization factor of density for mass terms, and $\mathbf{H}_i$ is used to store the mass matrix for each subdivided element in the multiresolution element, as:

$$\mathbf{H}_i = \rho_m \left(\mathbf{N}^{\mathrm{T}} \mathbf{N} \right)\Big|_i A_i \tag{2.14}$$

2.2.4. Verification of polygonal elements

Mesh variations with quadrilateral, triangular and general polygonal meshes are tested as shown in Figures 2.7 (a) through 2.7 (f). The irregular geometry swept panel (Figure 2.7 (a)) is adopted from Cook et al. (2007). Figure 2.7 (g) shows the error convergence plot in the estimation of real part of displacements in the steady state solution at point C in Figure 2.7 (a) under a harmonic excitation. The excitation is applied to the right edge, and its angular frequency is 0.01 rad/s with a force magnitude 1. For the force vibration problem, the Rayleigh damping model, $\mathbf{C} = 0.001\mathbf{M} + 0.001\mathbf{K}$, is used to construct a damping matrix. Because there are no analytical solutions for the tested problem, a solution was obtained by using a much finer discretization of about 10^5 degrees of freedom (DOFs) to calculate a reference solution. For the same number of DOFs, the polygonal mesh where the Lloyd algorithm was used to refine the mesh (Figure 2.7 (e)), provides a better approximation for structural dynamic properties. The results of the polygonal mesh are the average errors of five individual simulations. Since a log-log scale is used it can be seen that the polygonal element mesh has better accuracy than the other mesh discretizations.

2.3. Topology optimization

2.3.1. Static compliance

A typical objective used for static optimization is the minimization of compliance, which provides the stiffest structure for a defined set of loads, and uses a constraint on the volume of the structure. The continuum problem is typically solved using finite elements and can be written in discrete form as:

$$\begin{aligned} &\max_{\rho} \; C(\rho, \mathbf{u}) = \mathbf{f}^{\mathrm{T}}\mathbf{u} \\ &\text{s.t} \quad V(\rho) = \int_{\Omega} \rho dV \le V_S \end{aligned} \tag{2.15}$$

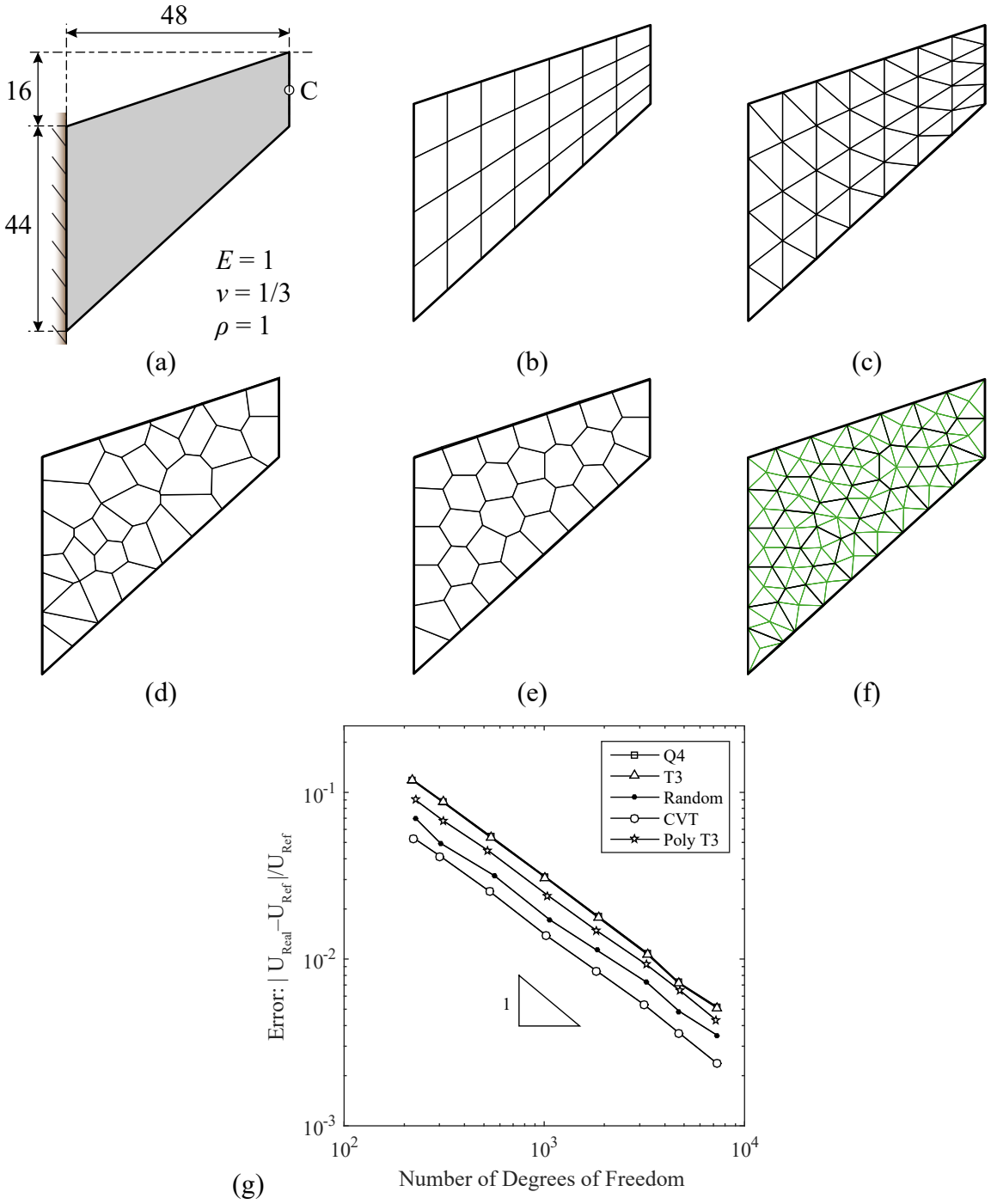

Figure 2.7: (a) Geometry, boundary conditions, and properties for Cook's swept panel problem (Cook et al. 2007, p.108), (b) Quadrilateral (Q4) mesh (28 elements, 40 nodes), (c) Triangular (T3) mesh (56 elements, 40 nodes), (d) Randomized polygonal mesh (30 elements and 58 nodes), (e) Polygonal CVT mesh (30 elements, 61 nodes), (f) Mesh in (e) divided into a mesh of T3 elements (156 elements, 91 nodes), and (g) Convergence of steady state solution with respect to mesh DOFs.

where **f** and **u** are the global force and displacement vectors, V is the volume as a function of the densities, and V_S is the prescribed volume fraction. In the above equation, the density is calculated as a function of the design variables **d**, ($\rho = f(\mathbf{d})$), and the displacement is calculated from the linear equation below:

$$\mathbf{K}(\rho)\mathbf{u} = \mathbf{f} \tag{2.16}$$

2.3.2. Forced vibrations

2.3.2.1. Equation of motion

Forced harmonic vibrations are of importance to practical mechanisms and are often encountered in engineering systems. The equation of motion of a linear dynamic system in a discretized form is:

$$\mathbf{M}\ddot{\mathbf{u}}(t) + \mathbf{C}\dot{\mathbf{u}}(t) + \mathbf{K}\mathbf{u}(t) = \mathbf{f}(t) \tag{2.17}$$

where $\ddot{\mathbf{u}}(t)$, $\dot{\mathbf{u}}(t)$ and $\mathbf{u}(t)$ are acceleration, velocity, displacement vectors at time t, respectively. **M**, **C**, **K** denote mass, damping, and stiffness matrices, and $\mathbf{f}(t)$ is the loading vector as a function of time. It is noted that the system matrices are dependent on a set of design variables **d**. By assuming that the system is subjected to time-harmonic excitations, the excitations and displacements can be described by the following forms

$$\begin{aligned} \mathbf{f}(t) &= \mathbf{F}_R \cos(\omega t) - \mathbf{F}_I \sin(\omega t) \\ \mathbf{u}(t) &= \mathbf{U}_R \cos(\omega t) - \mathbf{U}_I \sin(\omega t) \end{aligned} \tag{2.18}$$

where $\mathbf{F}_R$ and $\mathbf{F}_I$ are the vectors of the excitation force amplitude, $\mathbf{U}_R$ and $\mathbf{U}_I$ denote the vector of the displacement amplitude. ω is the forcing frequency. The substitution Equation 2.18 into Equation 2.17 yields the following equation

$$\begin{aligned} &\omega^2\mathbf{M}\left[-\mathbf{U}_R \cos(\omega t) + \mathbf{U}_I \sin(\omega t)\right] + \omega\mathbf{C}\left[-\mathbf{U}_R \sin(\omega t) - \mathbf{U}_I \cos(\omega t)\right] \\ &+\mathbf{K}\left[\mathbf{U}_R \cos(\omega t) - \mathbf{U}_I \sin(\omega t)\right] = \mathbf{F}_R \cos(\omega t) - \mathbf{F}_I \sin(\omega t) \end{aligned} \tag{2.19}$$

After arranging coefficients of cos(ωt) and sin(ωt), equality condition can be held for all time t as following in a matrix form

$$\begin{bmatrix} \mathbf{K}-\omega^2\mathbf{M} & -\omega\mathbf{C} \\ \omega\mathbf{C} & \mathbf{K}-\omega^2\mathbf{M} \end{bmatrix} \begin{pmatrix} \mathbf{U}_R \\ \mathbf{U}_I \end{pmatrix} = \begin{pmatrix} \mathbf{F}_R \\ \mathbf{F}_I \end{pmatrix} \tag{2.20}$$

Herein, two complex vectors are introduced such as

$$\mathbf{U} = \mathbf{U}_R + i\mathbf{U}_I, \quad \mathbf{F} = \mathbf{F}_R + i\mathbf{F}_I, \quad i \in \mathbb{C} \ \text{(i.e. } i^2 = -1\text{)} \tag{2.21}$$

The real parts of **U** and **F** are denoted by $\mathbf{U}_R$ and $\mathbf{F}_R$, and the imaginary parts of **U** and **F** are denoted by $\mathbf{U}_I$ and $\mathbf{F}_I$. With the complex vector, Equation 2.20 can be expressed in a compact form of complex linear algebraic equations as

$$\left[\mathbf{K} + i\omega\mathbf{C} - \omega^2\mathbf{M}\right]\mathbf{U} = \mathbf{F} \tag{2.22}$$

where the dynamic stiffness matrix **S** is defined as

$$\mathbf{S} = \mathbf{K} + i\omega\mathbf{C} - \omega^2\mathbf{M} \tag{2.23}$$

and thus

$$\mathbf{S}\mathbf{U} = \mathbf{F} \tag{2.24}$$

The complex displacement **U** in Equation 2.22 can be directly solved by a complex matrix solver. Alternatively, Yoon (2010a) implemented the model reduction scheme which can reduce computational resources to solve the complex system equation.

2.3.2.2. Dynamic compliance

The steady-state response of the system under harmonic excitations was considered in the frequency domain to define dynamic compliance (Ma et al. 1995; Jog 2002; Jensen 2007). The dynamic compliance can be expressed as

$$\begin{aligned}\Phi(\rho,\mathbf{U}_{\mathrm{R}}(\rho),\mathbf{U}_{\mathrm{I}}(\rho)&=\int_{\omega_s}^{\omega_e}\left|\mathbf{F}^{\mathrm{T}}\mathbf{U}(\rho)\right|d\omega\\&=\int_{\omega_s}^{\omega_e}\sqrt{\left(\mathbf{F}_{\mathrm{R}}^{\mathrm{T}}\mathbf{U}_{\mathrm{R}}-\mathbf{F}_{\mathrm{I}}^{\mathrm{T}}\mathbf{U}_{\mathrm{I}}\right)^2+\left(\mathbf{F}_{\mathrm{R}}^{\mathrm{T}}\mathbf{U}_{\mathrm{I}}-\mathbf{F}_{\mathrm{I}}^{\mathrm{T}}\mathbf{U}_{\mathrm{R}}\right)^2}\,d\omega\end{aligned}\tag{2.25}$$

where ω_s, ω_e denote the initial and final angular frequency of the external forces, respectively (i.e. the range of frequencies used in optimization). The problem statement of the dynamic compliance optimization with the volume constraint V_S can be described as

$$\begin{aligned}&\min_{\rho}\quad \Phi(\rho,\mathbf{U}_{\mathrm{R}}(\rho),\mathbf{U}_{\mathrm{I}}(\rho))=\int_{\omega_s}^{\omega_e}\left|\mathbf{F}^{\mathrm{T}}\mathbf{U}(\rho)\right|d\omega\\&s.t.\quad V(\rho)=\int_{\Omega}\rho dV\le V_S\\&\text{with}\quad \left[\mathbf{K}+i\omega\mathbf{C}-\omega^2\mathbf{M}\right]\mathbf{U}=\mathbf{F}\end{aligned}\tag{2.26}$$

2.4. Sensitivity analysis

To find optimal solutions for the problems defined in Section 2.3, the sensitivity analysis of the objective functions, and constraints with respect to the density variables is required. Since these are composed of the stiffness and mass terms, the derivatives of $\mathbf{K}_e$ and $\mathbf{M}_e$ are obtained as:

$$\begin{aligned}\frac{\partial\mathbf{K}_e}{\partial d_n}&=\sum_{i=1}^{N_d}\left(\frac{\partial\mathbf{K}_e}{\partial\rho_i}\frac{\partial\rho_i}{\partial d_n}\right)=\sum_{i=1}^{N_d}\left(\frac{\partial\left(\sum_{j=1}^{N_n}\left(\rho_j\right)^p\mathbf{I}_j\right)}{\partial\rho_i}\frac{\partial\rho_i}{\partial d_n}\right)\\&=\sum_{i=1}^{N_d}\left(p\left(\rho_i\right)^{p-1}\mathbf{I}_i\frac{\partial\rho_i}{\partial d_n}\right)\end{aligned}\tag{2.27}$$

and

$$\begin{aligned}\frac{\partial\mathbf{M}_e}{\partial d_n}&=\sum_{i=1}^{N_d}\left(\frac{\partial\mathbf{M}_e}{\partial\rho_i}\frac{\partial\rho_i}{\partial d_n}\right)=\sum_{i=1}^{N_d}\left(\frac{\partial\left(\sum_{j=1}^{N_m}\left(\rho_j\right)^q\mathbf{H}_j\right)}{\partial\rho_i}\frac{\partial\rho_i}{\partial d_n}\right)\\&=\sum_{i=1}^{N_d}\left(q\left(\rho_i\right)^{q-1}\mathbf{H}_i\frac{\partial\rho_i}{\partial d_n}\right)\end{aligned}\tag{2.28}$$

where N_d denotes the number of design variables. Note that the calculation of the sensitivity of the density variables with respect to design variables ($\partial\rho_i/\partial d_n$) is presented in Section 2.5. Subsequently, the sensitivity of static compliance can be calculated from the element displacement $\mathbf{u}_e$ as:

$$\frac{\partial C}{\partial d_n} = -\mathbf{u}_e \frac{\partial \mathbf{K}_e}{\partial d_n} \mathbf{u}_e \tag{2.29}$$

2.4.1. Sensitivity analysis of eigenfrequencies

For free body vibrations, the sensitivity of the fundamental eigenvalue λ for a specific element can be calculated as:

$$\frac{\partial \lambda_j}{\partial d_n} = -\phi_{je}^T \left(\frac{\partial \mathbf{K}_e}{\partial d_n} - \lambda_j \frac{\partial \mathbf{M}_e}{\partial d_n} \right) \phi_{je} \tag{2.30}$$

Where ϕ_{je} is the eigenvector map for element e (Haftka and Adelman 1989). Furthermore the sensitivity of the first eigenvector for the entire structure can be re-written in vector form as:

$$\nabla \lambda_j = \left[-\phi_j^{\mathrm{T}} \left(\frac{\partial \mathbf{K}}{\partial d_1} - \lambda_j \frac{\partial \mathbf{M}}{\partial d_1} \right) \phi_j, \ldots, -\phi_j^{\mathrm{T}} \left(\frac{\partial \mathbf{K}}{\partial d_{N_d}} - \lambda_j \frac{\partial \mathbf{M}}{\partial d_{N_d}} \right) \phi_j \right] \tag{2.31}$$

2.4.2. Sensitivity analysis of dynamic compliance

Sensitivity analysis for the dynamic compliance defined in Equation 2.25 with respect to a design variable d_n is derived by a chain rule for mathematical programming:

$$\frac{\partial \Phi}{\partial d_n} = \sum_{i=1}^{N_d} \left(\frac{\partial \Phi}{\partial \rho_i} \frac{\partial \rho_i}{\partial d_n} \right) \tag{2.32}$$

The derivatives of $\partial\Phi/\partial\rho_i$ can be obtained as follows

$$\frac{\partial \Phi}{\partial \rho_i} = \begin{pmatrix} \nabla_{\mathbf{U}_\mathrm{R}} \Phi \\ \nabla_{\mathbf{U}_\mathrm{I}} \Phi \end{pmatrix}^{\mathrm{T}} \begin{pmatrix} \nabla_{\rho_i} \mathbf{U}_\mathrm{R} \\ \nabla_{\rho_i} \mathbf{U}_\mathrm{I} \end{pmatrix} \tag{2.33}$$

where

$$\begin{pmatrix} \nabla_{\rho_i} \mathbf{U}_{\mathrm{R}} \\ \nabla_{\rho_i} \mathbf{U}_{\mathrm{I}} \end{pmatrix} = \begin{bmatrix} \mathbf{K} - \omega^2 \mathbf{M} & -\omega \mathbf{C} \\ \omega \mathbf{C} & \mathbf{K} - \omega^2 \mathbf{M} \end{bmatrix}^{-1} \cdot \frac{\partial}{\partial \rho_i} \begin{bmatrix} \mathbf{K} - \omega^2 \mathbf{M} & -\omega \mathbf{C} \\ \omega \mathbf{C} & \mathbf{K} - \omega^2 \mathbf{M} \end{bmatrix} \begin{pmatrix} \mathbf{U}_{\mathrm{R}} \\ \mathbf{U}_{\mathrm{I}} \end{pmatrix} \tag{2.34}$$

Equation 2.34 is obtained from derivatives of Equation 2.22. It is assumed that $\mathbf{F}_{\mathrm{R}}$ and $\mathbf{F}_{\mathrm{I}}$ are independent of the filtered density. The term in the first parentheses of Equation 2.33 is used as

$$\begin{pmatrix} \boldsymbol{\lambda}_{\mathrm{R}} \\ \boldsymbol{\lambda}_{\mathrm{I}} \end{pmatrix} = \begin{bmatrix} \mathbf{K} - \omega^2 \mathbf{M} & -\omega \mathbf{C} \\ \omega \mathbf{C} & \mathbf{K} - \omega^2 \mathbf{M} \end{bmatrix}^{-\mathrm{T}} \begin{pmatrix} \nabla_{\mathbf{U}_{\mathrm{R}}} \Phi \\ \nabla_{\mathbf{U}_{\mathrm{I}}} \Phi \end{pmatrix} \tag{2.35}$$

where $\nabla_{\mathbf{U}_{\mathrm{R}}}$ and $\nabla_{\mathbf{U}_{\mathrm{I}}}$ are the gradients of Φ with respect to $\mathbf{U}_{\mathrm{R}}$ and $\mathbf{U}_{\mathrm{I}}$, respectively. Those gradients can be computed as

$$\begin{aligned} \nabla_{\mathbf{U}_{\mathrm{R}}} \Phi &= \frac{1}{\Phi} \left[\left(\mathbf{F}_{\mathrm{R}}^{\mathrm{T}} \mathbf{U}_{\mathrm{R}} - \mathbf{F}_{\mathrm{I}}^{\mathrm{T}} \mathbf{U}_{\mathrm{I}} \right) \mathbf{F}_{\mathrm{R}} + \left(\mathbf{F}_{\mathrm{R}}^{\mathrm{T}} \mathbf{U}_{\mathrm{I}} + \mathbf{F}_{\mathrm{I}}^{\mathrm{T}} \mathbf{U}_{\mathrm{R}} \right) \mathbf{F}_{\mathrm{I}} \right] \\ \nabla_{\mathbf{U}_{\mathrm{I}}} \Phi &= \frac{1}{\Phi} \left[\left(-\mathbf{F}_{\mathrm{R}}^{\mathrm{T}} \mathbf{U}_{\mathrm{R}} + \mathbf{F}_{\mathrm{I}}^{\mathrm{T}} \mathbf{U}_{\mathrm{I}} \right) \mathbf{F}_{\mathrm{I}} + \left(\mathbf{F}_{\mathrm{R}}^{\mathrm{T}} \mathbf{U}_{\mathrm{I}} + \mathbf{F}_{\mathrm{I}}^{\mathrm{T}} \mathbf{U}_{\mathrm{R}} \right) \mathbf{F}_{\mathrm{R}} \right] \end{aligned} \tag{2.36}$$

Similar to Equation 2.21, let $\lambda = \lambda_{\mathrm{R}} + i\lambda_{\mathrm{I}}$, $\nabla_{\mathbf{U}} \Phi = \nabla_{\mathbf{U}_{\mathrm{R}}} \Phi + i \nabla_{\mathbf{U}_{\mathrm{I}}} \Phi$ and assume **M**, **C** and **K** are symmetric. The complex vector form of Equation 2.35 can be described as

$$\nabla_{\mathbf{U}} \Phi = \frac{\mathbf{F}^{\mathrm{T}} \mathbf{U}}{\Phi} \overline{\mathbf{F}} \tag{2.37}$$

where $\overline{\mathbf{F}}$ denotes the complex conjugate of **F**. In addition, Equation 2.35 can be written in the complex form as:

$$\left[\mathbf{K} + i\omega \mathbf{C} - \omega^2 \mathbf{M} \right] \overline{\boldsymbol{\lambda}} = \overline{\nabla_{\mathbf{U}} \Phi} = \frac{\overline{\mathbf{F}}^{\mathrm{T}} \overline{\mathbf{U}}}{\Phi} \mathbf{F} \tag{2.38}$$

where $\overline{\boldsymbol{\lambda}}$ and $\overline{\nabla_{\mathbf{U}} \Phi}$ denote the complex conjugate of $\boldsymbol{\lambda}$ and $\nabla_{\mathbf{U}} \Phi$. For the linear system, one can show that the solution of Equation 2.38 in terms of $\overline{\boldsymbol{\lambda}}$ is proportional to the solution of Equation 2.22 in terms of **U**. Therefore, the conjugate of $\overline{\boldsymbol{\lambda}}$ can be computed by a scalar factor, that is

$$\overline{\boldsymbol{\lambda}} = \frac{\overline{\mathbf{F}}^{\mathrm{T}}\overline{\mathbf{U}}}{\Phi}\mathbf{U} \tag{2.39}$$

Finally, substitution of Equation 2.35 and Equation 2.39 into Equation 2.33 yields the following

$$\begin{aligned}\frac{\partial\Phi}{\partial\rho_i} &= -\begin{pmatrix}\boldsymbol{\lambda}_{\mathrm{R}}\\ \boldsymbol{\lambda}_{\mathrm{I}}\end{pmatrix}^{\mathrm{T}}\left\{\frac{\partial}{\partial\rho_i}\begin{bmatrix}\mathbf{K}-\omega^2\mathbf{M} & -\omega\mathbf{C}\\ \omega\mathbf{C} & \mathbf{K}-\omega^2\mathbf{M}\end{bmatrix}^{-\mathrm{T}}\begin{pmatrix}\mathbf{U}_{\mathrm{R}}\\ \mathbf{U}_{\mathrm{I}}\end{pmatrix}\right\}\\ &= -\mathrm{Re}\left\{\frac{\overline{\mathbf{F}}^{\mathrm{T}}\overline{\mathbf{U}}}{\Phi}\mathbf{U}^{\mathrm{T}}\frac{\partial(\mathbf{K}+i\omega\mathbf{C}-\omega^2\mathbf{M})}{\partial\rho_i}\mathbf{U}\right\}\\ &= -\mathrm{Re}\left\{\boldsymbol{\lambda}^{*}\frac{\partial(\mathbf{K}+i\omega\mathbf{C}-\omega^2\mathbf{M})}{\partial\rho_i}\mathbf{U}\right\}\end{aligned} \tag{2.40}$$

where $\boldsymbol{\lambda}^*$ is the Hermitian transpose of $\boldsymbol{\lambda}$. That is $\boldsymbol{\lambda}^* := \overline{\boldsymbol{\lambda}}^{\mathrm{T}}$.

2.5. Projection scheme

Although the polygonal elements tend to reduce checkerboard and islanding effects in topology optimization, they cannot by themselves provide independence for mesh refinement. Instead, a projection method can be used to achieve a minimum length scale and mesh independence. Previous literature on the subject (Dıaz and Sigmund 1995; Sigmund and Petersson 1998; Bourdin 2001; Guest 2009; Wang et al. 2011) provide different approaches on filtering the sensitivities and densities to obtain mesh independent results. Herein, the previously reported projection method (Guest et al. 2004; Almeida et al. 2009) to filter the density variables is used. This approach employs a linear function to calculate the density ρ of an element i associated with the surrounding design variable mesh. The density of the element would be computed based on the weighted average of the nearby design variables as

$$\rho_i = \frac{\sum_{j\in\Omega_i} w(x_n - x_i)\cdot d_j}{\sum_{j\in\Omega_i} w(x_n - x_i)} \tag{2.41}$$

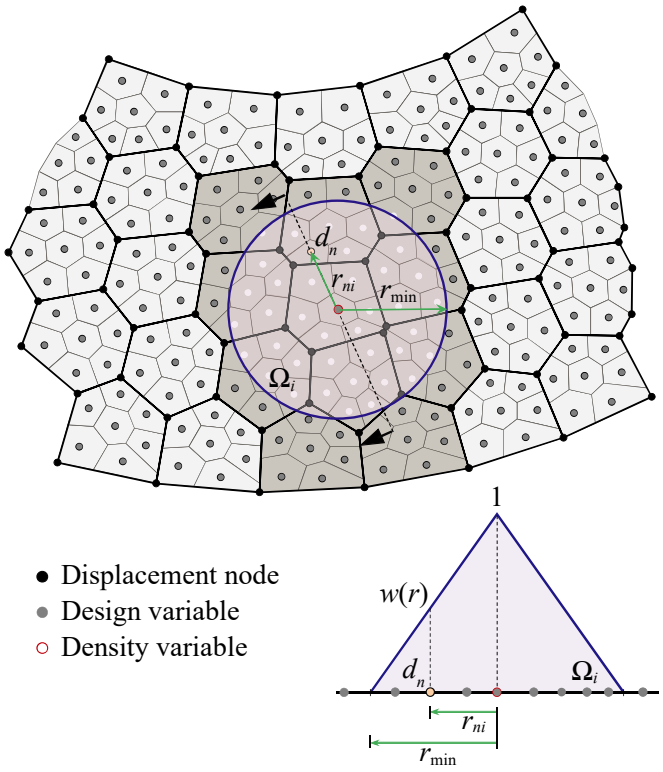

Figure 2.8: Projection scheme from the design variables to the density variable.

where Ω_i is the sub-domain corresponding to density element i, x_n is the position of the centroid of the design variable d_n. The weight function for this linear approach can be defined as

$$w(x_n - x_i) = \begin{cases} \dfrac{r_{\min} - r_{ni}}{r_{\min}} & \text{if } r_{ni} \le r_{\min} \\ 0 & \text{otherwise} \end{cases} \tag{2.42}$$

where r_{ni} is the distance between the centroid of the density element i and the design variable d_n, and $r_{\min}$ is a user defined variable that defines the length scale of the filter. The sensitivities of the element density with respect to the design variables are obtained as:

$$\frac{\partial \rho_i}{\partial d_n} = \frac{w(x_n - x_i)}{\sum_{j \in \Omega_i} w(x_n - x_i)} \tag{2.43}$$

Finally, the projection is written in matrix form **P** as:

$$\mathbf{y} = \mathbf{P}\mathbf{d} \tag{2.44}$$

where **y** is a vector of the filtered densities. As such the projection needs to be calculated only once, at the beginning of the algorithm, whether a linear (above) or nonlinear projection is used. Figure 2.8 shows a graphical representation of the filtering scheme.

2.6. Numerical applications

2.6.1. Static optimization example

The multiresolution scheme presented above is applied to the serpentine domain presented in Talischi et al. (2012b) (Figure 2.9 (a)), with Young's modulus $E = 100$, Poisson's ratio $v = 0.3$, and volume fraction V_S set to be at 50 % of the design domain. The optimality criteria based optimizer is used as the update scheme for the design variables, where Lagrangian multipliers control the upper and lower bounds, and a move limit is used to control the step size (Bendsøe and Sigmund 2004). A minimum length scale parameter of $r_{\min} = 0.3$ is used, and a penalty parameter $p = 4$ is used in the SIMP model. The discretization adopted employs 1,000 elements with the regular polygonal code, as well as with variants of the different multiresolution approaches. Finally, meshes of 10,000 and 20,000 elements are considered with the regular PolyTOP code to compare the solutions between the conventional and the PolyMTOP frameworks when a similar number of design variables are used. For a sample mesh of 1,000 elements, the distribution of n-gons was 8 P4, 236 P5, 633 P6, and 123 P7, and the average diameter of the elements was 0.3. This is a typical element size distribution produced by the PolyMesher software, and there were no elements lower than a P4 or higher than a P7, although the code can use such elements as well. Figure 2.9 shows the static optimal results for the different meshes, where the multiresolution approaches provide a high resolution solution (Figure 2.9 (e) and 2.9 (f)) that is essentially the same as that of the fine finite element case (Figure 2.9 (c) and 2.9 (d)). Table 2.1 shows the averaged parameters and computational time for five analyses of each different case[1] carried out to 200 optimization

[1] A modern (2014) quad-core 3.30 GHz Inter Xeon(R) processor is used for the analysis.

iterations. The multiresolution approach takes roughly the same time in the FE analysis as the coarse mesh since there is the same number of DOFs in the system, while there is an increase in the initialization time (meshing and initial calculation of the **K** and **M** matrices) and optimization time (calculating gradients and using optimization algorithm). The multiresolution approaches are still about four times faster than the fine conventional polygonal mesh, where most of the additional time is spent in the FE analysis. From Table 2.1, the meshes with 1,000 elements have roughly the same compliance whereas the fine element discretization has a somewhat higher compliance. This is because the finer mesh can better estimate the displacement field for the same structure. As noted in Nguyen et al. (2009) the MTOP methods can provide mesh independence even when a small $r_{\min}$ is used, and in such cases, the MTOP approach could still estimate the displacement field accurately. The convergence history of static compliance for the first 50 steps of individual analyses is shown in Figure 2.10. Note that all methods follow the same convergence pattern and result in essentially the same optimal compliance (only 1 % difference).

Table 2.1: Computational time for static optimization using regular and PolyMTOP approaches.

Discretization	Elements	Design/ Density	Initialization time (Seconds)		Optimization time (Seconds)		Static	Total
		variables	PolyMesher	K	FE Analysis	Optimization	Compliance	time
Coarse polygonal	1000	100	6.7	1.2	7.4	5.4	4.71	20.7
Fine polygonal	10000	10000	27.2	11.9	112.6	52.2	4.77	203.9
Fine polygonal	20000	20000	55.2	23.9	331.7	106.9	4.78	517.7
PolyMTOP/n10	1000	10000	9.2	10.3	12.8	13.0	4.70	45.4
PolyMTOP/n20	1000	20000	12.6	21.2	19.5	21.1	4.69	74.4

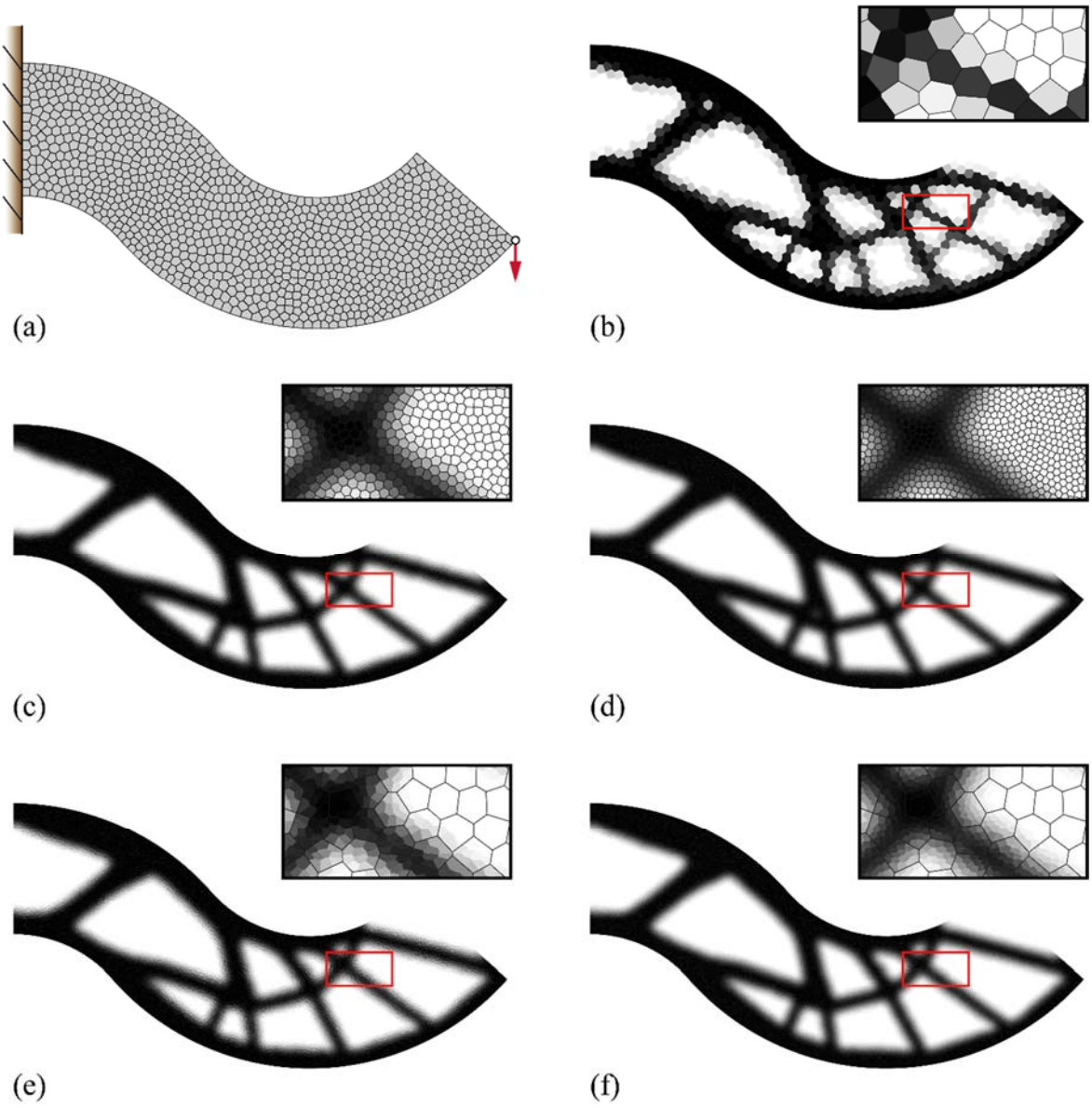

Figure 2.9: Static optimization of serpentine domain (Talischi et al. 2012b): (a) Design domain discretized with polygonal elements, loading and boundary conditions, (b) 1000 n-gons, (c) 10000 n-gons, (d) 20000 n-gons, (e) Pn/n10 approach, 1000 n-gons, 10000 design variables, and (f) Pn/n20 approach, 1000 n-gons, 20000 design variables.

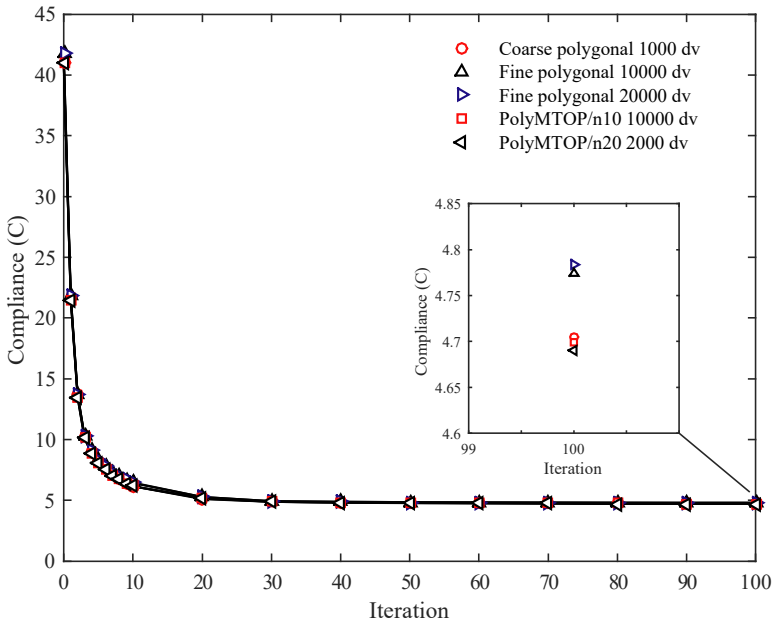

Figure 2.10: Convergence history for static compliance minimization of serpentine domain (dv = design/density variables).

2.6.2. Forced vibration optimization example

A numerical example for minimization of the dynamic compliance is considered under harmonic excitations. The geometry of a curved structure is generated using PolyMesher (Talischi et al. 2012a) based on the parameters shown in Figure 2.11. The structure is anchored at the bottom end and restrained in the horizontal direction at the left end. Harmonic excitations are applied at the arrows inscribed in Figure 2.11. For the topology optimization, Young's modulus E, Poisson's ratio ν and mass density are set to 1 N/m^2, 0.3 and 1 kg/m^3, respectively. The volume fraction V_S is constrained to be 40 % of the design domain. The natural mode shapes and frequencies of the initial design domain which is the continuum domain completely filled with initial volume fraction are shown in Figure 2.12. The initial angular frequency of the forced vibration ω_s = 0.0 and the final one ω_e = 0.015 are set with the magnitude of force **F** =1, in Equation 2.25. Two loading conditions such as a single load case where all four loads act simultaneously and multiple load cases where $\mathbf{F}_1$, $\mathbf{F}_2$, $\mathbf{F}_3$, and $\mathbf{F}_4$ represent each load case are considered for the optimization problem.

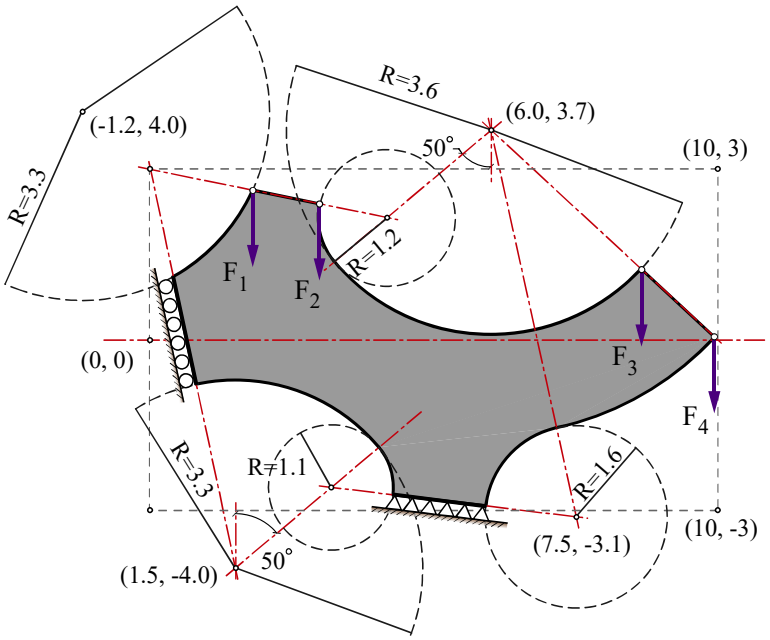

Figure 2.11: Geometry of design domain, loadings, and boundary configuration.

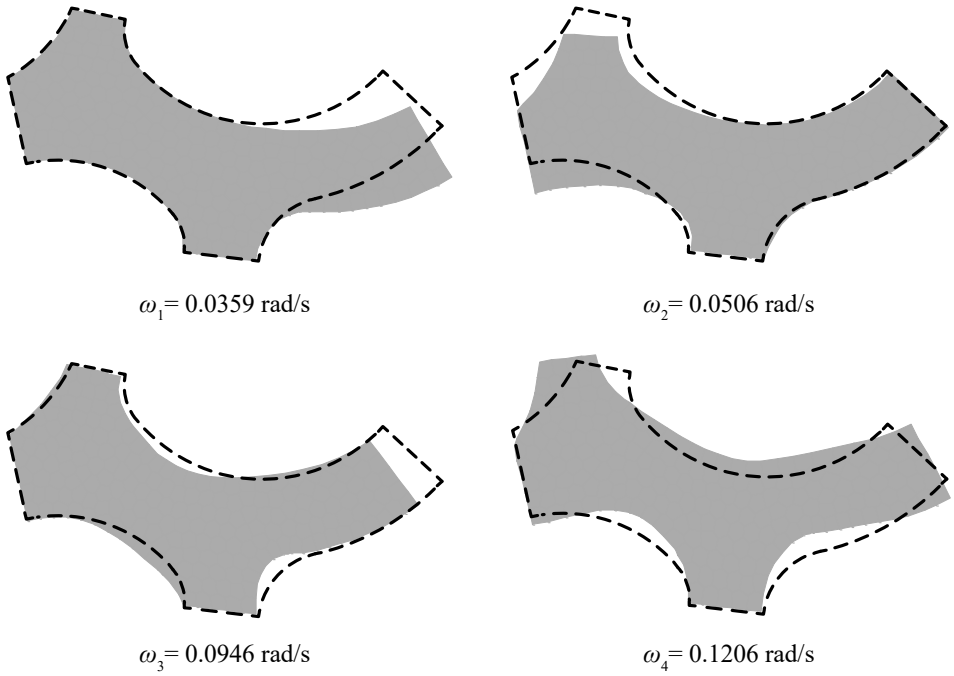

Figure 2.12: Natural mode shapes and natural frequencies.

For the multiple load cases, the optimization problem can be formulated as minimizing the sum of dynamic compliance induced by all loads. Therefore, the optimization problem considering multiple load cases can be stated as follows.

$$\begin{aligned} \min_{\rho} \quad & \sum_{i=1}^{4} \int_{\omega_s}^{\omega_e} \left| \mathbf{F}_i^{\mathrm{T}} \mathbf{U}_i(\rho) \right| d\omega \\ s.t. \quad & V(\rho) = \int_{\Omega} \rho dV \le V_S \\ with \quad & \left[\mathbf{K} - i\omega \mathbf{C} - \omega^2 \mathbf{M} \right] \mathbf{U}_i = \mathbf{F}_i \end{aligned} \tag{2.45}$$

The design domain is discretized with 900 n-gons for both coarse and PolyMTOP analyses, and the projection function with a radius $r_{\min} = 0.14$ is used. The penalization factors for the stiffness and mass are chosen as $p = 3$ and $q = 1$, respectively. The Method of Moving Asymptotes (MMA) (Svanberg 1987) is implemented in this example to solve the optimization problem for dynamic compliance. Coarse meshes with the optimal topology are presented in Figure 2.13 (a) and 2.13 (d) (multiple and single load case respectively), while parts (c) and (f) of that figure show the improved solutions through the use of the PolyMTOP approach. The length of the parameter $r_{\min}$ is shown graphically as a black line next to the element mesh in cutouts of Figure 2.13 and subsequent figures. It is noted that the solution for the single load case is significantly different from the multiple load cases problem, particularly the material distributions on the left part of the design domain. Furthermore, a fine conventional mesh with 13,500 elements (Figure 2.13 (b) and 2.13 (e)) is also optimized to verify the solution and to compare the time improvement from the PolyMTOP scheme. For all cases, the dynamic response of the initial structure subject to periodic excitations is compared with the response of the optimized (Figure 2.14). As can be seen from Figure 2.14, the dynamic resonant response in the range of interest (ω_s = 0.0 to ω_e = 0.015) is significantly reduced for all cases through the optimization. While keeping the volume the same, the area underneath the dynamic response curve is reduced (Figure 2.14), and there is improved dynamic behavior for both the single and multiple load cases. The optimal designs are similar for the coarse, the fine, and the MTOP meshes, however, the dynamic resonance, although similar is

not identical after the optimization. The difference in the higher frequency response (i.e. above ω = 0.03) can be attributed to the different performance of the FE analysis for each method as discussed in Section 2.2.3. Finally, the convergence results of the dynamic compliance for the six cases are shown in Figure 2.15. Furthermore, topology optimization for the dynamic compliance problem is carried out using the SIMP and RAMP continuation schemes. That is, SIMP penalization is performed with continuation starting with p = 1 and being incremented by 0.5 until 4. RAMP penalization s is set to zero for one step, and continuation is subsequently performed by doubling s from 1 to 64. 900 n-gon meshes identical to the previous example were implemented for this problem in order to investigate the influence of the SIMP, RAMP, and the continuation approach on optimal topologies. Figure 2.16 shows optimal topologies for the single and multiple load cases with both the SIMP and RAMP schemes using the continuation approach. Based on results of part (c) and part (f) in Figure 2.13 and results of part (a) and (b) in Figure 2.16, one can notice that the continuation of the penalization factor has affected the optimal solutions, especially in the scenario with multiple load cases. Moreover, different topologies are obtained with each SIMP and RAMP scheme as shown in Figure 2.16. Although the topologies are different for these cases, the optimal dynamic response for all cases is somewhat similar. Note that in the continuation cases the optimized response is not necessarily lower than that of the initial configuration since a different penalization factor is used in each case. Again, the compliance converges in the same manner for all methods. Finally, Figure 2.17 shows the normalized computational time of the cases in Figure 2.13 for 50 iterations of the optimization scheme. It can be noted that using a fine mesh in PolyTOP alone is about four times more expensive than using the PolyMTOP method with less finite elements and a similar number of density, and design variables.

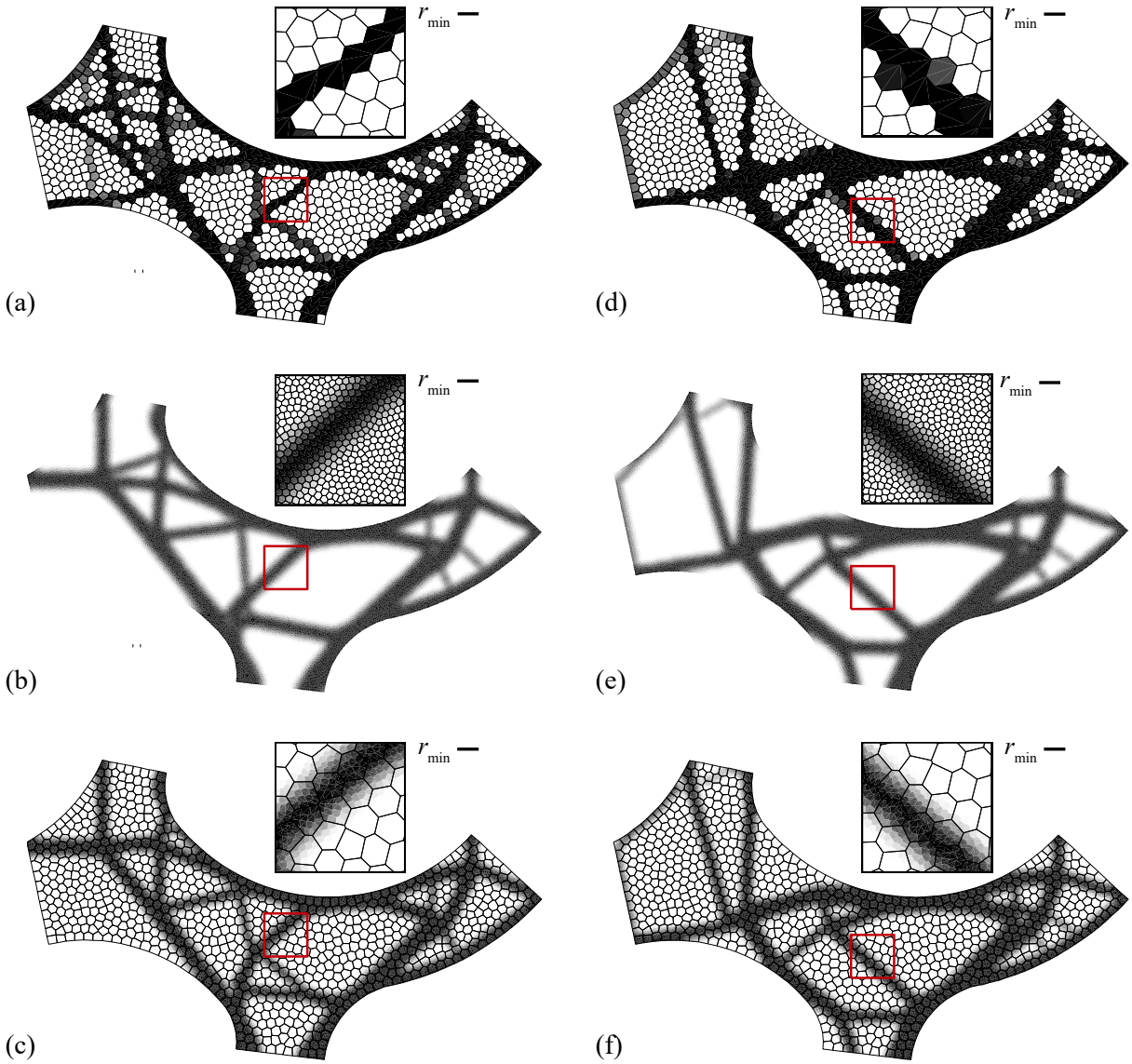

Figure 2.13: Comparison of optimal topologies for multipoint forced vibration problem. Multiple load cases: (a) 900 n-gons, (b) 13500 n-gons, and (c) Pn/n15 approach, 900 n-gons, 13500 design variables. Single load case: (d) 900 n-gons, (e) 13500 n-gons, and (f) Pn/n15 approach, 900 n-gons, 13500 design variables.

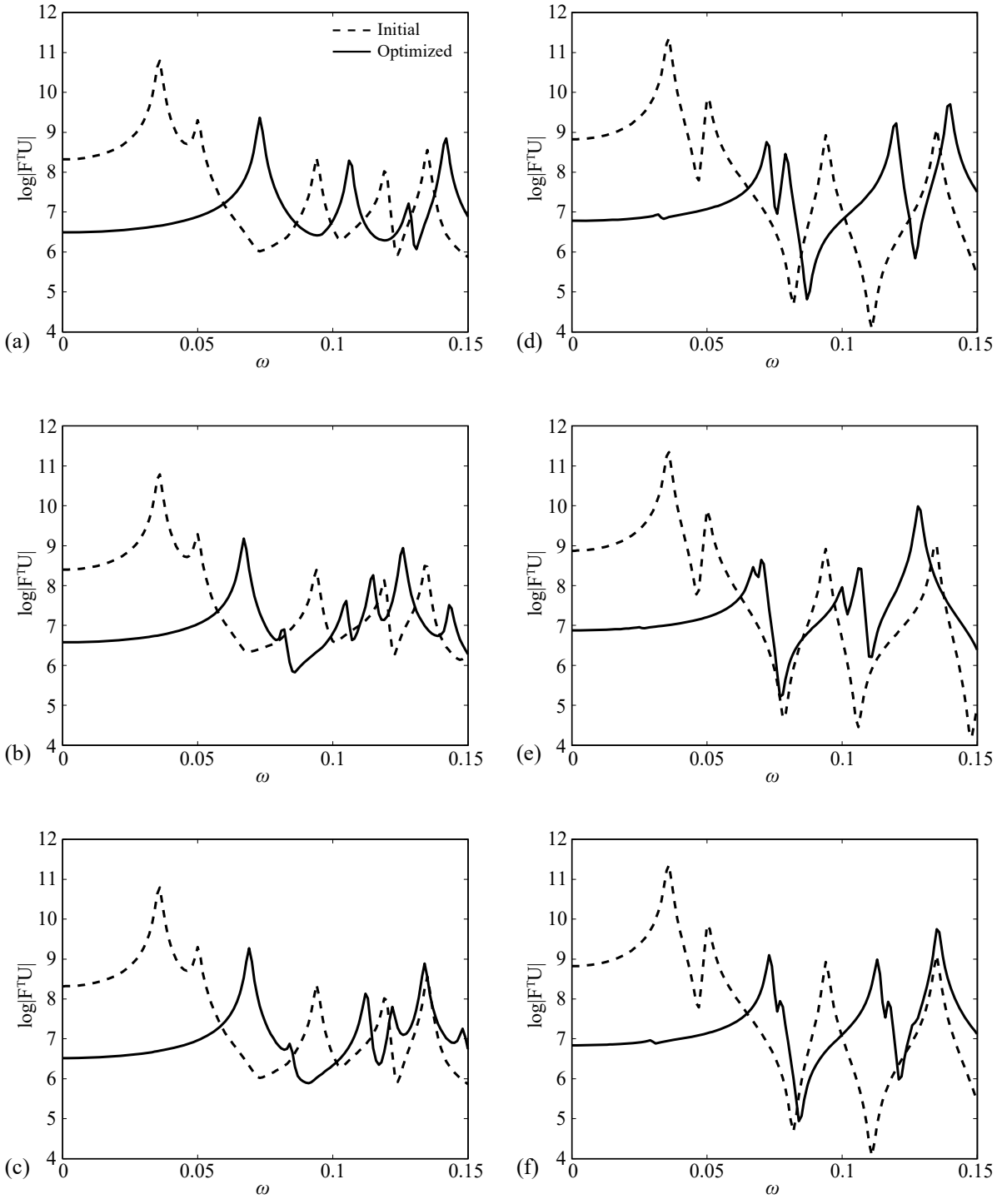

Figure 2.14: The initial and optimized resonant response of the structures: Multiple load cases: (a) 900 n-gons, (b) 13500 n-gons, (c) Pn/n15 approach, 900 n-gons, 13500 design variables. Single load case: (d) 900 n-gons, (e) 13500 n-gons, and (f) Pn/n15 approach, 900 n-gons, 13500 design variables.

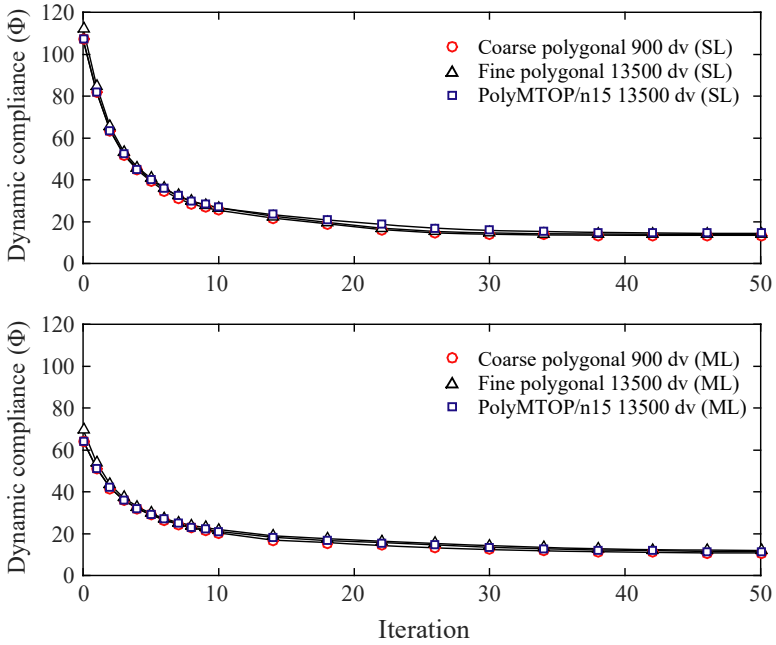

Figure 2.15: Convergence history for optimization of dynamic compliance of multipoint excitation domain (dv = design/density variables, SL = single load case, ML = multiple load cases).

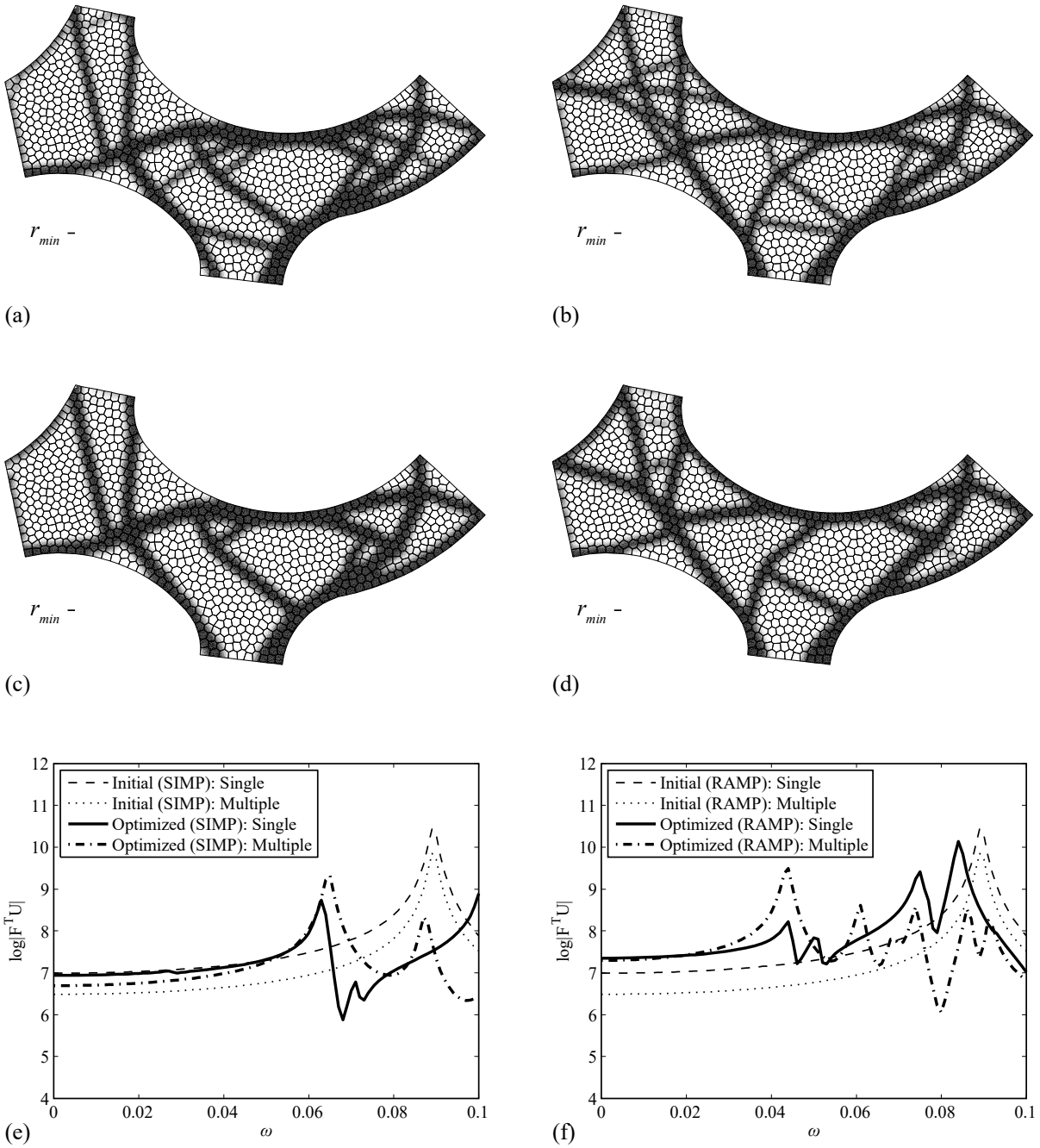

Figure 2.16: Minimization of dynamic compliance. SIMP, continuation of p (1 − 4): (a) Single load case, and (b) Multiple load cases. RAMP, continuation of s (0 − 64): (c) Single load case, (d) Multiple load cases, (e) resonant response of the structures (SIMP), and (f) resonant response of the structures (RAMP).

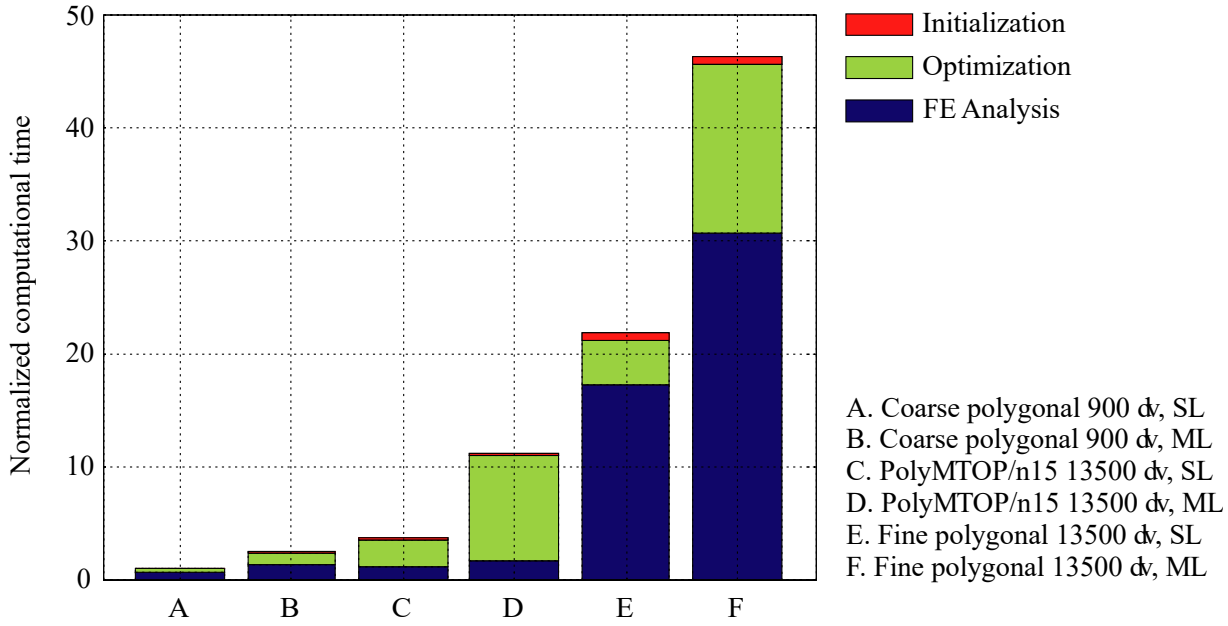

Figure 2.17: Comparison of normalized computational times for optimization of forced vibration of multipoint excitation domain (dv = design/density variables, SL = single load case, ML = multiple load cases). Times are normalized with respect to the SL coarse mesh computation (89 seconds in this case).

2.7. Concluding remarks

This chapter introduces a method for combining a coarse finite element mesh with finer design and density meshes to obtain high quality optimization solutions for a reduced computational cost. Polygonal elements presented in recently published PolyTOP software are shown to approximate dynamic behaviors better than other conventional elements and are thereby used as the focus for this study. Non-matching sub-discretization is investigated to split up the polygonal elements in order to facilitate the multiresolution analysis. The computational approach is shown to be particularly beneficial for structural dynamics problems such as forced vibration optimization since these problems require substantial time in finite element analysis. The multiresolution approach produces solutions with high resolution through an increase in the time required for optimizing the design variables. However, the approach can use a smaller number of elements and nodes, and can thereby avoid increasing the costlier finite element calculations. Several examples

of the polygonal multiresolution topology optimization are shown for static and dynamic cases. These include: a curved beam domain and a complex beam domain. The results show that the algorithm is effective at producing high resolution results suitable for efficient and computationally effective structural design. The efficient scheme for optimization of structures with dynamic loads could be useful in civil, mechanical, and aerospace engineering applications where the structural dynamic properties need to be controlled. The concepts shown herein could further be extended to acoustic and wave propagation problems where eigenfrequency response needs to be controlled.

Chapter 3

Structural topology optimization under constraints on instantaneous failure probability

Accurate prediction of stochastic responses of a structure caused by natural hazards or operations of nonstructural components is crucial to achieve an effective design. In this regard, it is of great significance to incorporate the impact of uncertainty on topology optimization of structures under constraints on their stochastic responses. Despite recent technological advances, the theoretical framework remains inadequate to overcome computational challenges of incorporating stochastic responses to topology optimization. Thus, this chapter presents a theoretical framework that integrates random vibration theories with topology optimization using a discrete representation of stochastic excitations. This chapter also discusses the development of parameter sensitivity of dynamic responses in order to enable the use of efficient gradient-based optimization algorithms. The proposed topology optimization framework and sensitivity method enable efficient topology optimization of structures under stochastic excitations, which is successfully demonstrated by numerical examples of structures under stochastic ground motion excitations.

3.1. Introduction

Topology optimization aims to identify optimal material layouts of problems through mathematical programming while fulfilling given design constraints (Bendsøe and Sigmund 2003). Extensive research in the field of topology optimization has led to development of many theories, methods and algorithms to overcome well-known issues such as numerical instability in checkerboard problems (Diaz and Sigmund 1995; Jog and Haber 1996), mesh dependency problems, and ill-posed and lacking solutions in continuum settings (Kohn and Strang 1986;

Sigmund and Petersson 1998). A topology problem can be well-posed by using relaxation (Bendsøe and Kikuchi 1988) or restriction of the design space (Kim and Yoon 2000; Poulsen 2002; Guest et al. 2004). An important example of such advancement in the field is the development of Solid Isotropic Material with Penalization (SIMP; Bendsøe 1989; Rozvany et al. 1992; Bendsøe and Sigmund 1999), a method designed to obtain physical properties of the intermediate densities. However, SIMP can lead to numerical instabilities such as "checker-board" effects, i.e. the formation of areas with alternating solid and void distribution in the design domain. To resolve issues associated with the checker-board (Diaz and Sigmund 1995) and the mesh dependency, various projection schemes (Guest et al. 2004; Sigmund 2007) and filtering techniques have been developed previously (Sigmund and Petersson 1998; Bourdin 2001).

Although the field of deterministic topology optimization has been well developed, various technical challenges still exist, especially in achieving reliable solutions under uncertainty. A recent trend has shown active research efforts in finding topologies under uncertainty, which is often termed as reliability based topology optimization (RBTO) (Maute and Frangopol 2003; Allen et al. 2004; Kang et al. 2004; Kharmanda et al. 2004; Kim et al. 2006; Guest and Igusa 2008; Rozvany 2008; Lógó et al. 2009; Luo et al. 2009; Chen et al. 2010; Jalalpour et al. 2013). These challenges further complicate topology optimization when it is necessary to maintain balance between architecture and engineering criteria and to solve large-scale problems for high-rise buildings. In order to address these issues, a new method for system reliability-based topology optimization (SRBTO; Nguyen et al. 2011) was recently developed so that a probabilistic constraint on a system event consisting of multiple component events can be satisfied. This methodology provides an effective way to overcome challenges in topology optimization under probabilistic constraints on system failure events by incorporating the matrix based system reliability (MSR) method (Song and Kang 2009) into topology optimization. Despite these recent technical advances, it still remains elusive how uncertain responses of structures under random vibrations need to be addressed. It is noted that one of the most fundamental requirements for

building structures is to withstand various uncertain loads such as earthquake ground motions, wind loads, and ocean waves. The structural design, therefore, needs to ensure safe and reliable operations over a prolonged period despite random excitations caused by hazardous events. Such a stochastic excitation is often described by a random process $f(t)$, which is the family (ensemble) of all possible random time histories (Lutes and Sarkani 2003). Alternatively, the random process can be understood as a collection of random variables defined at an infinite number of points along the time axis. For instance, at a given time point $t = t_i$, $f(t_i)$ is a random variable that represents a set of possible realizations across the ensemble. Since the future realization of the random process is not completely represented by some specific cases or scenarios, predictions need to be made on the basis of probability. Therefore, a reasonable representation of the uncertainty in the random process is needed to obtain a meaningful solution for given engineering problems. This has led to active research efforts in developing random process models that can describe the uncertainty in input stochastic processes during dynamic analysis of structures subjected to random excitations.

To model and simulate stochastic processes properly, many approaches, algorithms, and methods were developed in the past. Some of the most widely used approaches are Monte Carlo simulation techniques (Shinozuka 1972; Kitagawa 1996; Liu and Chen 1998), autoregressive methods (Spanos and Mignolet 1987; Mignolet and Spanos 1987; Deodatis and Shinozuka 1988; Novak et al. 1995), and autoregressive moving average methods (Spanos and Mignolet 1990; Gersch and Yonemoto 1977). The spectral representation method (Shinozuka and Jan 1972; Shinozuka and Deodatis 1991, 1996; Grigoriu 1993; Grigoriu 2003; Chen and Kareem 2005; Chen and Letchford 2005) has been widely utilized to simulate the random process by using a series of deterministic basis functions with uncorrelated random coefficients. The discrete representation method describes the stochastic processes in terms of a finite number of uncorrelated random variables and filters describing frequency contents and nonstationarity of the processes. Der Kiureghian (2000), Rezaeian and Der Kiureghian (2008, 2010, 2012) used the discrete representation method along with modulating functions to model random ground motions. Konakli

and Der Kiureghian (2012) used the discrete representation method to define statistical characteristic of ground motions considering various soil properties. Based on the discrete representation of input stochastic processes, Fujimura and Der Kiureghian (2007) developed a Tail-Equivalent Linearization Method (TELM) to find an equivalent linear system by matching a first-order approximation of a tail probability between a linear response and nonlinear response.

The most recent research on topology optimization has been primarily focused on structures under static loadings. Such approaches may fail to address important concerns caused by random excitations in structural design practices. For example, lateral-force-resisting structural systems should be designed to effectively control random dynamic responses caused by natural hazards or operations of non-structural components. In response to such needs and challenges, research efforts in topology optimization of structures under constraints on dynamic response have been increased recently. However, high computational cost remains as a major obstacle in incorporating dynamic/stochastic responses of structures into topology optimization. Some advances have been made in the field of research by dealing with dynamic characteristics of the structure under special loading conditions instead of actual response time histories under given deterministic or stochastic input excitations. For example, Diaz and Kikuchi (1992) dealt with eigenfrequencies as the key dynamic characteristic during topology optimization of structures under dynamic loadings. Since then, several methods and formulations related to frequencies optimization have been developed (Ma et al. 1994; Ma et al. 1995; Jensen and Pedersen 2006; Du and Olhoff 2007). Such a topology optimization approach often aims to maximize the fundamental frequency to indirectly control dynamic responses. An alternative approach is to minimize the dynamic response of a structure for a given dominant frequency of dynamic loadings (Maeda et al. 2006; Rubio et al. 2011). Min et al. (1999) used a relaxation-homogenization theory to address minimal compliance during a certain time interval in structural topology optimization problems under dynamic loadings. Such methods, however, are limited in terms of incorporating general structural behavior addressed in actual design practices into objective functions and constraints of topology optimization.

In order to overcome these challenges, this chapter introduces a new method that incorporates random vibration theories into topology optimization to satisfy probabilistic constraints defined in terms of stochastic responses. The discrete representation method of the stochastic process is adopted in the chapter because the discretized form of a continuous process has practical advantages such as reducing the computational effort, facilitating implementation and identifying characteristics of the stochastic process. Moreover, an analytical sensitivity formulation is derived to enable the use of gradient-based optimizers.

The remainder of the chapter is structured as follows. First, the theoretical basis of the discrete representation method of random vibration is provided. It is followed by a discussion on how to characterize a linear structural system subjected to Gaussian stochastic excitations using the structural reliability theory. Next, the details of the proposed topology optimization method and a new formulation for parameter sensitivities of dynamic responses are discussed. The chapter demonstrates the proposed methods with numerical examples and provides a discussion of the results. Finally, the chapter concludes with future directions and possible extension of our findings.

3.2. Discrete representation of stochastic excitations

In order to effectively incorporate stochastic processes into topology optimization, this work adopts the discrete representation method. In particular, random ground motions are described by the discrete representation method for topology optimization of structures under seismic excitations.

3.2.1. Discrete representation of stochastic process

The discrete representation method describes an input stochastic process in terms of a finite number of standard normal random variables by use of a deterministic function representing the frequency content and nonstationarity (Rezaeian and Der Kiureghian 2008, 2012). This allows for evaluation of the failure probability associated with stochastic response exceeding a threshold at a given time point ("instantaneous failure probability") or crossing events during a time period ("first-passage probability") using structural reliability analysis methods, such as First- and Second-Order Reliability Methods (FORM and SORM; Der Kiureghian 2000, Der Kiureghian 2005). For example, a zero-mean stationary Gaussian input process $f(t)$ is discretized as

$$f(t) = \sum_{i=1}^{n} v_i s_i(t) = \mathbf{s}(t)^{\mathrm{T}} \mathbf{v} \tag{3.1}$$

where $\mathbf{v} = [v_1, v_2 \ldots, v_n]^{\mathrm{T}}$ is a vector of n uncorrelated standard normal random variables. Thus, $\mathrm{E}[v_i] = 0$ and $\mathrm{E}[v_j v_k] = \delta_{jk}$ in which $\mathrm{E}[\cdot]$ denotes the mathematical expectation and δ_{jk} is the Kronecker delta. $\mathbf{s}(t) = [s_1(t),\ldots, s_n(t)]^{\mathrm{T}}$ is a vector of deterministic basis functions representing the spectral characteristics of the process. To obtain the basis function, one can use one of the available methods such as the Karhunen-Loève orthogonal expansion (Spanos and Ghanem 1989), the orthogonal series expansion approach (Zhang and Ellingwood 1994), and the optimal linear estimation method (Li and Der Kiureghian 1993).

3.2.2. Discrete representation of earthquake ground motions

A stochastic ground motion can be modeled as the response of a linear filter to a random pulse train. The filter may represent the characteristic of soil medium, which earthquake ground motion passes through. For instance, the response of the linear filter excited by the white noise $W(t)$ can be expressed by a convolution integral employing the impulse-response function of the filter, $h_f(\cdot)$, i.e.

$$f(t) = \int_0^t h_f(t-\tau) W(\tau) d\tau \tag{3.2}$$

The power spectral density function of the white noise $W(t)$ is given as constant, i.e. $\Phi_{WW}(\omega) = \Phi_0$. The white noise process can be represented approximately by rectangular pulses in closely spaced time steps. A random height of the pulse, which may stand for sporadic ground ruptures, is defined by the temporal average of W(t) over each time interval, i.e.

$$W(t) \cong W_i = \frac{1}{\Delta t} \int_{t_i}^{t_{i+1}} W(\tau) d\tau, \quad t \in (t_i, t_{i+1}] \tag{3.3}$$

where $\Delta t = t_{i+1} - t_i$. Assuming $W(t)$ is a zero-mean Gaussian process, the integration of Equation 3.3 results in a Gaussian random variable W_i. The mean of W_i is derived as

$$\mathrm{E}[W_i] = \mathrm{E}\left[\frac{1}{\Delta t} \int_{t_i}^{t_{i+1}} W(\tau) d\tau \right] = \frac{1}{\Delta t} \cdot \mathrm{E}\left[\int_{t_i}^{t_{i+1}} W(\tau) d\tau \right] = 0 \tag{3.4}$$

The variance of W_i is derived as

$$\begin{aligned} \mathrm{Var}[W_i] &= \mathrm{E}\left[\frac{1}{(\Delta t)^2} \int_{t_i}^{t_{i+1}} \int_{t_i}^{t_{i+1}} W(\tau_1) W(\tau_2) d\tau_1 d\tau_2 \right] = \frac{1}{(\Delta t)^2} \int_{t_i}^{t_{i+1}} \int_{t_i}^{t_{i+1}} R_{WW}(\tau_1, \tau_2) d\tau_1 d\tau_2 \\ &= \frac{1}{(\Delta t)^2} \int_{t_i}^{t_{i+1}} \int_{t_i}^{t_{i+1}} \left[2\pi\Phi_0 \cdot \delta(\tau_2 - \tau_1) \right] d\tau_1 d\tau_2 = \frac{1}{(\Delta t)^2} \int_{t_i}^{t_{i+1}} 2\pi\Phi_0 d\tau_2 = \frac{2\pi\Phi_0}{\Delta t} \end{aligned} \tag{3.5}$$

where $R_{WW}(\cdot)$ is the auto-correlation function of $W(t)$, and $\delta(\cdot)$ is the Dirac delta function. In summary, W_i is the zero-mean Gaussian random variable with the variance $2\pi\Phi_0 / \Delta t$. One can also show that W_i and W_j ($i \neq j$) are uncorrelated. Therefore, the Gaussian white noise process $W(t)$ can be represented by a set of uncorrelated standard normal random variables,

$$W_i = \sqrt{2\pi\Phi_0 / \Delta t} \cdot v_i, \quad i = 1, \ldots, n \tag{3.6}$$

where n denotes the number of the time intervals for the time period (0, t). Substituting Equations 3.3 and 3.6 into Equation 3.2, the filter response of the Gaussian white noise process is approximately derived in a discrete form

$$
\begin{aligned}
f(t) &\cong \sum_{i=1}^{n} W_i \cdot h_f(t-t_i)\Delta t = \sum_{i=1}^{n} \sqrt{2\pi\Phi_0 / \Delta t} \cdot v_i \cdot h_f(t-t_i)\Delta t \\
&= \sum_{i=1}^{n} \sqrt{2\pi\Phi_0 \Delta t} \cdot h_f(t-t_i) \cdot v_i \\
&= \mathbf{s}(t)^{\mathrm{T}} \mathbf{v}
\end{aligned}
\tag{3.7}
$$

In this case, the basis functions in the vector $\mathbf{s}(t)$ are thus derived as $s_i(t) = \sqrt{2\pi\Phi_0\Delta t} \cdot h_f(t-t_i)$. It should be noted that the model in Equation 3.7 is just one example of modeling stochastic ground motions by the discrete representation method, and one can construct such a model fitted for the characteristics of ground motions at a specific site. For example, Rezaeian and Der Kiureghian (2008, 2012) incorporated non-stationarity of spatially varying ground motions into such models and developed a method for simulating an ensemble of synthetic ground motions. Konakli and Der Kiureghian (2012) developed a conditioning simulation method for generating stationary processes and extended the method to non-stationary models.

3.2.3. Characterization of linear system under stochastic excitations

If a stochastic excitation is described by the discrete representation method discussed above, the stochastic responses of a structural system can be also described by a finite number of random variables. For example, a displacement time history $u(t)$ of the linear system under the stochastic excitation $f(t)$ is derived as

$$
\begin{aligned}
u(t) &= \int_0^t f(\tau) h_s(t-\tau) d\tau = \int_0^t \left[\mathbf{s}(\tau)^{\mathrm{T}} \mathbf{v} \right] \cdot h_s(t-\tau) d\tau = \int_0^t \sum_{i=1}^{n} s_i(\tau) v_i h_s(t-\tau) d\tau \\
&= \sum_{i=1}^{n} a_i(t) \cdot v_i = \mathbf{a}(t)^{\mathrm{T}} \mathbf{v}
\end{aligned}
\tag{3.8}
$$

where $h_s(t)$ is the unit impulse response function of the structural system, and $\mathbf{a}(t)$ denotes a vector of deterministic basis functions

$$
a_i(t) = \int_0^t s_i(\tau) h_s(t-\tau) d\tau, \quad i = 1, \ldots, n \tag{3.9}
$$

As a result, failure events defined in terms of dynamic response can be described in the space of standard normal random variables **v**. For example, an 'instantaneous' failure event described in terms of the displacement of the linear system at time $t = t_0$, i.e. $E_f = \{u(t_0) \geq u_0\}$ where u_0 is a selected threshold can be represented by a linear half space $u_0 - u(t_0) = u_0 - \mathbf{a}(t_0)^{\mathrm{T}}\mathbf{v} \leq 0$, as illustrated in Figure 3.1. From theories of structural reliability, the failure probability $P(E_f)$ is then obtained by a closed-form solution $P(u(t_0) \geq u_0) = \Phi[-\beta(u_0,t_0)]$ where $\Phi[\cdot]$ is the cumulative distribution function (CDF) of the standard normal distribution, and $\beta(u_0,t_0) = u_0/\|\mathbf{a}(t_0)\|$ is the reliability index. The reliability index is alternatively computed by $\beta = \hat{\boldsymbol{\alpha}}(t_0) \cdot \mathbf{v}^*$ where $\hat{\boldsymbol{\alpha}}(t_0)$ denotes the negative normalized gradient vector of the limit-state function evaluated at the so-called design point or most probable point (MPP) $\mathbf{v}^*$, which is obtained by $u_0 \cdot \mathbf{a}(t_0)/\|\mathbf{a}(t_0)\|^2$ (Der Kiureghian 2000). To facilitate finding $\mathbf{a}(t)$ in finite element settings without deriving the impulse response function necessarily, the following procedure is proposed in this work: First, a random sample of **v** is created by generating n uncorrelated standard normal random variables. Second, an input time history $f(t)$ is computed by substituting **v** into Equation 3.7. Third, the displacement time history $u(t_i),\ i = 1,2,...,n$ of structures for the input time history $f(t)$ is computed using a time integration scheme such as Newmark method (1959). Then, substituting the computed time history $u(t_i),\ i = 1,2,...,n$, and the random sample of **v** into Equation 3.8, one can obtain

$$\begin{aligned}
u(t_1) &= a_1(t_1)v_1 \\
u(t_2) &= a_1(t_2)v_1 + a_2(t_2)v_2 \\
u(t_3) &= a_1(t_3)v_1 + a_2(t_3)v_2 + a_3(t_3)v_3 \\
&\vdots \\
u(t_{n-1}) &= a_1(t_{n-1})v_1 + a_2(t_{n-1})v_2 + \ldots + a_{n-1}(t_{n-1})v_{n-1} \\
u(t_n) &= a_1(t_n)v_1 + a_2(t_n)v_2 + \ldots + a_{n-1}(t_n)v_{n-1} + a_n(t_n)v_n
\end{aligned} \tag{3.10}$$

It is noted that $a_i(t_j) = 0$ for $i > j$ because $s_i(\tau) = \sqrt{2\pi\Phi_0\Delta t} \cdot h_f(\tau - t_i)$ in Equation 3.9 is zero for $\tau < t_i$. When a uniform step size is used, i.e. $t_i - t_{i-1} = \Delta t,\ \ i = 1,2,....,n$ and $t_n = t_0$, it is found from Equation 3.7 and Equation 3.9 that

$$a_i(j\Delta t) = a_{n+i-j}(t_0),\ \ i = 1,2,...,n,\quad j = i,...,n \tag{3.11}$$

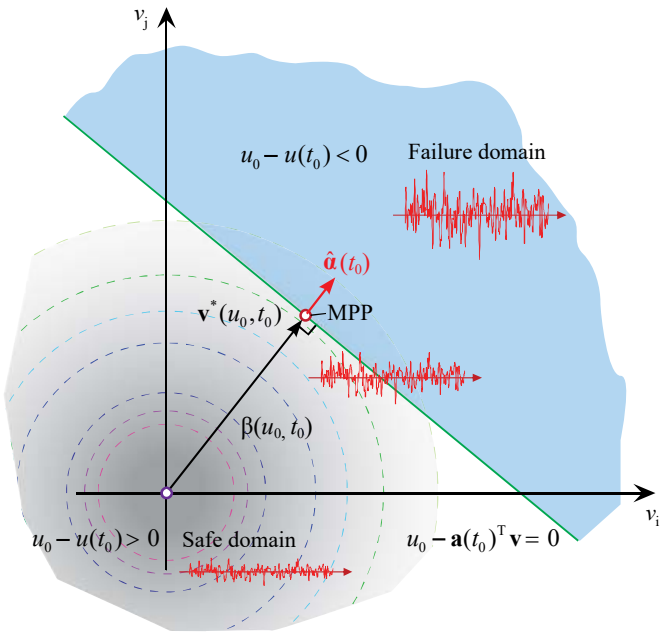

Figure 3.1: Geometric representation of instantaneous failure at time t_0 (MPP: Most Probable Point).

Appendix A provides the details of the derivation. As a result, the system equation in Equation 3.10 is given in the following matrix equation:

$$\begin{pmatrix} u(t_1) \\ u(t_2) \\ \vdots \\ u(t_{n-1}) \\ u(t_n) \end{pmatrix} = \begin{pmatrix} u(\Delta t) \\ u(2\Delta t) \\ \vdots \\ u(t_0 - \Delta t) \\ u(t_0) \end{pmatrix} = \begin{bmatrix} a_n(t_0) & 0 & \cdots & 0 & 0 \\ a_{n-1}(t_0) & a_n(t_0) & \cdots & 0 & 0 \\ \vdots & \vdots & \ddots & \vdots & \vdots \\ a_2(t_0) & a_3(t_0) & \cdots & a_n(t_0) & 0 \\ a_1(t_0) & a_2(t_0) & \cdots & a_{n-1}(t_0) & a_n(t_0) \end{bmatrix} \begin{pmatrix} v_1 \\ v_2 \\ \vdots \\ v_{n-1} \\ v_n \end{pmatrix} \tag{3.12}$$

Each element a_i of the vector **a** can then be calculated using the forward-substitution method or solving the following equivalent matrix equations by use of a solver developed for the lower triangular matrix:

$$\begin{pmatrix} u(t_1) \\ u(t_2) \\ \vdots \\ u(t_{n-1}) \\ u(t_n) \end{pmatrix} = \begin{pmatrix} u(\Delta t) \\ u(2\Delta t) \\ \vdots \\ u(t_0 - \Delta t) \\ u(t_0) \end{pmatrix} = \begin{bmatrix} 0 & 0 & \cdots & 0 & v_1 \\ 0 & 0 & \cdots & v_1 & v_2 \\ \vdots & \vdots & \ddots & \vdots & \vdots \\ 0 & v_1 & \cdots & v_{n-2} & v_{n-1} \\ v_1 & v_2 & \cdots & v_{n-1} & v_n \end{bmatrix} \begin{pmatrix} a_1(t_0) \\ a_2(t_0) \\ \vdots \\ a_{n-1}(t_0) \\ a_n(t_0) \end{pmatrix} \tag{3.13}$$

In both methods, the absolute value of the first element in the sample, v_1 needs to be sufficiently large for numerical stability. It is found that the procedure using Equation 3.13 is less sensitive to the numerical issue. The obtained vector of deterministic basis function $\mathbf{a}(t_0)$ is used in order to compute the reliability index and its associated failure probability aforementioned.

3.2.4. Stationarity

In general, evaluating the instantaneous failure probability $P(E_f)$ requires iterative computations through random vibration analysis and structural reliability analysis. It generates additional demands for computational resources and time in optimization. Using the discrete representation method, the instantaneous failure probability can be obtained by the closed-form solution as described in Section 3.2.3. It should be noted that the instantaneous failure probabilities are constant over the time period if the response achieves stationarity. This stationarity can be confirmed by investigating the autocovariance function $K_{xx}(\cdot)$ (Lutes and Sarkani 2003), which can be computed from the following form

$$K_{xx}(t_1,t_2)=\int_{-\infty}^{\infty}\Phi_{FF}(\omega)H(\omega,t_1)H(\omega,t_2)e^{i\omega(t_1-t_2)}d\omega \tag{3.14}$$

where $\Phi_{FF}(\omega)$ is the power spectral density function and $H(\omega,t_i),i=1,2$ denotes an incomplete Fourier transform of $h_s(t)$. Because $H(\cdot)$ is time-variant, responses of the linear system subjected to the stationary process may not be stationary in general. The stationarity of responses can be achieved when t_1, t_2 go to infinity because $H(\omega,t_1)$, $H(\omega,t_2)$ converge to a frequency response function $H(\omega)$ which does not depend on time *t*. For a general single degree-of-freedom oscillator, $H(\omega,t)$ can be written as

$$H(\omega,t)=H(\omega)\left[1-\left(\cos\omega_D t+\frac{\xi\omega_o+i\omega}{\omega_D}\sin\omega_D t\right)e^{-\xi\omega_o t}\cdot e^{-i\omega t}\right] \tag{3.15}$$

where ω_o is a natural frequency of the system, ξ denotes a damping ratio and ω_D is a damped natural frequency. Based on Equation 3.15, a time *t* taking $e^{-\xi\omega_o t}$ to $\varepsilon \ll 1$ can be identified as the

time that leads to $H(\omega,t) \cong H(\omega)$. For instance, a reduction of $e^{-\xi\omega_o t}$ to about 4 % can be achieved by taking $-\xi\omega_o t = \pi$. Therefore, one can compute a sufficient time for achieving stationarity using the following expression:

$$t_{\approx 4\%} = T_o / 2\xi \tag{3.16}$$

The primary focus of this work is topology optimization of linear structures subjected to the stationary Gaussian process, for which the aforementioned closed-form solution of the failure probability can be used. To achieve stationarity, the instantaneous failure probability is computed at a time point, after stationarity is achieved, according to Equation 3.16.

3.3. Stochastic topology optimization framework

This section presents our proposed stochastic topology optimization framework. That incorporates the discrete representation method discussed above into the topology optimization for an effective treatment of uncertainties in stochastic excitations.

3.3.1. Topology optimization framework

In this chapter, a linear elastic and isotropic constituent material with an elasticity tensor $\mathbf{D}_0$ is considered. The Solid Isotropic Material with Penalization (SIMP; Bendsøe 1989; Rozvany et al. 1992; Bendsøe and Sigmund 1999) model is adopted. The SIMP model uses a smooth convex function defined by a power function representation, i.e.

$$\psi(x) = x^p \tag{3.17}$$

where $p > 0$ is a penalization factor. In order to avoid singularity of a stiffness matrix in finite element analysis, one needs to set a lower bound on the element density $\tilde{\rho}_e(\mathbf{d})$ i.e., $0 < \tilde{\rho}_{\min} \leq \tilde{\rho}_e(\mathbf{d}) < 1$ with a vector of deterministic design variables, $\mathbf{d}$. The element density can be obtained by using a density filtering method such as the projection technique (e.g. Guest et al. 2004, Sigmund 2007) to avoid checkerboard-patterns. By using a linear "hat" kernel of radius *r*,

the element density can be computed as a weighted average of the design variables within an influence domain Ω_e such as

$$\tilde{\rho}_e(\mathbf{d}) = \frac{\sum_{j \in \Omega_e} w_j d_j}{\sum_{j \in \Omega_e} w_j} \tag{3.18}$$

where $w_j = (r - r_j)/r > 0$ is a weight, and r_j is the distance between the centroids of element e and element j, which lies within the radius r of element e.

Therefore, an elasticity tensor of an isotropic material in the state of plane stress is determined as

$$\mathbf{D}(\tilde{\rho}_e(\mathbf{d})) = \psi(\tilde{\rho}_e(\mathbf{d}))\mathbf{D}_0 = \frac{\psi(\tilde{\rho}_e(\mathbf{d})) \cdot E_0}{1 - \nu^2} \cdot \begin{bmatrix} 1 & \nu & 0 \\ \nu & 1 & 0 \\ 0 & 0 & (1-\nu)/2 \end{bmatrix} \tag{3.19}$$

where E_0 denotes Young's modulus of the solid phase, ν is the Poisson's ratio, and $\mathbf{D}_0$ is the elasticity tensor of the solid material, where the density is 1. Using the SIMP model, the stiffness matrix of the e^{th} element and its sensitivity are obtained as follows in the element-based computational framework (Bendsøe and Sigmund 2003):

$$\mathbf{K}_e(\tilde{\rho}_e) = \tilde{\rho}_e{}^p \mathbf{K}_e^0, \qquad \frac{\partial \mathbf{K}_e(\tilde{\rho}_e)}{\partial \tilde{\rho}_e} = p\tilde{\rho}_e{}^{p-1}\mathbf{K}_e^0 \tag{3.20}$$

where $\mathbf{K}_e^0$ is computed by

$$\mathbf{K}_e^0 = \int_{\Omega_e} \mathbf{B}^{\mathrm{T}} \mathbf{D}_0 \mathbf{B} \, \partial\Omega_e \tag{3.21}$$

in which $\mathbf{B}$ denotes a strain-displacement matrix of shape function derivatives in the domain Ω_e of element e. When considering transient problems, one obtains the mass matrix and its sensitivity as follows

$$\mathbf{M}_e(\tilde{\rho}_e) = \tilde{\rho}_e{}^q \mathbf{M}_e^0, \qquad \frac{\partial \mathbf{M}_e(\tilde{\rho}_e)}{\partial \tilde{\rho}_e} = q\tilde{\rho}_e{}^{q-1}\mathbf{M}_e^0 \tag{3.22}$$

where $\mathbf{M}_e^0$ is the mass matrix of the solid material, and q is the penalization parameter. To calculate the mass matrix in the domain of element e, a consistent mass matrix $\mathbf{M}_e^0$ is obtained as

$$\mathbf{M}_e^0 = \int_{\Omega_e} \mathbf{N}^{\mathrm{T}} \rho_m \mathbf{N} \, d\Omega_e \tag{3.23}$$

which has been adopted in this work. Here ρ_m is the mass density of material and $\mathbf{N}$ is the shape function of element e. The numerical examples in this chapter use penalization parameter values $p = 3$ and $q = 1$, which are widely used in the field of topology optimization (Pedersen 2000; Du and Olhoff 2007). As usual, the global stiffness matrix $\mathbf{K}$ and mass matrix $\mathbf{M}$ for the finite element analysis can be assembled over the total number of finite elements n_e in the design domain, that is,

$$\mathbf{K} = \sum_{e=1}^{n_e} \mathbf{K}_e(\tilde{\rho}_e), \qquad \mathbf{M} = \sum_{e=1}^{n_e} \mathbf{M}_e(\tilde{\rho}_e) \tag{3.24}$$

3.3.2. Stochastic topology optimization formulation

For structures under stochastic excitations, a topology optimization problem can be formulated as

$$\begin{aligned} &\min_{\mathbf{d}} \quad f_{obj}(\tilde{\boldsymbol{\rho}}(\mathbf{d})) \\ &s.t \quad P(E_f) \le P_f^{\text{target}} \\ &with \quad \mathbf{M}(\tilde{\boldsymbol{\rho}})\ddot{\mathbf{u}}(t,\tilde{\boldsymbol{\rho}}) + \mathbf{C}(\tilde{\boldsymbol{\rho}})\dot{\mathbf{u}}(t,\tilde{\boldsymbol{\rho}}) + \mathbf{K}(\tilde{\boldsymbol{\rho}})\mathbf{u}(t,\tilde{\boldsymbol{\rho}}) = \mathbf{f}(t,\tilde{\boldsymbol{\rho}}) \end{aligned} \tag{3.25}$$

where $\tilde{\boldsymbol{\rho}} = \tilde{\boldsymbol{\rho}}(\mathbf{d})$ is the element density vector, $\mathbf{M}(\tilde{\boldsymbol{\rho}})$, $\mathbf{C}(\tilde{\boldsymbol{\rho}})$ and $\mathbf{K}(\tilde{\boldsymbol{\rho}})$ are the mass, damping and stiffness matrices of the design domain, respectively. The quantities $\ddot{\mathbf{u}}(t,\tilde{\boldsymbol{\rho}})$, $\dot{\mathbf{u}}(t,\tilde{\boldsymbol{\rho}})$, $\mathbf{u}(t,\tilde{\boldsymbol{\rho}})$ and $\mathbf{f}(t,\tilde{\boldsymbol{\rho}})$ denote the acceleration, velocity, displacement and external force vectors at time t. P_f^{target} denotes the target failure probability which is allowable failure probability in the probabilistic constraints. The force vector for the structure subjected to ground acceleration $\ddot{u}_g(t)$ which is generated in the form of Equation 3.7 can be expressed as $\mathbf{f}(t,\tilde{\boldsymbol{\rho}}) = -\mathbf{M}(\tilde{\boldsymbol{\rho}})\mathbf{l}\ddot{u}_g(t)$, in which the vector $\mathbf{l}$ represents the directional distribution of masses with unity. It can be derived from the behavior of structures subjected to earthquake excitation of the base of the structure. The total displacement of the mass $\mathbf{M}$ by $\mathbf{u}^t(t,\tilde{\boldsymbol{\rho}})$ is a summation of the relative displacement between the ground and the mass by $\mathbf{u}(t,\tilde{\boldsymbol{\rho}})$ and the displacement of the ground denoted by $u_g(t)\mathbf{l}$. Because elastic and damping forces are only generated by the relative motion $\mathbf{u}(t,\tilde{\boldsymbol{\rho}})$, the inertial force related to the acceleration becomes $\mathbf{M}(\tilde{\boldsymbol{\rho}})\left(\ddot{\mathbf{u}}(t) + \mathbf{l}\ddot{u}_g(t)\right)$. Thus, the external force vector is

expressed as $\mathbf{f}(t,\tilde{\boldsymbol{\rho}}) = -\mathbf{M}(\tilde{\boldsymbol{\rho}})\mathbf{l}\ddot{u}_g(t)$. In this chapter, the damping matrix is constructed by using a Rayleigh damping model, $\mathbf{C} = \kappa_0\mathbf{M} + \kappa_1\mathbf{K}$. The coefficients κ_0 and κ_1 in the Rayleigh damping model are determined under the assumption of 2 % damping ratio for structures.

Optimization of nonlinear systems and/or systems subjected to non-stationary or non-Gaussian processes can also be achieved by modulating various filters (Rezaeian and Der Kiureghian 2008, 2010) and utilizing structural reliability analysis methods such as FORM and SORM. In order to update design variables during optimization procedures, nonlinear optimization algorithms such as the sequential quadratic programming (SQP) or the method of moving asymptotes (MMA; Svanberg 1987) can be used. In this chapter, MMA is used along with the special purpose sensitivity formulation described below. The MMA was chosen because the algorithm can handle the multiple constraints effectively and shows faster convergence compared to SQP and interior point method in the numerical examples.

3.3.3. Overall topology optimization process

Figure 3.2 illustrates the proposed procedure of topology optimization of structures under stochastic excitations. The procedure begins with an initial design and a stochastic model of excitation. For instance, the Kanai-Tajimi power spectral density model (Clough and Penzien 1993) can be implemented to approximately match the spectral characteristics of ground motions. The failure probability, i.e. the probability that the current design violates the given probabilistic constraint, is computed by structural reliability analysis (Der Kiureghian 2000; Der Kiureghian 2005). As described above, the instantaneous failure probability of the linear structure under the Gaussian excitations can be computed by the closed-form solution. Next, the objective function, constraint functions, and their sensitivities are computed to update design variables using an optimization algorithm such as MMA. The convergence check based on the total change in the material distribution is performed at the end of each iteration. This process is repeated until a tolerance threshold of 0.5 % is reached.

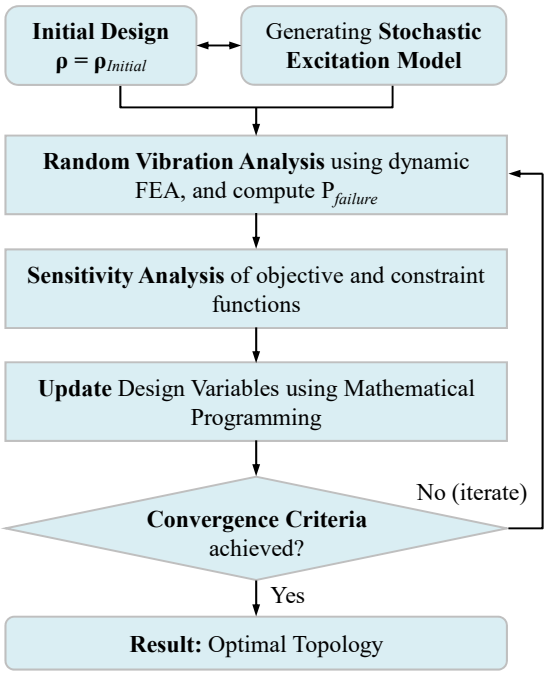

Figure 3.2: Flow chart for topology optimization under stochastic excitations.

3.4. Sensitivity calculations

Computing the sensitivity of structural responses with respect to various design parameters is essential for efficient gradient-based optimization. Therefore, various approaches have been developed for computing sensitivity of static as well as dynamic responses (Haug and Arora 1978, Haftka and Gürdal 1992). Computing gradients of responses of the system under stochastic process, however, differs from aforementioned sensitivity calculations, in that this system requires an additional layer of complexity due to the randomness of the input process. In this chapter, a new sensitivity formulation employing the adjoint method is developed for linear structures subjected to stochastic excitations modeled by the discrete representation method.

Consider the following constraint on the probability of the instantaneous failure event described by the discrete representation method:

$$P(E_f) = P(u_0 - \mathbf{a}(t_0, \tilde{\boldsymbol{\rho}})^{\mathrm{T}} \mathbf{v} \le 0) \le P_f^{\text{target}} \tag{3.26}$$

Alternatively, the constraint in Equation 3.26 can also be described using the CDF of the standard normal distribution and the reliability index, i.e.

$$\Phi[-\beta(u_0, t_0, \tilde{\boldsymbol{\rho}})] \le \Phi(-\beta^{\text{target}}) \;\text{ or }\; \beta(u_0, t_0, \tilde{\boldsymbol{\rho}}) \ge \beta^{\text{target}} \tag{3.27}$$

where β^{target} denotes the target reliability index which is $(1 - P_f^{\text{target}})$ quantile of the standard normal distribution, i.e. $\Phi(-\beta^{\text{target}}) = P_f^{\text{target}}$. Therefore, the sensitivity of the reliability index with respect to the design variables **d** needs to be evaluated to enable the use of gradient-based optimization algorithms. As described above, the reliability index is computed as

$$\beta(u_0, t_0, \tilde{\boldsymbol{\rho}}) = \frac{u_0}{\left\|\mathbf{a}(t_0, \tilde{\boldsymbol{\rho}})\right\|} = \frac{u_0}{\sqrt{a_1(t_0, \tilde{\boldsymbol{\rho}})^2 + a_2(t_0, \tilde{\boldsymbol{\rho}})^2 + \cdots + a_n(t_0, \tilde{\boldsymbol{\rho}})^2}} \tag{3.28}$$

By applying the chain rule to Equation 3.28, the sensitivity of the reliability index with respect to the design variable $d_e \in \mathbf{d}$ is derived as

$$\begin{aligned}
\frac{\partial \beta(u_0, t_0, \tilde{\boldsymbol{\rho}})}{\partial d_e} &= \sum_{k=1}^{n_e} \frac{\partial \beta(u_0, t_0, \tilde{\boldsymbol{\rho}})}{\partial \tilde{\rho}_k} \cdot \frac{\partial \tilde{\rho}_k}{\partial d_e} \\
&= \left[-\frac{u_0}{\left(a_1(t_0, \tilde{\boldsymbol{\rho}})^2 + \cdots + a_n(t_0, \tilde{\boldsymbol{\rho}})^2 \right)^{3/2}} \right] \cdot \sum_{k=1}^{n_e} \sum_{i=1}^{n} \left(a_i(t_0, \tilde{\boldsymbol{\rho}}) \cdot \frac{\partial a_i(t_0, \tilde{\boldsymbol{\rho}})}{\partial \tilde{\rho}_k} \right) \cdot \frac{\partial \tilde{\rho}_k}{\partial d_e} \\
&= \sum_{k=1}^{n_e} \sum_{i=1}^{n} \left(c_i(u_0, t_0, \tilde{\boldsymbol{\rho}}) \cdot \frac{\partial a_i(t_0, \tilde{\boldsymbol{\rho}})}{\partial \tilde{\rho}_k} \right) \cdot \frac{\partial \tilde{\rho}_k}{\partial d_e}
\end{aligned} \tag{3.29}$$

where

$$c_i(u_0, t_0, \tilde{\boldsymbol{\rho}}) = -u_0 \cdot a_i(t_0, \tilde{\boldsymbol{\rho}}) [a_1(t_0, \tilde{\boldsymbol{\rho}})^2 + \cdots + a_n(t_0, \tilde{\boldsymbol{\rho}})^2]^{-3/2} \tag{3.30}$$

In Equation 3.29, the index *j* represents the *j*-th element, $j = 1, \ldots, n_e$, and the partial derivative $\partial \tilde{\rho}_k / \partial d_e$ can be obtained from the filtering function in Equation 3.18. However, the sensitivity formulation in Equation 3.29 cannot be completed as it is because of the implicitly defined sensitivities with respect to the element density, i.e. $\partial a_i(t_0, \tilde{\boldsymbol{\rho}}) / \partial \tilde{\rho}_k$. To enable the sensitivity calculation, a new sensitivity calculation procedure based on the adjoint method is developed as presented below.

3.4.1. Direct differentiation method

By directly differentiating the second order governing equation in Equation 3.25 with respect to $\tilde{\rho}_k$ and rearranging terms, the following equation is obtained.

$$\begin{aligned}\mathbf{M}(\tilde{\boldsymbol{\rho}})\cdot\frac{\partial\ddot{\mathbf{u}}(t,\tilde{\boldsymbol{\rho}})}{\partial\tilde{\rho}_k}+\mathbf{C}(\tilde{\boldsymbol{\rho}})\cdot\frac{\partial\dot{\mathbf{u}}(t,\tilde{\boldsymbol{\rho}})}{\partial\tilde{\rho}_k}+\mathbf{K}(\tilde{\boldsymbol{\rho}})\cdot\frac{\partial\mathbf{u}(t,\tilde{\boldsymbol{\rho}})}{\partial\tilde{\rho}_k}\\ =\frac{\partial\mathbf{f}(t)}{\partial\tilde{\rho}_k}-\frac{\partial\mathbf{M}(\tilde{\boldsymbol{\rho}})}{\partial\tilde{\rho}_k}\cdot\ddot{\mathbf{u}}(t,\tilde{\boldsymbol{\rho}})-\frac{\partial\mathbf{C}(\tilde{\boldsymbol{\rho}})}{\partial\tilde{\rho}_k}\cdot\dot{\mathbf{u}}(t,\tilde{\boldsymbol{\rho}})-\frac{\partial\mathbf{K}(\tilde{\boldsymbol{\rho}})}{\partial\tilde{\rho}_k}\cdot\mathbf{u}(t,\tilde{\boldsymbol{\rho}})\end{aligned} \tag{3.31}$$

By considering the right hand side of Equation 3.31 as a new force vector, and assuming the "response gradients," $\partial\ddot{\mathbf{u}}(t,\tilde{\boldsymbol{\rho}})/\partial\tilde{\rho}_k$, $\partial\dot{\mathbf{u}}(t,\tilde{\boldsymbol{\rho}})/\partial\tilde{\rho}_k$ and $\partial\mathbf{u}(t,\tilde{\boldsymbol{\rho}})/\partial\tilde{\rho}_k$ as new acceleration, velocity and displacement vectors, the equation becomes another system equation of equilibrium. Solving Equation 3.31 using a method of numerical integration developed for differential equations lead to the gradients of the displacement, $\partial\mathbf{u}(t,\tilde{\boldsymbol{\rho}})/\partial\tilde{\rho}_k$ computed at each time point. From Equation 3.8, the sensitivity of a selected degree-of-freedom (DOF) of the displacement vector, i.e. $u(t)\in\mathbf{u}(t)$, is determined as

$$\frac{\partial u(t,\tilde{\boldsymbol{\rho}})}{\partial\tilde{\rho}_k}=\frac{\partial\mathbf{a}(t,\tilde{\boldsymbol{\rho}})^{\mathrm{T}}}{\partial\tilde{\rho}_k}\mathbf{v} \tag{3.32}$$

By means of a procedure similar to the one described in Equations 3.10-3.13, the following matrix equation is derived to obtain $\partial a_i(t_0,\tilde{\boldsymbol{\rho}})/\partial\tilde{\rho}_k$, $i=1\ldots,n$:

$$\begin{pmatrix}\partial u(t_1)/\partial\tilde{\rho}_k\\ \partial u(t_2)/\partial\tilde{\rho}_k\\ \vdots\\ \partial u(t_{n-1})/\partial\tilde{\rho}_k\\ \partial u(t_n)/\partial\tilde{\rho}_k\end{pmatrix}=\begin{bmatrix}\partial a_n(t_0)/\partial\tilde{\rho}_k & 0 & \cdots & 0 & 0\\ \partial a_{n-1}(t_0)/\partial\tilde{\rho}_k & \partial a_n(t_0)/\partial\tilde{\rho}_k & \cdots & 0 & 0\\ \vdots & \vdots & \ddots & \vdots & \vdots\\ \partial a_2(t_0)/\partial\tilde{\rho}_k & \partial a_3(t_0)/\partial\tilde{\rho}_k & \cdots & \partial a_n(t_0)/\partial\tilde{\rho}_k & 0\\ \partial a_1(t_0)/\partial\tilde{\rho}_k & \partial a_2(t_0)/\partial\tilde{\rho}_k & \cdots & \partial a_{n-1}(t_0)/\partial\tilde{\rho}_k & \partial a_n(t_0)/\partial\tilde{\rho}_k\end{bmatrix}\begin{pmatrix}v_1\\ v_2\\ \vdots\\ v_{n-1}\\ v_n\end{pmatrix} \tag{3.33}$$

One can compute $\partial a_i(t_0,\tilde{\boldsymbol{\rho}})/\partial\tilde{\rho}_k$ using the forward substitution method or solving the equivalent matrix system of equations. The sensitivity of the reliability index in Equation 3.29 can finally be calculated.

3.4.2. Adjoint sensitivity analysis

The basic idea of the adjoint method is introducing an adjoint system of equations so that computing implicitly defined terms in sensitivity analysis can be avoided and thus the computational cost can be reduced (Haug et al. 1986; Haftka and Gürdal 1992; Choi and Kim 2005). In the sensitivity analysis of the reliability index, the discretized system in the last line of Equation 3.25 is considered as the adjoint system. The equation of motion can be solved numerically using one of the time integration schemes such as the central difference method (Hulbert and Chung 1996), Houbolt method (Houbolt 1950) or Newmark method (Newmark 1959). The implicit Newmark time integration method is presented because the approach shows more stable and accurate results for the numerical examples. The Newmark method is based on the following time-stepping rules:

$$\dot{\mathbf{u}}(t_{j+1}) = \dot{\mathbf{u}}(t_j) + [(1-\gamma)\Delta t]\ddot{\mathbf{u}}(t_j) + (\gamma\Delta t)\ddot{\mathbf{u}}(t_{j+1}) \tag{3.34}$$

$$\mathbf{u}(t_{j+1}) = \mathbf{u}(t_j) + \Delta t\dot{\mathbf{u}}(t_j) + [(0.5-\eta)\Delta t^2]\ddot{\mathbf{u}}(t_j) + [\eta\Delta t^2]\ddot{\mathbf{u}}(t_{j+1}) \tag{3.35}$$

The parameters γ and η determine the stability and accuracy characteristic of the method ($\gamma = 0.5$ and $\eta = 0.25$ are used in this research). Substituting Equations 3.34-3.35 for $\ddot{\mathbf{u}}(t_{j+1})$ and $\dot{\mathbf{u}}(t_{j+1})$ into the second-order governing equation in Equation 3.25 at $t = t_{j+1}$, one can obtain the following expression

$$\begin{aligned}\left(\frac{1}{\eta(\Delta t)^2}\mathbf{M}(\tilde{\boldsymbol{\rho}}) + \frac{\gamma}{\eta\Delta t}\mathbf{C}(\tilde{\boldsymbol{\rho}}) + \mathbf{K}(\tilde{\boldsymbol{\rho}})\right)\mathbf{u}(t_{j+1},\tilde{\boldsymbol{\rho}}) &= \mathbf{f}(t_{j+1},\tilde{\boldsymbol{\rho}}) \\ &+ \mathbf{C}(\tilde{\boldsymbol{\rho}})\left[\frac{\gamma}{\eta\Delta t}\mathbf{u}(t_j,\tilde{\boldsymbol{\rho}}) + \left(\frac{\gamma}{\eta}-1\right)\dot{\mathbf{u}}(t_j,\tilde{\boldsymbol{\rho}}) + \Delta t\left(\frac{\gamma}{2\eta}-1\right)\ddot{\mathbf{u}}(t_j,\tilde{\boldsymbol{\rho}})\right] \\ &+ \mathbf{M}(\tilde{\boldsymbol{\rho}})\left[\frac{1}{\eta(\Delta t)^2}\mathbf{u}(t_j,\tilde{\boldsymbol{\rho}}) + \frac{1}{\eta\Delta t}\dot{\mathbf{u}}(t_j,\tilde{\boldsymbol{\rho}}) + \left(\frac{1}{2\eta}-1\right)\ddot{\mathbf{u}}(t_j,\tilde{\boldsymbol{\rho}})\right]\end{aligned} \tag{3.36}$$

Based on a general recurrence relation associated with three sequential displacements (Chan et al. 1962, Zienkiewicz 1977), the equilibrium equations of motion can be solved for $\mathbf{u}(t_{j+1},\tilde{\boldsymbol{\rho}})$:

$$\left(\mathbf{M}(\tilde{\boldsymbol{\rho}})+\gamma\Delta t\mathbf{C}(\tilde{\boldsymbol{\rho}})+\eta\left(\Delta t\right)^2\mathbf{K}(\tilde{\boldsymbol{\rho}})\right)\mathbf{u}(t_{j+1},\tilde{\boldsymbol{\rho}})=\eta\left(\Delta t\right)^2\mathbf{f}(t_{j+1},\tilde{\boldsymbol{\rho}})+(0.5+\gamma-2\eta)\left(\Delta t\right)^2\mathbf{f}(t_j,\tilde{\boldsymbol{\rho}})$$
$$+(0.5-\gamma+\eta)\left(\Delta t\right)^2\mathbf{f}(t_{j-1},\tilde{\boldsymbol{\rho}})\ -\left[-2\mathbf{M}(\tilde{\boldsymbol{\rho}})+(1-2\gamma)\Delta t\mathbf{C}(\tilde{\boldsymbol{\rho}})+(0.5+\gamma-2\eta)\left(\Delta t\right)^2\mathbf{K}(\tilde{\boldsymbol{\rho}})\right]\mathbf{u}(t_j,\tilde{\boldsymbol{\rho}})$$
$$-\left[\mathbf{M}(\tilde{\boldsymbol{\rho}})+(\gamma-1)\Delta t\mathbf{C}(\tilde{\boldsymbol{\rho}})+(0.5-\gamma+\eta)\left(\Delta t\right)^2\mathbf{K}(\tilde{\boldsymbol{\rho}})\right]\mathbf{u}(t_{j-1},\tilde{\boldsymbol{\rho}}) \tag{3.37}$$

It should be noted that the force vector $\mathbf{f}(t_{j+1},\tilde{\boldsymbol{\rho}})$ can be replaced by the inertia force vector $-\mathbf{M}(\tilde{\boldsymbol{\rho}})\mathbf{1}f(t_{j+1})$ for structures subjected to ground excitations aforementioned. The following notations are introduced in order to simplify the derivations:

$$\begin{aligned}
\underline{\underline{\mathbf{A}}}(\tilde{\boldsymbol{\rho}})&=\mathbf{M}(\tilde{\boldsymbol{\rho}})+\gamma\Delta t\cdot\mathbf{C}(\tilde{\boldsymbol{\rho}})+\eta\left(\Delta t\right)^2\mathbf{K}(\tilde{\boldsymbol{\rho}})\\
\underline{\underline{\mathbf{B}}}(\tilde{\boldsymbol{\rho}})&=-2\mathbf{M}(\tilde{\boldsymbol{\rho}})+(1-2\gamma)\Delta t\mathbf{C}(\tilde{\boldsymbol{\rho}})+(0.5+\gamma-2\eta)\left(\Delta t\right)^2\mathbf{K}(\tilde{\boldsymbol{\rho}})\\
\underline{\underline{\mathbf{E}}}(\tilde{\boldsymbol{\rho}})&=\mathbf{M}(\tilde{\boldsymbol{\rho}})+(\gamma-1)\Delta t\mathbf{C}(\tilde{\boldsymbol{\rho}})+(0.5-\gamma+\eta)\left(\Delta t\right)^2\mathbf{K}(\tilde{\boldsymbol{\rho}})
\end{aligned} \tag{3.38}$$

Substituting Equation 3.37 with Equation 3.38 and differentiating the equation with respect to the element density, one can obtain the discretized adjoint system as follows:

$$\begin{aligned}
&\frac{\partial\underline{\underline{\mathbf{A}}}(\tilde{\boldsymbol{\rho}})}{\partial\tilde{\rho}_k}\cdot\mathbf{u}(t_{j+1},\tilde{\boldsymbol{\rho}})+\underline{\underline{\mathbf{A}}}(\tilde{\boldsymbol{\rho}})\cdot\frac{\partial\mathbf{u}(t_{j+1},\tilde{\boldsymbol{\rho}})}{\partial\tilde{\rho}_k}-\eta\left(\Delta t\right)^2\frac{\partial\mathbf{f}(t_{j+1},\tilde{\boldsymbol{\rho}})}{\partial\tilde{\rho}_k}\\
&-(0.5+\gamma-2\eta)\left(\Delta t\right)^2\frac{\partial\mathbf{f}(t_j,\tilde{\boldsymbol{\rho}})}{\partial\tilde{\rho}_k}-(0.5-\gamma+\eta)\left(\Delta t\right)^2\frac{\partial\mathbf{f}(t_{j-1},\tilde{\boldsymbol{\rho}})}{\partial\tilde{\rho}_k}\\
&+\frac{\partial\underline{\underline{\mathbf{B}}}(\tilde{\boldsymbol{\rho}})}{\partial\tilde{\rho}_k}\cdot\mathbf{u}(t_j,\tilde{\boldsymbol{\rho}})+\underline{\underline{\mathbf{B}}}(\tilde{\boldsymbol{\rho}})\cdot\frac{\partial\mathbf{u}(t_j,\tilde{\boldsymbol{\rho}})}{\partial\tilde{\rho}_k}+\frac{\partial\underline{\underline{\mathbf{E}}}(\tilde{\boldsymbol{\rho}})}{\partial\tilde{\rho}_k}\cdot\mathbf{u}(t_{j-1},\tilde{\boldsymbol{\rho}})+\underline{\underline{\mathbf{E}}}(\tilde{\boldsymbol{\rho}})\cdot\frac{\partial\mathbf{u}(t_{j-1},\tilde{\boldsymbol{\rho}})}{\partial\tilde{\rho}_k}=0
\end{aligned} \tag{3.39}$$

It should be noted that this adjoint system is self-adjoint because **M**, **C** and **K** are symmetric based on Equation 3.21 and Equation 3.23. Pre-multiplying the discretized adjoint system with a n_{dof} dimensional adjoint variable vector $\boldsymbol{\lambda}_{n-j+1}$ and adding to right-hand side terms of Equation 3.29, one obtains

$$\begin{aligned}
\frac{\partial\beta(u_0,t_0,\tilde{\boldsymbol{\rho}})}{\partial\tilde{\rho}_k}=&\sum_{i=1}^{n}\left(c_i(u_0,t_0,\tilde{\boldsymbol{\rho}})\cdot\frac{\partial a_i(t_0,\tilde{\boldsymbol{\rho}})}{\partial\tilde{\rho}_k}\right)+\sum_{j=1}^{n}\boldsymbol{\lambda}_{n-j+1}^{\mathrm{T}}\left[\frac{\partial\underline{\underline{\mathbf{A}}}(\tilde{\boldsymbol{\rho}})}{\partial\tilde{\rho}_k}\cdot\mathbf{u}(t_j,\tilde{\boldsymbol{\rho}})+\underline{\underline{\mathbf{A}}}(\tilde{\boldsymbol{\rho}})\cdot\frac{\partial\mathbf{u}(t_j,\tilde{\boldsymbol{\rho}})}{\partial\tilde{\rho}_k}\right.\\
&-\eta\left(\Delta t\right)^2\frac{\partial\mathbf{f}(t_j,\tilde{\boldsymbol{\rho}})}{\partial\tilde{\rho}_k}-(0.5+\gamma-2\eta)\left(\Delta t\right)^2\frac{\partial\mathbf{f}(t_{j-1},\tilde{\boldsymbol{\rho}})}{\partial\tilde{\rho}_k}-(0.5-\gamma+\eta)\left(\Delta t\right)^2\frac{\partial\mathbf{f}(t_{j-2},\tilde{\boldsymbol{\rho}})}{\partial\tilde{\rho}_k}\\
&\left.+\frac{\partial\underline{\underline{\mathbf{B}}}(\tilde{\boldsymbol{\rho}})}{\partial\tilde{\rho}_k}\cdot\mathbf{u}(t_{j-1},\tilde{\boldsymbol{\rho}})+\underline{\underline{\mathbf{B}}}(\tilde{\boldsymbol{\rho}})\cdot\frac{\partial\mathbf{u}(t_{j-1},\tilde{\boldsymbol{\rho}})}{\partial\tilde{\rho}_k}+\frac{\partial\underline{\underline{\mathbf{E}}}(\tilde{\boldsymbol{\rho}})}{\partial\tilde{\rho}_k}\cdot\mathbf{u}(t_{j-2},\tilde{\boldsymbol{\rho}})+\underline{\underline{\mathbf{E}}}(\tilde{\boldsymbol{\rho}})\cdot\frac{\partial\mathbf{u}(t_{j-2},\tilde{\boldsymbol{\rho}})}{\partial\tilde{\rho}_k}\right]
\end{aligned} \tag{3.40}$$

It is noted that the first summation on the right-hand side of Equation 3.40 includes gradients of $\mathbf{a}(t)$ which was introduced to describe a certain degree-of-freedom, i.e. $u(t)=\mathbf{a}^{\mathrm{T}}(t)\mathbf{v}$ while the added terms in the second summation are expressed with gradients of the displacement vector $\mathbf{u}$ including all degrees-of-freedom. To derive the sensitivity in Equation 3.40 in terms of derivatives of $\mathbf{u}(t)$, the terms in the first summation are alternatively described as

$$\sum_{i=1}^{n}\left(c_i(t_0,\tilde{\boldsymbol{\rho}})\cdot\frac{\partial a_i(t_0,\tilde{\boldsymbol{\rho}})}{\partial\tilde{\rho}_k}\right)=\sum_{i=1}^{n}\left(T_i\cdot\mathbf{z}^{\mathrm{T}}\cdot\frac{\partial\mathbf{u}(t_i,\tilde{\boldsymbol{\rho}})}{\partial\tilde{\rho}_k}\right) \tag{3.41}$$

where $\mathbf{z}$ is a binary vector that indicates which degree-of-freedom of $\mathbf{a}(t)$ indicates. If the sensitivity of the l-th degree-of-freedom is of interest, all elements of $\mathbf{z}$ vector are zeroes except that the l-th element is 1.

Substituting Equation 3.33 into Equation 3.41, one obtains the following expression

$$\begin{aligned}
&c_1(t_0,\tilde{\boldsymbol{\rho}})\cdot\frac{\partial a_1(t_0,\tilde{\boldsymbol{\rho}})}{\partial\tilde{\rho}_k}+c_2(t_0,\tilde{\boldsymbol{\rho}})\cdot\frac{\partial a_2(t_0,\tilde{\boldsymbol{\rho}})}{\partial\tilde{\rho}_k}+\ldots+c_n(t_0,\tilde{\boldsymbol{\rho}})\cdot\frac{\partial a_n(t_0,\tilde{\boldsymbol{\rho}})}{\partial\tilde{\rho}_k}=\\
&T_1\cdot\frac{\partial a_n(t_0,\tilde{\boldsymbol{\rho}})}{\partial\tilde{\rho}_k}\cdot v_1+T_2\cdot\left(\frac{\partial a_{n-1}(t_0,\tilde{\boldsymbol{\rho}})}{\partial\tilde{\rho}_k}\cdot v_1+\frac{\partial a_n(t_0,\tilde{\boldsymbol{\rho}})}{\partial\tilde{\rho}_k}\cdot v_2\right)+\ldots\\
&+T_n\cdot\left(\frac{\partial a_1(t_0,\tilde{\boldsymbol{\rho}})}{\partial\tilde{\rho}_k}\cdot v_1+\frac{\partial a_2(t_0,\tilde{\boldsymbol{\rho}})}{\partial\tilde{\rho}_k}\cdot v_2+\ldots\frac{\partial a_n(t_0,\tilde{\boldsymbol{\rho}})}{\partial\tilde{\rho}_k}\cdot v_n\right)
\end{aligned} \tag{3.42}$$

Comparing the coefficients of the left and right hand sides of Equation 3.42, one can find

$$\begin{aligned}
&T_n v_1=c_1(t_0,\tilde{\boldsymbol{\rho}})\\
&T_{n-1}v_1+T_n v_2=c_2(t_0,\tilde{\boldsymbol{\rho}})\\
&\vdots\\
&T_1v_1+T_2v_2+\ldots+T_nv_n=c_n(t_0,\tilde{\boldsymbol{\rho}})
\end{aligned} \tag{3.43}$$

The coefficients T_i, $i=1,\ldots,n$, can be obtained by solving Equation 3.43. Substituting Equation 3.41 into Equation 3.40 and isolating implicitly defined terms $\partial\mathbf{u}(t_j,\tilde{\boldsymbol{\rho}})/\partial\tilde{\rho}_k$, one obtains:

$$\frac{\partial \beta(u_0,t_0,\tilde{\boldsymbol{\rho}})}{\partial \tilde{\rho}_k} = \sum_{i=1}^{n}\left(T_i \cdot \mathbf{z}^{\mathrm{T}} \frac{\partial \mathbf{u}(t_i,\tilde{\boldsymbol{\rho}})}{\partial \tilde{\rho}_k} \right)$$
$$+\sum_{j=1}^{n} \boldsymbol{\lambda}_{n-j+1}^{\mathrm{T}} \left[\frac{\partial \underline{\underline{\mathbf{A}}}(\tilde{\boldsymbol{\rho}})}{\partial \tilde{\rho}_k} \cdot \mathbf{u}(t_j,\tilde{\boldsymbol{\rho}}) - \eta(\Delta t)^2 \frac{\partial \mathbf{f}(t_j,\tilde{\boldsymbol{\rho}})}{\partial \tilde{\rho}_k} - (0.5+\gamma-2\eta)(\Delta t)^2 \frac{\partial \mathbf{f}(t_{j-1},\tilde{\boldsymbol{\rho}})}{\partial \tilde{\rho}_k} \right.$$
$$\left. -(0.5-\gamma+\eta)(\Delta t)^2 \frac{\partial \mathbf{f}(t_{j-2},\tilde{\boldsymbol{\rho}})}{\partial \tilde{\rho}_k} + \frac{\partial \underline{\underline{\mathbf{B}}}(\tilde{\boldsymbol{\rho}})}{\partial \tilde{\rho}_k} \cdot \mathbf{u}(t_{j-1},\tilde{\boldsymbol{\rho}}) + \frac{\partial \underline{\underline{\mathbf{E}}}(\tilde{\boldsymbol{\rho}})}{\partial \tilde{\rho}_k} \cdot \mathbf{u}(t_{j-2},\tilde{\boldsymbol{\rho}}) \right]$$
$$+\sum_{j=1}^{n} \boldsymbol{\lambda}_{n-j+1}^{\mathrm{T}} \left[\underline{\underline{\mathbf{A}}}(\tilde{\boldsymbol{\rho}}) \cdot \frac{\partial \mathbf{u}(t_j,\tilde{\boldsymbol{\rho}})}{\partial \tilde{\rho}_k} + \underline{\underline{\mathbf{B}}}(\tilde{\boldsymbol{\rho}}) \cdot \frac{\partial \mathbf{u}(t_{j-1},\tilde{\boldsymbol{\rho}})}{\partial \tilde{\rho}_k} + \underline{\underline{\mathbf{E}}}(\tilde{\boldsymbol{\rho}}) \cdot \frac{\partial \mathbf{u}(t_{j-2},\tilde{\boldsymbol{\rho}})}{\partial \tilde{\rho}_k} \right] \tag{3.44}$$

It is noted that this procedure requires knowledge of $\mathbf{u}(t_{-1},\tilde{\boldsymbol{\rho}})$, $\mathbf{u}(0,\tilde{\boldsymbol{\rho}})$ and their partial derivatives so that a special starting procedure such as initial displacements by the central difference method can be used to generate initial results. The terms including $\partial \mathbf{u}(t_j,\tilde{\boldsymbol{\rho}}) / \partial \tilde{\rho}_k$, $j = 1,...,n,$ are identified and grouped in Equation 3.44. Then, the value of the adjoint vector $\boldsymbol{\lambda}_n$ is found such that the coefficients of unknown derivatives $\partial \mathbf{u}(t_j,\tilde{\boldsymbol{\rho}}) / \partial \tilde{\rho}_k$, $j = 1,...,n,$ are zero, i.e.

$$\begin{aligned}
&T_n \cdot \mathbf{z}^{\mathrm{T}} + \boldsymbol{\lambda}_1^{\mathrm{T}} \cdot \underline{\underline{\mathbf{A}}}(\tilde{\boldsymbol{\rho}}) = 0 \\
&T_{n-1} \cdot \mathbf{z}^{\mathrm{T}} + \boldsymbol{\lambda}_2^{\mathrm{T}} \cdot \underline{\underline{\mathbf{A}}}(\tilde{\boldsymbol{\rho}}) + \boldsymbol{\lambda}_1^{\mathrm{T}} \cdot \underline{\underline{\mathbf{B}}}(\tilde{\boldsymbol{\rho}}) = 0 \\
&T_{n-2} \cdot \mathbf{z}^{\mathrm{T}} + \boldsymbol{\lambda}_3^{\mathrm{T}} \cdot \underline{\underline{\mathbf{A}}}(\tilde{\boldsymbol{\rho}}) + \boldsymbol{\lambda}_2^{\mathrm{T}} \cdot \underline{\underline{\mathbf{B}}}(\tilde{\boldsymbol{\rho}}) + \boldsymbol{\lambda}_1^{\mathrm{T}} \cdot \underline{\underline{\mathbf{E}}}(\tilde{\boldsymbol{\rho}}) = 0 \\
&\vdots \\
&T_1 \cdot \mathbf{z}^{\mathrm{T}} + \boldsymbol{\lambda}_n^{\mathrm{T}} \cdot \underline{\underline{\mathbf{A}}}(\tilde{\boldsymbol{\rho}}) + \boldsymbol{\lambda}_{n-1}^{\mathrm{T}} \cdot \underline{\underline{\mathbf{B}}}(\tilde{\boldsymbol{\rho}}) + \boldsymbol{\lambda}_{n-2}^{\mathrm{T}} \cdot \underline{\underline{\mathbf{E}}}(\tilde{\boldsymbol{\rho}}) = 0
\end{aligned} \tag{3.45}$$

Finally, substitution of the value of the adjoint vector obtained from Equation 3.45 into Equation 3.44 gives the sensitivity from the following equation that does not involve implicitly defined derivative terms:

$$\frac{\partial \beta(u_0,t_0,\tilde{\boldsymbol{\rho}})}{\partial \tilde{\rho}_k} = \sum_{j=1}^{n} \boldsymbol{\lambda}_{n-j+1}{}^{\mathrm{T}} \left[\frac{\partial \underline{\underline{\mathbf{A}}}(\tilde{\boldsymbol{\rho}})}{\partial \tilde{\rho}_k} \cdot \mathbf{u}(t_j,\tilde{\boldsymbol{\rho}}) - \eta(\Delta t)^2 \frac{\partial \mathbf{f}(t_j,\tilde{\boldsymbol{\rho}})}{\partial \tilde{\rho}_k} - (0.5+\gamma-2\eta)(\Delta t)^2 \frac{\partial \mathbf{f}(t_{j-1},\tilde{\boldsymbol{\rho}})}{\partial \tilde{\rho}_k} \right.$$
$$\left. -(0.5-\gamma+\eta)(\Delta t)^2 \frac{\partial \mathbf{f}(t_{j-2},\tilde{\boldsymbol{\rho}})}{\partial \tilde{\rho}_k} + \frac{\partial \underline{\underline{\mathbf{B}}}(\tilde{\boldsymbol{\rho}})}{\partial \tilde{\rho}_k} \cdot \mathbf{u}_{j-1}(\tilde{\boldsymbol{\rho}}) + \frac{\partial \underline{\underline{\mathbf{E}}}(\tilde{\boldsymbol{\rho}})}{\partial \tilde{\rho}_k} \cdot \mathbf{u}(t_{j-2},\tilde{\boldsymbol{\rho}}) \right]$$
$$+\boldsymbol{\lambda}_n{}^{\mathrm{T}} \left[\underline{\underline{\mathbf{B}}}(\tilde{\boldsymbol{\rho}}) \cdot \frac{\partial \mathbf{u}(0,\tilde{\boldsymbol{\rho}})}{\partial \tilde{\rho}_k} + \underline{\underline{\mathbf{E}}}(\tilde{\boldsymbol{\rho}}) \cdot \frac{\partial \mathbf{u}(t_{-1},\tilde{\boldsymbol{\rho}})}{\partial \tilde{\rho}_k} \right] + \boldsymbol{\lambda}_{n-1}{}^{\mathrm{T}} \left[\underline{\underline{\mathbf{E}}}(\tilde{\boldsymbol{\rho}}) \cdot \frac{\partial \mathbf{u}(0,\tilde{\boldsymbol{\rho}})}{\partial \tilde{\rho}_k} \right] \tag{3.46}$$

3.4.3. Performance of the proposed method for sensitivity calculations

The performance of the proposed methods for sensitivity calculation is tested through a numerical example in terms of efficiency and accuracy. For this purpose, the example considers a structure shown in Figure 3.3 (a), which is subjected to the filtered stationary process which is represented in the form of Equation 3.1 with the basis functions $s_i(t) = \exp[-2.4\pi(t-t_i)] \times \sin[3.2\pi(t-t_i)] \cdot H(t-t_i)$ (Der Kiureghian 2000) where $H(\cdot)$ is a unit step function. The basis functions are normalized such that $\|\mathbf{s}(t)\| = 1$. The continuum structure is discretized with quadrilateral elements (Q4). The frame elements illustrated as straight lines in Figure 3.3(a) are divided into smaller elements. Those are then connected to the nodes of Q4 elements along the straight lines. The thickness of the Q4 element is 0.1m, the size of frame elements is 0.45 m × 0.45 m, and Young's modulus E = 21,000 MPa and density ρ_m = 2,400 kg/m^3 are used to describe the material properties of the structure. The uniform distribution of the material density 0.5 over the Q4 domain is assumed in the sensitivity calculation. The probabilistic constraint is given on tip-displacements which are evaluated at red dots as shown in Figure 3.3(a). The failure event E_f occurs when the average tip-displacement exceeds a given threshold value $u_0 (= 0.02 \text{ m})$ at $t_0 = 8$, i.e.

$$E_f = u_0 - \left(\frac{u_{Left} + u_{Right}}{2} \right) \leq 0 \tag{3.47}$$

where $u_{Left} = \mathbf{a}(t_0, \tilde{\boldsymbol{\rho}})_{Left}^{\mathrm{T}} \mathbf{v}$ and $u_{Right} = \mathbf{a}(t_0, \tilde{\boldsymbol{\rho}})_{Right}^{\mathrm{T}} \mathbf{v}$ respectively denote displacements at time t_0 computed using $\mathbf{a}(t_0, \tilde{\boldsymbol{\rho}})$ functions evaluated at the left and the right red dots in Figure 3.3(a), respectively. The direct differentiation method (DDM) and the proposed adjoint method (AJM) are carried out to calculate the sensitivity $\partial\beta(u_0 = 0.02, t_0 = 8, \tilde{\boldsymbol{\rho}}) / \partial d_j$. The finite difference method (FDM) with varying perturbations from $\Delta d = 10^{-1}$ to $\Delta d = 10^{-16}$ is also implemented to verify the proposed method. Table 3.1 summarizes sensitivity results from the FDM at selected three elements shown in Figure 3.3 (a) and those from the proposed AJM and the DDM. Figures 3.3 (b) through 3.3 (d) show normalized sensitivities computed by the three methods. The DDM and

proposed AJM yield results that are consistent with those from the FDM. Figure 3.4 shows normalized computational times for different levels of discretization of the structure. The computational times are normalized by the result of the AJM for 800 finite elements. The proposed AJM shows the most efficient performance in terms of computational time while providing accurate results.

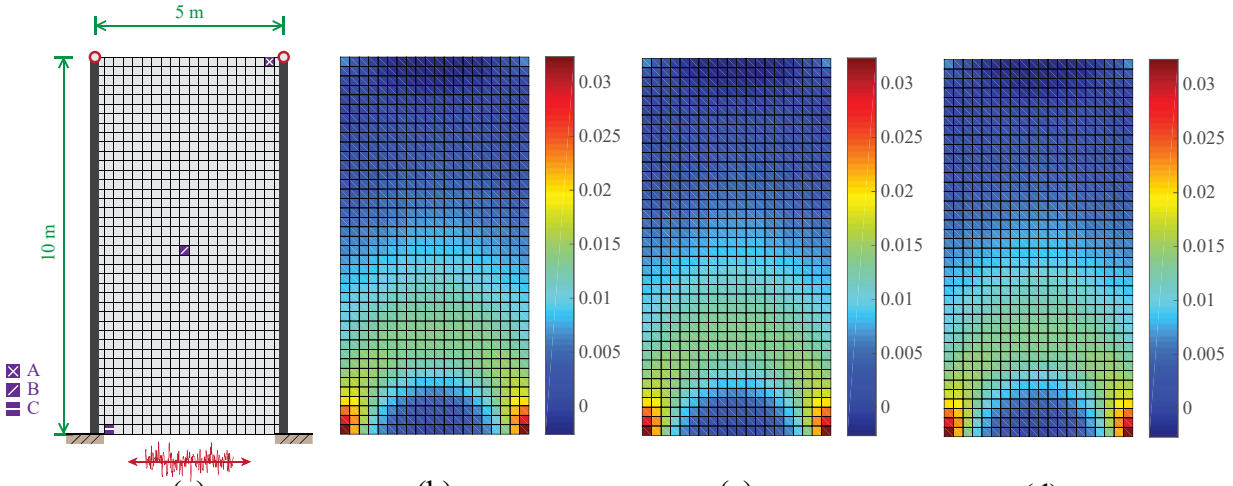

Figure 3.3: Sensitivities by different approaches: (a) geometry of the structure, (b) adjoint method, (c) direct differentiation method, and (d) finite difference method ($\Delta d = 1\times10^{-5}$).

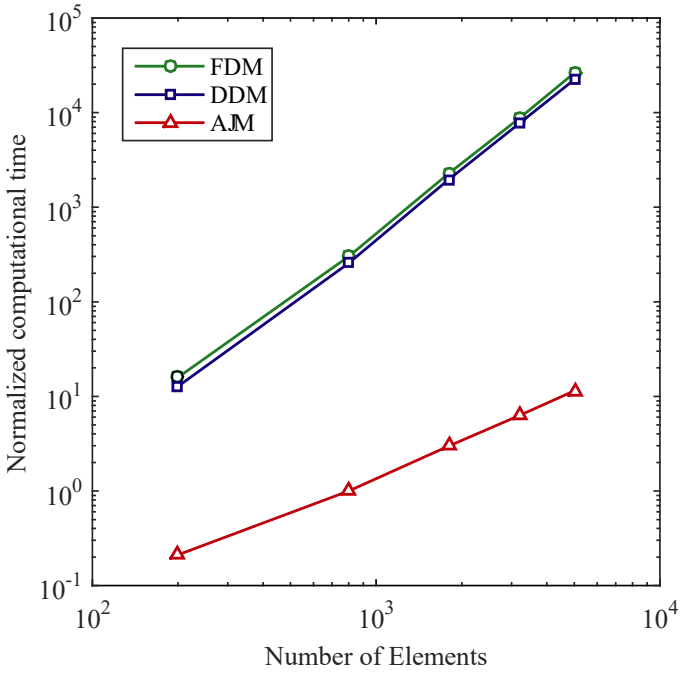

Figure 3.4: Normalized computational time (FDM: finite difference method, DDM: direct differentiation method, and AJM: adjoint method).

Table 3.1: Sensitivities at the element A, B, and C using the proposed AJM, DDM, and FDM with a perturbation Δd.

	Elem. A	Elem. B	Elem. C				
AJM	0.003110	0.008650	0.021623				
DDM	0.003110	0.008650	0.021623				
FDM							
Δd	Elem. A	Elem. B	Elem. C	Δd	Elem. A	Elem. B	Elem. C
1×10^{-1}	0.002585	0.007872	0.020308	1×10^{-9}	0.003361	0.008789	0.022355
1×10^{-2}	0.003053	0.008570	0.021484	1×10^{-10}	0.018385	0.018541	0.029197
1×10^{-3}	0.003104	0.008642	0.021609	1×10^{-11}	0.159606	0.143707	0.081490
1×10^{-4}	0.003109	0.008650	0.021621	1×10^{-12}	0.311751	−0.32685	0.567768
1×10^{-5}	0.003110	0.008650	0.021623	1×10^{-13}	13.37375	9.74998	5.90417
1×10^{-6}	0.003112	0.008652	0.021624	1×10^{-14}	85.7980	242.6503	71.7870
1×10^{-7}	0.003128	0.008635	0.021620	1×10^{-15}	−1345.81	206.501	315.525
1×10^{-8}	0.002872	0.008645	0.021704	1×10^{-16}	1725.286	4276.579	11146.63

3.5. Numerical applications

The proposed method is applied to obtain a lateral bracing system with minimum volume for a building structure subjected to stochastic ground motion excitations. The topology optimization formulation in Equation 3.25 is used while the objective function $f_{obj}(\tilde{\boldsymbol{\rho}}(\mathbf{d}))$ is defined as the volume of the structure determined by the material density distribution. The material distribution in the design domain is optimized under probabilistic constraints on inter-story drift ratios (ASCE7 2010, NEHRP 2009) during random excitations of an earthquake event, which are important criteria for seismic designs. Topology optimization is performed for a variety of multi-story buildings and conditions in order to investigate the impact of prescribed probabilistic parameters, characteristics of the filtered white noise, and building dimensions on topology optimization solutions.

3.5.1. Input stochastic process

In subsequent numerical examples presented in this chapter, the stochastic seismic excitation is modeled as the filtered white-noise process. Accordingly, the unit-impulse response function $h_f(\cdot)$ in Equation 3.7 follows the Kanai-Tajimi filter model (Clough and Penzien 1993; Fujimura and Der Kiureghian 2007), i.e.

$$h_f(t) = \exp(-\zeta_f \omega_f t)\left[\frac{(2\zeta_f^2 - 1)\omega_f}{\sqrt{1-\zeta_f^2}}\sin(\omega_f\sqrt{1-\zeta_f^2}\cdot t) - 2\zeta_f\omega_f\cos(\omega_f\sqrt{1-\zeta_f^2}\cdot t)\right] \tag{3.48}$$

where ω_f and ζ_f are filter parameters representing the predominant frequency and the bandwidth of the process. The corresponding power spectral density (PSD) function (Lutes and Sarkani 2003) of the input process is

$$\Phi(\omega) = \frac{1 + 4\zeta_f^2(\omega/\omega_g)^2}{\left(1-(\omega/\omega_g)^2\right)^2 + (2\zeta_f\omega/\omega_g)^2}\Phi_0 \tag{3.49}$$

where Φ_0 represents the power spectral density of the underlying white noise process. Typical values for predominant frequency and the bandwidth of ground motions on a firm ground are $\omega_f = 5\pi$ rad/s and $\zeta_f = 0.4$.

3.5.2. Topology optimization of three-story buildings

Figure 3.5 shows a three-story building with a width of 5 m, a height of 15 m, and a uniform thickness of 0.1 m. The design domain, represented by the gray area, is modeled by bilinear quadrilateral (Q4) elements, and the material densities in the elements are optimized to minimize the volume while satisfying the probabilistic constraints on the inter-story drift ratio. The two vertical lines represent the structural columns modeled by frame elements, whose material properties or dimensions remain constant during the optimization process. The frame element is discretized into many smaller frame elements, which are attached at every node of quadrilateral meshes along the column lines and move together with quadrilateral elements.

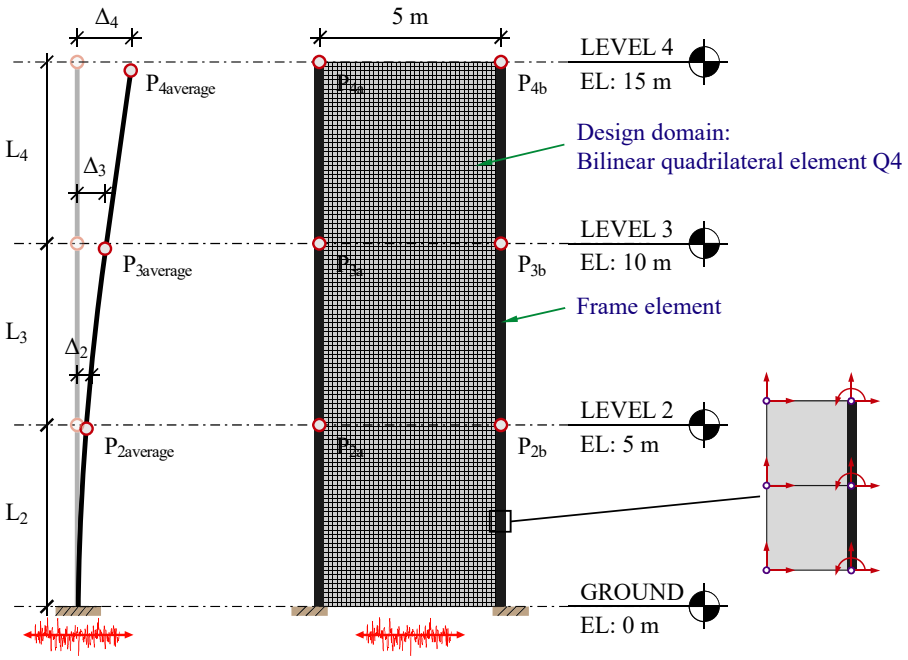

Figure 3.5: Three-story building subjected to stochastic excitations.

Young's modulus $E = 21{,}000$ MPa and density $\rho_m = 2{,}400$ kg/m^3 are used as material properties to represent normal-weight concrete. The filtering radius $r = 0.1625$ m and initial volume fraction 0.7 over the Q4 domain are employed. The coefficients used in the Rayleigh damping model are $\kappa_0 = 1.93$, $\kappa_1 = 1.52\times10^{-4}$ under the assumption of 2 % damping ratio for the three-story building. For each of the floor levels 2, 3 and 4 shown in Figure 3.5, the averages of the inter-story drift ratios (Δ_i/L_i) are evaluated at specified points for the left and right columns as the stochastic response of the structure. Constraints are given on the probabilities of the failure events, which are defined as those exceeding the average inter-story drift ratios for the given threshold value. More precisely, the failure event of the i-th floor level is defined as

$$E_{f_i} = \begin{cases} \left\{ u_{i0} - \left(\dfrac{(\mathbf{a}(t_0,\tilde{\boldsymbol{\rho}})^{\mathrm{T}}_{i,Left} + \mathbf{a}(t_0,\tilde{\boldsymbol{\rho}})^{\mathrm{T}}_{i,Right})\mathbf{v}}{2L_i} \right) \le 0 \right\} & \text{for } i = 2 \\ \left\{ u_{i0} - \left(\dfrac{(\mathbf{a}(t_0,\tilde{\boldsymbol{\rho}})^{\mathrm{T}}_{i,Left} + \mathbf{a}(t_0,\tilde{\boldsymbol{\rho}})^{\mathrm{T}}_{i,Right})\mathbf{v}}{2L_i} - \dfrac{(\mathbf{a}(t_0,\tilde{\boldsymbol{\rho}})^{\mathrm{T}}_{(i-1),Left} + \mathbf{a}(t_0,\tilde{\boldsymbol{\rho}})^{\mathrm{T}}_{(i-1),Right})\mathbf{v}}{2L_i} \right) \le 0 \right\} & \text{for } i = 3,4 \end{cases} \tag{3.50}$$

where $L_i (= 5\text{ m})$, $u_{i0} (= 0.02)$, $\mathbf{a}(t_0,\tilde{\boldsymbol{\rho}})^{\mathrm{T}}_{i,Left}$ and $\mathbf{a}(t_0,\tilde{\boldsymbol{\rho}})^{\mathrm{T}}_{i,Right}$ represent the floor height, the threshold value of the inter-story drift ratio respectively, as well as **a** vectors to determine the lateral displacement at the left and right columns of the i-th floor level at $t = t_0$, for $i = 2, 3, 4$. Although the events described in Equation 3.50 have a different form from Equation 3.26, it is noted that the inter-story drift ratios in Equation 3.50 are still linear functions of the random vector **v**, i.e. $\mathbf{b}(t_0,\tilde{\boldsymbol{\rho}})^{\mathrm{T}}_i \mathbf{v}$. Therefore, the closed-form solution in Equation 3.27 and the sensitivity calculation methods developed in Section 3.4 can be still used just by replacing **a** vectors (displacement) in the formulations by **b** vector (inter-story drift). Table 3.2 provides filter parameters, column size, and parameters used for probabilistic constraints, which include the threshold values of average drift ratios. The filter parameters in Table 3.2 are considered to represent ground motions on a typical firm ground. The threshold value of the inter-story drift ratio is chosen as one of design criteria in ASCE7 (2010).

Table 3.2: Three-story building: parameters used for design domain, probabilistic constraint, and ground motion model.

	Filter parameters		Column size (m × m)	u_0
	ω_f	ζ_f		
Case I	5π	0.4	0.5 × 0.5	0.02
Case II	5π	0.4	0.5 × 0.5	0.0175
Case III	5π	0.4	0.6 × 0.6	0.02

In these examples, constraints are given on the instantaneous probability during the strong motion duration, during which the earthquake excitation can be approximated as a stationary process (Soong and Grigoriu 1993). Even when a stationary input is used for a linear structure, it takes a while to achieve the stationarity in the structural response. In order to achieve stationarity, the drift ratio at t_0=6 *s* is used when computing the instantaneous failure probability. The optimization problem is solved with different column sizes, intensities of filtered Gaussian excitations, and target reliability indices which correspond to allowable failure probabilities.

First, topology optimization solutions are obtained (see Figures 3.6 and 3.7) while the intensity of the ground motion is varied for Cases I-III as tabulated in Table 3.2. As the intensity increases, the converged topologies become significantly different at the lower level. In particular, the intersection point of the bracing at the lower level moves up vertically with increasing intensity, and the thickness of the bracing increases at the lower level but remains relatively stable at higher levels. The results shown in Figures 3.6 and 3.7 indicate that topology optimization satisfies probabilistic constraints for increased intensities by strengthening the lower level first, i.e. by placing more materials and changing the geometry of the bracings. This is the reason why the bracing of the top level almost remains constant and maintains its 45 degree angle as the intensity increases. It is also noted that the points where the bracing meets the column around the second floor (termed as "bracing-column points" hereafter) level move up as the intensity increases. Based on this observation, an efficient way to control the inter-story drift ratio is strengthening lower parts of the structural system. Comparing results of Case I and Case II show that the decreased

threshold value of drift ratios (Case II) moves up both bracing-column points and intersection points of the bracings at the lower floor level. It is also important to note that a change in the threshold value can affect the optimization result as shown in both Case I and Case II. Distinct changes of topologies are observed at the lower floor level with additional branches of the material distribution for the case with reduced threshold value. The change in the column size (Case III) leads to overall increases in the thickness of material distributions. Volumes of the optimization solutions are tabulated in Table 3.3. The values in the parentheses are volumes for discrete material distributions converted from intermediate densities. A detailed discussion of the conversion process and its impact on the results will be included in Section 3.5.3. The volumes of optimization solutions for Case I are lower than those of Case II because the lower threshold values of inter-story drift ratios in Case I requires more strict the constraints. Compared to Case I, the larger column size in Case III results in the increased optimized volume. Note that the column size does not change during topology optimization, and thus the stiffness and mass matrices of the column remain the same. Therefore, in Case III, applied earthquake loads to degrees of freedom along column locations would be greater than dynamic forces applied to columns in Case I, resulting in the increased volume.

Table 3.3: Volume of final topologies ($\beta^{\text{target}} = 2.5$, $P_f = 0.62$ %).

Φ_0	Case I	Case II	Case III
250	1.717 (1.734) m^3	2.049 (2.059) m^3	2.157 (2.169) m^3
300	1.904 (1.928) m^3	2.251 (2.278) m^3	2.402 (2.419) m^3

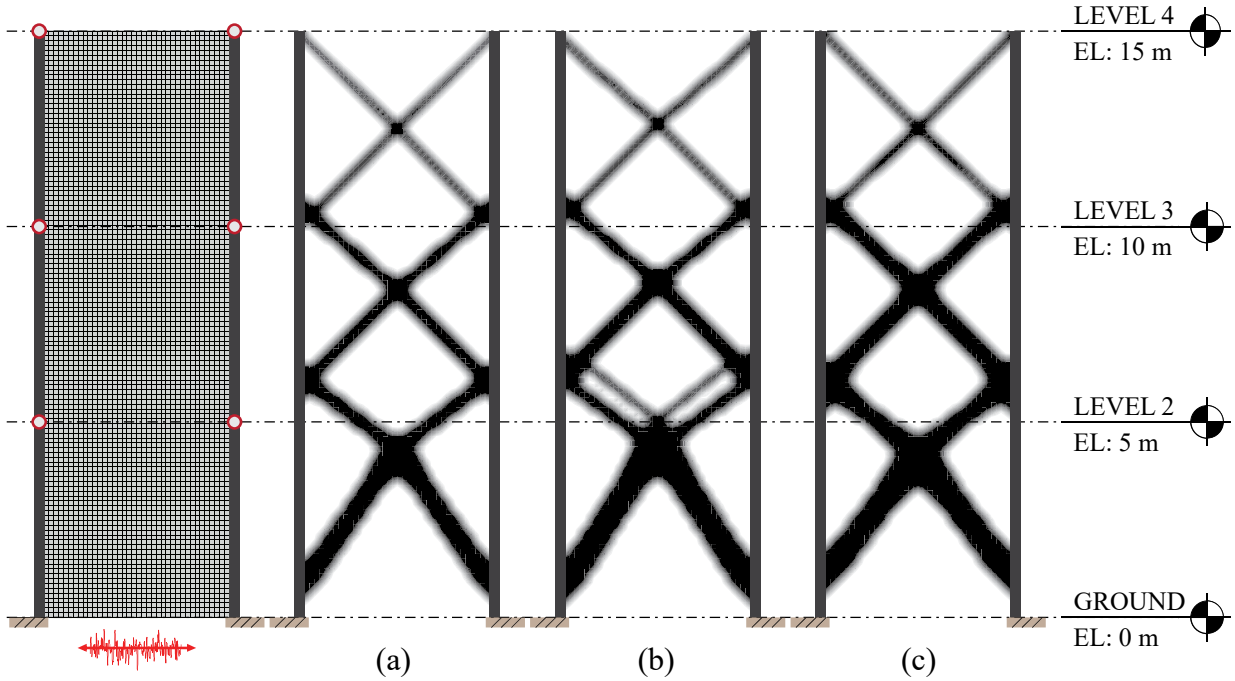

Figure 3.6: Topology optimization solutions to the three-story building example ($\Phi_0 = 250$, $\beta^{target} = 2.5$, $P_f = 0.62$ %). (a) Case I: column size 0.5 m × 0.5 m, $u_0 = 0.02$, (b) Case II: column size 0.5 m × 0.5 m, $u_0 = 0.0175$, and (c) Case III: column size 0.6 m × 0.6 m, $u_0 = 0.02$.

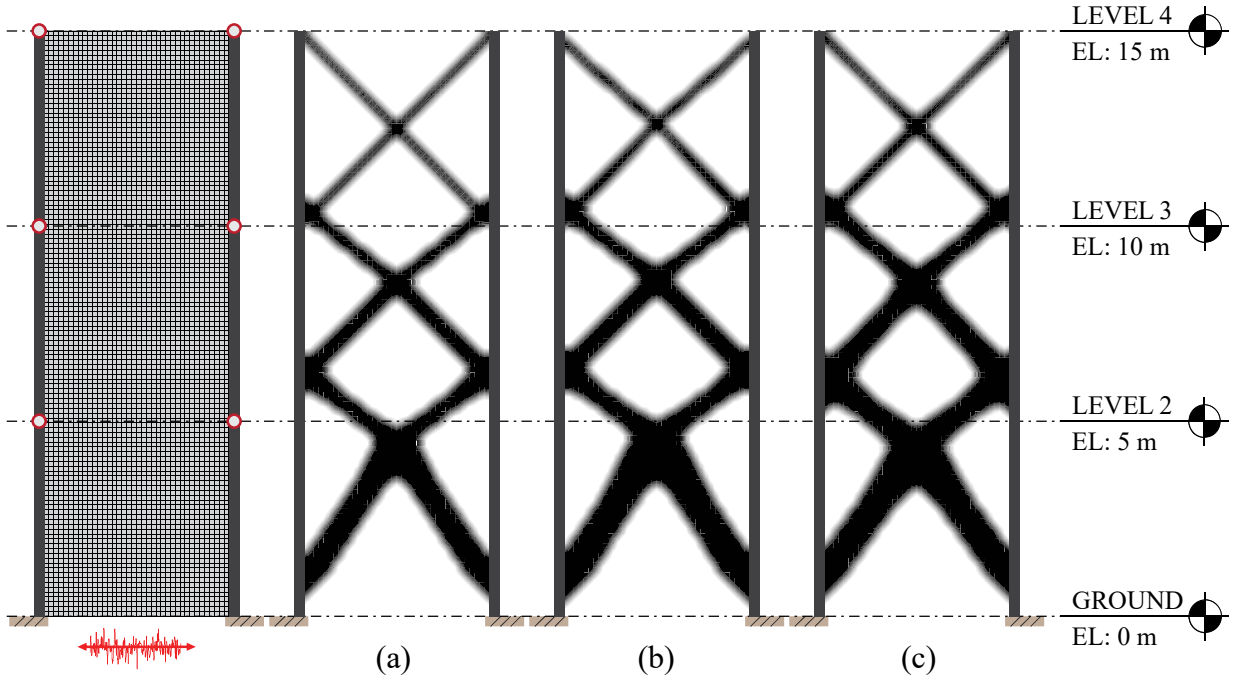

Figure 3.7: Topology optimization solutions to the three-story building example ($\Phi_0 = 300$, $\beta^{target} = 2.5$, $P_f = 0.62$ %). (a) Case I: column size 0.5 m × 0.5 m, $u_0 = 0.02$, (b) Case II: column size 0.5 m × 0.5 m, $u_0 = 0.0175$, and (c) Case III: column size 0.6 m × 0.6 m, $u_0 = 0.02$.

Second, the target reliability index of the cases is changed to 2.0 and 3.0 which correspond to the target failure probabilities $P_f^{\text{target}} = \Phi(-2.0) = 2.28$ % and $P_f^{\text{target}} = \Phi(-3.0) = 0.13$ %, respectively. The optimization solutions using changed target reliability indices are illustrated in Figures 3.8 and 3.9. This shows the impact of changing the target reliability index on optimal bracings. More specifically, the increase in the reliability index results in thicker bracings and alters intersection points on the first two bottom floor levels. Additional branches of material distributions are also observed and the volumes obtained for the cases in Figures 3.8 and 3.9 are summarized in Table 3.4. Figure 3.10 shows the convergence histories of the objective function (volume), the reliability index and the failure probability of Case II, shown in Figure 3.9 (b), whose parameters are $\Phi_0 = 300$, $\beta^{\text{target}} = 3.0$, $u_0 = 0.0175$. The convergence histories confirm that the proposed topology optimization method and the sensitivity formulation can successfully achieve the topology optimization solution under constraints on the instantaneous failure probabilities defined in terms of the drift ratios. Additionally, a neighborhood in the design domain that satisfies the constraints is quickly identified, and the remaining design iterations are to achieve the minimum volume within the identified neighborhood. Figure 3.11 shows time histories of inter-story drift ratios (Case II, $\Phi_0 = 300$, $\beta^{\text{target}} = 3.0$, $u_0 = 0.0175$) of the initial design (i.e. the continuum domain completely filled) and the optimal design for an input process randomly generated from the Kanai-Tajimi filter model. The optimized system shows improved dynamic performance even though 40.1 % of the original volume is used.

A manufacturing constraint on pattern repetition in topology optimization (Almeida et al. 2010; Stromberg 2011) can be implemented for practical engineering applications. This constraint allows engineers to achieve constructability of the structural system such as same connection details, re-usages of formworks for bracing and considering aesthetic perspective as well. Topology optimization results of Case I with $\beta^{\text{target}} = 2.5$, and varying Φ_0 of 250 or 300 are shown in Figures 3.12 and 3.13. The number of pattern repetitions m = 2, 3 and 4 are used to obtain these results. Volumes of topology optimization results are summarized in Table 3.5.

Table 3.4: Volume of final topologies ($\Phi_0 = 300$).

β^{target}	Case I	Case II	Case III
2.0	1.505 (1.531) m^3	1.720 (1.731) m^3	1.870 (1.884) m^3
3.0	2.401 (2.409) m^3	3.004 (3.022) m^3	3.077 (3.100) m^3

Table 3.5: Volume of final topologies with the pattern repetition constraint ($\beta^{target} = 2.5$, P_f = 0.62 %).

Φ_0	$m = 2$	$m = 3$	$m = 4$
250	2.627 (2.656) m^3	2.590 (2.616) m^3	2.995 (3.037) m^3
300	3.117 (3.144) m^3	2.966 (3.001) m^3	3.318 (3.363) m^3

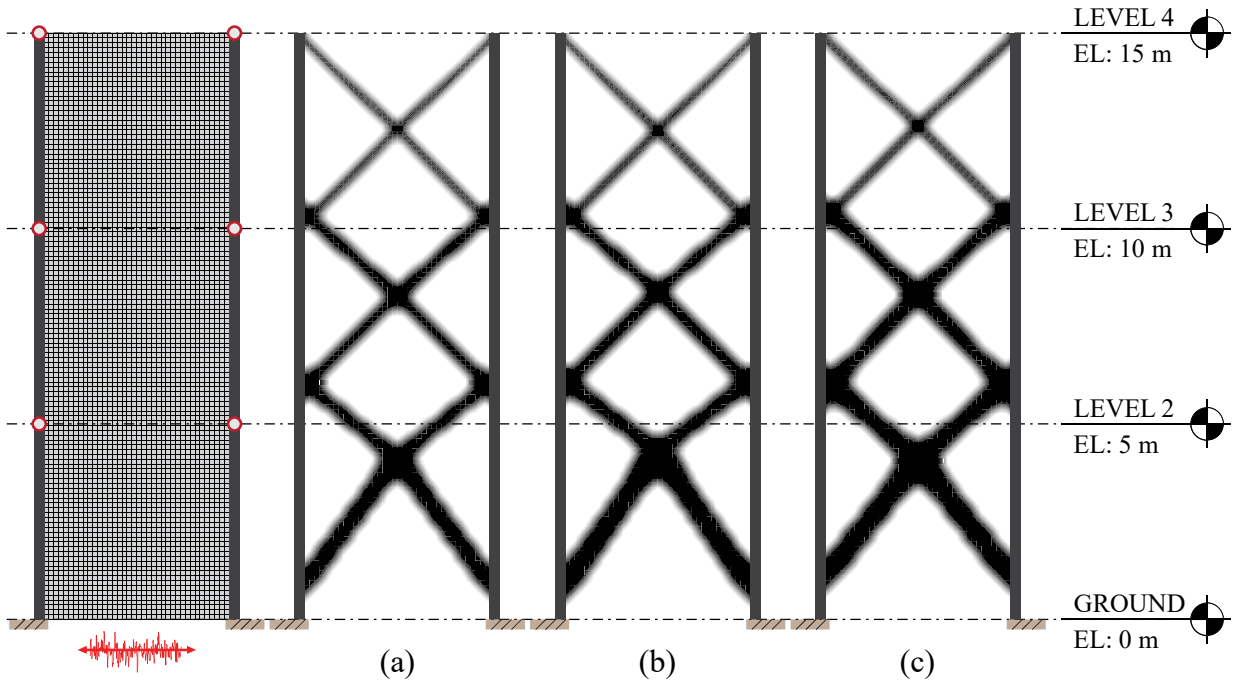

Figure 3.8: Topology optimization solutions to the three-story building example ($\Phi_0 = 300$, $\beta^{target} = 2.0$, $P_f = 2.28$ %). (a) Case I: column size 0.5 m × 0.5 m, $u_0 = 0.02$, (b) Case II: column size 0.5 m × 0.5 m, $u_0 = 0.0175$, and (c) Case III: column size 0.6 m × 0.6 m, $u_0 = 0.02$.

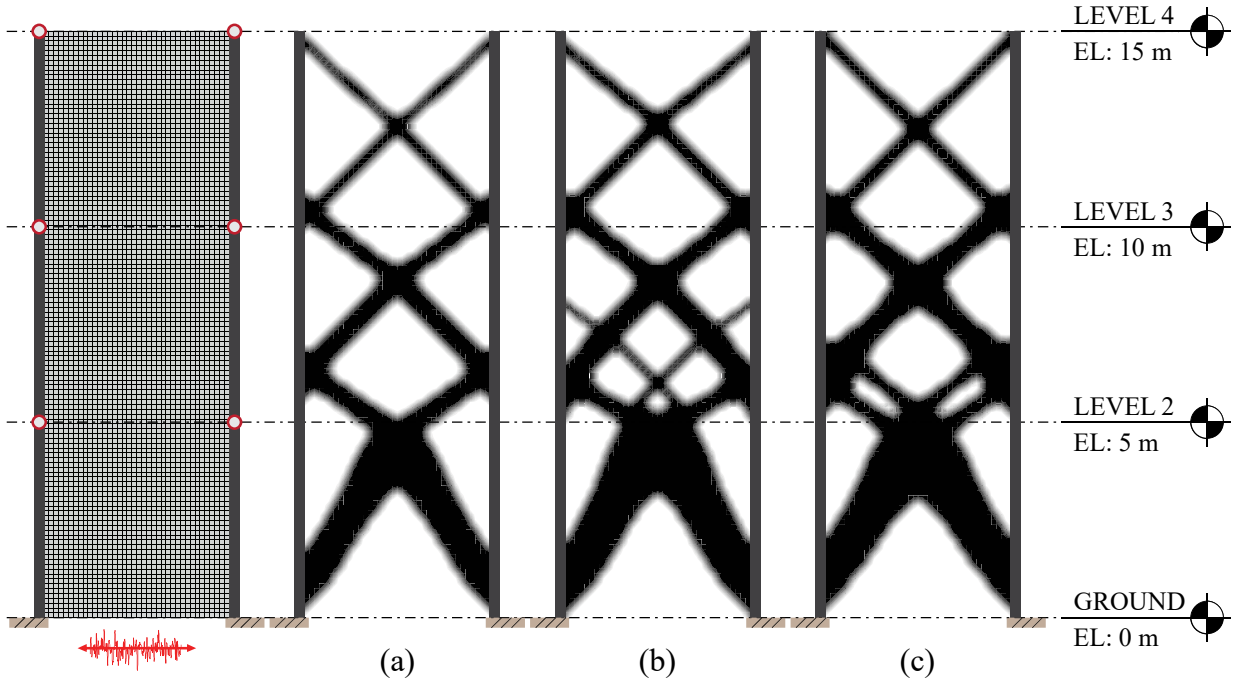

Figure 3.9: Topology optimization solutions to the three-story building example ($\Phi_0 = 300$, $\beta^{target} = 3.0$, $P_f = 0.13$ %). (a) Case I: column size 0.5 m × 0.5 m, $u_0 = 0.02$, (b) Case II: column size 0.5 m × 0.5 m, $u_0 = 0.0175$, and (c) Case III: column size 0.6 m × 0.6 m, $u_0 = 0.02$.

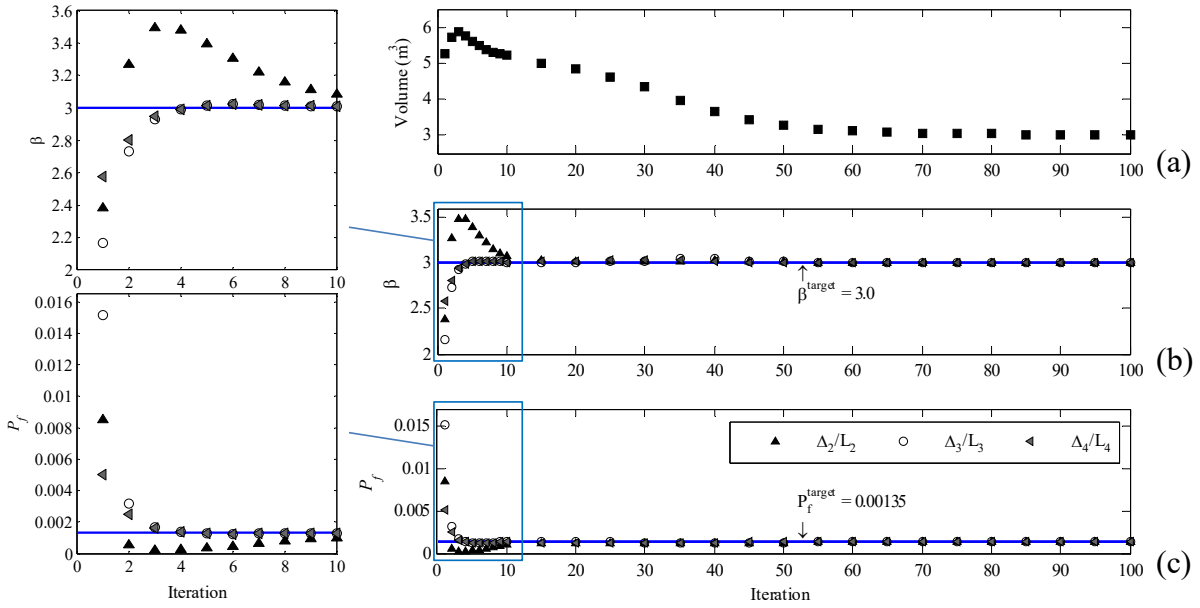

Figure 3.10: Convergence history of the problem shown in Figure 3.9 (b): (a) volume, (b) reliability index, and (c) failure probability.

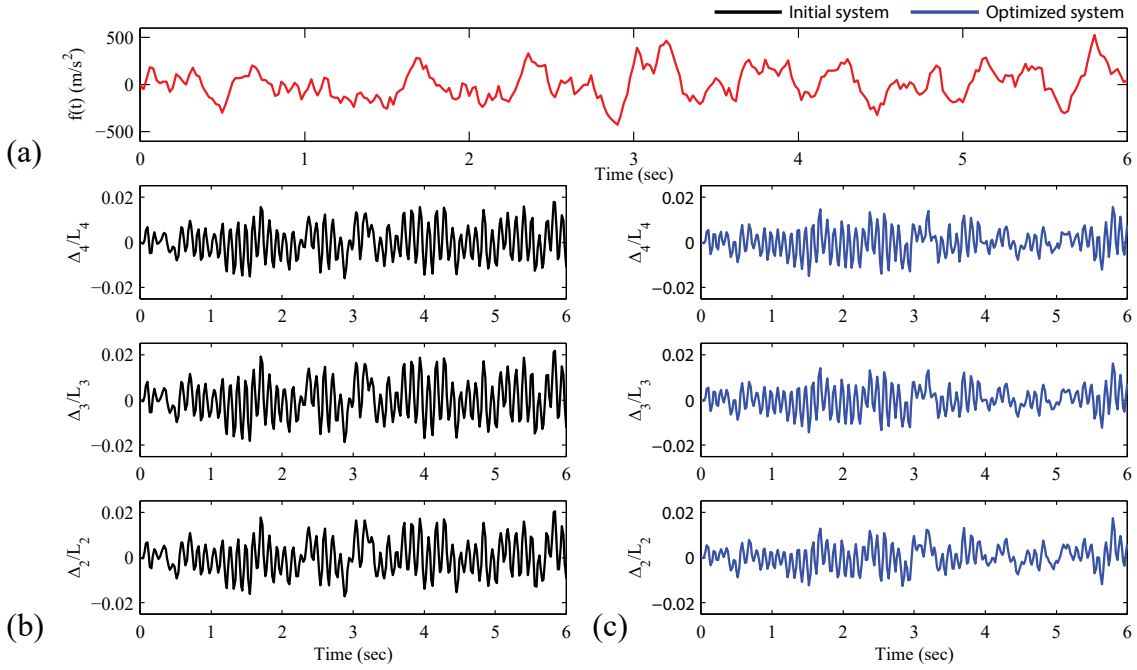

Figure 3.11: Dynamic response comparison of the problem shown in Figure 3.9 (b): (a) Randomly generated ground motion excitations, (b-c) corresponding dynamic responses of the initial design and the optimal design.

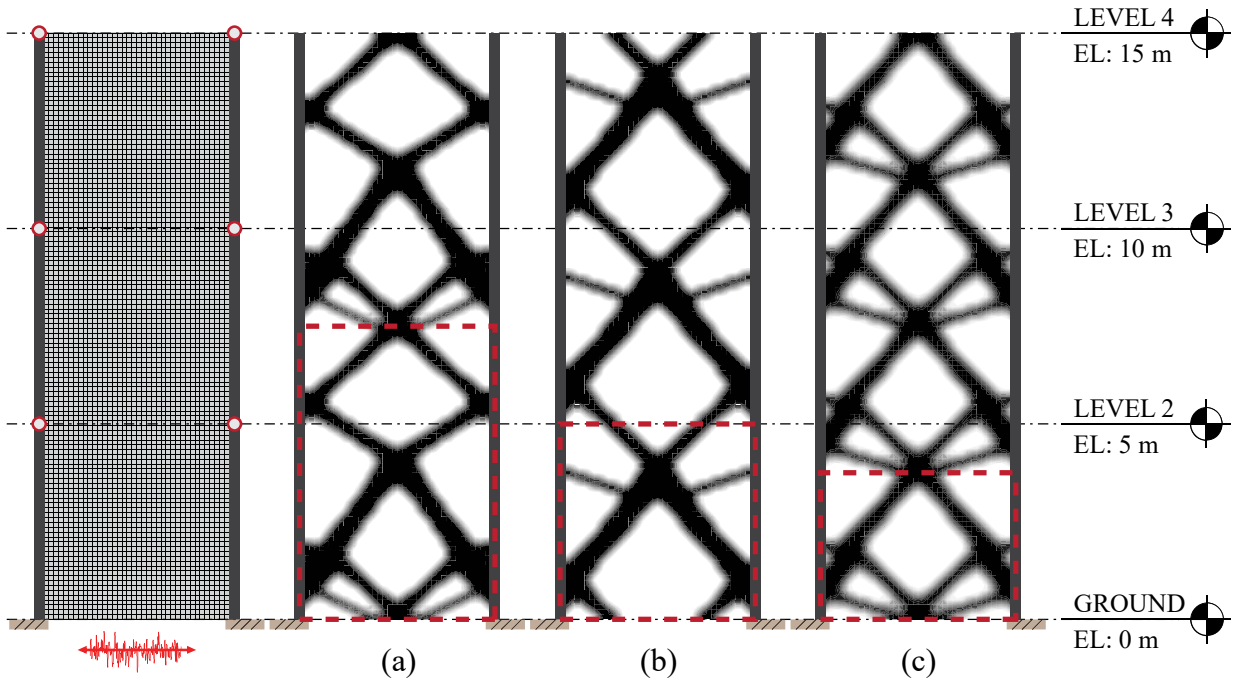

Figure 3.12: Topology optimization solutions to the three-story building example with the pattern repetition constraint. $\Phi_0 = 250$, $\beta^{target} = 2.5$, $P_f = 0.62$ %: (a) $m = 2$, (b) $m = 3$, and (c) $m = 4$.

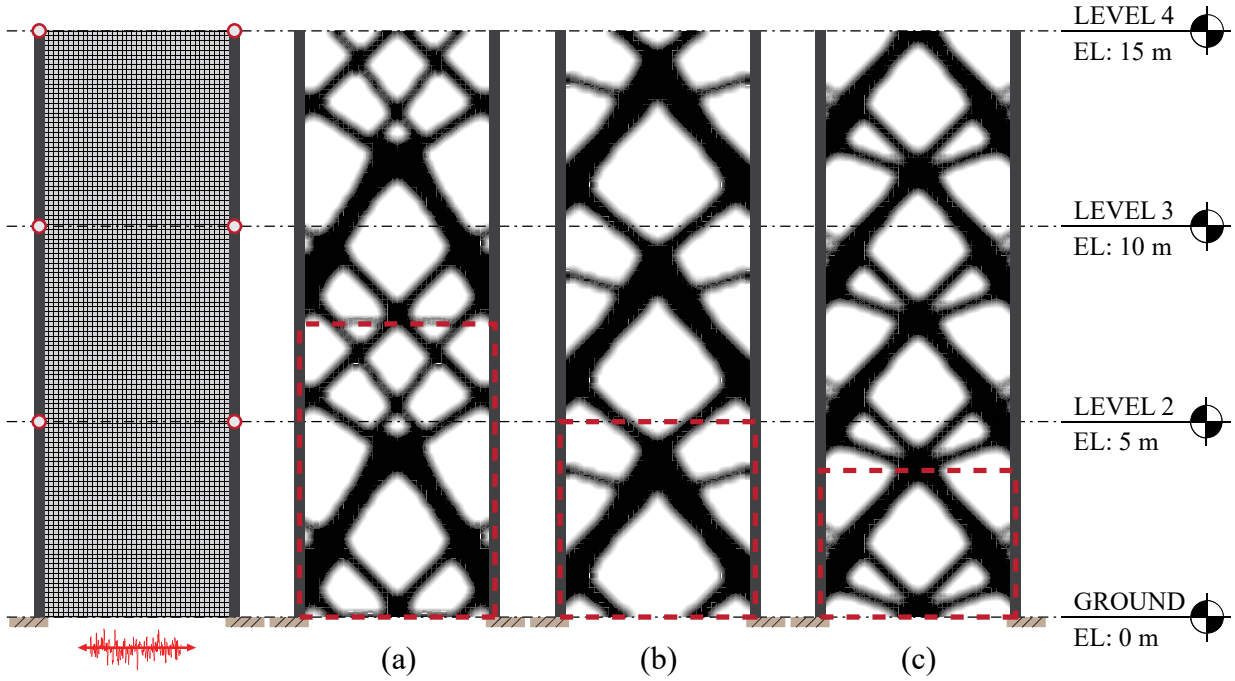

Figure 3.13: Topology optimization solutions to the three-story building example with the pattern repetition constraint. $\Phi_0 = 300$, $\beta^{target} = 2.5$, $P_f = 0.62$ %: (a) $m = 2$, (b) $m = 3$, and (c) $m = 4$.

3.5.3. Study of stochastic responses over topology optimization results

After the topology optimization result is obtained with the constraint on the instantaneous failure probability at the time point $t_0 = 6$ *s*, reliability indices and failure probabilities of the obtained topology layout solution at different time points from 0.5 *s* to 10 *s* are studied. For this study, the topology optimization result with the pattern repetition shown in Figure 3.13 (c) is used. Our results show that failure probabilities (and reliability indices) remain constant within the time duration considered after approximately 3 seconds (see Figure 3.14). This confirms that the optimization solution at the specific time point ($t_0 = 6$ *s*) by the proposed method under the filtered Gaussian input process can represent the reliability of the system during the stationary strong motion period.

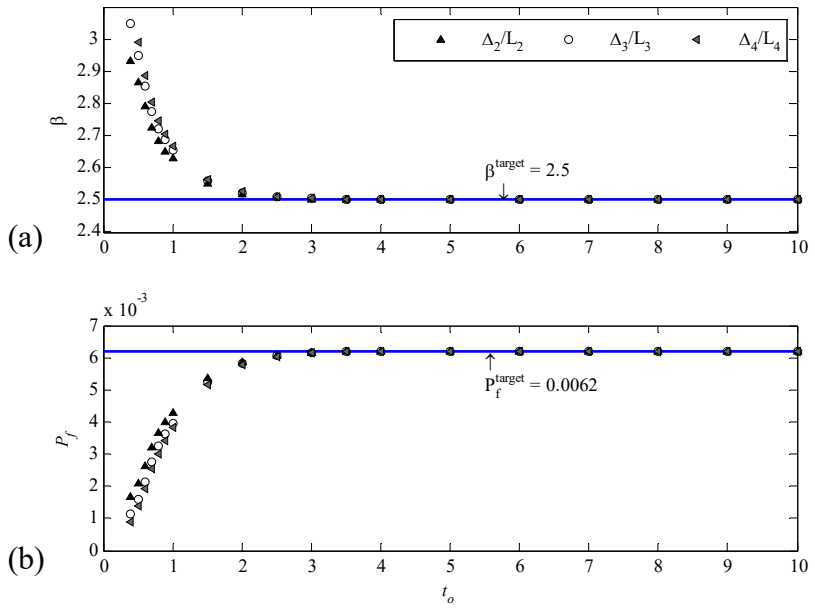

Figure 3.14: (a) Reliability index and (b) failure probability of the topology optimization solution in Figure 3.12 (c) with varying time points.

The effects of solutions converted to discrete material layouts on dynamic responses and failure probabilities are studied for practical engineering purposes. During a post-processing stage, material densities less than 0.5 are converted to zero, and those that are greater than 0.5 are

converted to one. The optimization results under the pattern repetition constraint (see Figures 3.12 and 3.13) are processed using converted material densities. The layout solutions of this process are illustrated in Figures 3.15 and 3.16. Comparison results between continuous solutions in Figures 3.11 and 3.12 and interpreted discrete solutions after the post-processing are tabulated in Table 3.6. Discrete solutions show increased reliability indices in all cases and result in lower failure probabilities. Dynamic responses of the continuous solution of $\Phi_0 = 300$, $\beta^{target} = 2.5$, and $m = 4$ (see Figure 3.13 (c)) in each floor level and the discrete solution (see Figure 3.16 (c)) under a randomly generated filtered ground motion are shown in Figure 3.17. Compared to the continuous solutions, the overall dynamic responses of the discrete layout solution show reduced magnitudes, which indicate the possibility of the lower failure probability.

Lastly, a cross-comparison among optimization results is performed to study whether different model parameters in topology optimization lead to significant changes of structural responses. As shown in Figure 3.18, differences in dynamic responses of Case I and Case III under $\Phi_0 = 250$, $\beta^{target} = 2.5$ are negligible. The topology optimization result of Case II which has $u_0 = 0.0175$ leads to overall reduced magnitude compared to others, resulting in an observable difference in structural responses. Further study of optimization solutions from the pattern repetition constraint was performed. Figure 3.19 illustrates structural responses of topology optimization results subjected to a randomly generated ground motion with $\Phi_0 = 300$, $\beta^{target} = 2.5$, $P_f = 0.62$ % considered in Figures 3.16 (a) through 3.16 (c) with the number of pattern repetitions m. Structural responses of these cases remain relatively constant despite changes in pattern numbers which led to different material layouts and final volumes.

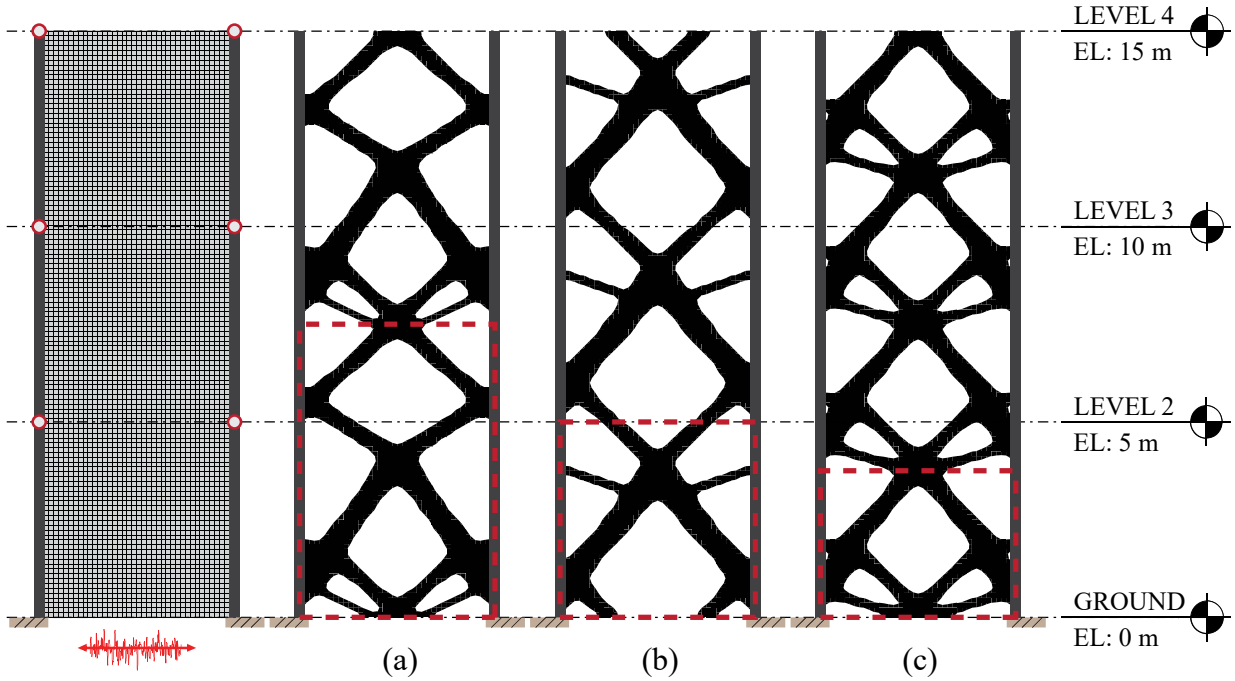

Figure 3.15: Discrete solutions to the three-story building example with the pattern repetition constraint. $\Phi_0 = 250$, $\beta^{target} = 2.5$, $P_f = 0.62$ %: (a) $m = 2$, (b) $m = 3$, and (c) $m = 4$.

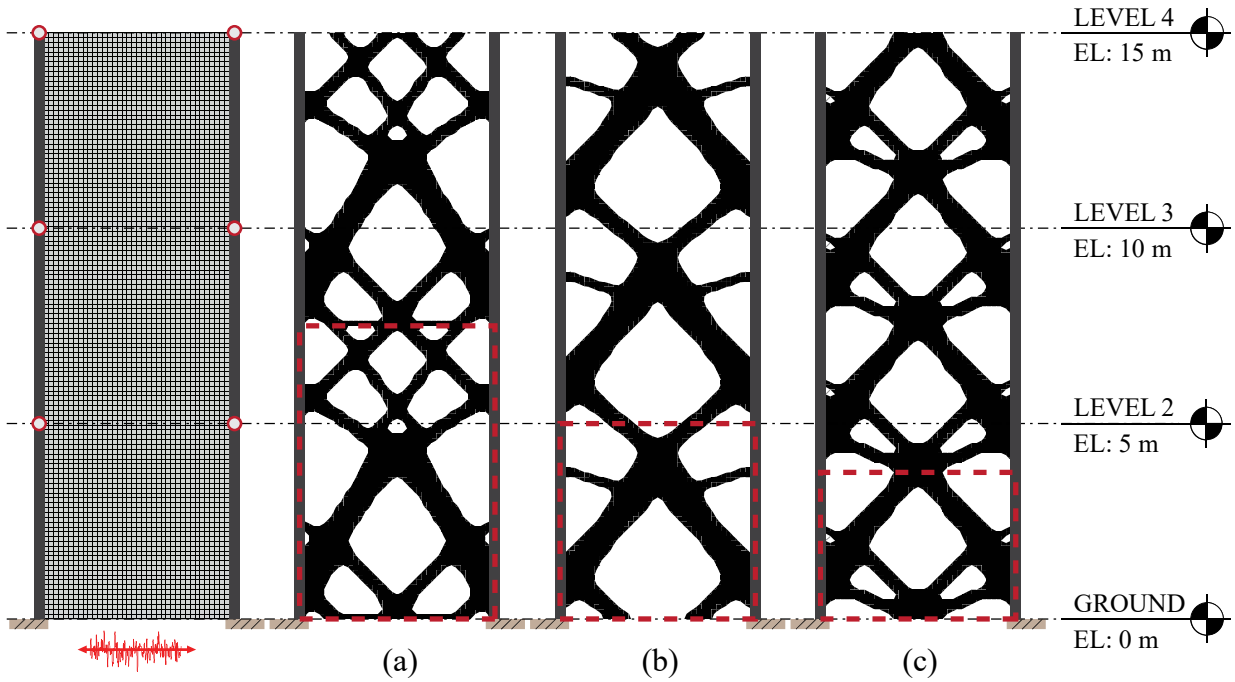

Figure 3.16: Discrete solutions to the three-story building example with the pattern repetition constraint. $\Phi_0 = 300$, $\beta^{target} = 2.5$, $P_f = 0.62$ %: (a) $m = 2$, (b) $m = 3$, and (c) $m = 4$.

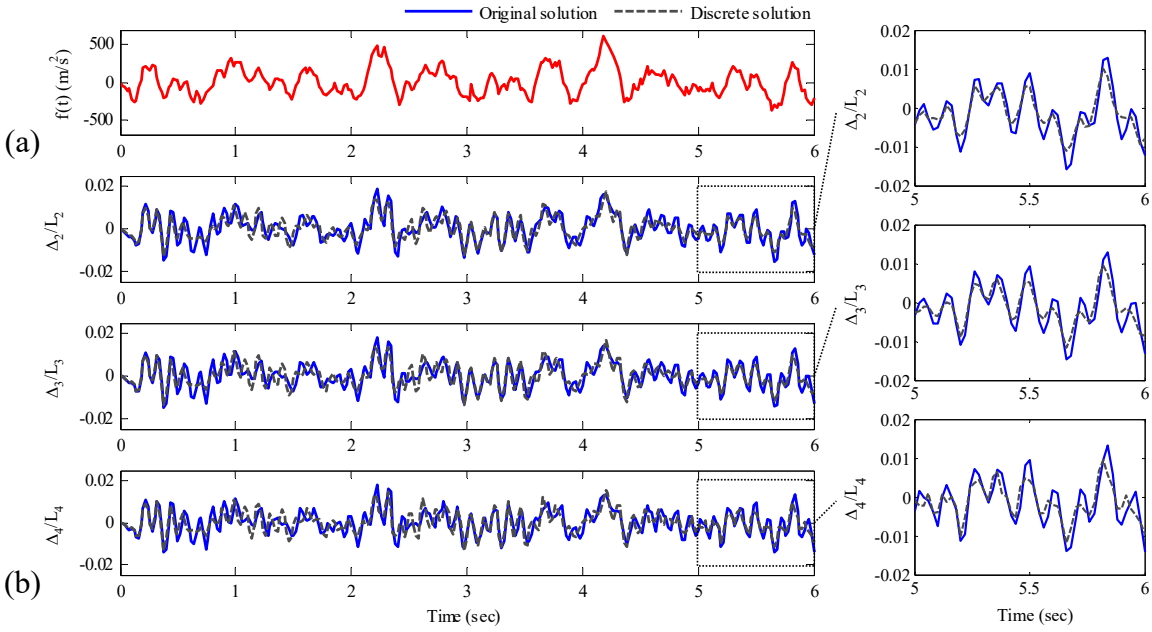

Figure 3.17: Dynamic response comparison between continuous solution shown in Figure 3.12 (c) and discrete solution of Figure 3.15 (c). Randomly generated ground motion excitations (a) and corresponding dynamic responses (b).

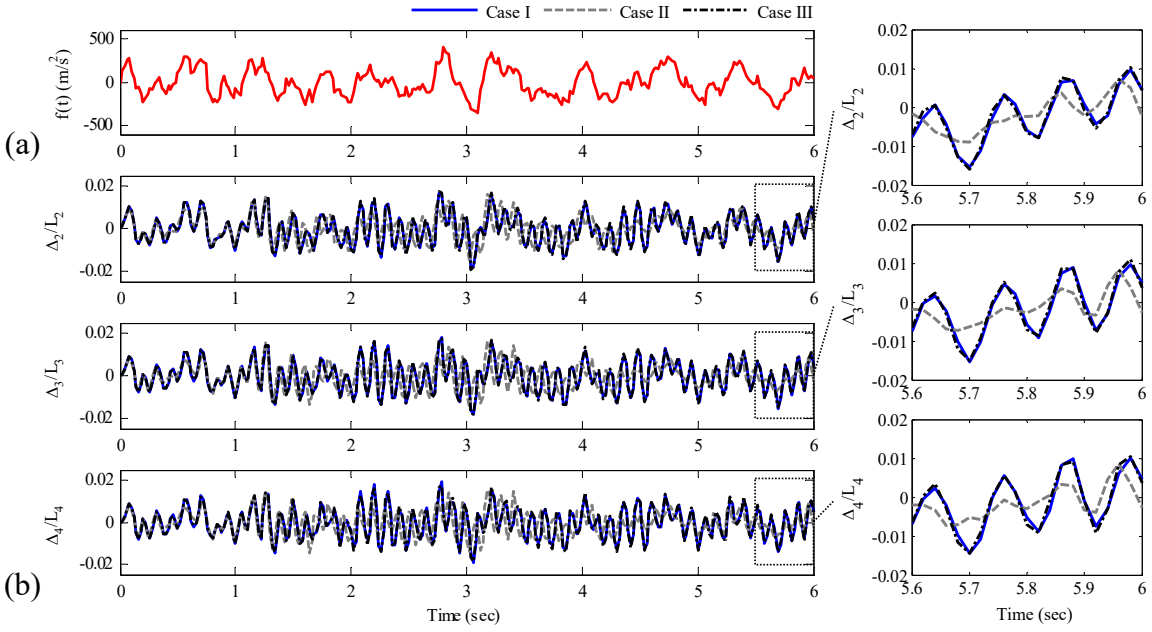

Figure 3.18: Comparison of topology optimization results to the three-story building example, Φ_0 = 250, β^{target} = 2.5, P_f = 0.62 %. Randomly generated ground motion excitations (a) and corresponding dynamic responses (b). (Case I: column size 0.5 m × 0.5 m, u_0 = 0.02. Case II: column size 0.5 m × 0.5 m, u_0 = 0.0175. Case III: column size 0.6 m × 0.6 m, u_0 = 0.02).

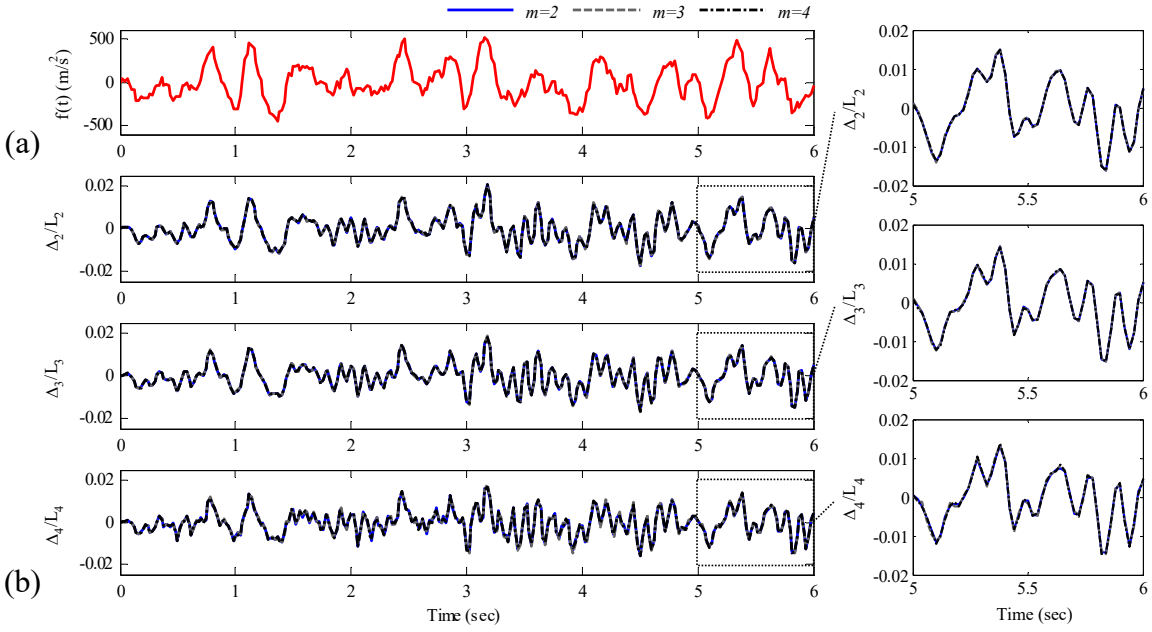

Figure 3.19: Comparison of topology optimization results to the three-story building example with the pattern repetition constraint, $\Phi_0 = 300$, $\beta^{target} = 2.5$, $P_f = 0.62$ %. Randomly generated ground motion excitations (a) and corresponding dynamic responses (b).

Table 3.6: Comparison of continuous solution and discrete solution ($\beta^{target} = 2.5$, $P_f = 0.62$ %).

	Continuous solution		Discrete solution											
			$\Phi_0 = 250$						$\Phi_0 = 300$					
			m=2	*m*=3	*m*=4	*m*=2	*m*=3	*m*=4	*m*=2	*m*=3	*m*=4	*m*=2	*m*=3	*m*=4
	β	P_f	β			P_f			β			P_f		
E_{f_1}	2.5	0.621	2.83	2.88	2.97	0.233	0.199	0.149	2.83	2.82	2.91	0.233	0.240	0.181
E_{f_2}	2.5	0.621	2.89	2.80	2.87	0.193	0.256	0.205	2.88	2.73	2.79	0.199	0.317	0.264
E_{f_3}	2.5	0.621	2.72	2.89	2.77	0.326	0.193	0.280	2.77	2.79	2.83	0.280	0.264	0.233

3.5.4. Study of geometric uncertainty of discrete material distribution

A further study on the geometry uncertainty is carried out. The geometry uncertainty may be caused during the converting process in practical fields from continuous topology optimization solutions to discrete ones aforementioned in Section 3.5.3. Thus, the cut-off value of material density is assumed that it follows the normal distribution with a mean $\mu_{m\_cut\text{-}off}$ and a standard deviation $\sigma_{cut\text{-}off}$ rather than the fixed value 0.5. Therefore, each density value in each finite element is compared to a random cut-off value in order to convert to discrete material layouts. Figure 3.20 shows discrete solutions of Case III ($\Phi_0 = 250$, $\beta^{target} = 2.5$) shown in Figure 3.6 (c) under the geometry uncertainty. It is noted that the result is one of 20 simulations of random cut-offs. A discrete solution without the geometry uncertainty is provided in Figure 3.20 (a) for comparisons. Figure 3.21 shows effects of geometry uncertainties on reliability indices associated inter-story drift ratio constraints after 20 simulations. The reliability indices are still between target reliability indices from continuous solutions and reliability indices from discrete solutions.

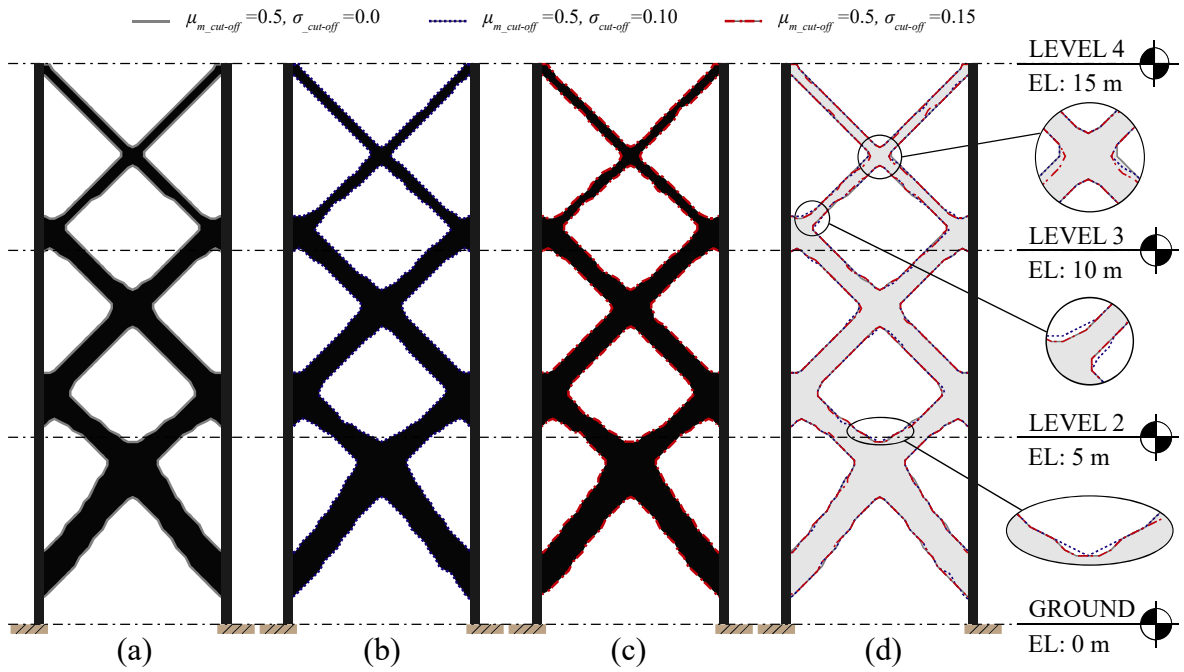

Figure 3.20: Discrete solutions under geometry uncertainty: (a) $\mu_{m\_cut\text{-}off} = 0.5$, $\sigma_{cut\text{-}off} = 0$, (b) $\mu_{m\_cut\text{-}off} = 0.5$, $\sigma_{cut\text{-}off} = 0.1$, (c) $\mu_{m\_cut\text{-}off} = 0.5$, $\sigma_{cut\text{-}off} = 0.15$, and (d) overlapped outlines of Figures 3.20 (a) through 3.20 (c).

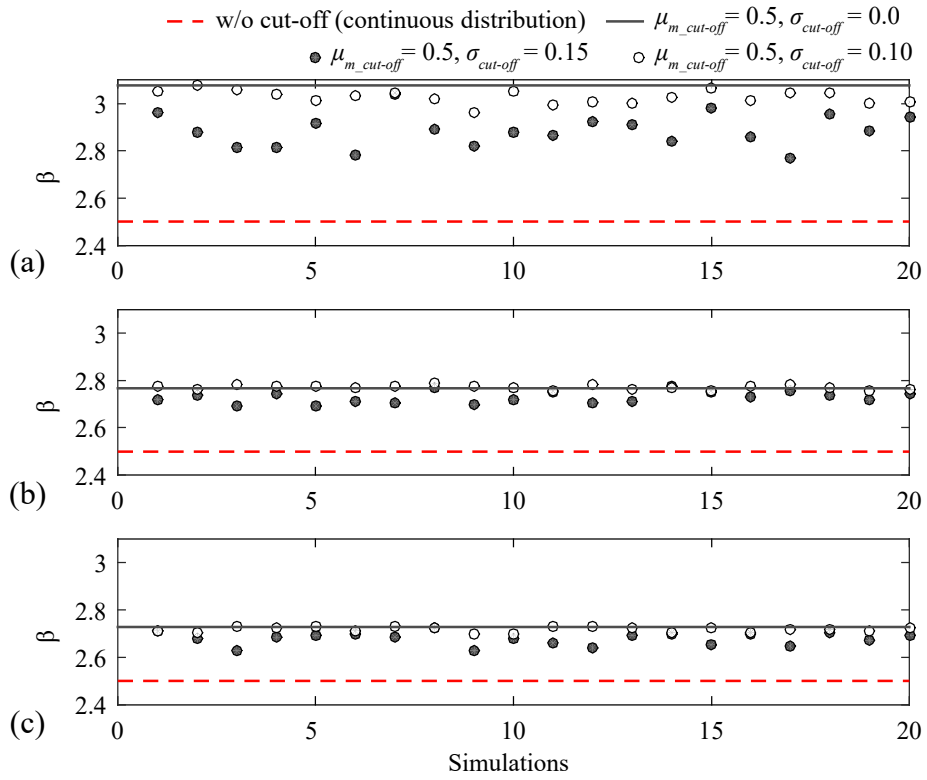

Figure 3.21: Reliability indices associated inter-story drift ratio constraints after geometry uncertainty simulations. (a) Δ_4/L_4, (b) Δ_3/L_3, and (c) Δ_2/L_2.

3.5.5. Parametric study on impact of ground motion characteristics

Next, a numerical example of a six-story building is considered for a parametric study on the impact of ground motion characteristics. The example employs the same parameters as those used for the three-story building example unless specified otherwise. Coefficients $\kappa_0 = 0.56$ and $\kappa_1 = 5.0\times10^{-4}$ are used for the Rayleigh damping model to achieve 2% damping. The column sizes and the target reliability indices are as shown in Table 3.7.

Table 3.7: Six-story building: Parameters used for design domain, probabilistic constraint, and ground motion model.

Φ_0	β^{target}	P_f^{target} (%)	Column size (m × m)	u_0
2	2.5	0.62	0.6 × 0.6	0.02

Three values of the dominant frequency and damping ratio (bandwidth) of the Kanai-Tajimi filter are applied respectively, i.e. $\omega_f = 4.7\pi, 5.0\pi, 5.3\pi$ (rad/sec) and $\zeta_f = 0.2, 0.3, 0.4$. The impact of the dominant frequency is shown in Figures 3.22 (a) through 3.22 (c), while Figures 3.22 (d) and 3.22 (e) demonstrate the impact of the bandwidth parameter. The convergence history of volumes for different parameters in damping ratios and dominant frequencies are shown in Figure 3.23. From the modal analysis of the original structure with the uniform distribution of the material density, 0.5 over the Q4 design domain, the first natural frequency of the six-story building is approximately 18.06 rad/s (the natural period $T_1 = 0.348$ s). A decrease in the damping ratio of the filter (the bandwidth of the process) increases the optimized volume, as shown in Figure 3.23. In order to investigate reasons for these results, the power spectral density function of the input ground motion is plotted in Figure 3.24 (a). For the given ground motion model, a decrease in the filter damping ratio increases the power spectral density at the natural frequency of the building structure, which explains the increase in the volume of the optimization solution. Figure 3.24 (b) shows that an increase in the predominant frequency of the filter increases the power spectral density at the natural frequency. This shows why an increase in the dominant frequency results in larger optimized volume for the given example, as shown in Figure 3.23.

It is observed that characteristics of the ground motion make significant impacts on the topologies such as geometries, intersection points, bracing-column points, and the shape of the bracings. Additionally, the match between the frequency content of the ground motion and the natural frequency of the structure affects how the ground motion characteristics determine topological solutions. Therefore, it is important to describe the frequency content of the ground motion accurately during topology optimization under stochastic excitations.

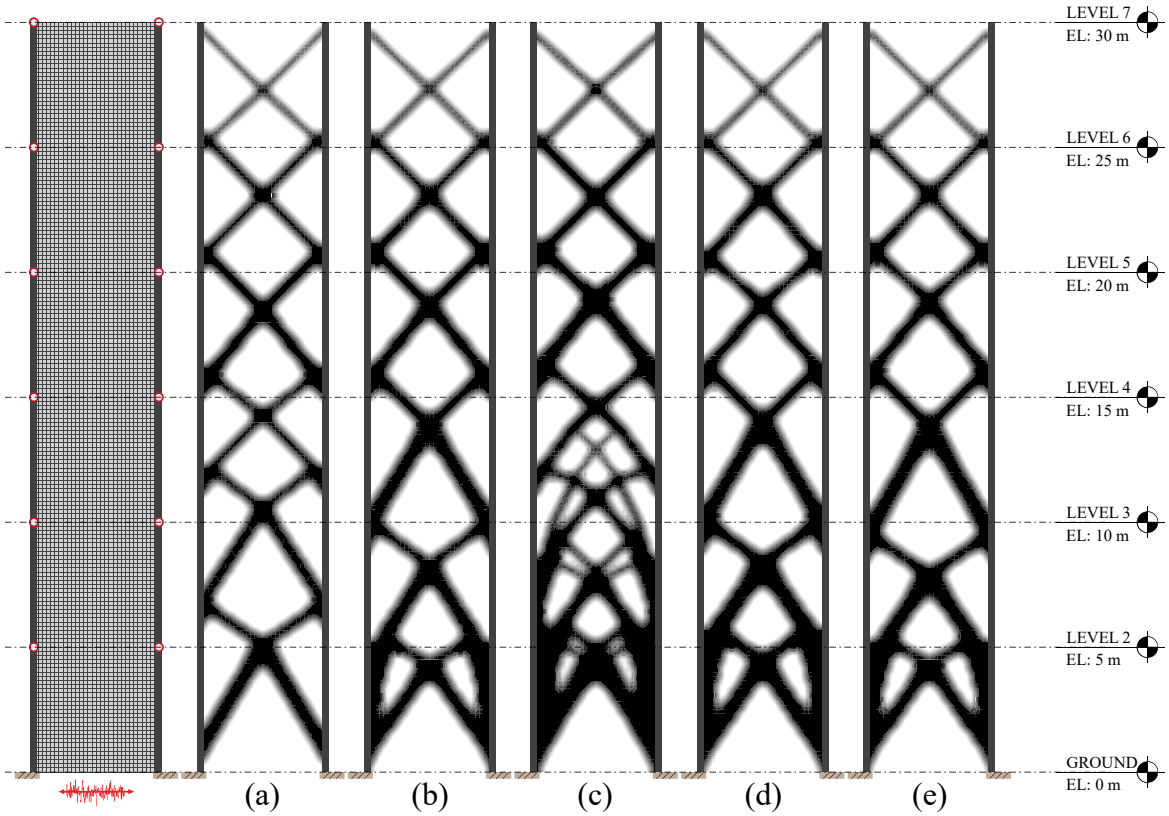

Figure 3.22: Topology optimization solutions to the six-story building ($\Phi_0 = 2$, $\beta^{target} = 2.5$): (a) $\omega_f = 4.7\pi$, $\zeta_f = 0.4$, (b) $\omega_f = 5.0\pi$, $\zeta_f = 0.4$, (c) $\omega_f = 5.3\pi$, $\zeta_f = 0.4$, (d) $\omega_f = 5.0\pi$, $\zeta_f = 0.2$, and (e) $\omega_f = 5.0\pi$, $\zeta_f = 0.3$.

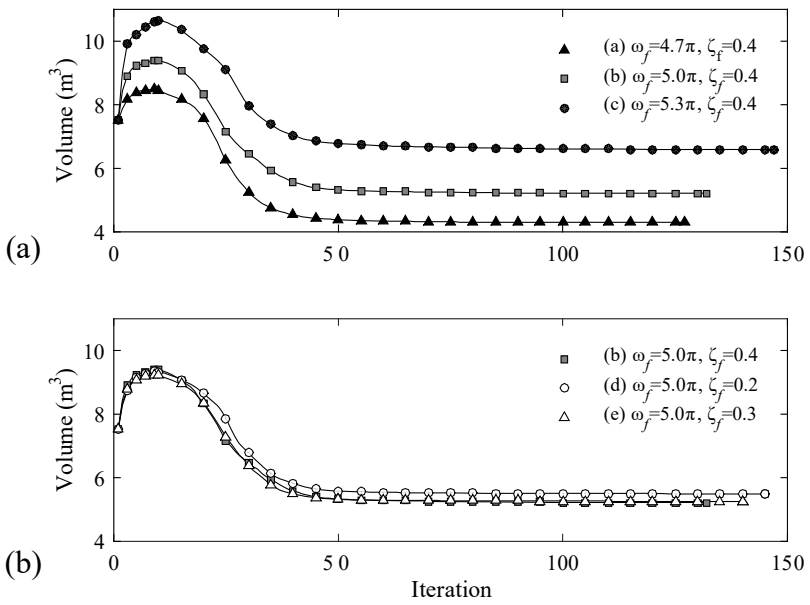

Figure 3.23: Convergence history of topology optimization solutions shown in Figure 3.22 ($\Phi_0 = 2$, $\beta^{target} = 2.5$): (a) change in the predominant frequency of the random process, (b) change in the bandwidth of the random process.

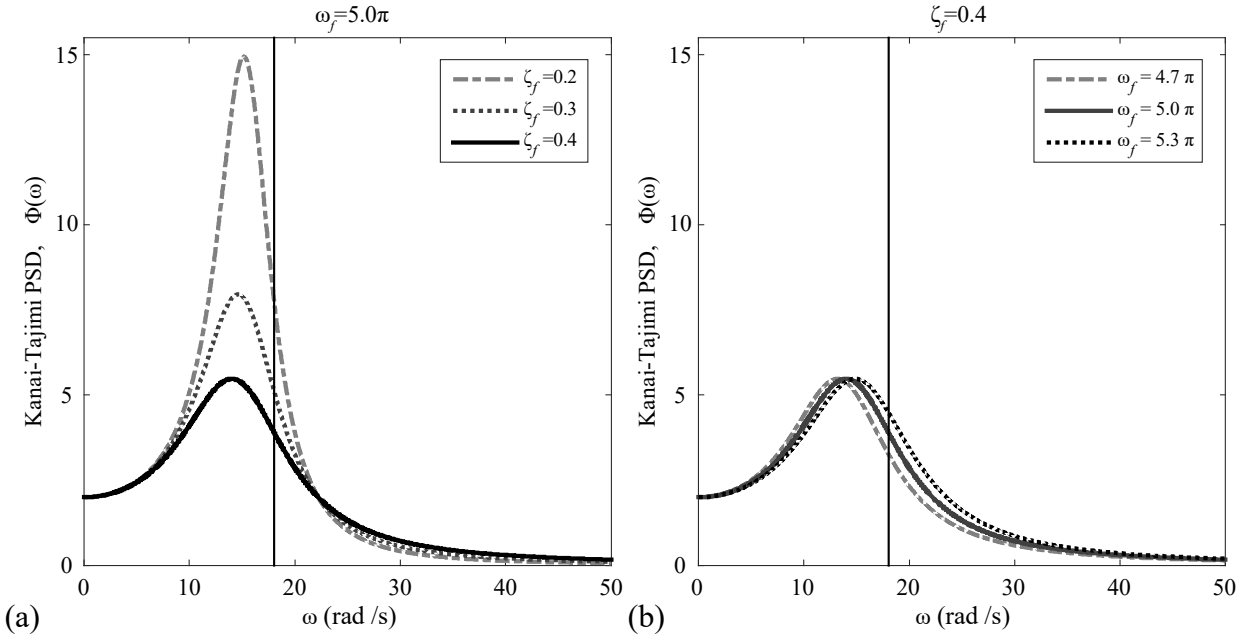

Figure 3.24: Power spectral density of ground excitations ($\Phi_0 = 2$) while changing (a) damping ratios and (b) predominant frequencies.

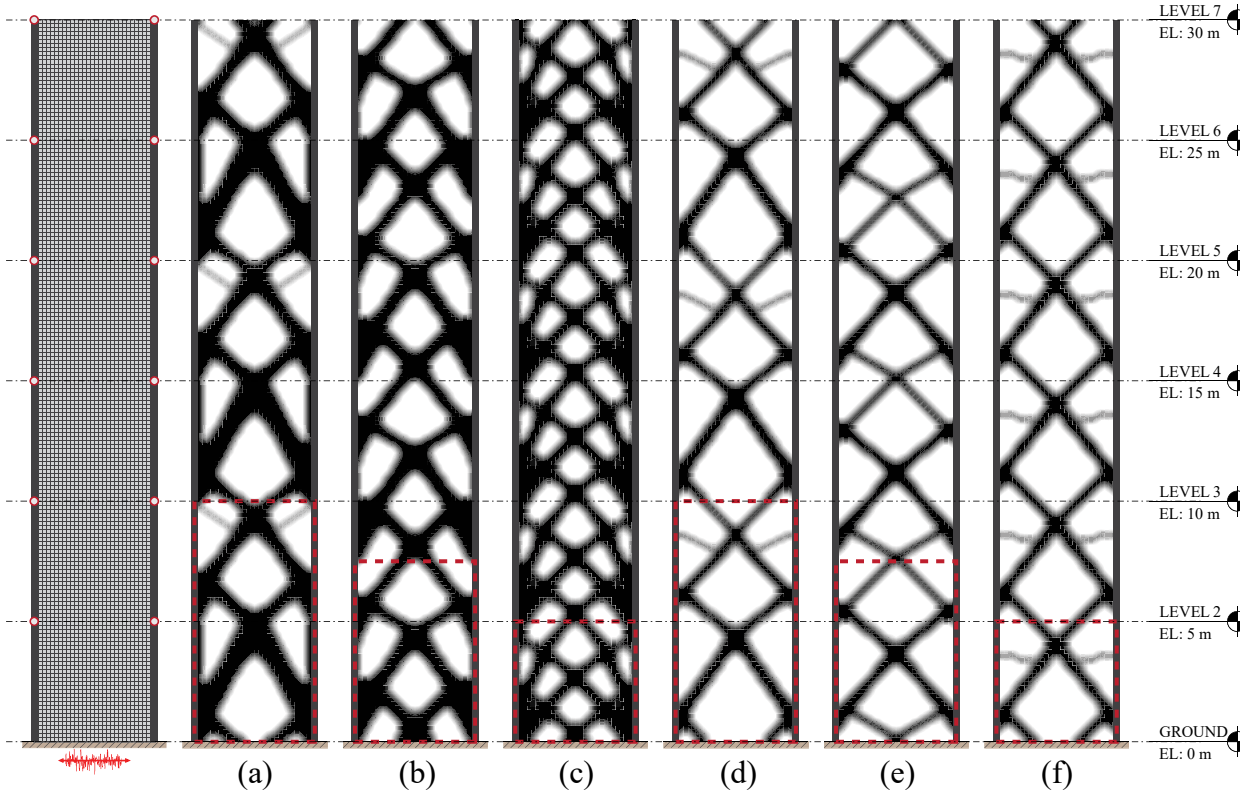

Figure 3.25: Topology optimization solutions to the six-story building example with the pattern repetition constraint ($\Phi_0 = 2$, $\omega_f = 5.0\pi$, $\zeta_f = 0.4$): (a) $m = 3$, $\beta^{\text{target}} = 2.5$, (b) $m = 4$, $\beta^{\text{target}} = 2.5$, (c) $m = 6$, $\beta^{\text{target}} = 2.5$, (d) $m = 3$, $\beta^{\text{target}} = 2.0$, (e) $m = 4$, $\beta^{\text{target}} = 2.0$, and (f) $m = 6$, $\beta^{\text{target}} = 2.0$.

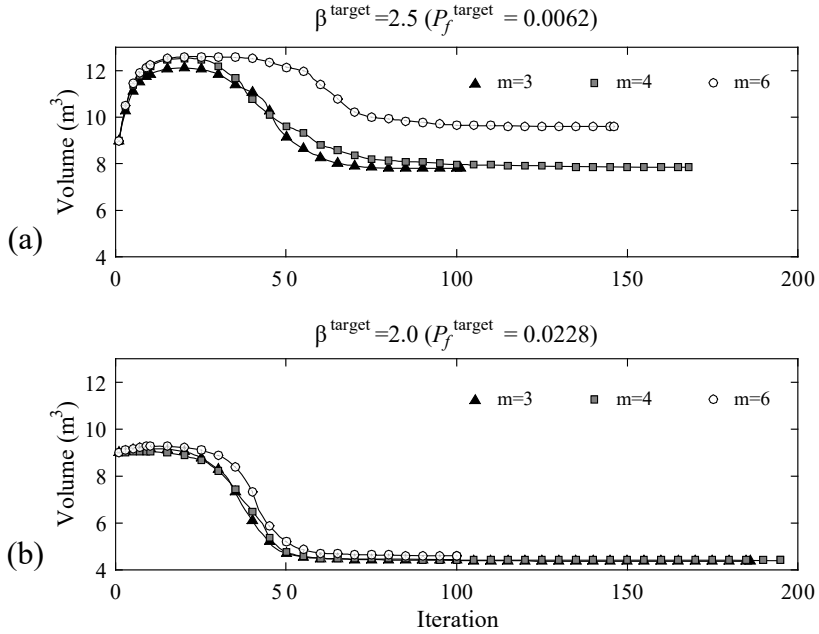

Figure 3.26: Convergence history of topology optimization solutions shown in Figure 3.25 (Φ_0 = 2, ω_f = 5.0π, ζ_f = 0.4): (a) target reliability index β^{target} = 2.5, (b) target reliability index β^{target} = 2.0.

The pattern repetition constraint of the aforementioned three story building example is further applied to the six story building problem. Figure 3.25 shows topology optimization solutions for the number of patterns under two target reliability indices β^{target} = 2.5 and β^{target} = 2.0. The different number of pattern repetition constraints in topology optimization result in various material distributions so that those can be implemented into aesthetical facades design with structural engineering. The convergence histories of solutions over the iterative procedure of the optimization are shown in Figure 3.26.

3.6. Concluding remarks

In this chapter, a new topology optimization framework is proposed for structures under stochastic excitations. For the linear structure subjected to the Gaussian excitation, the instantaneous failure probability regarding stochastic response is obtained from the closed form solution by using the discrete representation method. A formulation of the adjoint method is created to evaluate the

sensitivities of the instantaneous failure probability described by the discrete representation method. The proposed stochastic topology optimization method and sensitivity formulations are applied to numerical examples for optimizing lateral bracing systems under stochastic ground motions. In the first numerical example, effects of varying model parameters and prescribed probabilistic values, such as column size, intensities of Gaussian white process, thresholds and reliability indices are studied. By investigating the failure probabilities of optimization solutions at different time points, it is also shown that the instantaneous failure probability can be a reasonable indicator for the entire process if the probability is evaluated after stationarity is achieved. In addition, studies on changes in structural responses of topology optimization solutions considering the standard density method (with the gray region) and the interpreted discrete solutions (i.e. black and white) show that the later (discrete) results in reduced overall response with respect to the former, which indicats lower failure probability. Effects of ground motion characteristics such as the predominant frequency and the damping ratio of the Kanai-Tajimi filter model on final topologies are investigated in the second example. In summary, the proposed topology optimization method can provide structural engineers with an efficient and accurate method to obtain optimal topologies while satisfying probabilistic constraints defined regarding instantaneous failure probability under stochastic input excitations. When the stochastic response of a structure is non-Gaussian due to either non-linear system or non-Gaussian input excitations, the framework proposed in this chapter is still able to compute the failure probability efficiently by utilizing structural reliability methods such as FORM or SORM, instead of using the closed-form solution described in this work. Furthermore, the proposed method can be extended to system reliability problems to incorporate the first-passage probability, multiple checkpoint locations in a structure or multiple failure modes into topology optimization under stochastic excitations. That extension will require evaluating multiple failure events at discretize time points and locations using an efficient structural reliability analysis. Also, a sensitivity analysis needs to be altered for the extension based on the proposed sensitivity approach in this chapter.

Chapter 4

Sensitivity of system reliability using sequential compounding method

Computation of sensitivities of the 'system' failure probability with respect to various parameters is essential for reliability based design optimization (RBDO) and uncertainty/risk management of a complex engineering system. The system failure event is defined as a logical function of multiple component events representing failure modes, locations or time points. Recently, the sequential compounding method (SCM) was developed for efficient calculations of the probabilities of large-size, general system events for a wide range of correlation properties. To facilitate the use of gradient-based optimization methods in RBDO and uncertainty/risk management under a constraint on the system failure probability, a method, termed as Chun–Song–Paulino (CSP) method, is developed in this chapter to compute parameter sensitivities of system failure probability using SCM. For a parallel or series system, the derivative of the system failure probability with respect to the reliability index is analytically derived at the last step of the sequential compounding. For a general system, the sensitivity of the probability of the set involving the component of interest and the sensitivity of the system failure probability with respect to the super-component representing the set are computed respectively using the CSP method and combined by the chain-rule. The CSP method is illustrated by numerical applications and successfully tested by examples covering a wide range of system event types, reliability indices, the number of components, and correlation properties. The method is also applied to compute the sensitivity of the first-passage probability of a building structure under stochastic excitations, modeled by use of finite elements.

4.1. Introduction

Sensitivity analysis is an important part of determining impacts of input variables on the function, system or performance output. Such an analysis not only provides quantitative measures that help identify the relative importance of variables in terms of their impact on the results, but also facilitate the use of gradient-based optimizers in efforts to optimize the system. In risk-based decision making processes to improve or optimize a system subjected to significant uncertainties, it is essential to identify relative contributions of various input random variables in terms of parameter sensitivities of the failure probability. To this end, various sensitivity-based importance measures have been developed. Such measures quantify the relative importance of random variables in terms of the difference in the failure probability caused by the changes in the distribution parameters proportional to the standard deviations or those made possible by the fixed upgrade cost (Hohenbichler and Rackwitz 1986; Der Kiureghian et al. 2007).

The recent emergence of research in reliability based design optimization (RBDO) (Enevoldsen and Sørensen 1994; Tu et al. 1999; Frangopol and Maute 2005; Tsompanakis et al. 2008; Nguyen et al. 2010; Nguyen 2010) also demands calculating parameter sensitivity of the failure probability. In fact, RBDO aims to find the values of design variables that maximize or minimize a given objective function describing the performance of the system while satisfying probabilistic constraints. A typical RBDO formulation is

$$\begin{aligned} &\min_{\mathbf{d}} \ f_{obj}(\mathbf{d}) \\ &s.t \quad P(E_i;\mathbf{d}) \le P_i^{\text{target}}, \ \ i = 1,...,n_c \\ &\qquad \mathbf{d}^{\text{lower}} \le \mathbf{d} \le \mathbf{d}^{\text{upper}} \end{aligned} \tag{4.1}$$

where $f_{obj}(\mathbf{d})$ is the objective function of a given design optimization problem, e.g. volume, total cost, performance measure, $\mathbf{d} = \{d_1,\ldots,d_n\}$ is the set of the design variables with the lower bounds $\mathbf{d}^{\text{lower}}$ and the upper bounds $\mathbf{d}^{\text{upper}}$ (box constraints), and E_i and P_i^{target} respectively denote the event that the i-th constraint is violated, $i = 1,\ldots,n_c$ (or the i-th failure event), and the corresponding target failure probability. Sensitivity analysis of the probabilistic constraints with respect to design

variables is a crucial part of the reliability based design optimization especially when a gradient-based optimization algorithm needs to be utilized.

In the aforementioned situations of RBDO, if the failure event is described as a *system* event E_{sys}, i.e. a logical function of multiple component events representing failure modes, locations or time points, parameter sensitivities of the *system* failure probability are needed. Among various examples of system failure events (Song and Der Kiureghian 2003; Song and Kang 2009), let us consider the first-passage probability of a structure subject to stochastic excitations (Vanmarcke 1975; Song and Der Kiureghian 2006; Fujimura and Der Kiureghian 2007; Lutes and Sarkani 2003; Chun et al. 2013). This is the probability that a stochastic response $X(t)$ exceeds a given threshold x_0 at least once for a given duration $t \in (0, t_n]$. This is commonly utilized to find the probability of the failure event described within a time interval. One of the available approaches for formulating the first-passage probability consists of defining the problem as a series system problem (Fujimura and Der Kiureghian 2007), i.e.

$$P(E_{sys}) = P(x_0 < \max_{0<t\le t_n} |\, X(t)\,|) = P\left(\bigcup_{i=1}^{n} |X(t_i)| > x_0\right) \tag{4.2}$$

where t_i is the i-th discretized time point, $i = 1,\ldots,n$. The first-passage probability defined in Equation 4.2 requires an evaluation of component failure probability at each time point and the statistical dependence between the failures at different time points. If a probabilistic constraint is associated with the first-passage probability in RBDO (Chun et al. 2013), an efficient, reliable and robust algorithm is required to compute the system failure probability during the iterative procedure.

In general, the sensitivity of the system failure probability with respect to a parameter θ is obtained by a chain rule, i.e.

$$\frac{\partial P(E_{sys})}{\partial \theta} = \sum_{i=1}^{n} \frac{\partial P(E_{sys})}{\partial \beta_i} \cdot \frac{\partial \beta_i}{\partial \theta} \tag{4.3}$$

where β_i is the reliability index of the i-th component failure event. It is noted that the impact of the correlation between component failure events on the partial derivative is assumed to be negligible. From Equation 4.3, the partial derivatives of the component reliability index with respect to the design variables are available from parameter sensitivities of component reliability analysis (Hohenbichler and Rackwitz 1986; Bjerager and Krenk 1989). However, the derivative of the system failure probability with respect to the reliability index has not yet been clearly addressed in the literature. Several methods have been developed to compute parameter sensitivities of the system failure probability. Song and Kang (2009) used the Matrix-based System Reliability method (Kang et al. 2008) for computing parameter sensitivities for systems under statistical dependence, and later the method was further developed (Kang et al. 2012). In Song and Kang (2009) and Kang et al. (2012), the sensitivity of the system failure probability was computed with respect to the mean and the standard deviation of the input random variables to facilitate the decision-making process and system reliability based design optimization (Nguyen et al. 2010; Nguyen et al. 2011). Sensitivity-based importance measures (Hohenbichler and Rackwitz 1986; Der Kiureghian et al. 2007) were also computed to quantify the relative importance of the design variables. Sues and Cesare (2005) proposed a method of computing parameter sensitivity of the system failure probability using the results of component reliability analysis by the first-order reliability method and Monte Carlo simulations. Song and Der Kiureghian (2005) utilized the linear programing bounds method (Song and Der Kiureghian 2003) in order to compute lower and upper bounds of the parameter sensitivities of general system events, even with incomplete information on component probabilities and their statistical dependence. Despite these proposed methods, computing parameter sensitivities of the system failure probability is still challenging if the system has a large number of components and/or the correlation properties of component failure events do not allow for achieving conditional independence between components given few number of common source random variables (Kang et al. 2012).

Therefore, in this chapter, a method of computing parameter sensitivity of the system failure probability is proposed using the sequential compounding method (SCM; Kang and Song 2010) which was recently developed to compute multivariate normal integrals of general system events with a wide range of correlation properties even for those with a large number of component events. The proposed method, termed as Chun-Song-Paulino (CSP) method, is illustrated and tested by a variety of numerical examples. The CSP method is further demonstrated by application to the first-passage probability of a structure described by a finite element model subjected to stochastic excitations.

The remainder of the chapter is structured as follows. After a brief summary of the SCM (Kang and Song 2010), the SCM-based parameter sensitivity formulations are derived for series, parallel and general systems (cut-set system) respectively. Numerical examples then illustrate and test the CSP method and demonstrate its application to first-passage problems. Finally, concluding remarks and discussions on future research needs are provided.

4.2. Sequential compounding method

In the sequential compounding method (SCM; Kang and Song 2010), two component events coupled by union or intersection operation in the system event are compound sequentially until a single compound event eventually represents the system event. Each compounding procedure consists of determining the probability of the new compound event and evaluating the correlation coefficient between the new compound event and each of the remaining component events.

First, when two events are coupled by an intersection operation, the compounding process starts by obtaining the reliability index of the compound event $E_{i\text{and}j} = E_i \bigcap E_j$ as

$$\beta_{i\text{and}j} = -\Phi^{-1}[P(E_i \bigcap E_j)] = -\Phi^{-1}[\Phi_2(-\beta_i, -\beta_j; \rho_{i,j})] \tag{4.4}$$

where $\beta_{i\text{and}j}$ denotes the reliability index of the compound event, $\Phi(\cdot)$ is the marginal cumulative distribution function (CDF) of the standard normal distribution, $\Phi_2(\cdot)$ is the joint CDF of the bi-variate standard normal distribution, and $\rho_{i,j}$ is the correlation coefficient between the standard

normal random variables representing E_i and E_j, which could be obtained from the inner-product of the negative normalized vectors of the design points (Der Kiureghian, 2005). After $\beta_{i\text{and}j}$ is obtained, the correlation coefficient between $E_{i\text{and}j}$ and each of the remaining component events E_k, $k = 1,\ldots,n$, $k \neq i,j$, denoted by $\rho_{(i\text{and}j),k}$, is computed. The correlation coefficient is determined such that the compound event can represent $E_i \bigcap E_j$ accurately in computing the probability of $E_i \bigcap E_j \bigcap E_k$, i.e.,

$$\Phi_3(-\beta_i, -\beta_j, -\beta_k; \rho_{i,j}, \rho_{i,k}, \rho_{j,k}) = \Phi_2(-\beta_{i\text{and}j}, -\beta_k; \rho_{(i\text{and}j),k}) \tag{4.5}$$

In Equation 4.5, $\rho_{(i\text{and}j),k}$ is the only unknown variable, which can be obtained numerically by nonlinear programing such as:

$$\begin{aligned} \min_{\rho_{(i\text{and}j),k}} \quad & \left|\Phi_3(-\beta_i, -\beta_j, -\beta_k; \rho_{i,j}, \rho_{i,k}, \rho_{j,k}) - \Phi_2(-\beta_{i\text{and}j}, -\beta_k; \rho_{(i\text{and}j),k})\right| \\ s.t \quad & -1 \le \rho_{(i\text{and}j),k} \le 1 \end{aligned} \tag{4.6}$$

The multi-fold integrals of the joint CDFs in the optimization problem can be performed by efficient algorithms such as the one by Genz (2004). To further reduce the computational costs for solving Equation 4.5 during the optimization process, Kang and Song (2010) proposed an approximate procedure as well, which deals with single-fold integrals only.

Similarly, components coupled by union operation can be compounded as follows. The equivalent reliability index $\beta_{i\text{or}j}$ is obtained by

$$\begin{aligned} \beta_{i\text{or}j} &= -\Phi^{-1}[P(E_i \bigcup E_j)] = -\Phi^{-1}[1 - P(\overline{E}_i \bigcap \overline{E}_j)] \\ &= \Phi^{-1}[\Phi_2(\beta_i, \beta_j; \rho_{i,j})] \end{aligned} \tag{4.7}$$

The equivalent correlation coefficients between the compound event $E_{i\text{or}j}$ and each of the remaining component events, E_k, $k = 1,\ldots, n$, $k \neq i, j$, denoted by $\rho_{(i\text{or}j),k}$, is determined such that the compound event can represent $E_i \bigcup E_j$ accurately in computing the probability of $(E_i \bigcup E_j) \bigcap E_k$.

The efficiency, accuracy, and applicability to series, parallel and general systems have been successfully demonstrated by numerical examples (Kang and Song 2010). The examples cover a

wide range of system event types, component probability levels, the number of components, and correlation properties. In one of the examples, the parameter sensitivity of a general (cut set) system consisting up to 1,000 component events was computed accurately and efficiently using the SCM.

4.3. Parameter sensitivity of system failure probability using SCM

To allow for efficient and accurate calculations of parameter sensitivities for general large-size system events and a wide range of correlation properties, the following sensitivity formulations are developed for series, parallel and cut-set system events, respectively.

4.3.1. Series systems

First, consider a series system event E_{series} consisting of n component events. The failure probability of the series system can be formulated as a multinormal integral problem

$$P(E_{series}) = P(E_1 \cup E_2 \cup \cdots \cup E_n) = P\left[\bigcup_{j=1}^{n}\left(\beta_j \le Z_j\right)\right] = \int_{\Omega} \varphi_n(\mathbf{z};\mathbf{R})d\mathbf{z} \tag{4.8}$$

where Z_j, j = 1,…., n, is the standard normal random variable representing E_j, $\mathbf{R}$ is the correlation coefficient matrix of $\mathbf{Z} = \{Z_1,\ldots, Z_n\}$, and $\varphi_n(\mathbf{z};\mathbf{R})$ is the joint probability density function (PDF) of the standard normal random variables with $\mathbf{R}$. For a parameter sensitivity calculation in Equation 4.3, the sensitivity of the system failure probability needs to be calculated with respect to the reliability index of the k-th event E_k, i.e.,

$$\frac{\partial P(E_{series})}{\partial \beta_k} = \frac{\partial}{\partial \beta_k}\left(\int_{\Omega} \varphi_n(\mathbf{z};\mathbf{R})d\mathbf{z}\right) \tag{4.9}$$

Numerical analysis schemes are commonly implemented to solve Equation 4.9 because the multi-fold integral defined in Equation 4.8 and its derivative cannot be computed analytically. However, such an approach might require large computational cost or suffer numerical issues. For example, the finite difference method requires finding an admissible perturbation for accurate results.

For SCM-based calculation of sensitivities of $P(E_{series})$ with respect to β_k, all components in the series system except E_k are first compounded to E_{S_k}, i.e.

$$E_{S_k} = \bigcup_{p \in S_k} E_p \tag{4.10}$$

where S_k denotes the index set of the components in the series system except k, i.e. $S_k = \{1, 2, ..., (k-1), (k+1), ..., n\}$. The sequential compounding process would be completed by compounding E_k and E_{S_k}, i.e.

$$\begin{aligned} P(E_{series}) &= P\left(E_k \cup E_{S_k}\right) \\ &= P(E_k) + P(E_{S_k}) - P(E_k \cap E_{S_k}) \\ &= \Phi(-\beta_k) + \Phi(-\beta_{S_k}) - \Phi_2(-\beta_k, -\beta_{S_k}; \rho_{k,S_k}) \end{aligned} \tag{4.11}$$

where ρ_{k,S_k} is the updated correlation coefficient between the component E_k and the compound event E_{S_k}. From Equation 4.11, the sensitivity of the system failure probability with respect to β_k is obtained as

$$\frac{\partial P(E_{series})}{\partial \beta_k} = -\varphi(-\beta_k) - \frac{\partial \Phi_2(-\beta_k, -\beta_{S_k}; \rho_{k,S_k})}{\partial \beta_k} \tag{4.12}$$

The partial derivative of the bivariate normal cumulative distribution in the last term of Equation 4.12 is then computed as followings:

$$\begin{aligned} \frac{\partial \Phi_2(-\beta_k, -\beta_{S_k}; \rho_{k,S_k})}{\partial \beta_k} &= \frac{\partial\left(\int_{-\infty}^{-\beta_k}\int_{-\infty}^{-\beta_{S_k}} \varphi_2(u, v; \rho_{k,S_k}) dv du\right)}{\partial \beta_k} \\ &= -\int_{-\infty}^{-\beta_{S_k}} \varphi_2(-\beta_k, v; \rho_{k,S_k}) dv \\ &= -\frac{1}{\sqrt{2\pi}} \exp\left(-\frac{\beta_k^2}{2}\right) \cdot \int_{-\infty}^{-\beta_{S_k}} \frac{1}{\sqrt{2\pi}\sqrt{1-\rho_{k,S_k}^2}} \exp\left[-\frac{\left(v + \beta_k \rho_{k,S_k}\right)^2}{2\left(1-\rho_{k,S_k}^2\right)}\right] dv \end{aligned} \tag{4.13}$$

Changing the variable of the integral to $v' = (v + \beta_k \rho_{k,S_k}) / \sqrt{1-\rho_{k,S_k}^2}$, Equation 4.13 is simplified as

$$\frac{\partial \Phi_2(-\beta_k, -\beta_{S_k}; \rho_{k,S_k})}{\partial \beta_k} = -\varphi(-\beta_k) \cdot \Phi\left[\frac{-\beta_{S_k} + \beta_k \rho_{k,S_k}}{\sqrt{1-\rho_{k,S_k}^2}}\right] \tag{4.14}$$

Finally, substituting Equation 4.14 into Equation 4.12, the sensitivity of the system failure probability is derived as

$$\frac{\partial P(E_{series})}{\partial \beta_k} = -\varphi(-\beta_k)\left\{1-\Phi\left[\frac{-\beta_{S_k}+\beta_k\rho_{k,S_k}}{\sqrt{1-\rho_{k,S_k}{}^2}}\right]\right\} \tag{4.15}$$

It is noteworthy that the proposed Chun-Song-Paulino (CSP) method allows us to compute the parameter sensitivity without additional computational cost other than the simple calculation in Equation 4.15 because β_{S_k} and ρ_{k,S_k} are already available from the sequential compounding procedure to obtain $P(E_{series})$. It is also seen from Equation 4.15 that when the k-th component is statistically independent of the others, i.e. $\rho_{k,S_k}=0$ the sensitivity in Equation 4.15 becomes $-\varphi(-\beta_k)[1-\Phi(-\beta_{S_k})]$. Whether independent or not, the sensitivity is always negative.

4.3.2. Parallel systems

Similarly, for SCM-based calculation of sensitivities of the parallel system failure probability $P(E_{parallel}) = P(\bigcap_{j=1}^{n} E_j)$ with respect to β_k, all components in the parallel system except E_k are first compounded to E_{P_k}, i.e.

$$E_{P_k} = \bigcap_{p\in P_k} E_p \tag{4.16}$$

where P_k denotes the index set of all components in the parallel system except k, i.e. $P_k = \{1,2,...,(k-1),(k+1),...,n\}$. The sequential compounding process would be completed by compounding E_k and E_{P_k}, i.e.

$$P(E_{parallel}) = P\left(E_k \cap E_{P_k}\right) = \Phi_2(-\beta_k, -\beta_{P_k}; \rho_{k,P_k}) \tag{4.17}$$

From Equation 4.14, the sensitivity is derived as

$$\frac{\partial P(E_{parallel})}{\partial \beta_k} = -\varphi(-\beta_k)\cdot\Phi\left[\frac{-\beta_{P_k}+\beta_k\rho_{k,P_k}}{\sqrt{1-\rho_{k,P_k}{}^2}}\right] \tag{4.18}$$

When the *k*-th component is statistically independent of the others, i.e. $\rho_{k,P_k} = 0$, the sensitivity in Equation 4.18 becomes $-\varphi(-\beta_k)\Phi(-\beta_{P_k})$. Whether independent or not, the sensitivity is always negative.

4.3.3. General systems

Let us next consider the probability of a general system event described by the union of cut-sets, i.e.

$$P(E_{cut-set}) = P\left(\bigcup_{m=1}^{n} E_{C_m}\right) = P\left[\bigcup_{m=1}^{n}\left(\bigcap_{j\in C_m} E_j\right)\right] \tag{4.19}$$

where C_m denotes the index set of the components that belong to the *m*-th cut-set. The SCM-based sensitivity of the probability in Equation 4.19 with respect to β_k is computed as follows. Suppose E_k, the component event of interest for sensitivity calculation, belongs to a cut-set C_l. From the chain rule, the sensitivity of the probability of the cut-set system with respect to β_k is derived as

$$\begin{aligned}\frac{\partial P(E_{cut-set})}{\partial \beta_k} &= \frac{\partial P(E_{cut-set})}{\partial P(E_{C_l})} \cdot \frac{\partial P(E_{C_l})}{\partial \beta_k} \\ &= \left[\frac{\partial P(E_{cut-set})}{\partial \beta_{C_l}} \cdot \frac{\partial \beta_{C_l}}{\partial P(E_{C_l})}\right] \cdot \frac{\partial P(E_{C_l})}{\partial \beta_k} \\ &= -\frac{1}{\varphi(-\beta_{C_l})} \cdot \frac{\partial P(E_{cut-set})}{\partial \beta_{C_l}} \cdot \frac{\partial P(E_{C_l})}{\partial \beta_k}\end{aligned} \tag{4.20}$$

In order to complete the calculation in Equation 4.20, all components in the cut set C_l are first compounded to determine the reliability index of the super-component representing the cut-set, i.e. β_{C_l}. Next, the sensitivity of $P(E_{C_l})$ with respect to β_k is computed using the CSP method for parallel systems. Then, considering C_l as a component in a series system, the sensitivity of the system failure probability with respect to β_{C_l} is computed using the CSP method for series systems. These are substituted into Equation 4.20 to compute the sensitivity. A similar procedure can be derived for a link-set system event, which is the intersection of unions.

4.4. Numerical examples

The CSP method is first illustrated by small-size numerical examples of series and cut-set systems. The method is then tested by series and parallel systems with equal or unequal reliability indices and a wide range of correlation coefficients. As an application example, the sensitivity of the first-passage probability of a structure is computed using the CSP method. For a verification purpose, the finite difference method (FDM) employing the SCM and the Monte Carlo Simulation (MCS) are also carried out. Unless stated otherwise, the five sensitivity calculations by the MCS use a sample size of 10^8 with perturbation sizes $\Delta\beta = 10^{-3}$ and 10^{-4}. Then, the resulting sensitivities from different perturbation values were averaged for comparison with the results obtained using the CSP method and the FDM.

4.4.1. Illustrative example: a series system with three components

For the illustration purpose of the proposed method, let us consider the series system event consisting of three components, i.e.

$$P(E_{sys}) = P\left(E_1 \cup E_2 \cup E_3\right) \tag{4.21}$$

Suppose that the components have unequal reliability indices, i.e. $\beta_1 = 2$, $\beta_2 = 1.5$ and $\beta_3 = 1$. The correlation coefficient matrix of the standard normal random variables representing the three components is given by

$$\mathbf{R} = \begin{bmatrix} 1 & 0.4 & 0.2 \\ 0.4 & 1 & 0.4 \\ 0.2 & 0.4 & 1 \end{bmatrix} \tag{4.22}$$

Suppose that the sensitivity of the system failure probability in Equation 4.21 with respect to the reliability index β_1 is of interest. Following the CSP method, two events E_2 and E_3 are compounded so that equivalent component $E_{2\text{or}3}$ is identified. Note that E_k and E_{S_k} in Equation 4.11 correspond to E_1 and $E_{2\text{or}3}$ in this example, respectively. From Equation 4.7, the reliability index $\beta_{1\text{or}2}$ is obtained as 0.8471. The equivalent correlation coefficient between E_1 and $E_{2\text{or}3}$ is computed as

0.3018 using the aforementioned procedure. The series system event then consists of two events E_1 and E_{2or3} with their correlation coefficient 0.3018. Using Equation 4.15, the sensitivity with respect to β_1 is computed as –0.0324. Sensitivities with respect to the other reliability indices are also computed similarly and are summarized in Table 4.1. The results are successfully verified by the FDM with a perturbation of $\Delta\beta_i = 10^{-8}$, $i = 1, 2, 3$ and the MCS as shown in Figure 4.1. Effects of varying perturbations from 10^{-1} to 10^{-16} in the FDM and the MCS on sensitivity results were tabulated in Table 4.2. Both FDM and MCS are sensitive to the perturbation size while it is hard to predict an optimal perturbation a priori. It is also noteworthy that the MCS, in particular, could provide fairly inaccurate results for small perturbations.

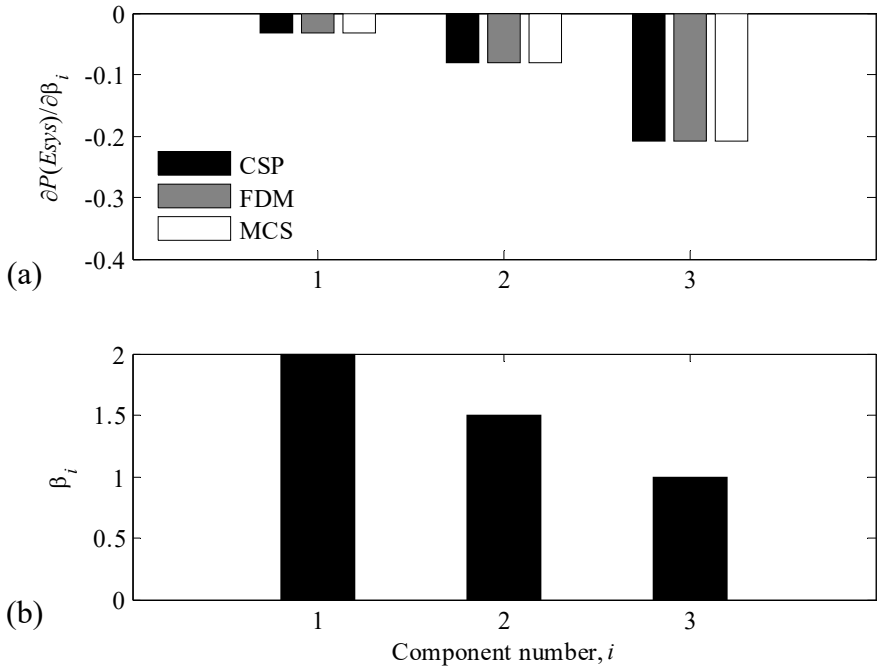

Figure 4.1: Series system consisting of 3 components: (a) sensitivities calculated by the CSP method, the FDM and the MCS, and (b) unequal reliability indices.

Table 4.1: CSP Sensitivity of the series system failure probability in Example 4.4.1.

Component	β_k	β_{S_k}	ρ_{k,S_k}	$\partial P(E_{sys})/\partial\beta_k$
k=1	2.0	0.8471	0.3018	−0.0324
k=2	1.5	0.9359	0.4299	−0.0811
k=3	1.0	1.3833	0.3753	−0.2085

Table 4.2: Sensitivities computed by the FDM employing the SCM and the Monte Carlo Simulations (Example 4.4.1).

	FDM: $\partial P(E_{sys})/\partial\beta_k$			MCS: $\partial P(E_{sys})/\partial\beta_k$		
$\Delta\beta_k$	k=1	k=2	k=3	k=1	k=2	k=3
1.0×10^{-1}	−0.0293	−0.0744	−0.1973	−0.0293	−0.0744	−0.1974
1.0×10^{-2}	−0.0324	−0.0807	−0.2076	−0.0324	−0.0807	−0.2076
1.0×10^{-3}	−0.0327	−0.0813	−0.2087	−0.0330	−0.0814	−0.2083
1.0×10^{-4}	−0.0327	−0.0814	−0.2088	−0.0335	−0.0785	−0.2105
1.0×10^{-5}	−0.0327	−0.0814	−0.2088	−0.0323	−0.0784	−0.2161
1.0×10^{-6}	−0.0327	−0.0814	−0.2088	−0.0310	−0.0800	−0.2140
1.0×10^{-7}	−0.0327	−0.0814	−0.2088	−0.0200	−0.1100	−0.2200
1.0×10^{-8}	−0.0327	−0.0814	−0.2088	0.0000	−0.1000	−0.1000
1.0×10^{-9}	−0.0327	−0.0814	−0.2088	0.0000	0.0000	0.0000
1.0×10^{-10}	−0.0327	−0.0814	−0.2088	0.0000	0.0000	0.0000
1.0×10^{-11}	−0.0327	−0.0814	−0.2088	0.0000	0.0000	0.0000
1.0×10^{-12}	−0.0326	−0.0813	−0.2087	0.0000	0.0000	0.0000
1.0×10^{-13}	−0.0322	−0.0799	−0.2087	0.0000	0.0000	0.0000
1.0×10^{-14}	−0.0333	−0.0777	−0.2109	0.0000	0.0000	0.0000
1.0×10^{-15}	0.1110	−0.1110	−0.2220	0.0000	0.0000	0.0000
1.0×10^{-16}	0.0000	0.0000	0.0000	0.0000	0.0000	0.0000

4.4.2. Illustrative example: a cut-set system with six components

As another illustrative example of the CSP method, consider the following cut-set system problem consisting of six components where each cut-set subsystem has three components:

$$P(E_{sys}) = P(E_{C_1} \bigcup E_{C_2}) = P\left(E_1E_2E_3 \bigcup E_4E_5E_6\right) \tag{4.23}$$

The reliability indices and correlation coefficients are given as

$$\boldsymbol{\beta} = \begin{bmatrix} 1.0 \\ 1.0 \\ 2.0 \\ 2.0 \\ 1.5 \\ 1.5 \end{bmatrix}, \quad \mathbf{R} = \begin{bmatrix} 1 & 0.24 & 0.12 & 0.06 & 0.03 & 0 \\ 0.24 & 1 & 0.24 & 0.12 & 0.06 & 0.03 \\ 0.12 & 0.24 & 1 & 0.24 & 0.12 & 0.06 \\ 0.06 & 0.12 & 0.24 & 1 & 0.24 & 0.12 \\ 0.03 & 0.06 & 0.12 & 0.24 & 1 & 0.24 \\ 0 & 0.03 & 0.06 & 0.12 & 0.24 & 1 \end{bmatrix} \tag{4.24}$$

Suppose that the sensitivity of the system probability with respect to the reliability index of the sixth component E_6 is of interest. Because E_6 belongs to the second cut-set C_2, $\partial P(E_{C_2}) / \partial \beta_6$, $\partial P(E_{sys}) / \partial \beta_{C_2}$, and β_{C_2} are computed using the CSP methods for parallel systems and series systems, and the SCM respectively, and substituted to the chain rule formulation in Equation 4.20. Figure 4.2 illustrates the procedure for sensitivity calculation of the cut-set system. First, all components except the component E_6 of interest in the second cut-set are compounded. Therefore, an equivalent component E_A is found by compounding the subsystem E_4E_5 and determining its reliability index $\beta_A = 2.644$. The updated system definition and the correlation coefficient matrix are given as follows

$$E_{sys} = E_{C_1} \bigcup E_{C_2} = \left(E_1E_2E_3\right) \bigcup \left(E_AE_6\right) \tag{4.25}$$

$$\mathbf{R} = \begin{bmatrix} 1 & 0.24 & 0.12 & 0.067 & 0 \\ & 1 & 0.24 & 0.113 & 0.03 \\ & & 1 & 0.226 & 0.06 \\ & \textit{sym.} & & 1 & 0.204 \\ & & & & 1 \end{bmatrix} \tag{4.26}$$

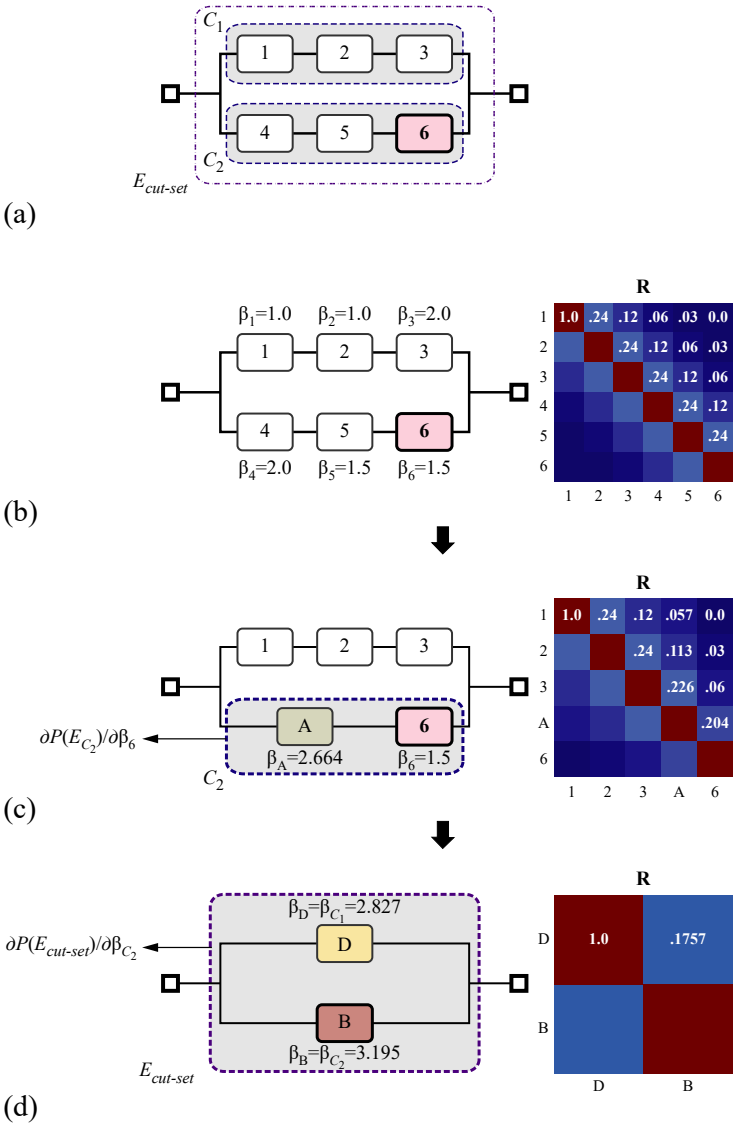

Figure 4.2: Illustration of the CSP method to compute sensitivity for a cut-set system with six components: (a) system definition, (b) reliability indices and correlation coefficient matrix, (c) compound component A, updated correlation coefficient matrix, and sensitivity calculation of the second cut-set system, and (d) sensitivity calculation of the system probability with respect to the reliability index of the second cut-set.

Next, the sensitivity of the second cut-set system failure probability with respect to the reliability index of interest, $\partial P(E_{C_2})/\partial\beta_6$ is computed as –0.001038 using Equation 4.18. Compounding the components in the cut-sets, the reliability indices of super-components E_D and E_B are obtained as

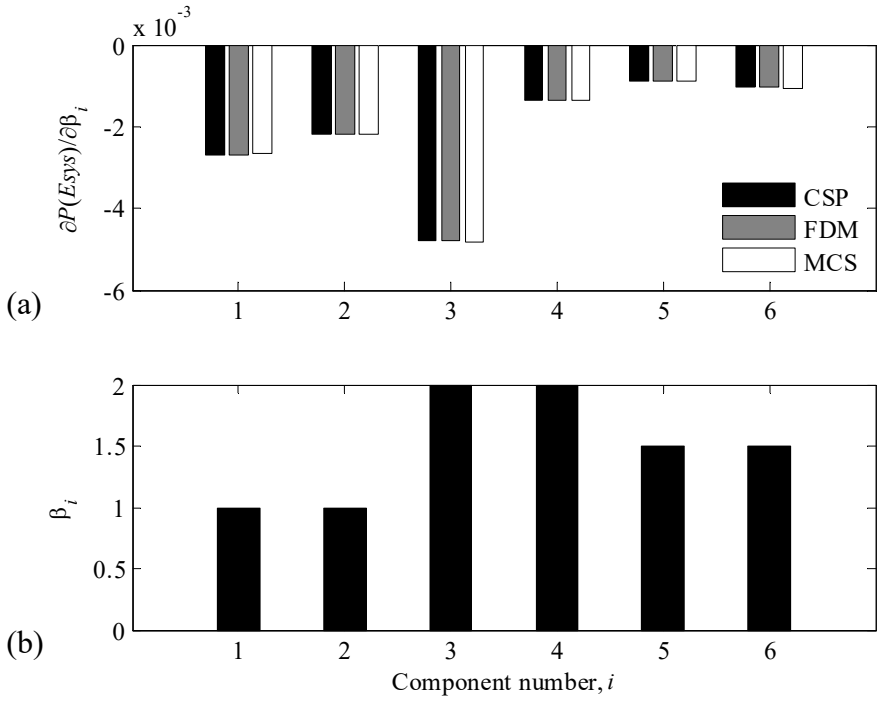

Figure 4.3: Cut-set system with two cut-sets and six components: (a) sensitivities computed by the CSP method, the FDM and the MCS, and (b) unequal reliability indices.

β_D = 2.827 and β_B = 3.195, respectively. The updated system definition and its correlation coefficient matrix are given as follows:

$$E_{sys} = E_{C_1} \bigcup E_{C_2} = E_D \bigcup E_B \tag{4.27}$$

$$\mathbf{R} = \begin{bmatrix} 1 & 0.1757 \\ 0.1757 & 1 \end{bmatrix} \tag{4.28}$$

Using Equation 4.15, the sensitivity of the system failure probability with respect to the reliability index of the super-component representing the second cut-set, $\partial P(E_{sys}) / \partial \beta_{C_2}$, is computed as –0.002398. Finally, using Equation 4.20, the sensitivity is calculated as

$$\begin{aligned} \frac{\partial P(E_{sys})}{\partial \beta_6} &= -\frac{1}{\varphi(-\beta_{C_2})} \cdot \frac{\partial P(E_{sys})}{\partial \beta_{C_2}} \cdot \frac{\partial P(E_{C_2})}{\partial \beta_6} \\ &= -\frac{1}{0.002423}(0.002398 \times 0.001038) \\ &= -0.001026 \end{aligned} \tag{4.29}$$

Table 4.3: CSP Sensitivity of the cut-set system failure probability in Example 4.4.2.

Component	$\partial P(E_{C_1}) / \partial \beta_k$	$\partial P(E_{C_2}) / \partial \beta_k$	$\partial P(E_{sys}) / \partial \beta_{C_j}$	$1 / \varphi(-\beta_{C_j})$	$\partial P(E_{sys})/\partial \beta_k$
k=1	−0.002701	-			−0.002692
k=2	−0.002205	-	−0.007317	136.25	−0.002198
k=3	−0.004804	-			−0.004789
k=4	-	−0.001359			−0.001345
k=5	-	−0.000882	−0.002398	412.41	−0.000873
k=6	-	−0.001038			−0.001026

Table 4.4: Finite difference sensitivity and Monte Carlo Simulation sensitivity computation in Example 4.4.2.

	FDM: $\partial P(E_{sys})/\partial \beta_k$					
$\Delta\beta_k$	$k = 1$	$k = 2$	$k = 3$	$k = 4$	$k = 5$	$k = 6$
1.0×10^{-1}	−0.002641	−0.002182	−0.004434	−0.001254	−0.000847	−0.000983
1.0×10^{-2}	−0.002703	−0.002195	−0.004767	−0.001345	−0.000870	−0.001027
1.0×10^{-3}	−0.002709	−0.002195	−0.004802	−0.001353	−0.000870	−0.001023
1.0×10^{-4}	−0.002709	−0.002195	−0.004805	−0.001354	−0.000870	−0.001023
1.0×10^{-5}	−0.002709	−0.002195	−0.004806	−0.001354	−0.000870	−0.001023
1.0×10^{-6}	−0.002709	−0.002195	−0.004806	−0.001354	−0.000870	−0.001023
1.0×10^{-7}	−0.002709	−0.002195	−0.004806	−0.001354	−0.000870	−0.001023
1.0×10^{-8}	−0.002709	−0.002195	−0.004806	−0.001354	−0.000870	−0.001023
1.0×10^{-9}	−0.002709	−0.002195	−0.004806	−0.001354	−0.000870	−0.001023
1.0×10^{-10}	−0.002708	−0.002195	−0.004805	−0.001353	−0.000869	−0.001023
1.0×10^{-11}	−0.002709	−0.002188	−0.004807	−0.001354	−0.000866	−0.001021
1.0×10^{-12}	−0.002668	−0.002223	−0.004774	−0.001332	−0.000890	−0.001001
1.0×10^{-13}	−0.002246	−0.002246	−0.004454	−0.001106	0.000000	−0.001106
1.0×10^{-14}	0.000000	0.000000	0.000000	0.000000	0.000000	0.000000
1.0×10^{-15}	0.000000	0.000000	0.000000	0.000000	0.000000	0.000000
1.0×10^{-16}	0.000000	0.000000	0.000000	0.000000	0.000000	0.000000

Table 4.4 (cont.): Finite difference sensitivity and Monte Carlo Simulation sensitivity computation in Example 4.4.2.

	MCS: $\partial P(E_{sys})/\partial\beta_k$					
$\Delta\beta_k$	$k=1$	$k=2$	$k=3$	$k=4$	$k=5$	$k=6$
1.0×10^{-1}	−0.002641	−0.002175	−0.004450	−0.001257	−0.000846	−0.000980
1.0×10^{-2}	−0.002706	−0.002180	−0.004719	−0.001327	−0.000885	−0.001014
1.0×10^{-3}	−0.002708	−0.002276	−0.004724	−0.001356	−0.000916	−0.001034
1.0×10^{-4}	−0.003120	−0.002220	−0.004520	−0.001220	−0.000960	−0.000860
1.0×10^{-5}	−0.002720	−0.002120	−0.004680	−0.001390	−0.000830	−0.000880
1.0×10^{-6}	−0.002000	−0.002000	−0.010000	0.000000	0.000000	0.000000
1.0×10^{-7}	0.000000	0.000000	0.000000	0.000000	0.000000	0.000000
1.0×10^{-8}	0.000000	0.000000	0.000000	0.000000	0.000000	0.000000
1.0×10^{-9}	0.000000	0.000000	0.000000	0.000000	0.000000	0.000000
1.0×10^{-10}	0.000000	0.000000	0.000000	0.000000	0.000000	0.000000
1.0×10^{-11}	0.000000	0.000000	0.000000	0.000000	0.000000	0.000000
1.0×10^{-12}	0.000000	0.000000	0.000000	0.000000	0.000000	0.000000
1.0×10^{-13}	0.000000	0.000000	0.000000	0.000000	0.000000	0.000000
1.0×10^{-14}	0.000000	0.000000	0.000000	0.000000	0.000000	0.000000
1.0×10^{-15}	0.000000	0.000000	0.000000	0.000000	0.000000	0.000000
1.0×10^{-16}	0.000000	0.000000	0.000000	0.000000	0.000000	0.000000

The sensitivities of the system failure probability with respect to the other components are shown in Table 4.3. The results are verified by the FDM with a perturbation of $\Delta\beta = 10^{-8}$, $i = 1,\ldots, 6$ and MCS. Comparison results are provided in Table 4.3 and are shown in Figure 4.3. Effects of varying perturbations from 10^{-1} to 10^{-16} in the FDM and the MCS on sensitivity results were tabulated in Table 4.4.

4.4.3. Test example: series system consisting of 20 components with equal reliability indices and equal correlation coefficients

The CSP method is tested for a series system consisting of 20 components that have equal reliability indices, i.e. $\beta_i = \beta_{constant}$, $i = 1,\ldots, 20$ and equal correlation coefficients $\rho_{i,j} = 0.3$, $i \neq j$. As shown in Figure 4.4, the results by the CSP method are successfully verified by the FDM with a perturbation of $\Delta\beta = 10^{-8}$ and the MCS.

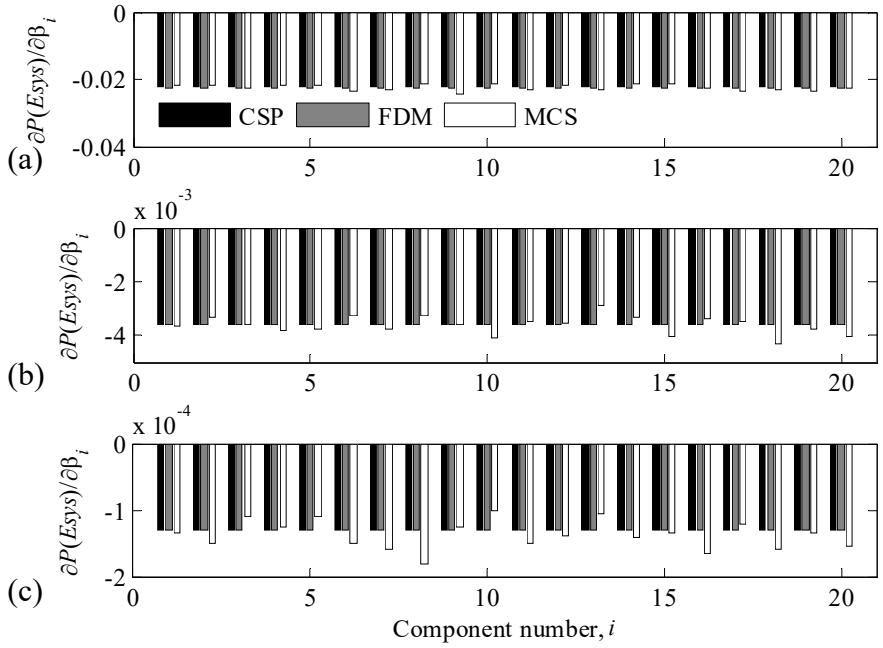

Figure 4.4: Sensitivities of series system with 20 components (equal reliability indices and equal correlation coefficients) computed by the CSP method, the FDM and the MCS: (a) $\beta = 1$, (b) $\beta = 2$, and (c) $\beta = 3$.

4.4.4. Test example: series system consisting of 20 components with unequal reliability indices and equal correlation coefficients

Suppose that a series system has 20 components having equal correlation coefficients $\rho_{i,j} = 0.3$, $i \neq j$ and their reliability indices are given by

$$\beta_i = 2 \cdot \left(1 - \frac{i-1}{19}\right), \; i = 1, ..., 20 \tag{4.30}$$

Figure 4.5 compares the results by the CSP method with those by the FDM with perturbation of $\Delta\beta = 10^{-8}$ and the MCS. It is noted that the system failure probability is most sensitive to β_{20} because the 20-th component contributes most to the system failure probability.

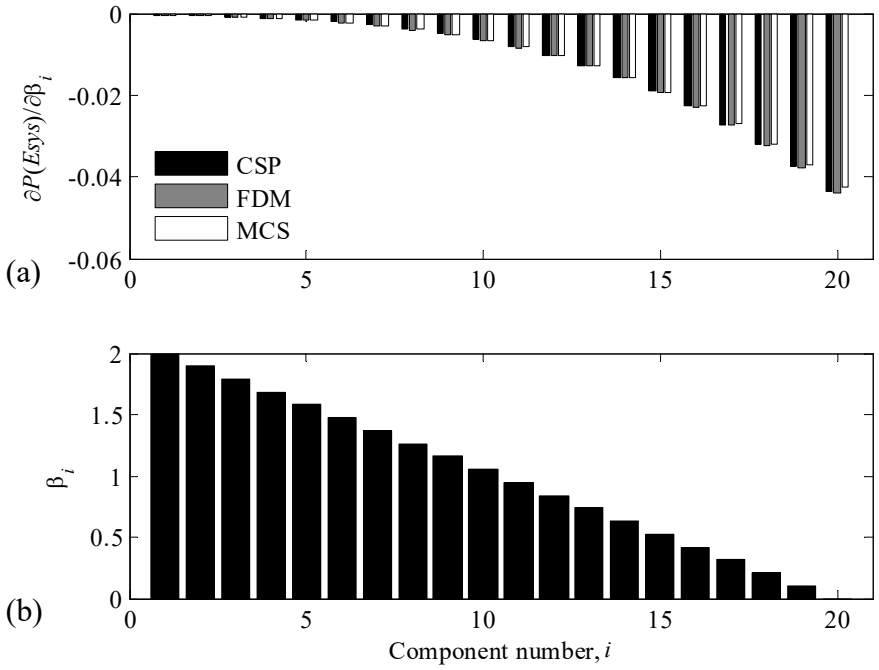

Figure 4.5: Sensitivities of the series system with 20 components (unequal reliability indices and equal correlation coefficients): (a) comparison between the CSP method, the FDM and the MCS, and (b) component reliability indices.

4.4.5. Test example: series system consisting of 20 components with equal reliability indices and unequal correlation coefficients

Consider a series system problem consisting of 20 components having equal reliability indices and unequal correlation coefficients determined by

$$\rho_{i,j} = 1 - \sqrt{\frac{|i-j|}{19}},\ i,j = 1,...,20 \tag{4.31}$$

The distribution of the correlation coefficients in the matrix is visualized in Figure 4.6. The equal reliability indices of the components are used, i.e. $\beta_i = 2$, $i = 1,\ldots, 9$. Figure 4.7 compares the results of sensitivity calculations by the CSP method, the FDM with a perturbation of $\Delta\beta = 10^{-8}$ and the MCS, which show symmetry due to the correlation structure.

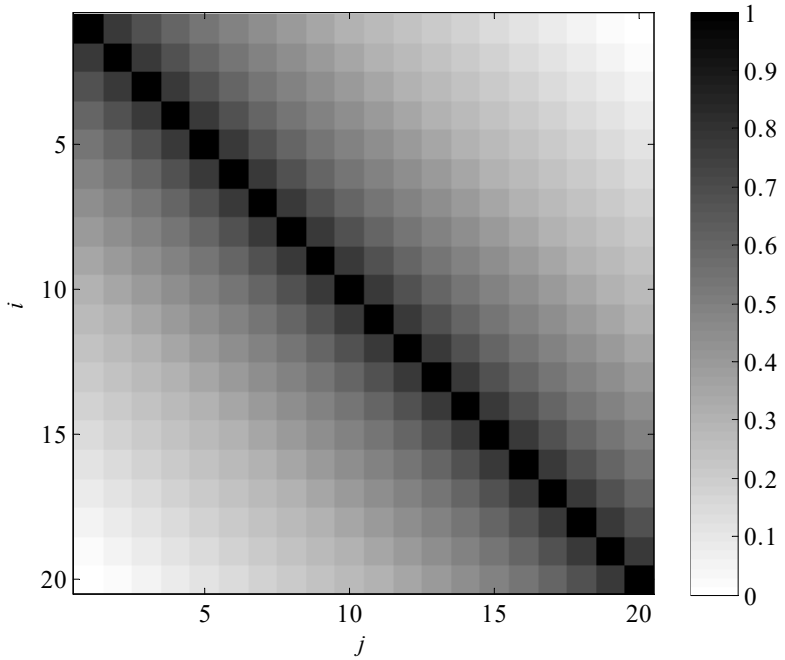

Figure 4.6: Correlation coefficient matrix, $\rho_{i,j} = 1 - \sqrt{|i-j|/19},\ i,j = 1,...,20$.

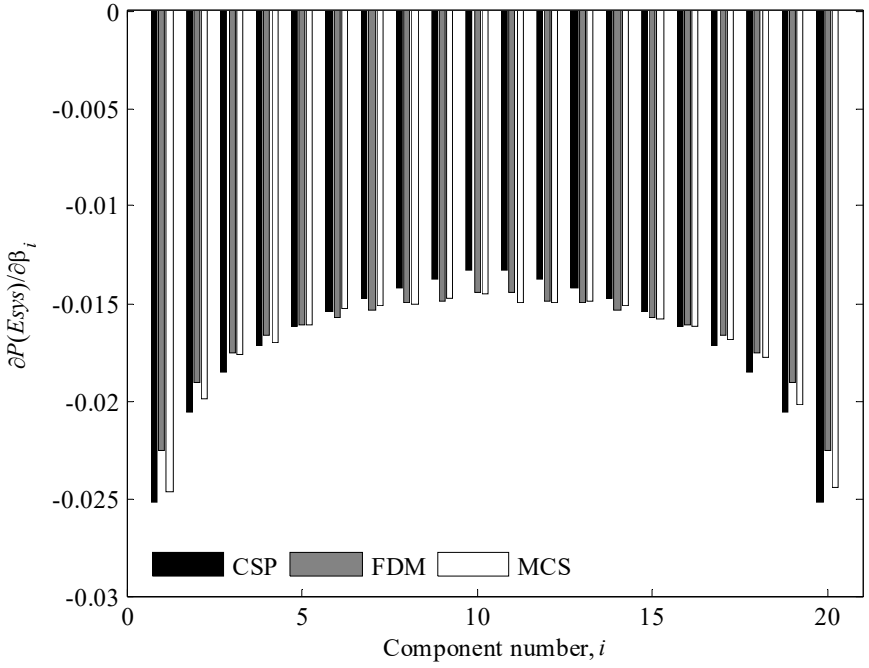

Figure 4.7: Sensitivities of the series system with 20 components (equal reliability indices $\beta = 2.0$ and unequal correlation coefficients in Figure 4.6): comparison between the CSP method, the FDM and the MCS.

4.4.6. Test example: series system consisting of 20 components with randomly generated reliability indices and correlation coefficients

The CSP method is tested for a series system consisting of 20 components with randomly generated unequal reliability indices (Table 4.5), and correlation coefficients (Figure 4.8). The results by the CSP method are verified by the FDM with varying perturbations of $\Delta\beta = 10^{-3,}$ $\Delta\beta = 10^{-8,}$ $\Delta\beta = 10^{-10}$ and MCS. It is noted that sensitivity calculations by the FDM may result in a large error or even different signs depending on perturbation values, as shown in Figure 4.9. This is the motivation of the development of the development of CSP method, which calculates sensitivity efficiently and accurately.

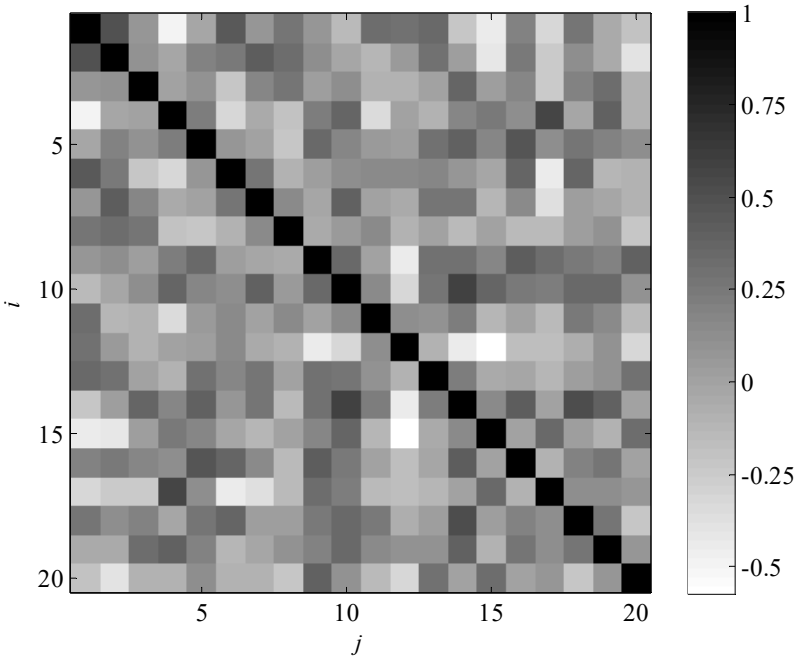

Figure 4.8: Randomly generated correlation coefficient matrix, $\rho_{i,j}$ in Example 4.4.6 and Example 4.4.7.

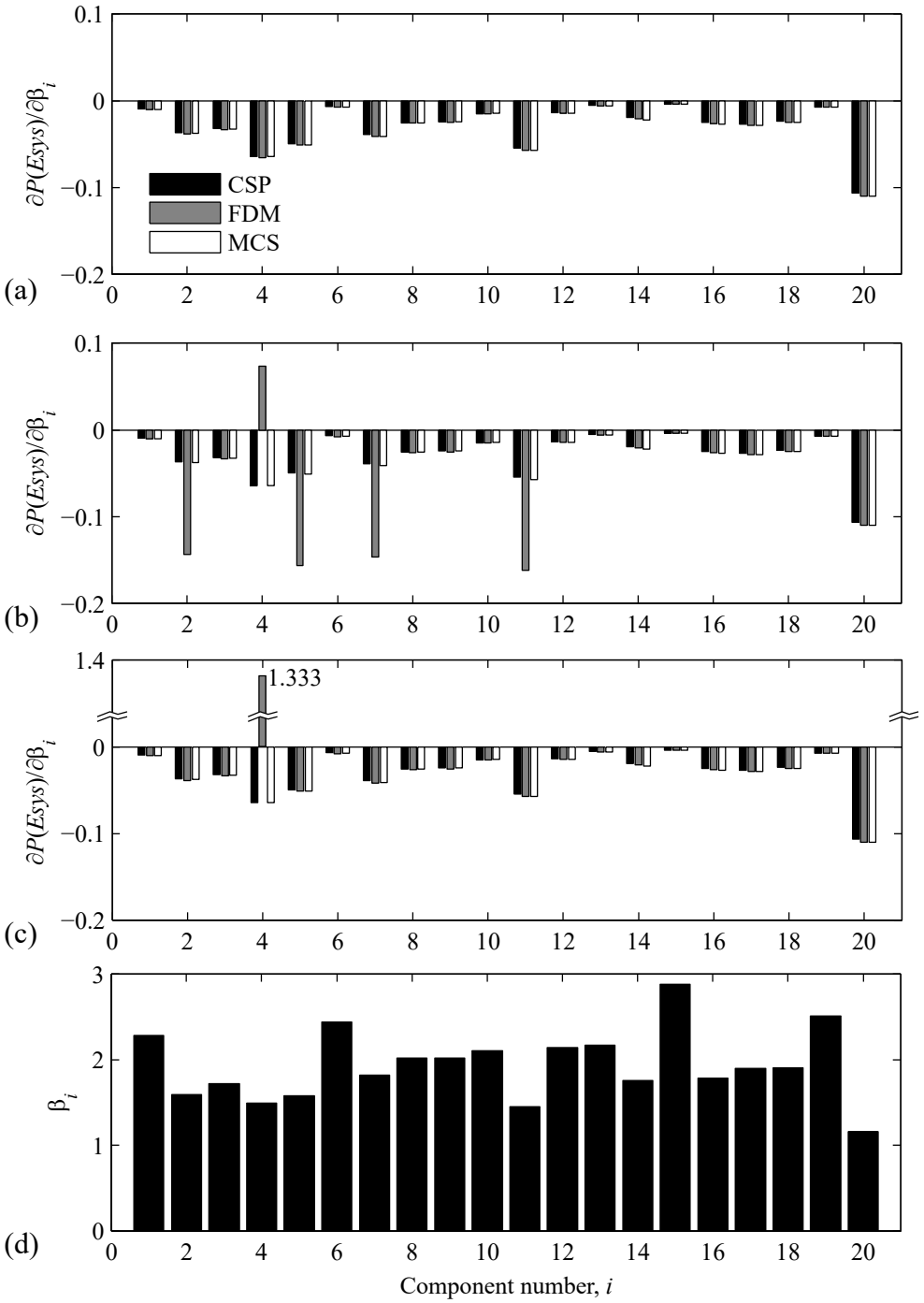

Figure 4.9: Sensitivities of the series system with 20 components (random reliability indices and unequal correlation coefficients): comparison between the CSP method, FDM, and MCS: (a) FDM perturbation, $\Delta\beta = 10^{-3}$, (b) FDM perturbation, $\Delta\beta = 10^{-8}$, (c) FDM perturbation, $\Delta\beta = 10^{-9}$, and (d) reliability indices.

Table 4.5: Reliability indices in Example 4.4.6.

Component, i	β_i	Component, i	β_i
1	2.28384	11	1.45275
2	1.59273	12	2.14048
3	1.72373	13	2.16704
4	1.49318	14	1.75261
5	1.57674	15	2.88052
6	2.43578	16	1.78762
7	1.81745	17	1.89771
8	2.01840	18	1.90212
9	2.02029	19	2.51031
10	2.10169	20	1.15859

4.4.7. Test example: parallel system consisting of 20 components with randomly generated reliability indices

A parallel system having 20 components with randomly generated reliability indices is tested. For the testing purpose, two correlation coefficient matrices are used: a randomly generated one (Figure 4.8), and the equal correlation coefficient (0.5). Figure 4.10 (a) and 4.10 (b) show comparison results for randomly generated reliability indices in Figure 4.10 (c). The randomly generated reliability indices are listed in Table 4.6. To test the method for cases in which components have both positive and negative signs, another set of reliability indexes are randomly generated as shown in Figure 4.10 (e) and Table 4.6. Sensitivities are calculated with equal correlation coefficients (0.5) as shown in Figure 4.10 (d). The CSP method shows overall good agreements.

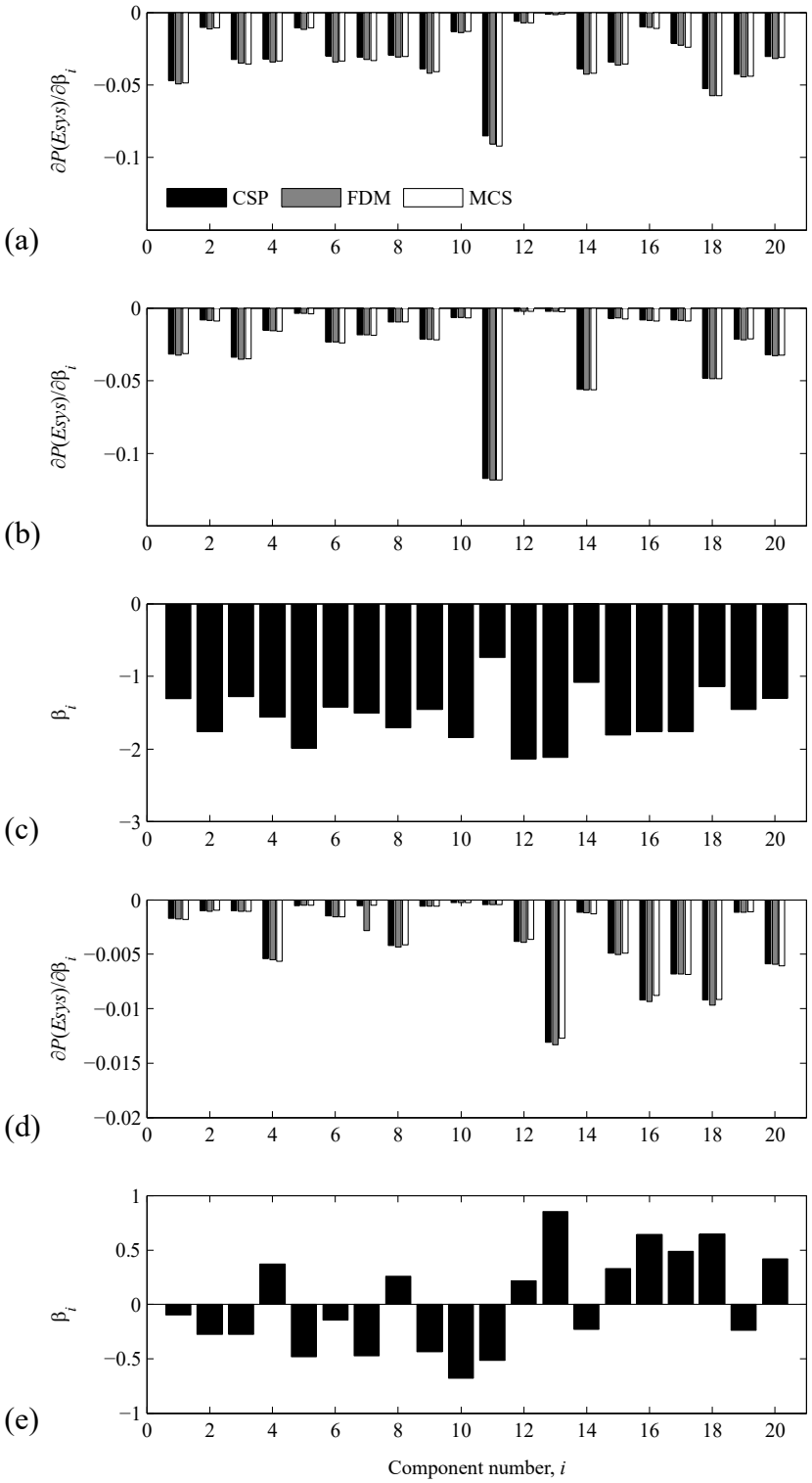

Figure 4.10: Sensitivities of parallel system with 20 components with random reliability indices: (a) sensitivities with the correlation coefficient matrix in the test example 4.4.6, (b) sensitivities with equal correlation coefficients $\rho_{i,j}$ = 0.5, (c) randomly generated reliability indices, (d) sensitivities with equal correlations $\rho_{i,j}$ = 0.5, and (e) randomly generated reliability indices.

Table 4.6: Reliability indices in Example 4.4.7.

Component, i	Fig. 4.10 (c) β_i	Fig. 4.10 (e) β_i	Component, i	Fig. 4.10 (c) β_i	Fig. 4.10 (e) β_i
1	−1.30407	−0.09583	11	−0.73897	−0.51614
2	−1.75792	−0.27721	12	−2.13813	0.21825
3	−1.27964	−0.27396	13	−2.11614	0.85414
4	−1.56172	0.37304	14	−1.07950	−0.23074
5	−1.99004	−0.48342	15	−1.80698	0.33008
6	−1.41823	−0.14431	16	−1.75581	0.64524
7	−1.50297	−0.47295	17	−1.75522	0.48637
8	−1.70968	0.25786	18	−1.14115	0.64556
9	−1.45271	−0.43553	19	−1.45254	−0.23998
10	−1.83899	−0.67939	20	−1.30119	0.41603

4.4.8. Test example: parallel system consisting of 65 components with equal reliability indices and unequal correlation coefficients

To test the CSP method for parallel systems and also for systems with larger number of components, consider a parallel system consisting of 65 components having equal reliability indices $\beta_i = -1.5$, $i = 1,\ldots, 65$. The correlation coefficients are given by

$$\rho_{i,j} = 1 - \sqrt{\frac{|i-j|}{64}},\ i, j = 1,...,65 \tag{4.32}$$

The results in Figure 4.11 show relatively larger difference among the CSP method, the FDM with perturbation of $\Delta\beta = 10^{-8}$ and the MCS (10^6 samples) than the previous examples. It should be noted that the probability of the parallel system keeps decreasing as the compounding continues, which may make the parameter sensitivity calculations more sensitive to the numerical errors for all three approaches.

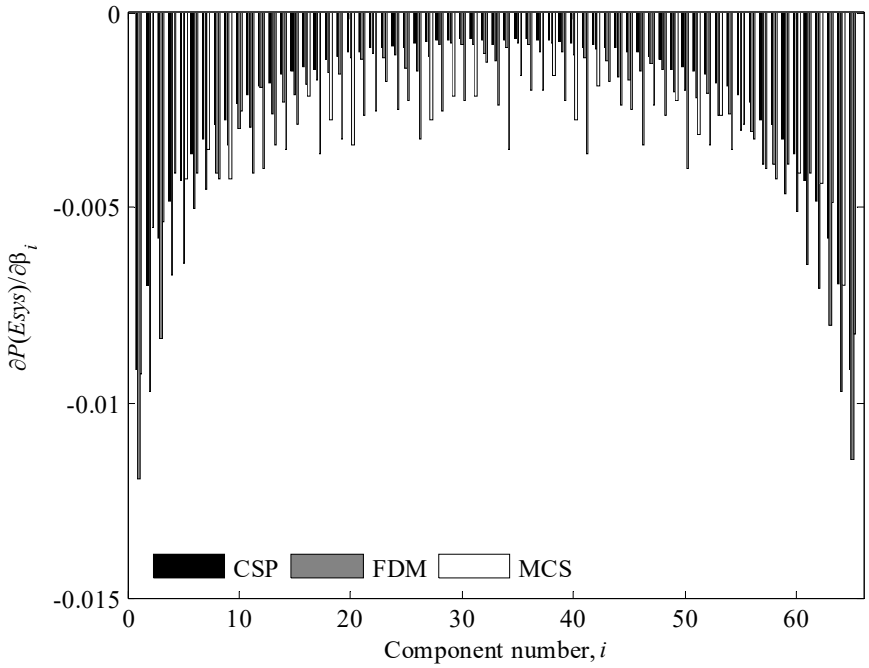

Figure 4.11: Sensitivities of the parallel system with 65 components (equal reliability indices β = –1.5 and unequal correlation coefficients): comparison between the CSP method, the FDM and the MCS.

4.4.9. Application example: sensitivity of the first-passage probability

The CSP method is applied to calculate the sensitivity of the first-passage probability. Let us consider a building subjected to a stochastic earthquake ground motion as shown in Figure 4.12. A discrete representation method (Der Kiureghian, 2000) can be used to model the continuous stochastic process by use of a finite number of standard normal random variables. In this example, the stochastic process of the ground acceleration, $f(t)$, is modeled as a filtered Gaussian process using the discrete representation method as follows:

$$f(t) \cong \sum_{i=1}^{n} \sqrt{2\pi\Phi_0 / \Delta t} \cdot v_i \cdot h_f(t - t_i)\Delta t = \mathbf{s}(t)^{\mathrm{T}} \mathbf{v} \tag{4.33}$$

where is the constant power spectral density (PSD) of the underlying white noise that enters the filter, Δt is the time step of the discretization, $\mathbf{v} = [v_1, v_2 \ldots, v_n]^{\mathrm{T}}$ is the vector of n uncorrelated

standard normal random variables, $h_f(\cdot)$ denotes the impulse-response function describing the filter, $t_i,\ i = 1,...,n$ is the discretized time point, and $\mathbf{s}(t)$ is the vector of the deterministic functions that describe the filter characteristics and the intensity of the input process. The displacement time history $u(t)$ of a linear structure subjected to the stochastic excitation $f(t)$ is derived as

$$u(t) = \int_0^t f(\tau) h_s(t-\tau) d\tau = \int_0^t \sum_{i=1}^{n} v_i s_i(\tau) h_s(t-\tau) d\tau = \sum_{i=1}^{n} v_i a_i(t) = \mathbf{a}(t)^{\mathrm{T}} \mathbf{v} \tag{4.34}$$

where $h_s(t)$ is the unit impulse response function of the structural response of interest and $\mathbf{a}(t)$ is the vector of the deterministic function describing the filter characteristics, the intensity of the input process and the dynamic characteristics of the structure. In this example, the stochastic seismic excitation is modeled as a filtered white-noise process using the Kanai-Tajimi filter model (Clough and Penzien, 1993). Its unit-impulse response function (Fujimura and Der Kiureghian, 2007) and the power spectral density (PSD) function are given as

$$h_f(t) = \exp(-\zeta_f \omega_f t) \left[\frac{(2\zeta_f^2 - 1)\omega_f}{\sqrt{1-\zeta_f^2}} \sin(\omega_f \sqrt{1-\zeta_f^2} \cdot t) - 2\zeta_f \omega_f \cos(\omega_f \sqrt{1-\zeta_f^2} \cdot t) \right] \tag{4.35}$$

$$\Phi(\omega) = \frac{1 + 4\zeta_f^2 (\omega / \omega_g)^2}{[1 - (\omega / \omega_g)^2]^2 + (2\zeta_f \omega / \omega_g)^2} \Phi_0 \tag{4.36}$$

where ω_f and ζ_f are the filter parameters representing the predominant frequency and the bandwidth of the process respectively.

For the dynamic finite element analysis, continuum elements in the building model are modeled by standard quadrilateral elements (see Figure 4.12). However, other types of elements could also be used – see, for example, reference (Talischi et al. 2012a, b). Frame elements model the structural columns represented by two vertical lines. Young's modulus E = 21,000 MPa and density ρ_m = 2,400 kg/m^3 are used as material properties for both the quadrilateral and frame elements. The damping matrix is constructed using a Rayleigh damping model such as

$$\mathbf{C} = \kappa_0 \mathbf{M} + \kappa_1 \mathbf{K} \tag{4.37}$$

where **M**, **C** and **K** are the mass, damping and stiffness matrices of the structure, respectively. The coefficients $\kappa_0 = 2.34$ and $\kappa_1 = 1.18\times10^{-4}$ are used for the Rayleigh damping model to achieve 2 % damping. Table 4.7 shows the Kanai-Tajimi filter parameters, column size, the time interval of interest, time step for the dynamic finite element analysis as well as the threshold value of the average drift ratio at each time point.

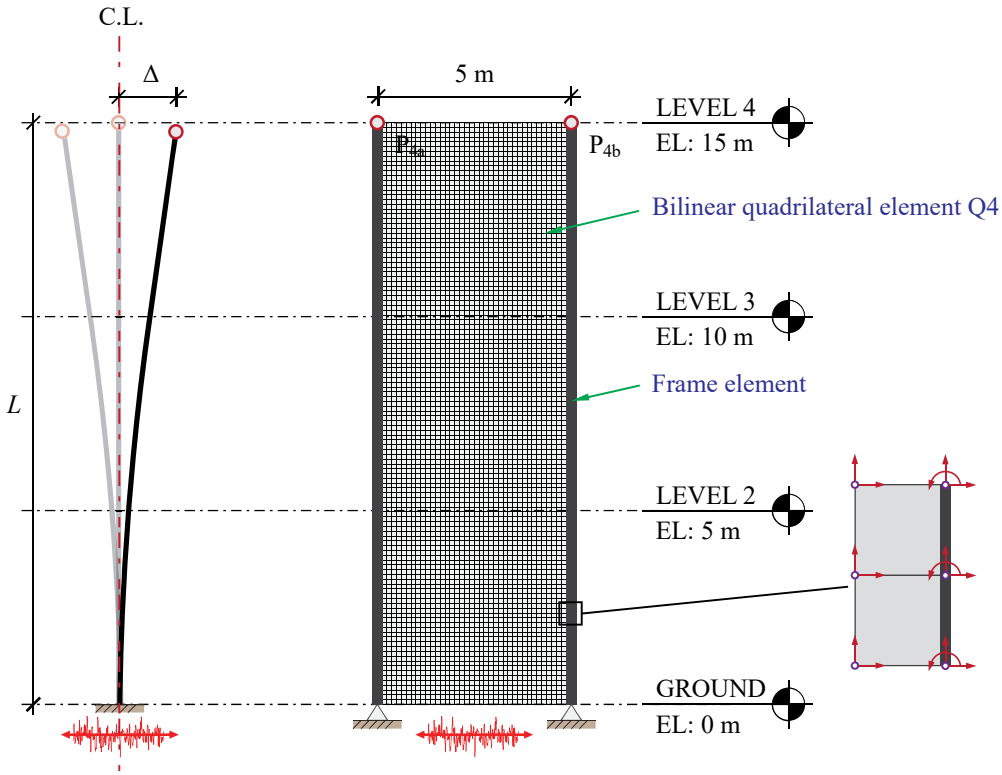

Figure 4.12: Structure geometry and loading configuration for the first-passage probability application example.

The component failure event is defined at each time point to describe the event that the average of the inter-story drift ratios computed at the marked (red) points in Figure 4.12 exceeds the given threshold value, i.e.

$$u_0 - \left(\frac{u(t_i)_{Left} + u(t_i)_{Right}}{2L} \right) = u_0 - \left(\frac{(\mathbf{a}(t_0, \tilde{\boldsymbol{\rho}})^{\mathrm{T}}_{Left} + \mathbf{a}(t_0, \tilde{\boldsymbol{\rho}})^{\mathrm{T}}_{Right})\mathbf{v}}{2} \right) \leq 0 \tag{4.38}$$

where u_0 is the threshold value of the inter-story drift ratio, $u(t_i)_{Left}$ and $u(t_i)_{Right}$ are respectively the displacement at the red points in Figure 4.12 at time $t = t_i$, and L is 15 m, and $\tilde{\boldsymbol{\rho}}$ is the vector of the design variables describing the material density distribution in the continuum elements. As explained above, the first-passage probability can be computed by obtaining the probability of the series system consisting of the component events described in Equation 4.38 defined at 125 discrete time points. The reliability index of each component failure event is computed from $\beta(u_0,t_i) = u_0/||\mathbf{a}(t_i)||$ (Der Kiureghian, 2000). The correlation coefficients are obtained by the inner-product of the negative normalized gradient vectors at the so-called design point or most probable point (Der Kiureghian 2000, 2004). Figure 4.13 shows the correlation coefficient matrix for the component failure events of this example. Figures 4.14 (a) and 4.14 (b) show one of the input excitation time histories that could be randomly generated from the Kanai-Tajimi filter model described above, and the corresponding time history of the average inter-story drift ratio at red points.

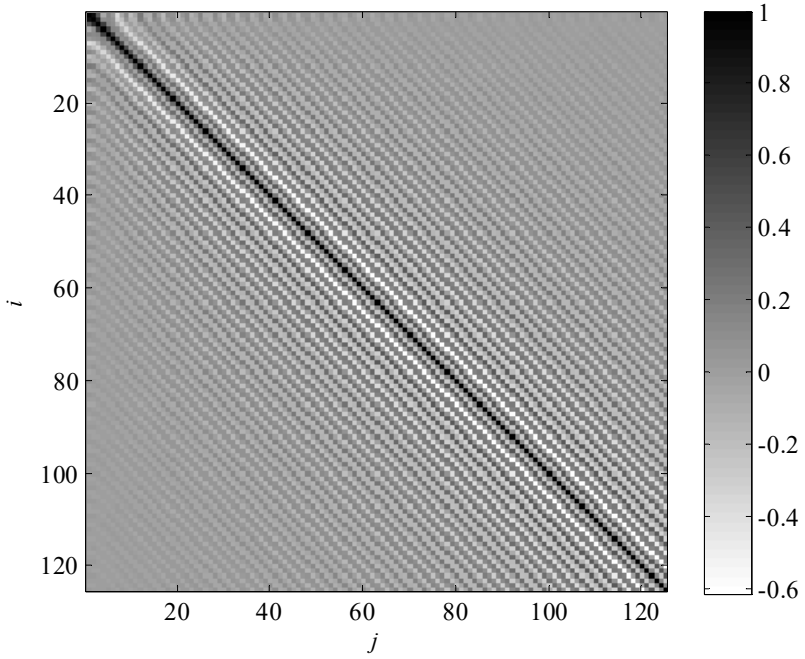

Figure 4.13: Correlation coefficient matrix between component failure events for the first-passage probability application example.

Figures 4.14 (c) and 4.14 (d) respectively show the reliability indices and the failure probabilities at the discretized time points. Figure 4.15 shows the sensitivity of the first-passage probability with respect to the reliability indices at the discretized points computed by the CSP method. The results are successfully verified by the comparison with the results by the finite difference method with perturbation of $\Delta\beta = 10^{-5}$. The calculated parameter sensitivities are useful for design or topology optimization under the constraint on the first-passage probability of a structural system (Nguyen 2010; Song and Kiureghian 2006; Bjerager and Krenk 1989).

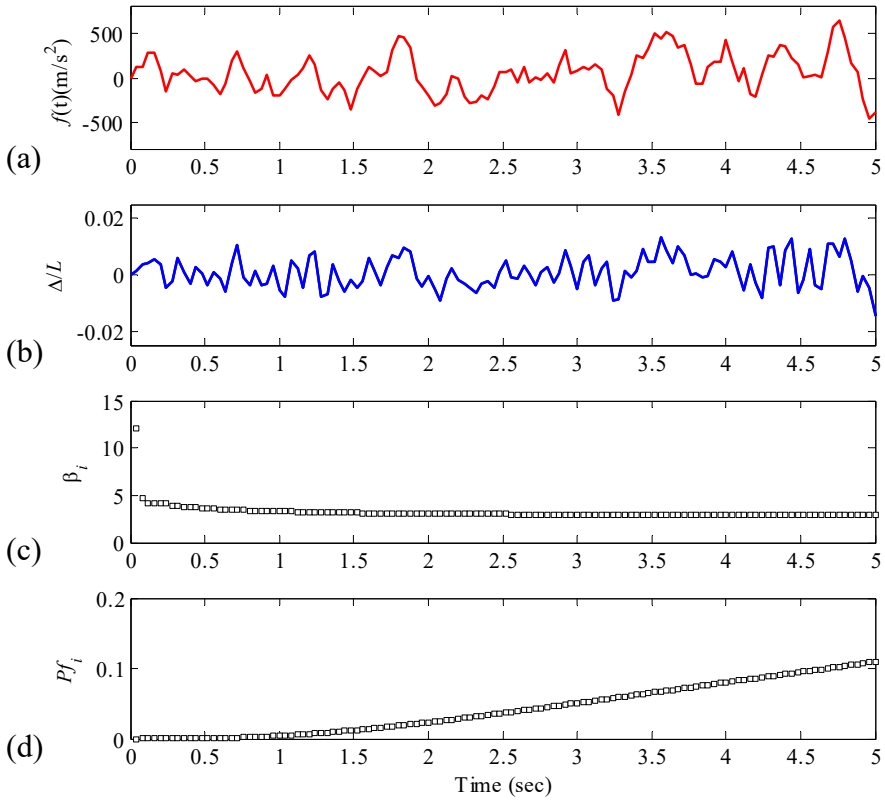

Figure 4.14: First-passage probability example: (a) a randomly generated excitation, (b) corresponding dynamic responses of story drift ratio, (c) reliability index (at each time instance), and (d) failure probability (at each time instance).

Table 4.7: One-story building example: parameters used for design domain, probabilistic constraint, and ground motion model.

Φ_0	ω_f	ζ_f	Column size	Thickness	t_{interval}	Δt	u_0
			m	m	sec	sec	
500	5π	0.4	0.5×0.5	0.1	5.0	0.04	0.02

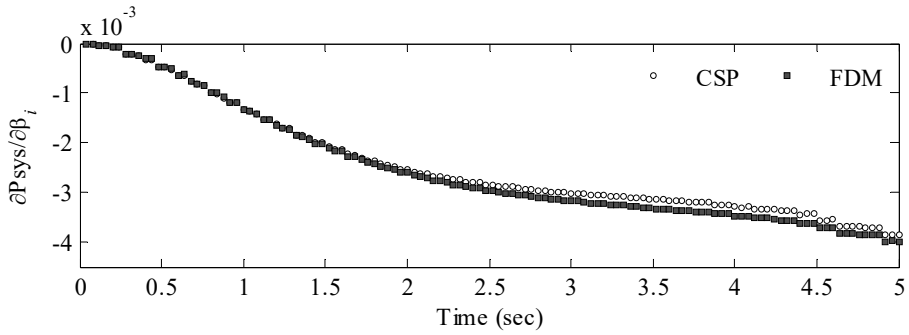

Figure 4.15: Sensitivity of the first-passage probability with respect to the reliability indices at discrete time points.

4.5. Concluding remarks

In this chapter, an efficient method to compute the parameter sensitivity of series, parallel and general system problems using the sequential compounding method (SCM) is developed. For series or parallel systems, the proposed Chun-Song-Paulino (CSP) method obtains the parameter sensitivity using the intermediate results of the second last sequential compounding. For general systems such as cut-set or link-set problems, the CSP method for series and parallel systems are used at the cut-set level or system-level to compute the sensitivity of interest. By means of a wide range of numerical examples, the accuracy of the CSP method is successfully demonstrated for series, parallel and cut-set systems under various conditions on the component reliability indices

and correlation coefficients. The accuracy of the sensitivities calculated for parallel systems seems to be more sensitive to numerical errors than other types of system events. The method is successfully applied to compute the sensitivities of the first-passage probability of the structure subjected to a stochastic ground motion. The CSP method is expected to facilitate efficient use of gradient-based optimization algorithms for design or topology optimization under constraints on system failure probability including the first-passage probability. When the sensitivity is computed with respect to each of the component events, the computational efficiency can be further improved in future research by recycling intermediate results of sequential compoundings. It is also noted that compounding orders may affect the probability and sensitivity computed by the sequential compounding method especially when component events are highly dependent. To address this issue, optimal orders of compounding procedures or general ordering schemes need to be explored in future research.

Chapter 5

System reliability-based design and topology optimization of structures constrained by first-passage probability

For the purpose of reliability assessment of a structure subject to stochastic excitations, the probability of the occurrence of at least one failure event over a time interval, i.e. the first-passage probability, often needs to be evaluated. In this chapter, a new method is proposed to incorporate probabilistic constraints on the first-passage probability into reliability-based optimization of structural design or topology. For efficient first-passage probability evaluations repeated during the optimization, the failure event is described as a series system event consisting of instantaneous failure events defined at discrete time points. The probability of the series system event is computed by use of a system reliability analysis method termed as the sequential compounding method. The adjoint sensitivity formulation is derived for calculating the parameter sensitivity of the first-passage probability to facilitate the use of efficient gradient-based optimization algorithms. The proposed method is successfully demonstrated by numerical examples of a space truss and building structures subjected to stochastic earthquake ground motions.

5.1. Introduction

Finding the optimal design of a structural system is one of the most essential tasks in structural engineering as it heavily influences the safety, cost, and performance of the structure. The optimal design should achieve major design objectives introduced for reliable operation and safety even under stochastic excitations caused by natural hazards such as earthquakes and wind loads. Due to inherent randomness in natural disasters, significant uncertainties may exist in the intensity and

characteristics of the excitations. Accordingly, the performance of such structural systems needs to be assessed probabilistically during the optimization process.

To deal with uncertainties effectively in structural design/topology optimization, various optimization algorithms and frameworks were developed recently. For instance, so-called *robust* design/topology optimization algorithms (Asadpoure et al. 2011; Wang et al. 2011; Jansen et al. 2015) aim to reduce the sensitivity of the optimal performance of a structure with respect to the randomness of interest. By contrast, *Reliability-based* design/topology optimization (Maute and Frangopol 2003; Frangopol and Maute 2005; Tsompanakis et al. 2008; Guest and Igusa 2008; Rozvany 2008; Nguyen et al. 2011; Jalalpour et al. 2013) aims to find optimal solutions satisfying the probabilistic constraints on the structural performance indicators. So far, these studies have been mainly focusing on accounting for uncertainties in static loads representing typical load patterns of the structure. Recent studies on structural optimization considering dynamic excitations employed few deterministic time histories representing possible future realizations (Salajegheh and Heidari 2005; Kaveh et al. 2012), or focused on partial descriptors of the dynamic responses such as mode frequencies (Filipov et al. 2016). These approaches have intrinsic limitations because (1) a single or few sample time histories do not represent all possible realizations of stochastic excitations, and (2) it is impossible to assess the probabilities that the structural design does not satisfy the constraints on performances, i.e. failure probabilities using this approach. Therefore, the probabilistic prediction of structural responses based on random vibration analysis is needed in the process for optimal design

To overcome this technical challenge, the authors recently proposed a new method for topology optimization of structures under stochastic excitations (Chun et al. 2016). In the proposed method, random vibration analysis based on the use of the discrete representation method (Der Kiureghian 2000) and structural reliability theories (see Der Kiureghian 2005 for a review) are integrated within a state-of-the-art topology optimization framework. The authors also developed a system reliability-based topology optimization framework under stochastic excitations (Chun et

al. 2013) to cope with *system* failure events consisting of statistical dependent components using the matrix-based system reliability method (Song and Kang 2009). The developed method helps satisfy probabilistic constraints on a system failure event, which consists of multiple limit-states defined in terms of different locations, failure modes or time points as it optimizes a structural system.

In these studies by the authors, the *instantaneous* failure probabilities of the structure were evaluated at discrete time points. However, to promote applications of design/topology optimization to engineering design practice, the first-passage probability, i.e. the probability of at least one occurrence of the failure over a time interval, needs to be estimated during the optimization process. This helps promote the use of the proposed stochastic optimization framework for the design of the lateral load-resisting system or sizing structural elements under stochastic excitations with a finite duration such as earthquake excitations. To this end, this chapter introduces a stochastic design and topology optimization method that can handle probabilistic constraints on the first-passage probability, and demonstrate the method using numerical examples.

5.2. Random vibration analysis using discrete representation method

In the aforementioned reliability based design optimization framework under stochastic excitations (Chun et al. 2013; Chun et al. 2016), the authors proposed to perform random vibration analysis by use of the discrete representation method (Der Kiureghian 2000) in order to compute the instantaneous failure probability of the stochastic response at discrete time points. In the proposed approach, for example, a zero-mean stationary Gaussian input excitation process $f(t)$ is discretized as

$$f(t) = \sum_{i=1}^{n} v_i s_i(t) = \mathbf{s}(t)^{\mathrm{T}} \mathbf{v} \tag{5.1}$$

where $\mathbf{s}(t)$ (= $[s_1(t),\ldots, s_n(t)]^{\mathrm{T}}$) is a vector of deterministic functions that describe the spectral characteristics of the process, and $\mathbf{v} = [v_1, v_2,\ldots, v_n]^{\mathrm{T}}$ is a vector of uncorrelated standard normal

random variables. Among a few methods available to develop a discrete representation model in Equation 5.1, a popular one for ground excitation modelling is using a filter representing the characteristic of soil medium and a random pulse train. For example, if a filtered white noise is used, the model in Equation 5.1 is constructed as

$$f(t) = \int_0^t h_f(t-\tau) W(\tau) d\tau = \mathbf{s}(t)^{\mathrm{T}} \mathbf{v}$$
$$s_i(t) = \begin{cases} \sqrt{2\pi\Phi_0 / \Delta t} \cdot \int_{t_{i-1}}^{t_i} h_f(t-\tau) d\tau & t_{i-1} < t < t_i,\ i = 1,...,n \\ 0 & t \le t_{i-1} \end{cases} \tag{5.2}$$

in which $W(\tau)$ denotes the white noise process whose power spectral density function is constant, i.e. $\Phi_{WW}(\omega) = \Phi_0$, $h_f(\cdot)$ is the impulse response function of the filter, $\Delta t = t_i - t_{i-1}$, and n denotes the number of the time intervals introduced for the given time period $(0, t)$. The details of the derivation of Equation 5.2 is available in Chun et al. (2016).

5.2.1. Response of linear system under stochastic excitations

The responses of linear systems to stochastic excitation can be determined by the convolution integral consisting of their impulse response function and the discretized input process in Equation 5.1. That is, a response time history $u(t)$ of the linear system subjected to the stochastic excitation $f(t)$ is derived as

$$u(t) = \int_0^t f(\tau) h_s(t-\tau) d\tau = \int_0^t \sum_{i=1}^n v_i s_i(\tau) h_s(t-\tau) d\tau = \sum_{i=1}^n v_i a_i(t) = \mathbf{a}(t)^{\mathrm{T}} \mathbf{v} \tag{5.3}$$

where $h_s(t)$ is the impulse response function of the linear structural system, and $\mathbf{a}(t)$ denotes a vector of deterministic basis functions

$$a_i(t) = \int_0^t s_i(\tau) h_s(t-\tau) d\tau, \quad i = 1,...,n \tag{5.4}$$

Deriving the impulse response function in a finite element setting can be computationally challenging or cumbersome. To facilitate the process, the authors proposed novel numerical procedures in Chun et al. (2016).

5.2.2. Instantaneous failure probability of linear system under stochastic excitations

In structural reliability analysis, the probability that the outcome of a random vector **X** is located inside the failure domain Ω_f, i.e. the failure probability, is computed by an integral

$$P_f = \int_{\Omega_f} f_{\mathbf{X}}(\mathbf{x}) d\mathbf{x} \tag{5.5}$$

where $f_{\mathbf{X}}(\mathbf{x})$ is the joint probability density function (PDF) of the random vector **X**. The failure domain is defined by the domain where the limit-state function $g(\mathbf{x})$, e.g. capacity minus demand, takes the negative sign. In general, computing the multi-fold integral in Equation 5.5 is non-trivial. Structural reliability methods such as FORM, SORM (see Der Kiureghian 2005 for a review) transform the space of the random variable **x** into the uncorrelated standard normal space **v**. Then, the limit-state function is approximated by a linear (FORM) or quadratic function (SORM) at the design point or the most probable failure point (MPP). For example, in FORM, the failure probability is approximated as

$$P_f = \Phi[-\beta] \tag{5.6}$$

where β is the reliability index, i.e. the shortest distance from the origin of the standard normal space to the linearized failure surface, and $\Phi[\cdot]$ denotes the cumulative distribution function (CDF) of the standard normal distribution.

Using the discrete representation method described above, limit-state functions defined for displacement or other structural responses can be described in the space of standard normal random variable **v**. For example, the instantaneous failure event E_f defined for a linear structure subjected to the Gaussian process in Equation 5.1 is given by

$$E_f(t_k, u_0, \mathbf{v}) = \{g(t_k, u_0, \mathbf{v}) \le 0\}$$
$$g(t_k, u_0, \mathbf{v}) = u_0 - u(t_k) = u_0 - \mathbf{a}(t_k)^{\mathrm{T}}\, \mathbf{v} \tag{5.7}$$

where u_0 is the prescribed threshold on the displacement response and. In this case, the reliability index β is computed from the geometric interpretation of the limit-state surface as a closed form expression (Der Kiureghian 2000)

$$\beta(t_k, u_0) = \frac{u_0}{\| \mathbf{a}(t_k) \|} \tag{5.8}$$

It is noted that the limit-state function in Equation 5.7 is linear in this case, and thus the failure probability by Equation 5.6, i.e. $P_f = \Omega[-\beta(t_k,u_0)]$ does not introduce errors caused by function approximation or require nonlinear optimization to find the design point. If the structure behaves nonlinearly or the input process is non-Gaussian, one needs to use reliability methods such as FORM or SORM to compute the failure probability approximately. Using this discrete representation method, one can reduce the computational cost of the random vibration, which should be repetitively performed during the optimization processes to compute the instantaneous failure probabilities at each updated set of design variables.

5.2.3. First-passage probability of linear system under stochastic excitations

The first-passage probability is commonly utilized to find the probability of the failure event described within a time interval (Vanmarcke 1975; Song and Der Kiureghian 2006; Fujimura and Der Kiureghian 2007). One of the available approaches for formulating the first-passage probability P_{fp} is defining the problem as a series system problem such as:

$$P_{fp} = P(u_0 < \max_{0<t<t_n} u(t)) = P\left(\bigcup_{k=1}^{n} \{u(t_k) > u_0\}\right) \tag{5.9}$$

Using the discrete representation, the first-passage probability of a system with n_c limit-state functions (defined for different failure modes or locations) is described as

$$P_{fp} = P\left(\bigcup_{i=1}^{n_c} E_{sys}^{i}\right) = P\left(\bigcup_{i=1}^{n_c}\bigcup_{k=1}^{n} E_{f_i}(t_k, u_0, \mathbf{v})\right) \tag{5.10}$$

where E_{sys}^{i} denotes the first-passage failure event regarding the i^{th} constraint, $E_{fi}(\cdot)$ denotes the instantaneous failure event of i^{th} limit-state function at time t_k, and n is the total number of discretized time points. To compute the first-passage probability in Equation 5.10, it is required to evaluate the failure probabilities of the component events at each time point within an interval. Moreover, an efficient, reliable and robust algorithm is required to evaluate the system failure probability with a proper consideration of statistical dependency between the component events. It is also desirable to compute the parameter sensitivity of the system failure probability to enable the use of efficient gradient-based optimizers. To address these requirements, the sequential compounding method (SCM; Kang and Song 2010) and the Chun-Song-Paulino (CSP; Chun et al. 2015) are adopted in this study.

5.3. Optimization of structures subjected to stochastic excitation under first-passage probability constraints

Reliability Based Design Optimization (RBDO) of a structure aims to achieve the optimal design under probabilistic constraints on uncertain performance, arising from uncertainties in material properties or loads. For example, Component Reliability Based Design Optimization (CRBDO) approach seeks to satisfy the probabilistic constraint for each failure mode. The CRBDO problem can be formulated as

$$\begin{aligned} &\min_{\mathbf{d}} \quad f_{obj}(\mathbf{d}) \\ &s.t \quad P\left(g_i(\mathbf{d}) \le 0\right) \le P_{f_i}^{\text{target}}, \quad i = 1, ..., n_c \\ &\qquad \mathbf{d}^{\text{lower}} \le \mathbf{d} \le \mathbf{d}^{\text{upper}} \end{aligned} \tag{5.11}$$

where $f_{obj}(\mathbf{d})$ denotes the objective function of the design, $\mathbf{d}^{\text{lower}}$ and $\mathbf{d}^{\text{upper}}$ are the lower and upper bounds of the vector of design variables $\mathbf{d}$, respectively. $g_i(\cdot)$ represents the limit-state function

whose negative sign indicates violating a given constraint, n_c is the number of the constraints, $P(g_i(\mathbf{d}) \le 0)$ is the failure probability of the failure event, and P_f^{target} is the target failure probability.

The RBDO problem of a structure under first-passage probability constraints can be formulated as a System Reliability Based Design Optimization (SRBDO) problem (Nguyen et al. 2011), i.e.

$$\begin{aligned} &\min_{\mathbf{d}} \ f_{obj}(\mathbf{d}) \\ &s.t \quad P(E_{sys}^i) = P\left(\bigcup_{k=1}^{n} E_{f_i}(t_k, \mathbf{d})\right) = P\left(\bigcup_{k=1}^{n} \{g_i(t_k, \mathbf{d}) \le 0\}\right) \le P_{f_i}^{\text{target}}, \quad i = 1, ..., n_c \\ &\quad \mathbf{d}^{\text{lower}} \le \mathbf{d} \le \mathbf{d}^{\text{upper}} \\ &\text{with } \mathbf{M}(\mathbf{d})\ddot{\mathbf{u}}(t, \mathbf{d}) + \mathbf{C}(\mathbf{d})\dot{\mathbf{u}}(t, \mathbf{d}) + \mathbf{K}(\mathbf{d})\mathbf{u}(t, \mathbf{d}) = \mathbf{f}(t, \mathbf{d}) \end{aligned} \tag{5.12}$$

where **M**, **C,** and **K** represent the global mass, damping and stiffness matrices of the structure, respectively, and $\ddot{\mathbf{u}}$, $\dot{\mathbf{u}}$, **u,** and **f** are the acceleration, velocity, displacement and force vectors at time *t*, respectively. A proportional damping model known as 'Rayleigh damping' (Clough and Penzien 1993) is used throughout this chapter. In this approach, the damping matrix is determined as a linear combination of the stiffness and mass matrix, that is $\mathbf{C} = \kappa_0\mathbf{M} + \kappa_1\mathbf{K}$. The coefficients κ_0 and κ_1 in the Rayleigh damping model can are determined to have a certain modal damping factors. For earthquake ground excitations, the force vector in Equation 5.12 is determined by a vector of effective earthquake forces, i.e.

$$\mathbf{f}(t, \mathbf{d}) = -\mathbf{M}(\mathbf{d})\mathbf{l}\ddot{u}_g(t) = -\mathbf{M}(\mathbf{d})\mathbf{l}f(t) \tag{5.13}$$

where **l** represents the directional distribution of mass with unity resulting from a unit ground displacement, and $\ddot{u}_g$ is the ground acceleration time history.

Topology optimization under stochastic excitation under the first-passage probability constraints can be formulated as follows:

$$\begin{aligned} &\min_{\mathbf{d}} \ f_{obj}(\tilde{\boldsymbol{\rho}}) \\ &s.t \quad P(E_{sys}^i) = P\left(\bigcup_{k=1}^{n} E_{f_i}(t_k, \tilde{\boldsymbol{\rho}})\right) = P\left(\bigcup_{k=1}^{n} \{g_i(t_k, \tilde{\boldsymbol{\rho}}) \le 0\}\right) \le P_{f_i}^{\text{target}}, \quad i = 1, ..., n_c \\ &\quad 0 < \varepsilon \le \tilde{\rho}_i \le 1 \ \ \forall i \in \Omega \\ &\text{with } \mathbf{M}(\tilde{\boldsymbol{\rho}})\ddot{\mathbf{u}}(t, \tilde{\boldsymbol{\rho}}) + \mathbf{C}(\tilde{\boldsymbol{\rho}})\dot{\mathbf{u}}(t, \tilde{\boldsymbol{\rho}}) + \mathbf{K}(\tilde{\boldsymbol{\rho}})\mathbf{u}(t, \tilde{\boldsymbol{\rho}}) = \mathbf{f}(t, \tilde{\boldsymbol{\rho}}) \end{aligned} \tag{5.14}$$

where **d** denotes the vector of design variables, Ω is a set of finite element indices and $\tilde{\boldsymbol{\rho}}$ is the vector of filtered densities defined as:

$$\tilde{\boldsymbol{\rho}} = \mathbf{P}\mathbf{d} \tag{5.15}$$

where **P** represents the filtering matrix whose element is determined by

$$(\mathbf{P})_{lk} = \frac{w_{lk}}{\sum_{j \in \square_l} w(r_j)}, \; w_{lk} = \begin{cases} w(r_k) & \text{if } k \in \square_l \\ 0 & \text{otherwise} \end{cases} \tag{5.16}$$

A flowchart for topology optimization of a structure constrained by first-passage probability is provided in Appendix B.

Various engineering constraints can be incorporated into the aforementioned formulations of reliability based design optimization and topology optimization under first-passage probability. To promote applications of the proposed method to truss and building structures, engineering constraints on stress in bar, drift ratio, and inter-story drift ratio are derived below.

5.3.1. First-passage probability constraints on stress in bar elements

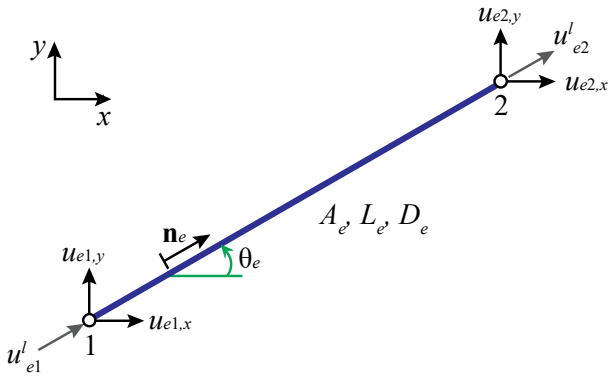

Figure 5.1: Bar geometry.

Consider a bar *e* in the truss with local node numbers 1 and 2 denoting the end points of the bar as shown in Figure 5.1. A unit vector $\mathbf{n}_e$ pointing from node 1 to node 2 is defined as

$$\mathbf{n}_e = \begin{pmatrix} \cos\theta_e \\ \sin\theta_e \end{pmatrix} \tag{5.17}$$

The global displacement vectors of the end nodes of bar *e* are written as

$$\mathbf{u}_e = \begin{pmatrix} \mathbf{u}_{e1}^g \\ \mathbf{u}_{e2}^g \end{pmatrix}, \text{ where } \mathbf{u}_{e1}^g = \begin{pmatrix} u_{e1,x} \\ u_{e1,y} \end{pmatrix}, \ \mathbf{u}_{e2}^g = \begin{pmatrix} u_{e2,x} \\ u_{e2,y} \end{pmatrix} \tag{5.18}$$

The stress $\sigma(t)$ in a truss element e under stochastic excitations can be computed from the stress-strain relationship based on Hooke's law as follows:

$$\begin{aligned} \sigma_e(t,\mathbf{d}) &= \frac{D_e}{L_e}\mathbf{n}_e \cdot (\mathbf{u}_{e2}^g(t,\mathbf{d}) - \mathbf{u}_{e1}^g(t,\mathbf{d})) = \frac{D_e}{L_e}\mathbf{B}_e\mathbf{u}_e \\ &= \frac{D_e}{L_e}(u_{e2}^l(t,\mathbf{d}) - u_{e1}^l(t,\mathbf{d})) \end{aligned} \tag{5.19}$$

where D_e denotes Young's modulus, L_e is the length of the element e, $u^l_{e1}(t)$ and $u^l_{e2}(t)$ are end displacements along the truss axis, and

$$\mathbf{B}_e = [-\mathbf{n}_e^{\mathrm{T}} \ \ \mathbf{n}_e^{\mathrm{T}}] \tag{5.20}$$

The elongation in Equation 5.19 can be described by using the discrete representation form in Equation 5.3, i.e.

$$\sigma_e(t,\mathbf{d}) = \frac{D_e}{L_e}(\mathbf{a}(t,\mathbf{d})_{e2}^{\mathrm{T}}\mathbf{v} - \mathbf{a}(t,\mathbf{d})_{e1}^{\mathrm{T}}\mathbf{v}) \tag{5.21}$$

The instantaneous failure probability at time t_k is expressed in terms of stress in the truss element *e* as

$$\begin{aligned} &P(E_{fe}(t_k,\mathbf{d})) = P(g_e(t_k,\mathbf{d}) \le 0) = P(\sigma_{0e} - \sigma_e(t_k,\mathbf{d}) \le 0) \\ &= P\left(\sigma_{0e} - \frac{D_e}{L_e}\left(\mathbf{a}(t_k,\mathbf{d})_{e2}^{\mathrm{T}}\mathbf{v} - \mathbf{a}(t_k,\mathbf{d})_{e1}^{\mathrm{T}}\mathbf{v}\right) \le 0\right) = \Phi\left[-\beta_{\sigma e}(t_k,\mathbf{d})\right] \end{aligned} \tag{5.22}$$

where σ_{0e} denotes the threshold value of stress. From the geometric representation associated with the failure event of element *e*, the reliability index at time t_k is computed as

$$\beta_{\sigma e}(t_k,\mathbf{d}) = \frac{L_e \cdot \sigma_{0e}}{D_e\left\|\mathbf{a}(t_k,\mathbf{d})_{e1}^{\mathrm{T}} - \mathbf{a}(t_k,\mathbf{d})_{e2}^{\mathrm{T}}\right\|} = \frac{L_e \cdot \sigma_{0e}}{D_e\left\|\mathbf{b}_e(t_k,\mathbf{d})\right\|} \tag{5.23}$$

The first-passage probability of the stress limit state function is then computed as

$$
\begin{aligned}
P_{fp\_\sigma}(E_{sys}) &= P\left(\bigcup_{k=1}^{n} E_{f\sigma}(t_k,\mathbf{d})\right) \\
&= P\left(\bigcup_{k=1}^{n}\left\{\sigma_{0e}-\sigma_e(t_k,\mathbf{d})\le 0\right\}\right) \\
&= P\left(\bigcup_{k=1}^{n}\left\{\sigma_{0e}-\frac{D_e}{L_e}\left(\mathbf{a}(t_k,\mathbf{d})_{e1}^{\mathrm{T}}\mathbf{v}-\mathbf{a}(t_k,\mathbf{d})_{e2}^{\mathrm{T}}\mathbf{v}\right)\le 0\right\}\right) \\
&= 1-\Phi_n\left[\beta_{\sigma e}(t_1,\mathbf{d}),\beta_{\sigma e}(t_2,\mathbf{d}),...,\beta_{\sigma e}(t_n,\mathbf{d});\rho_{1,2},\rho_{1,3},...,\rho_{n-1,n}\right] \\
&= 1-\Phi_n\left[\boldsymbol{\beta}_{\sigma e},\mathbf{R}\right]
\end{aligned}
\tag{5.24}
$$

where Φ_n denotes the multivariate normal CDF, $\rho_{i,j}$ represents the correlation coefficient between the failure event i and j, and $\boldsymbol{\beta}$ and $\mathbf{R}$ are the vector of the reliability indices and the correlation coefficient matrix, respectively. The correlation coefficient matrix $\mathbf{R}$ is constructed as

$$
\mathbf{R}=\begin{bmatrix}\rho_{1,1} & \cdots & \rho_{1,n}\\ \vdots & \ddots & \vdots \\ \rho_{n,1} & \cdots & \rho_{n,n}\end{bmatrix},\quad \rho_{k,l}=\boldsymbol{\alpha}(t_k)\cdot\boldsymbol{\alpha}(t_l)^{\mathrm{T}} \tag{5.25}
$$

where $\boldsymbol{\alpha}(t_i)=\mathbf{a}(t_i)/\|\mathbf{a}(t_i)\|$ denotes the negative normalized gradient vector of the limit-state function evaluated at the design point which is obtained by $u_0\cdot\mathbf{a}(t_i)/\|\mathbf{a}(t_i)\|^2$.

5.3.2. First-passage probability constraint on drift ratio

The drift ratio of a structure is defined as the ratio of the drift Δ to the height H of the structure. The instantaneous failure probability given in terms of the drift ratio at time t_k is

$$
\begin{aligned}
&P(E_{f_\Delta}(t_k,\mathbf{d})) = P(g_\Delta(t_k,\mathbf{d})\le 0) = P\left(u_{0\Delta}-\frac{\Delta(t_k,\mathbf{d})}{H}\le 0\right) \\
&= P\left(u_{0\Delta}-\frac{\mathbf{a}(t_k,\mathbf{d})_\Delta^{\mathrm{T}}\mathbf{v}}{H}\le 0\right) \\
&= \Phi\left[-\beta_\Delta(t_k,\mathbf{d})\right]
\end{aligned}
\tag{5.26}
$$

where $u_{0\Delta}$ denotes the threshold value of the drift ratio. The shortest distance from the origin in the standard normal space to the limit state function at time t_k can be obtained from the geometric representation as

$$\beta_{\Delta}(t_k,\mathbf{d}) = \frac{Hu_{0\Delta}}{\left\|\mathbf{a}(t_k,\mathbf{d})_{\Delta}^{\mathrm{T}}\right\|} \tag{5.27}$$

Moreover, the first-passage probability in terms of the drift ratio then can be expressed as

$$\begin{aligned} P_{fp\_\Delta}(E_{sys}) &= P\left(\bigcup_{k=1}^{n}\left(E_{f_{\Delta}}(t_k,\mathbf{d}) : u_{0\Delta} - \frac{\Delta(t_k,\mathbf{d})}{H} \le 0\right)\right) \\ &= P\left(\bigcup_{k=1}^{n}\left(E_{f_{\Delta}}(t_k,\mathbf{d}) : u_{0\Delta} - \frac{\mathbf{a}(t_k,\mathbf{d})_{\Delta}^{\mathrm{T}}\mathbf{v}}{H} \le 0\right)\right) \\ &= 1-\Phi_n\left[\beta_{\Delta}(t_1,\mathbf{d}),\beta_{\Delta}(t_2,\mathbf{d}),...,\beta_{\Delta}(t_n,\mathbf{d});\rho_{1,2},\rho_{1,3},...,\rho_{n-1,n}\right] \\ &= 1-\Phi_n\left[\boldsymbol{\beta}_{\Delta},\mathbf{R}\right] \end{aligned} \tag{5.28}$$

5.3.3. First-passage probability constraint on inter-story drift ratio

In addition, the first-passage probability can be computed in terms of the inter-story drift ratio, which is one of the significant design criteria in structural engineering, defined as

$$\frac{\Delta_i(t,\mathbf{d})}{H_i} = \begin{cases} \dfrac{\mathbf{a}(t,\mathbf{d})_i^{\mathrm{T}}\mathbf{v}}{H_i} & \text{for } i=2 \\ \left(\mathbf{a}(t,\mathbf{d})_i^{\mathrm{T}} - \mathbf{a}(t,\mathbf{d})_{i-1}^{\mathrm{T}}\right)\dfrac{\mathbf{v}}{H_i} & \text{for } i=3,4,...,n_s \end{cases} \tag{5.29}$$

where Δ_i denotes the story drift at floor level I and H_i represents the story height below level i, and n_s is the number of story levels. The instantaneous failure probability in terms of the inter story-drift ratios is

$$\begin{aligned} P(E_{f_{\Delta i}}(t_k,\mathbf{d})) &= P(g_{\Delta i}(t_k,\mathbf{d}) \le 0) = P\left(u_{0\Delta i} - \frac{\Delta_i(t_k,\mathbf{d})}{H_i} \le 0\right) \\ &= \Phi\left[-\beta_{\Delta i}(t_k,\mathbf{d})\right],\ i=1,...,n_s \end{aligned} \tag{5.30}$$

where $u_{0\Delta i}$ denotes a threshold value of the inter-story drift ratio and $\beta_{\Delta i}$ represents the reliability index which can be computed as

$$\beta_{\Delta i}\left(t_k,\mathbf{d}\right)=\begin{cases}\dfrac{H_i u_{0\Delta i}}{\left\|\mathbf{a}(t_k,\mathbf{d})_i^{\mathrm{T}})\right\|} & \text{for } i=2\\ \dfrac{H_i u_{0\Delta i}}{\left\|\mathbf{a}(t_k,\mathbf{d})_i^{\mathrm{T}}-\mathbf{a}(t_k,\mathbf{d})_{i-1}^{\mathrm{T}}\right\|} & \text{for } i=3,4,...,n_s\end{cases} \tag{5.31}$$

Finally, the first-passage probability is

$$\begin{aligned}P_{fp\_\Delta i}(E_{sys}) &= P\left(\bigcup_{k=1}^{n}E_{f_{\Delta i}}(t_k,\mathbf{d})\right)\\ &= P\left(\bigcup_{k=1}^{n}\left\{u_{0\Delta i}-\frac{\Delta_i(t_k,\mathbf{d})}{H_i}\le 0\right\}\right)\\ &= 1-\Phi_n\left[\beta_{\Delta i}\left(t_1,\mathbf{d}\right),\beta_{\Delta i}\left(t_2,\mathbf{d}\right),...,\beta_{\Delta i}\left(t_{nt},\mathbf{d}\right);\rho_{1,2},\rho_{1,3},...,\rho_{n-1,n}\right]\\ &= 1-\Phi_n\left[\boldsymbol{\beta}_{\Delta i},\mathbf{R}\right]\end{aligned} \tag{5.32}$$

5.4. Calculating sensitivity of first-passage probability

To use efficient gradient-based optimization algorithms for RBDO, it is essential to calculate the sensitivity of the failure probability with respect to various design parameters. In this chapter, a sensitivity formulation employing the adjoint method (Choi and Kim 2005) is derived for linear structures subjected to stochastic excitations modeled by the discrete representation method. It is noted that the sensitivity of the system failure probability with respect to a parameter θ is obtained by a chain rule, i.e.

$$\frac{\partial P_f(E_{sys})}{\partial\theta}=\sum_{i=1}^{n}\frac{\partial P_f(E_{sys})}{\partial\beta_i(\theta)}\cdot\frac{\partial\beta_i(\theta)}{\partial\theta} \tag{5.33}$$

Recently, Chun et al. (2015) proposed the CSP method to compute the derivatives of the system failure probability with respect to the reliability index by using the SCM. The CSP method computes sensitivities of parallel and series systems, as well as general systems with respect to reliability indices efficiently and accurately.

5.4.1. Sensitivity of first-passage probability in RBDO

To facilitate the use of a gradient-based optimizer in RBDO under probabilistic constraints on first-passage probability, the sensitivity of the first-passage probability in RBDO is computed using the chain rule, i.e.

$$\frac{\partial P_{fp}(E_{sys})}{\partial d_i} = \frac{\partial\left(1-\Phi_n\left[\boldsymbol{\beta},\mathbf{R}\right]\right)}{\partial d_i} = \sum_{j=1}^{n}\left(\frac{\partial\left(-\Phi_n\left[\boldsymbol{\beta},\mathbf{R}\right]\right)}{\partial \beta_j}\cdot\frac{\partial \beta_j(\mathbf{d})}{\partial d_i}\right) = \sum_{j=1}^{n}\left(c_j\cdot\frac{\partial \beta_j(\mathbf{d})}{\partial d_i}\right) \tag{5.34}$$

where $c_j=\partial(-\Phi[\boldsymbol{\beta},\mathbf{R}])/\partial\beta_j$ can be computed using Equation 4.12. The partial derivative $\partial\beta_j/\partial d_i$ is obtained by

$$\frac{\partial \beta_j(\mathbf{d})}{\partial d_i} = -\frac{C_{cst}\cdot\left(\sum_{k=1}^{j}\left(a_k(t_j,\mathbf{d})\cdot\frac{\partial a_k(t_j,\mathbf{d})}{\partial d_i}\right)\right)}{\left(\sum_{k=1}^{j}a_k(t_j,\mathbf{d})^2\right)^{3/2}} \tag{5.35}$$

where C_{cst} is the coefficient determined depending on the constraint used in optimization, e.g.

$$C_{cst} = \begin{cases} L_e\sigma_{0e}/D_e & \text{: stress in bar} \\ Hu_{0\Delta} & \text{: drift ratio} \\ H_i u_{0\Delta i} & \text{: inter-story drift ratio} \end{cases} \tag{5.36}$$

When a uniform time step size is used, i.e. $t_i - t_{i-1} = \Delta t,\ \ i = 1,2,....,n$ and $t_n = t_0$, Equation 5.35 can be rewritten from Equation 3.11 as follows (see more details of the derivation in Appendix A):

$$\frac{\partial \beta_j(\mathbf{d})}{\partial d_i} = -\frac{C_{cst}\cdot\left(\sum_{k=n-j+1}^{n}\left(a_k(t_n,\mathbf{d})\cdot\frac{\partial a_k(t_n,\mathbf{d})}{\partial d_i}\right)\right)}{\left(\sum_{k=n-j+1}^{n}a_k(t_n,\mathbf{d})^2\right)^{3/2}} \tag{5.37}$$

Furthermore, the uniform step size leads to the followings for the parameter sensitivity in Equation 5.34:

$$\frac{\partial P_{fp}(E_{sys})}{\partial d_i} = \sum_{j=1}^{n}\left(c_j \cdot \frac{\partial \beta_j(\mathbf{d})}{\partial d_i} \right)$$
$$= -C_{cst} \cdot \left[\left(\frac{c_1}{\left(\sum_{k=n}^{n} a_k(t_n,\mathbf{d})^2 \right)^{3/2}} + \cdots + \frac{c_n}{\left(\sum_{k=1}^{n} a_k(t_n,\mathbf{d})^2 \right)^{3/2}} \right) a_n(t_n,\mathbf{d}) \frac{\partial a_n(t_n,\mathbf{d})}{\partial d_i} + \ldots \right.$$
$$\left. + \frac{c_n}{\left(\sum_{k=1}^{n} a_k(t_n,\mathbf{d})^2 \right)^{3/2}} a_1(t_n,\mathbf{d}) \frac{\partial a_1(t_n,\mathbf{d})}{\partial d_i} \right]$$
$$= \left(C_{cst} \cdot \sum_{l=1}^{n} \left(\chi_l a_{n-l+1}(t_n,\mathbf{d}) \frac{\partial a_{n-l+1}(t_n,\mathbf{d})}{\partial d_i} \right) \right) = \sum_{s=1}^{n} \left(\kappa_s(t_n,\mathbf{d}) \frac{\partial a_s(t_n,\mathbf{d})}{\partial d_i} \right) \tag{5.38}$$

where

$$\chi_l = -\left(\sum_{i=l}^{n} \left(c_i \Big/ \left(\sum_{k=n-i+1}^{n} a_k(t_n,\mathbf{d})^2 \right)^{3/2} \right) \right), \quad \kappa_s(t_n,\mathbf{d}) = C_{cst} \cdot \chi_{n-s+1} \cdot a_s(t_n,\mathbf{d}) \tag{5.39}$$

5.4.2. Adjoint variable method

The sensitivity in Equation 5.38 includes the implicitly defined derivative term of $\partial a_s(t_n,\mathbf{d})/\partial d_i$, s = 1,…, n. Those implicit derivatives can be computed using the direct differentiation method (DDM), the finite difference method (FDM) and the adjoint variable method (AJM) (Choi and Kim 2005). Chun et al. (2016) derived an approach of sensitivity calculations associated with $\partial a_s(t_n,\mathbf{d})/\partial d_i$ using the adjoint variable method. The numerical tests confirmed superior performance of AJM compared to DDM and FDM. Based on the AJM derivation, the sensitivity of the first-passage probability in Equation 5.38 is rewritten as

$$\frac{\partial P_{fp}(E_{sys})}{\partial d_i} = \sum_{j=1}^{n} \boldsymbol{\lambda}_{n-j+1}^{\mathrm{T}} \left[\frac{\partial \underline{\underline{\mathbf{A}}}(\mathbf{d})}{\partial d_i} \cdot \mathbf{u}(t_j, \mathbf{d}) - \eta \left(\Delta t\right)^2 \frac{\partial \mathbf{f}(t_j, \mathbf{d})}{\partial d_i} - (0.5 + \gamma - 2\eta) \left(\Delta t\right)^2 \frac{\partial \mathbf{f}(t_{j-1}, \mathbf{d})}{\partial d_i} \right.$$
$$\left. -(0.5 - \gamma + \eta) \left(\Delta t\right)^2 \frac{\partial \mathbf{f}(t_{j-2}, \mathbf{d})}{\partial d_i} + \frac{\partial \underline{\underline{\mathbf{B}}}(\mathbf{d})}{\partial d_i} \cdot \mathbf{u}(t_{j-1}, \mathbf{d}) + \frac{\partial \underline{\underline{\mathbf{E}}}(\mathbf{d})}{\partial d_i} \cdot \mathbf{u}(t_{j-2}, \mathbf{d}) \right]$$
$$+ \boldsymbol{\lambda}_n^{\mathrm{T}} \left[\underline{\underline{\mathbf{B}}}(\mathbf{d}) \cdot \frac{\partial \mathbf{u}(0, \mathbf{d})}{\partial d_i} + \underline{\underline{\mathbf{E}}}(\mathbf{d}) \cdot \frac{\partial \mathbf{u}(t_{-1}, \mathbf{d})}{\partial d_i} \right] + \boldsymbol{\lambda}_{n-1}^{\mathrm{T}} \left[\underline{\underline{\mathbf{E}}}(\mathbf{d}) \cdot \frac{\partial \mathbf{u}(0, \mathbf{d})}{\partial d_i} \right] \tag{5.40}$$

where $\boldsymbol{\lambda}_{n-j+1}$ denotes the adjoint variable vector. $\underline{\underline{\mathbf{A}}}(\mathbf{d})$, $\underline{\underline{\mathbf{B}}}(\mathbf{d})$, and $\underline{\underline{\mathbf{E}}}(\mathbf{d})$ represent followings respectively:

$$\begin{aligned} \underline{\underline{\mathbf{A}}}(\mathbf{d}) &= \mathbf{M}(\mathbf{d}) + \gamma \Delta t \cdot \mathbf{C}(\mathbf{d}) + \eta \left(\Delta t\right)^2 \mathbf{K}(\mathbf{d}) \\ \underline{\underline{\mathbf{B}}}(\mathbf{d}) &= -2\mathbf{M}(\mathbf{d}) + (1 - 2\gamma) \Delta t \mathbf{C}(\mathbf{d}) + (0.5 + \gamma - 2\eta) \left(\Delta t\right)^2 \mathbf{K}(\mathbf{d}) \\ \underline{\underline{\mathbf{E}}}(\mathbf{d}) &= \mathbf{M}(\mathbf{d}) + (\gamma - 1) \Delta t \mathbf{C}(\mathbf{d}) + (0.5 - \gamma + \eta) \left(\Delta t\right)^2 \mathbf{K}(\mathbf{d}) \end{aligned} \tag{5.41}$$

5.4.3. Sensitivity analysis of first-passage probability in RBTO

Sensitivity analysis of first-passage probability in stochastic *topology* optimization is similar to the derivation for RBDO described above. The main difference of sensitivity analysis in topology optimization comes from the projection method to obtain the filtered density as shown below.

$$\begin{aligned} &\frac{\partial P_{fp}(E_{sys})}{\partial d_i} = \frac{\partial \left(1 - \Phi_n\left[\boldsymbol{\beta}, \mathbf{R}\right]\right)}{\partial d_i} = \sum_{j=1}^{n} \left(\frac{\partial \left(-\Phi_n\left[\boldsymbol{\beta}, \mathbf{R}\right]\right)}{\partial \beta_j} \cdot \frac{\partial \beta_j(\tilde{\boldsymbol{\rho}})}{\partial d_i} \right) \\ &= \sum_{j=1}^{n} \left(\frac{\partial \left(-\Phi_n\left[\boldsymbol{\beta}, \mathbf{R}\right]\right)}{\partial \beta_j} \cdot \sum_{l=1}^{n_e} \left(\frac{\partial \beta_j(\tilde{\boldsymbol{\rho}})}{\partial \tilde{\rho}_l} \cdot \frac{\partial \tilde{\rho}_l}{\partial d_i} \right) \right) = \sum_{j=1}^{n} \left(\frac{\partial \left(-\Phi_n\left[\boldsymbol{\beta}, \mathbf{R}\right]\right)}{\partial \beta_j} \cdot \left(\mathbf{P}\right)_{li}^{\mathrm{T}} \frac{\partial \beta_j(\tilde{\boldsymbol{\rho}})}{\partial \tilde{\boldsymbol{\rho}}} \right) \\ &= \left(\mathbf{P}\right)_{li}^{\mathrm{T}} \sum_{j=1}^{n} \left(\frac{\partial \left(-\Phi_n\left[\boldsymbol{\beta}, \mathbf{R}\right]\right)}{\partial \beta_j} \cdot \frac{\partial \beta_j(\tilde{\boldsymbol{\rho}})}{\partial \tilde{\boldsymbol{\rho}}} \right) \end{aligned} \tag{5.42}$$

where $\mathbf{P}^{\mathrm{T}}$ is the transpose of the filtering matrix in Equation 5.16. Thus,

$$\frac{\partial P_{fp}(E_{sys})}{\partial \mathbf{d}} = \mathbf{P}^{\mathrm{T}} \sum_{j=1}^{n} \left(\frac{\partial \left(-\Phi_n\left[\boldsymbol{\beta}, \mathbf{R}\right]\right)}{\partial \beta_j} \cdot \frac{\partial \beta_j(\tilde{\boldsymbol{\rho}})}{\partial \tilde{\boldsymbol{\rho}}} \right) \tag{5.43}$$

where the partial derivative of $\beta_j(\cdot)$ with respect to an element density can be computed as explained in Sections 5.4.1 and 5.4.2.

5.4.4. Verification of calculated sensitivity

The adjoint sensitivity method derived for the first-passage probability constraints is tested through comparison with the finite difference method to verify accuracy and efficiency. Sensitivity analysis is performed for the 2-Bar truss example in Figure 5.2 in which the constraint is given on the first-passage probability of a stress limit and a drift ratio limit.

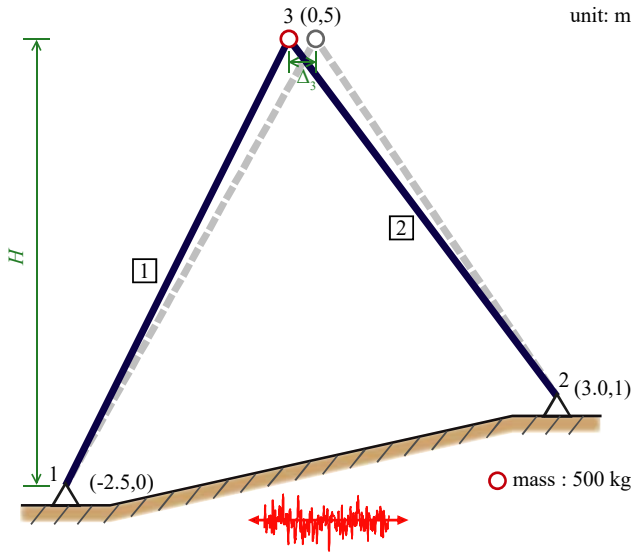

Figure 5.2: 2-Bar truss example used for testing the adjoint sensitivity formulation.

The stochastic seismic acceleration $f(t)$ is modeled as a filtered white-noise process using the Kanai-Tajimi filter model with the intensity Φ_0 (Clough and Penzien 1993; Fujimura and Der Kiureghian 2007). The unit-impulse response function of the filter and the effective force vector caused by the earthquake excitation are determined as follows, respectively:

$$h_f^{\mathrm{KT}}(t) = \exp(-\zeta_f \omega_f t)\left[\frac{(2\zeta_f^2 - 1)\omega_f}{\sqrt{1-\zeta_f^2}}\sin(\omega_f\sqrt{1-\zeta_f^2}\cdot t) - 2\zeta_f\omega_f\cos(\omega_f\sqrt{1-\zeta_f^2}\cdot t)\right] \tag{5.44}$$

$$\mathbf{f}(\mathbf{d},t) = -\mathbf{M}(\mathbf{d})\mathbf{l}f(t) = -\mathbf{M}(\mathbf{d})\mathbf{l}\cdot\left(\int_0^t h_f^{\mathrm{KT}}(t-\tau)W(\tau)d\tau\right) \tag{5.45}$$

Table 5.1 summarizes the Kanai-Tajimi filter parameters of dominant frequency ω_f and bandwidth ζ_f, time interval of interest, and the threshold value of the drift ratio and stress at each time point. The cross sectional area of each bar is 0.2 m^2. Young's modulus E = 20,000 MPa and mass density ρ_m= 2,400 kg/m^3 are used as material properties. The sensitivity values calculated by the derived adjoint method shows a good agreement with those by the FDM as shown in Tables 5.2 and 5.3.

In addition, the adjoint sensitivity method is tested for the topology optimization problem in Figure 5.3 (a). The sensitivities of the first-passage probability with respect to the design variables located at the three points A, B and C in Figure 5.3 (a) are computed by the proposed adjoint method and the FDM, respectively. The structural columns represented by two vertical lines in Figure 5.3 (a) are modeled by frame elements. Young's modulus E = 21,000 MPa and mass density ρ_m = 2,400 kg/m^3 are used as material properties for both the quadrilateral and frame elements. The instantaneous failure event at a discretized time point is considered in terms of an averaged drift ratio evaluated at two nodes of interest. Thus, the first-passage event is defined as

$$E_{sys} = \bigcup_{k=1}^{n} E_{f_{\Delta i}}(t_k, \tilde{\boldsymbol{\rho}}) = \bigcup_{k=1}^{n} \left(u_{0\Delta} - \frac{(\mathbf{a}(t_k, \tilde{\boldsymbol{\rho}})_{Left}^{\mathrm{T}} + \mathbf{a}(t_k, \tilde{\boldsymbol{\rho}})_{Right}^{\mathrm{T}})\mathbf{v}}{2H} \leq 0 \right) \tag{5.46}$$

Table 5.1: Two-bar truss example (Figure 5.2): filtering parameters for ground excitations and threshold values of probabilistic constraints.

Φ_0	ω_f	ζ_f	t (sec)	Δt (sec)	σ_{0e}	$u_{0\Delta}$
100	5π	0.4	5	0.1	20 MPa	1/400

Table 5.2: Sensitivity comparison of first-passage probability on a stress constraint in 2-bar truss.

	FDM		AJM	
Δd	$\partial P_f/\partial d_1$	$\partial P_f/\partial d_2$	$\partial P_f/\partial d_1$	$\partial P_f/\partial d_2$
1×10^{-1}	-8.00×10^{-6}	3.50×10^{-5}		
1×10^{-2}	-5.80×10^{-5}	1.60×10^{-5}		
1×10^{-3}	-9.90×10^{-5}	1.40×10^{-5}		
1×10^{-4}	-1.06×10^{-4}	1.40×10^{-5}		
1×10^{-5}	-1.06×10^{-4}	1.40×10^{-5}		
1×10^{-6}	-1.06×10^{-4}	1.40×10^{-5}	-1.05×10^{-4}	1.40×10^{-5}
1×10^{-7}	-1.06×10^{-4}	1.40×10^{-5}		
1×10^{-8}	-1.06×10^{-4}	1.40×10^{-5}		
1×10^{-9}	-1.05×10^{-4}	1.40×10^{-5}		
1×10^{-10}	-1.04×10^{-4}	1.80×10^{-5}		
1×10^{-11}	-5.60×10^{-5}	1.10×10^{-5}		
1×10^{-12}	0.00	0.00		

Table 5.3: Sensitivity comparison of first-passage probability on a displacement constraint in 2-bar truss.

	FDM		AJM	
Δd	$\partial P_f/\partial d_1$	$\partial P_f/\partial d_2$	$\partial P_f/\partial d_1$	$\partial P_f/\partial d_2$
1×10^{-1}	-1.40×10^{-8}	-1.40×10^{-8}		
1×10^{-2}	-7.30×10^{-8}	-8.30×10^{-8}		
1×10^{-3}	-1.03×10^{-7}	-1.23×10^{-7}		
1×10^{-4}	-1.06×10^{-7}	-1.28×10^{-7}		
1×10^{-5}	-1.07×10^{-7}	-1.29×10^{-7}		
1×10^{-6}	-1.07×10^{-7}	-1.29×10^{-7}	-1.06×10^{-7}	-1.27×10^{-7}
1×10^{-7}	-1.05×10^{-7}	-1.30×10^{-7}		
1×10^{-8}	-8.90×10^{-8}	-1.00×10^{-7}		
1×10^{-9}	0.00	0.00		
1×10^{-10}	0.00	0.00		
1×10^{-11}	0.00	0.00		
1×10^{-12}	0.00	0.00		

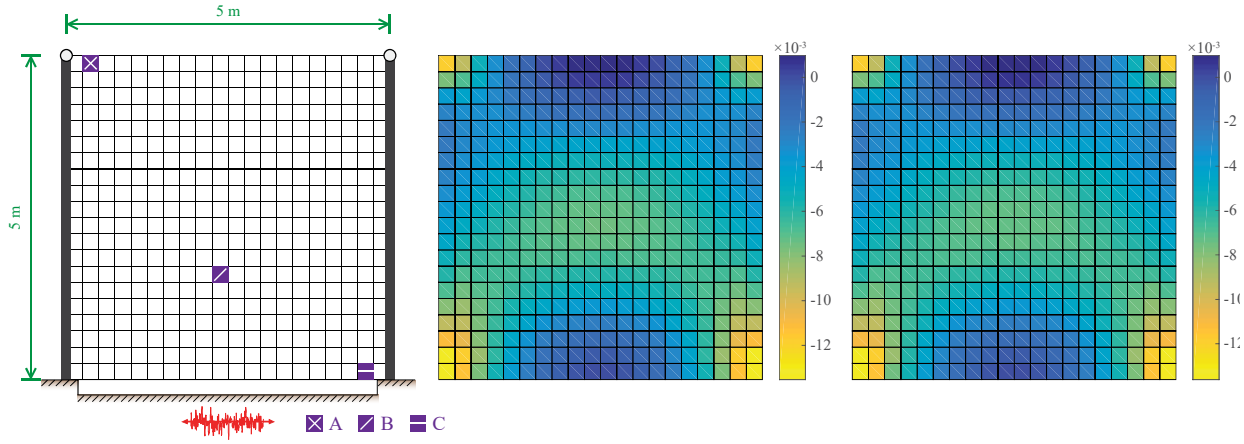

Figure 5.3: Sensitivity comparison: (a) geometry, loading condition, and locations where sensitivity are reported (Table 5.4), (b) sensitivities from the adjoint method (AJM), and (c) sensitivities from the finite difference method (FDM).

Table 5.4: Sensitivity comparison of first-passage probability on a displacement constraint in topology optimization.

	FDM			AJM		
Δd	$\partial P_f/\partial d_A$	$\partial P_f/\partial d_B$	$\partial P_f/\partial d_C$	$\partial P_f/\partial d_A$	$\partial P_f/\partial d_B$	$\partial P_f/\partial d_C$
1×10^{-1}	-0.000452	-0.000293	-0.000569			
1×10^{-2}	-0.000483	-0.000310	-0.000596			
1×10^{-3}	-0.000486	-0.000312	-0.000599			
1×10^{-4}	-0.000487	-0.000312	-0.000599			
1×10^{-5}	-0.000487	-0.000312	-0.000599			
1×10^{-6}	-0.000486	-0.000312	-0.000599	-0.000486	-0.000312	-0.000599
1×10^{-7}	-0.000485	-0.000309	-0.000598			
1×10^{-8}	-0.000479	-0.000301	-0.000619			
1×10^{-9}	-0.000444	-0.000391	-0.000632			
1×10^{-10}	0.000250	0.000289	-0.000012			
1×10^{-11}	-0.000166	-0.001532	-0.004141			
1×10^{-12}	0.050625	0.025424	0.036526			

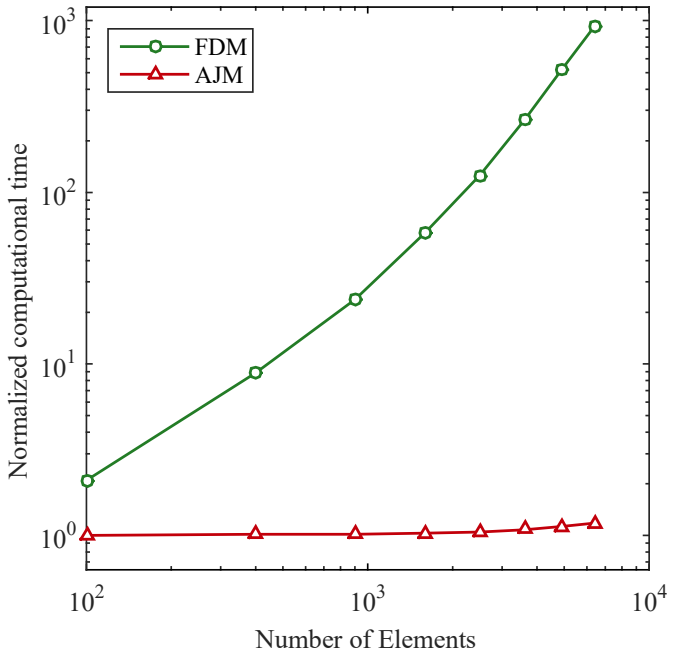

Figure 5.4: Computational time comparison for sensitivity analysis by the FDM and the AJM.

The sensitivities of the first-passage probability constraint in Equation 5.46 are shown in Figure 5.3 (b) and 5.3 (c), which show a good agreement. The sensitivities by the FDM employing a range of perturbations (from 10^{-1} to 10^{-12}) are tabulated in Table 5.4 for comparison with the results by the AJM, and the influence of the perturbation size on the results by the FDM. Figure 5.3 shows that sensitivities calculated by the FDM and the AJM match well. The computational costs by the two methods are compared in Figure 5.4 while varying the number of elements in the problem. The computational costs are normalized by that of the AJM for the 100-element case. It is noted that the proposed AJM requires dramatically less computational time than the FDM. It should be also noted that AJM does not require determining the perturbation size, for which an optimal choice is generally not known a priori. The complex-step derivative approximation (Martins et al. 2003) can alternatively be considered to avoid the loss of precision inherent in the FDM.

5.5. Numerical applications

5.5.1. Two dimensional bracing optimization

The proposed method is applied to identify optimal member sizes of a lateral bracing system subjected to a stochastic earthquake ground motion (See Figure 5.5). The formulation in Equation 5.12 is used with $d^{\text{lower}} = 0.02$ m^2, while the volume of the design domain is considered as the objective function. Three types of probabilistic constraints associated with the first-passage probability (Case I - compressive stress and Case II – maximum (tip) drift ratio (at node 13 and 14) and story drift ratios) are considered in optimization respectively. The stochastic seismic excitation $f(t)$ is modeled as a filtered white-noise process using the Kanai-Tajimi filter model with the intensity Φ_0. The lateral bracing system shown in Figure 5.5 is modeled with truss elements.

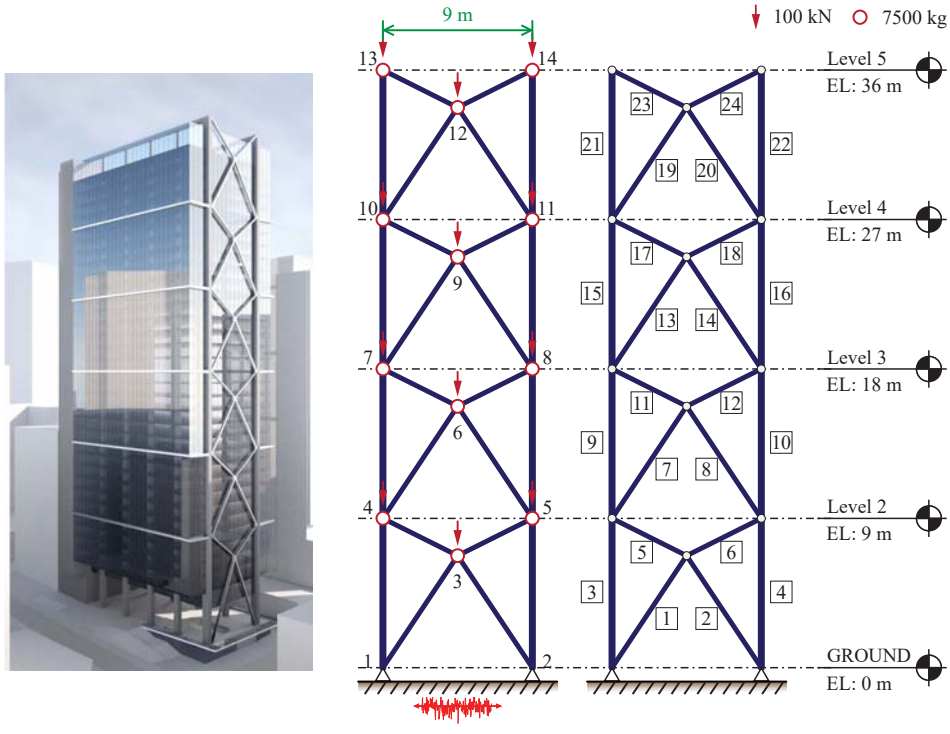

Figure 5.5: (a) Rendering of a bracing system (image courtesy of Skidmore, Owings & Merrill, LLP), (b) design geometry, boundary and loading conditions, and (c) element numbering.

Young's modulus E = 21,000 MPa and density ρ_m = 2,400 kg/m^3 are used as material properties. The damping matrix is constructed using the Rayleigh damping model. Table 5.5 summarizes the parameter values used for the optimization. An additional mass at each node is applied to represent a non-structural mass such as a cladding, and static vertical forces are applied as shown in Figure 5.5 (b). The structural optimization is performed with the method of moving asymptotes (MMA; Svanberg 1987) for three different target reliability indices.

Table 5.5: Parameters for a filter of ground motion model and constraints in optimization (2D bracing optimization example).

Case	Φ_0	ω_f	ζ_f	t (sec)	Δt (sec)	Initial cross section areas (m^2)	Threshold value
I	0.2	5π	0.4	6.0	0.10	0.5	σ_{0e} = 35 MPa
II	1	5π	0.4	6.0	0.06	0.3	$u_{0\Delta}$ = 1/50
III	1	5π	0.4	6.0	0.06	0.3	$u_{0\Delta i}$ = 1/50, i=1,2,3,4

5.5.1.1. Case I: Stress constraint

A probabilistic constraint on the first-passage probability is employed for the stress time history of each element. Figure 5.6 shows the sizes of the truss elements after optimization based on three different target first-passage failure probabilities. Because the axial forces in vertical members at the lowest level are greater than others during the ground excitation, the sizes of element 3 and 4 are largest. The convergence history of the objective function and the first-passage probability of selected elements over iterations are plotted in Figure 5.7. The proposed method facilitates finding optimal member sizes satisfying target failure probabilities under random ground motions during the preliminary design stage. To investigate the performance of the optimized system, the stress time histories of the optimized structure under a randomly generated earthquake ground motion are compared with time histories with those of the initial structure (Figure 5.8). The amplitudes of the stress time histories are reduced such that the likelihood of exceeding the threshold values

(dashed line) is below the target probability. In particular, a dramatic reduction of gap between the maximum and the minimum stress is observed at element 3. It is also noteworthy that, after optimization, stress time histories in bars are more uniform compared to the various stress levels observed in the initial structure.

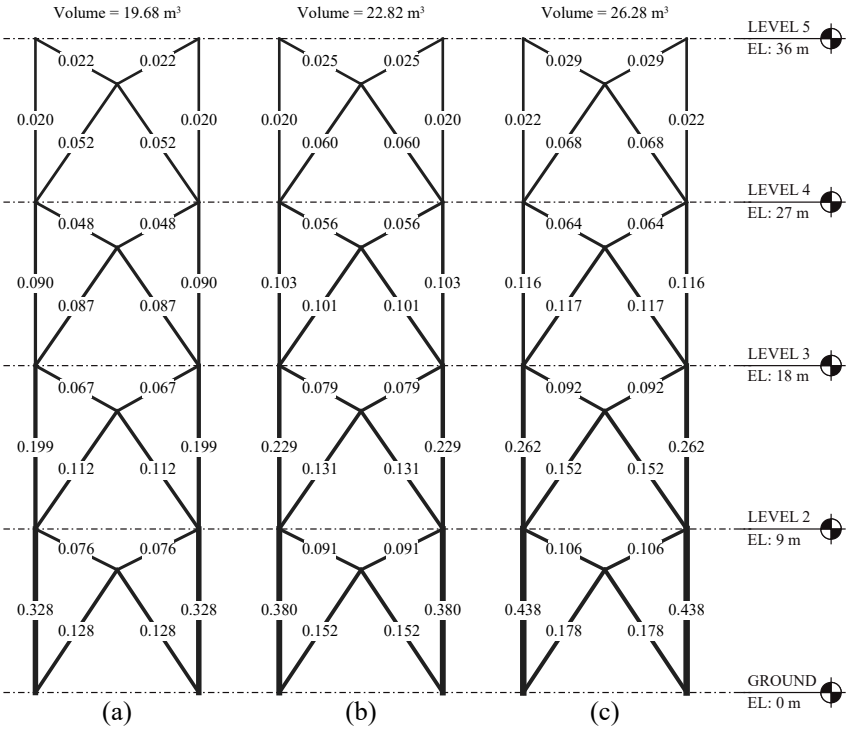

Figure 5.6: Optimal truss member sizes under constraints on first-passage probabilities of stress time histories: (a) $\beta^{target} = 1.5$ ($P_f^{target} = 0.0668$), (b) $\beta^{target} = 2.0$ ($P_f^{target} = 0.0228$), and (c) $\beta^{target} = 2.5$ ($P_f^{target} = 0.0062$).

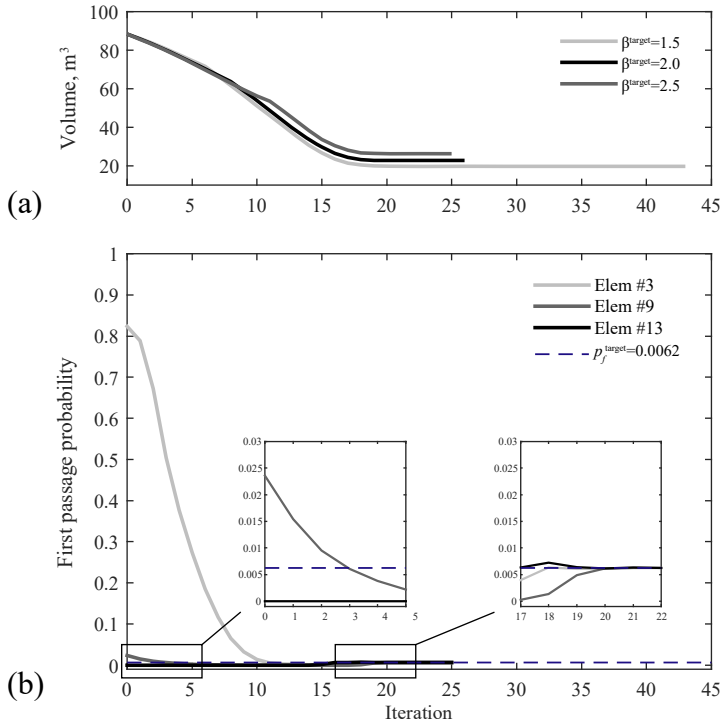

Figure 5.7: Convergence histories of (a) the volume, and (b) first-passage probabilities of element #3, #9 and #13 with $\beta^{target} = 2.5$ ($P_f^{target} = 0.0062$).

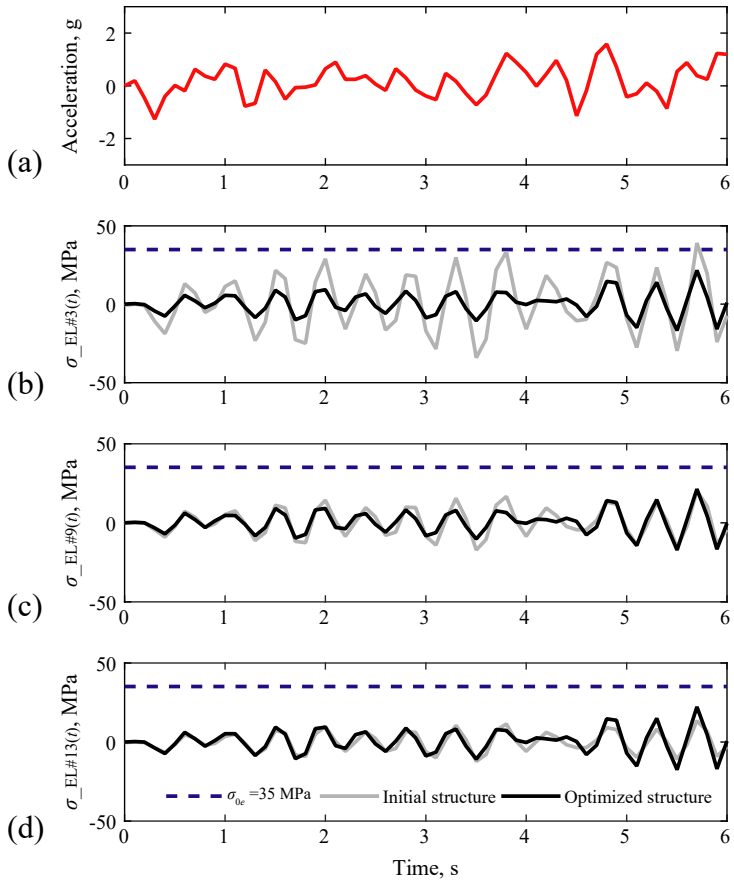

Figure 5.8: Investigation of dynamic performances of optimized systems: (a) randomly generated input ground acceleration used for the test. Comparison between dynamic responses (stresses) of the initial system and the optimized system ($\beta^{target} = 2.5$ ($P_f^{target} = 0.0062$)): (b) element #3, (c) element #9, and (d) element #13.

5.5.1.2. Case II: Maximum (tip) drift ratio constraint

A maximum tip drift ratio which is evaluated at node 13 and 14 is utilized for computing first-passage failure probability. Optimization results shown in Figure 5.9 indicate that the increase in ratios of vertical members is significant especially for the bottom level as the target failure probability is reduced, which is related to the decrease of the tip drift ratio. Furthermore, varying target failure probability leads to significant changes in the size ratio of a vertical element to a bracing element, which indicates that the target reliability level affects relative contributions from vertical elements and bracings in the optimal structural system. The convergence time histories of the objective function (volume) and the first-passage probabilities in Figure 5.10 show that the proposed method can achieve target failure probabilities while minimizing volumes. The structural optimization reduces dynamic drift ratios (Figure 5.11) although the volume has been significantly reduced (Figure 5.10).

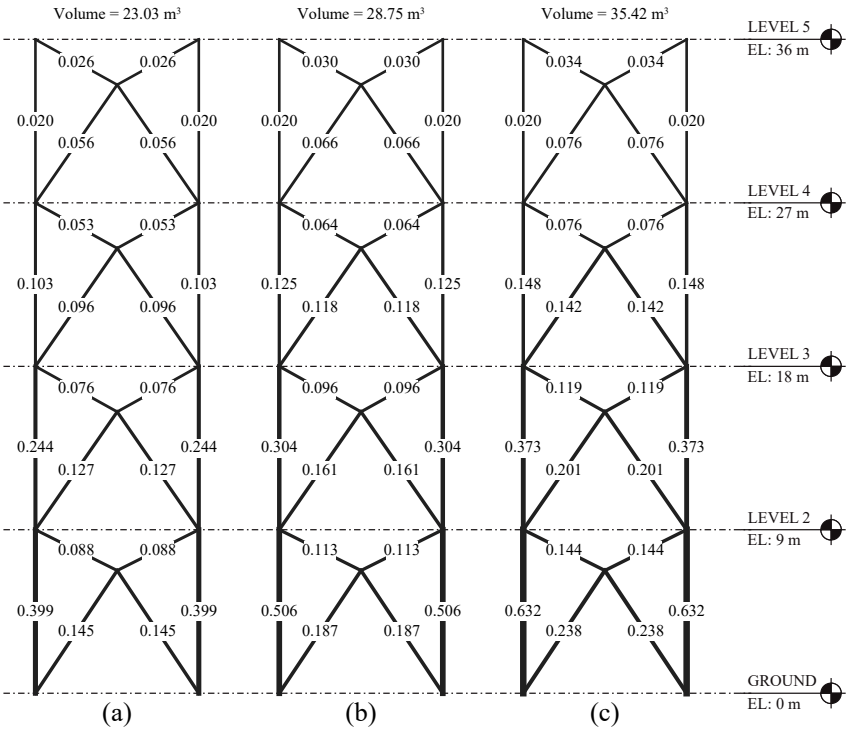

Figure 5.9: Optimal truss member sizes under first-passage probability for tip drift ratio constraint: (a) $\beta^{target} = 1.5$ ($P_f^{target} = 0.0668$), (b) $\beta^{target} = 2.5$ ($P_f^{target} = 0.0062$), and (c) $\beta^{target} = 3.5$ ($P_f^{target} = 0.00023$).

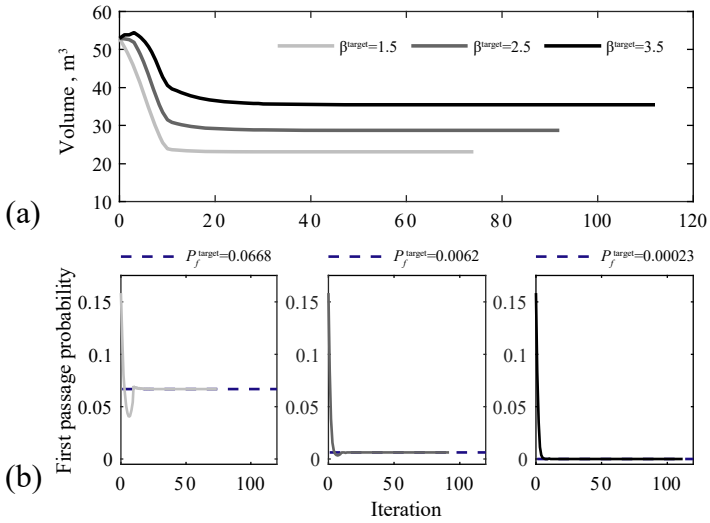

Figure 5.10: Convergence history: (a) volume, and (b) first-passage probabilities of tip drift ratio with $\beta^{target} = 1.5$ ($P_f^{target} = 0.0668$), $\beta^{target} = 2.5$ ($P_f^{target} = 0.0062$), and $\beta^{target} = 3.5$ ($P_f^{target} = 0.00023$).

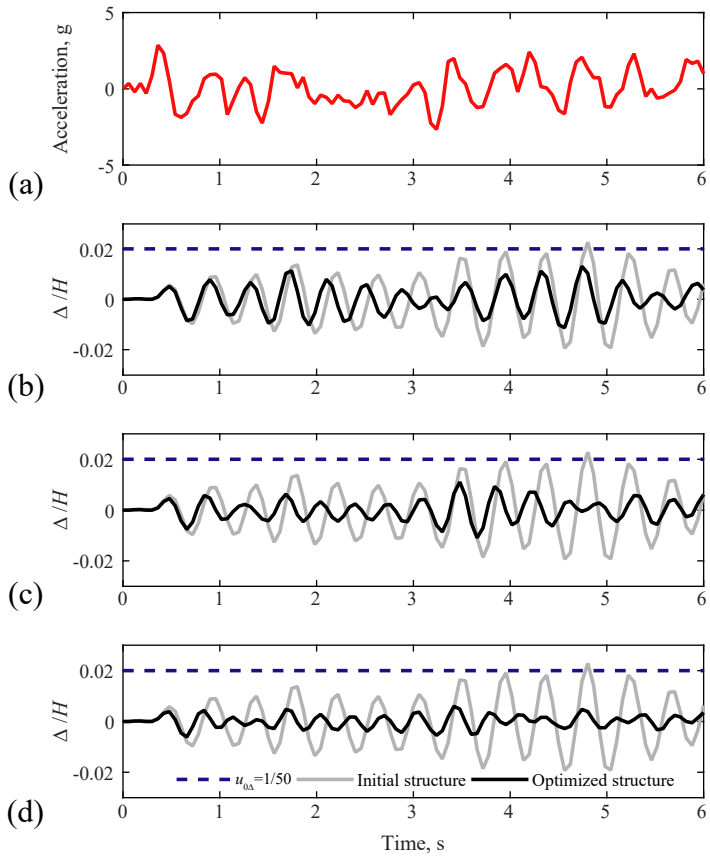

Figure 5.11: Investigation of dynamic performances of optimized systems: (a) randomly generated input ground acceleration used for the test, and comparison between dynamic responses (tip drift ratios) of the initial and the optimized systems for (b) $\beta^{target} = 1.5$ ($P_f^{target} = 0.0668$), (c) $\beta^{target} = 2.5$ ($P_f^{target} = 0.0062$), and (d) $\beta^{target} = 3.5$ ($P_f^{target} = 0.00023$).

5.5.1.3. Case III: Inter-story drift ratio constraints

This case considers the inter-story drift ratio for each floor in calculating the first-passage probability. Optimal member sizes for three different target failure probabilities are shown in Figure 5.12. First-passage failure probabilities of inter-story drift ratios (Δ_i/H_i, i = 2,…,5) in the initial structure are 3.1×10^{-8}, 0.15, 0.61, and 0.68, respectively. After optimization, the first-passage probabilities are converged to the target failure probabilities as shown in Figure 5.13, except for the bottom level which is excluded due to the low likelihood of such failure at the bottom level (which is, of course, a feasible solution). Vertical elements at lower levels are still important because they make significant contributions to the control of inter-story drift ratios as shown in Figure 5.12. Compared to the results from Case II, bracings in the case have less impact on controlling dynamic behaviors. Finally, Figure 5.14 shows the significant reduction of inter-story drift ratios in the optimized structure compared to that of the initial structure.

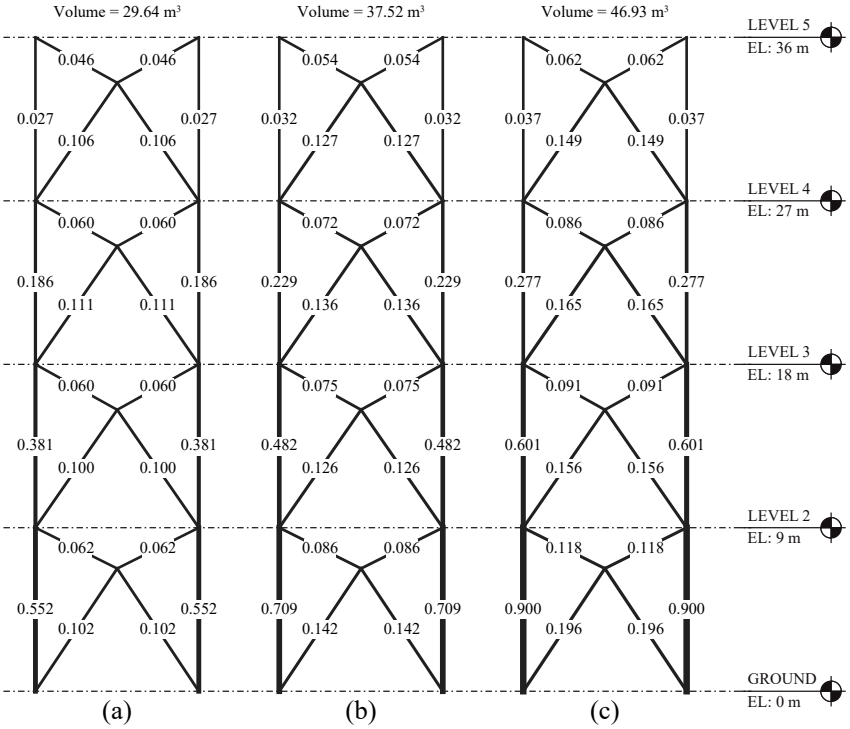

Figure 5.12: Optimal truss member sizes under first-passage probabilities for inter-story drift ratio constraints: (a) $\beta^{target} = 1.5$ ($P_f^{target} = 0.0668$), (b) $\beta^{target} = 2.5$ ($P_f^{target} = 0.0062$), and (c) $\beta^{target} = 3.5$ ($P_f^{target} = 0.00023$).

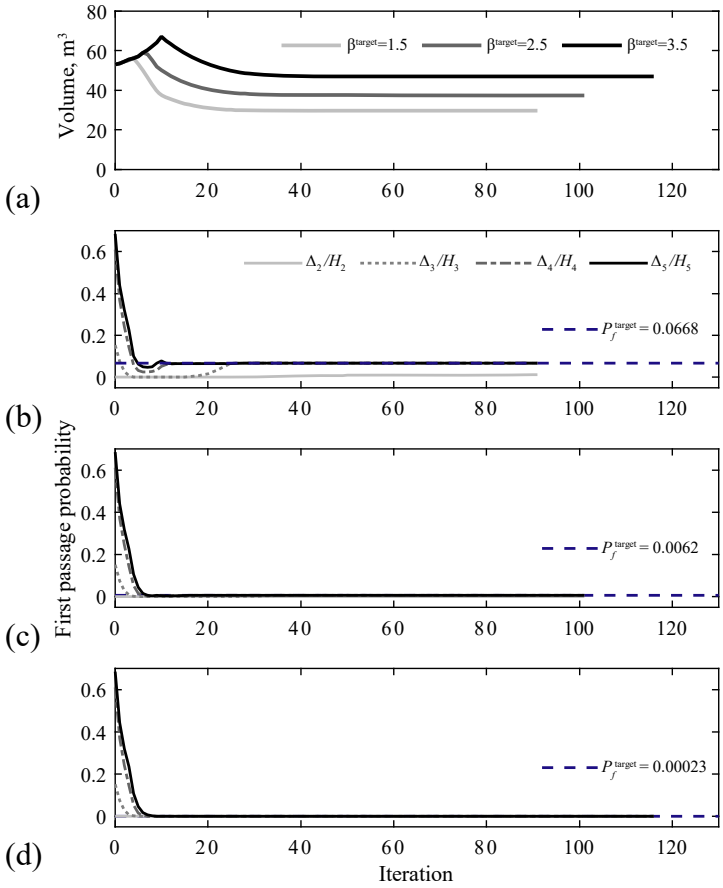

Figure 5.13: Convergence history: (a) volume, and first-passage probabilities of floors with (b) $\beta^{target} = 1.5$ ($P_f^{target} = 0.0668$), (c) $\beta^{target} = 2.5$ ($P_f^{target} = 0.0062$), and (d) $\beta^{target} = 3.5$ ($P_f^{target} = 0.00023$).

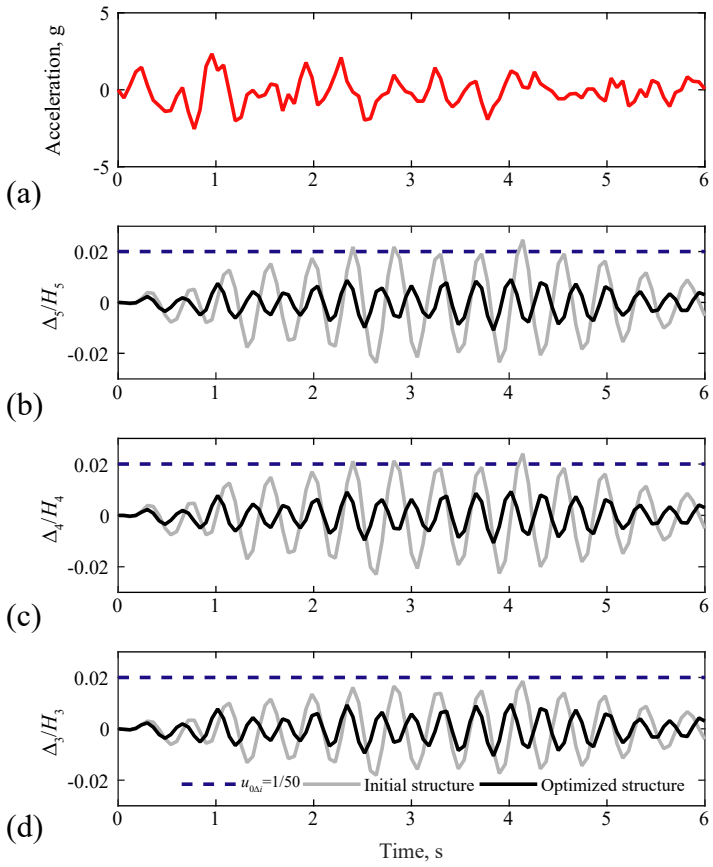

Figure 5.14: Investigation of dynamic performances of optimized systems: (a) randomly generated input ground acceleration used for the test and (b)-(d) comparison between dynamic responses (inter-story drift ratios) of the initial and the optimized system ($\beta^{target} = 3.5$ ($P_f^{target} = 0.00023$)).

5.5.2. Space truss dome optimization

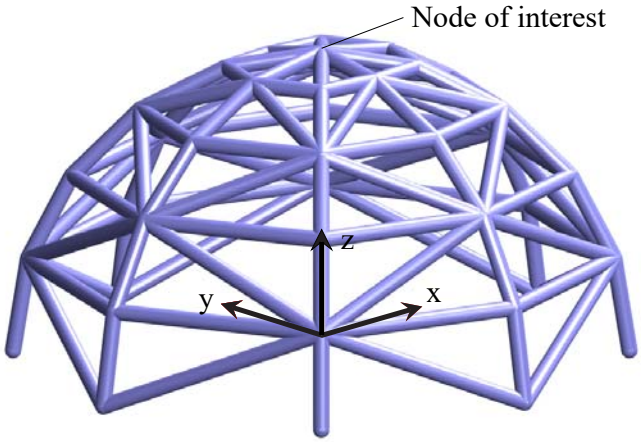

Figure 5.15: A space truss dome example.

In this example, the weight of an asymmetric space truss dome composed of 104 elements (Figure 5.15) is minimized under constraints on the first-passage probability of the drift ratios evaluated at the node of interest, the highest elevation. The basic grid of the structure, plan view and section views are provided in Figure 5.16. Figure 5.17 shows the element numbering choices of the space truss dome. At each node of the structure, additional masses (10,000 kg) representing non-structural masses such as claddings are equally applied. Young's modulus E = 210 GPa and mass density ρ_m = 7,850 kg are used as material properties for each truss element. The ground acceleration is generated by using the Kanai-Tajimi filter. The filter and optimization parameters are presented in Table 5.6. The probabilistic constraint is defined in terms of the tip drift ratio evaluated at the top (z = 15 m). For a loading scenario, two direction components of earthquake ground excitations at angles (θ_{g1}, θ_{g2}) shown in Figure 5.16 (b) are considered simultaneously and applied to the structure. The target failure probability and a lower bound of design variables are set to $P_f^{\text{target}} = 0.0013$ ($\beta_f^{\text{target}} = -\Phi[P_f^{\text{target}}]^{-1} = 3.0$) and 0.02 m^2. The optimization formulation considering multiple ground accelerations with constraints on drift ratios in both x- and y-directions is developed as

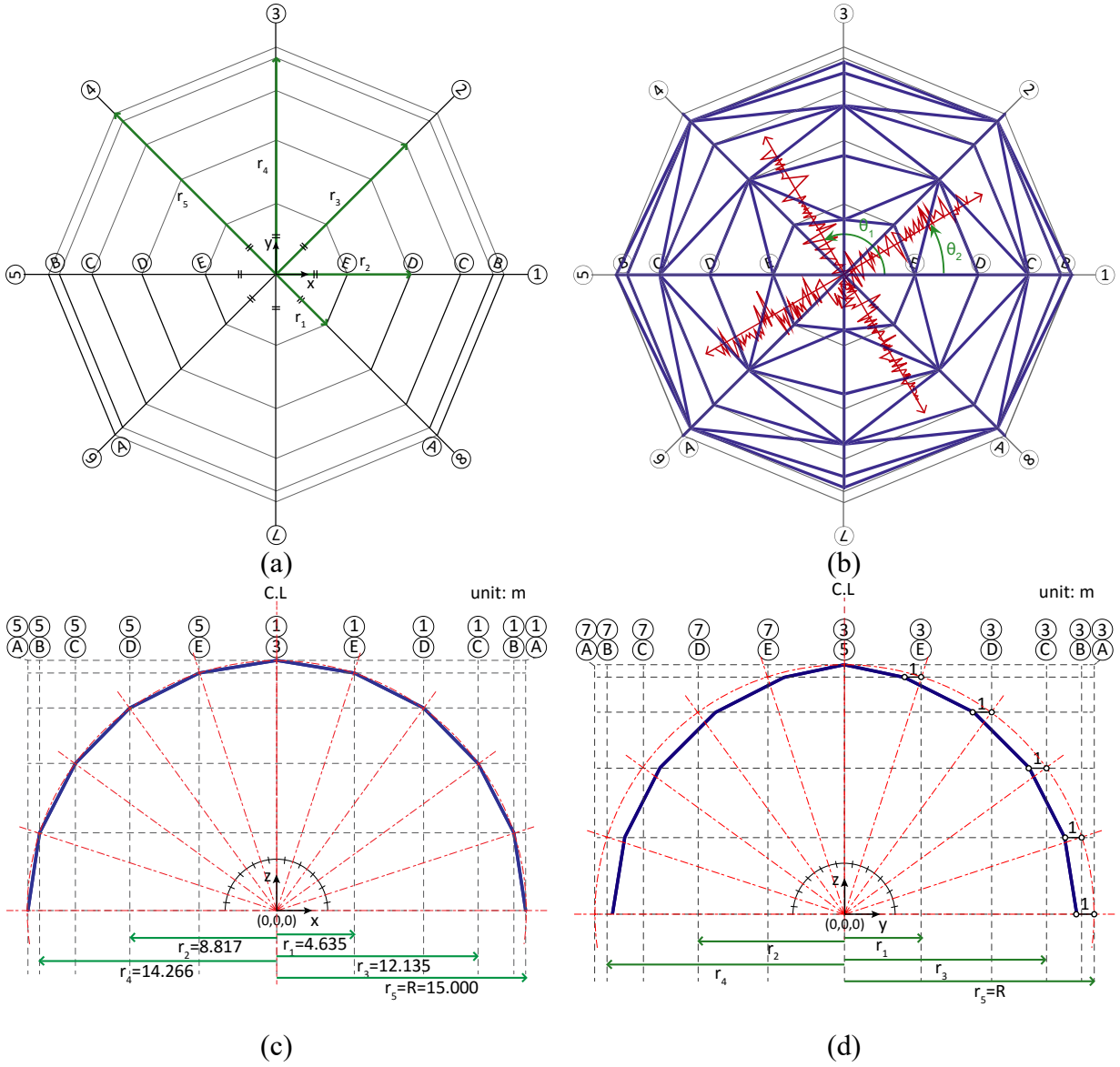

Figure 5.16: Geometry of a space truss dome: (a) basic grid, (b) plan view and directions of applied ground accelerations, (c) section view along grid line 1-5, and (d) section view along grid line 3-7.

Table 5.6: Parameters for filters of ground motion models and constraints in optimization (space truss dome optimization example).

Φ_{0_g1}	Φ_{0_g2}	ω_f	ζ_f	t (sec)	Δt (sec)	Initial cross section areas (m^2)	Threshold value
4.0	3.0	5π	0.4	6.0	0.06	0.25	$u_{0\Delta x} = 1/800$ $u_{0\Delta y} = 1/800$

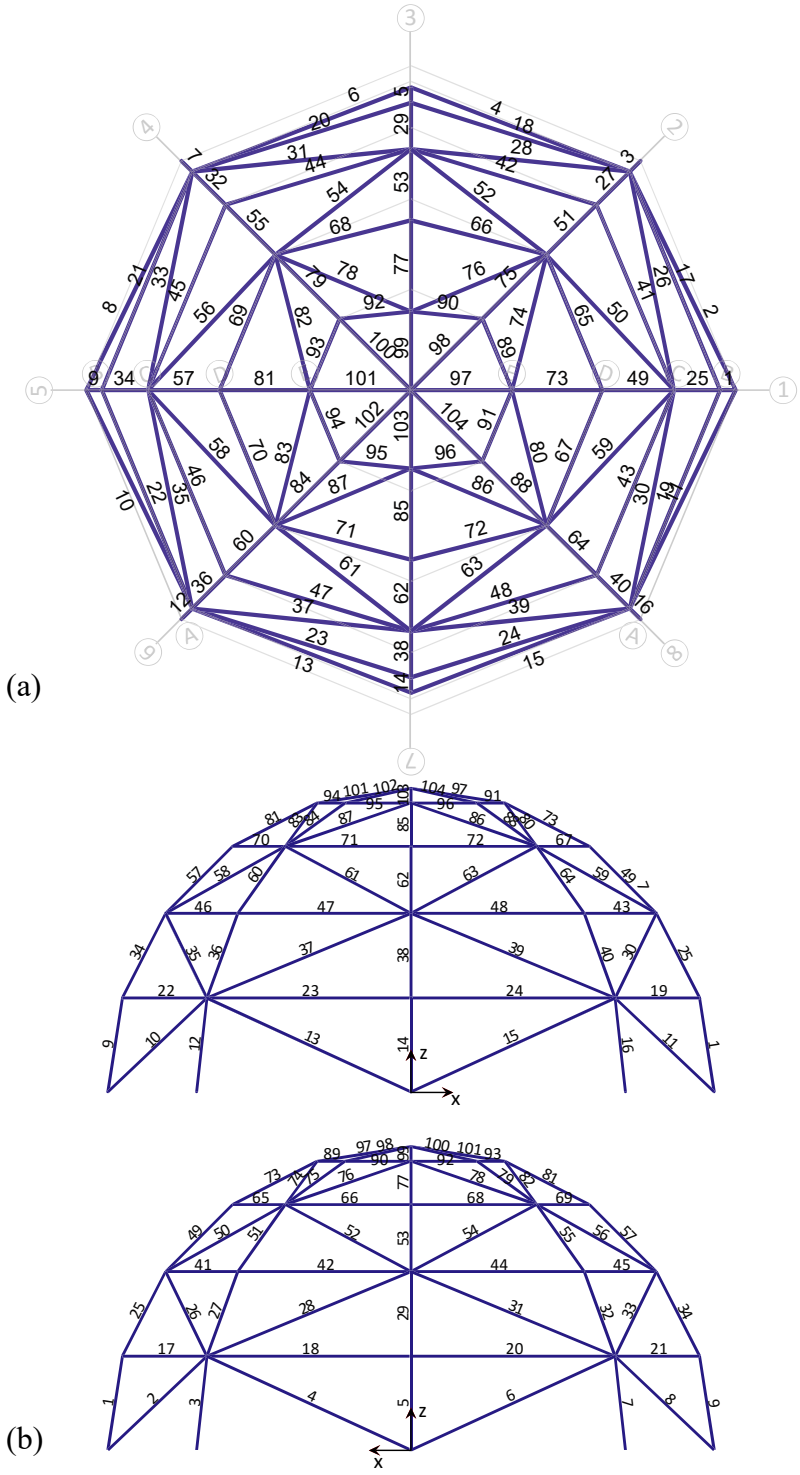

Figure 5.17: Element numbering choices of the space truss dome: (a) top view, (b) section views.

$$
\begin{aligned}
&\min_{\mathbf{d}} \; f_{obj}(\mathbf{d}) \\
&s.t \quad P_{fp,x-\mathrm{dir}}\left(\bigcup_{k=1}^{n}\left(E_{f_{\mathrm{x}}}(t_k,\mathbf{d}) : g_{\mathrm{x}}(t_k,\mathbf{d}) \le 0\right)\right) \le P_{f_{\text{x-dir}}}^{\text{target}} \\
&\qquad P_{fp,y-\mathrm{dir}}\left(\bigcup_{k=1}^{n}\left(E_{f_{\mathrm{y}}}(t_k,\mathbf{d}) : g_{\mathrm{y}}(t_k,\mathbf{d}) \le 0\right)\right) \le P_{f_{\text{y-dir}}}^{\text{target}} \qquad (5.47) \\
&\qquad 0.02 \text{ m}^2 \le \mathbf{d} \le 1.5 \text{ m}^2 \\
&\text{with } \mathbf{M}(\mathbf{d})\ddot{\mathbf{u}}(t,\mathbf{d}) + \mathbf{C}(\mathbf{d})\dot{\mathbf{u}}(t,\mathbf{d}) + \mathbf{K}(\mathbf{d})\mathbf{u}(t,\mathbf{d}) = -\mathbf{M}(\mathbf{d})\mathbf{l}(\theta_{g1}) f_{g1}(t) - \mathbf{M}(\mathbf{d})\mathbf{l}(\theta_{g2}) f_{g2}(t)
\end{aligned}
$$

Figure 5.18 shows that the space truss domes optimized with fixed θ_{g1} while varying θ_{g2} to three different angles. Optimal results from the case of the applied ground acceleration with $\theta_{g1} = 0°$, $\theta_{g2} = 90°$ show that the cross- sectional areas of bracings and vertical elements, especially at a lower level, are increased in order to reduce displacements in both x- and y-directions and failure probabilities. In addition, by getting the angle θ_{g2} closer to θ_{g1}, the optimal volume is getting higher. By changing θ_{g2} from 90° to 60° (or 30°), the increase in the failure probability in the x-direction is much higher than the decrease in the failure probability in the y-direction. The optimized area of each element are plotted in Figure 5.19. As expected, truss members, which are closely aligned to the applied ground accelerations are enlarged especially for lower levels. Thus, truss members are sized more symmetrically in both x- and y- directions for ground accelerations with $\theta_{g1} = 0°$, $\theta_{g2} = 90°$ compared to $\theta_{g2} = 30°$ or $\theta_{g2} = 60°$. Figure 5.20 shows convergence histories of the volume and the first-passage probability. The proposed method enables achieving the target failure probability with reduced volumes. The comparison of dynamic responses of the initial structure and the optimized structure are shown in Figure 5.21 under randomly generated samples of ground excitations with the filter parameters reported in Table 5.6. Overall reductions in the drift ratio in the optimized structure are observed, which naturally reduces the likelihood of exceedance of the threshold value during the excitation.

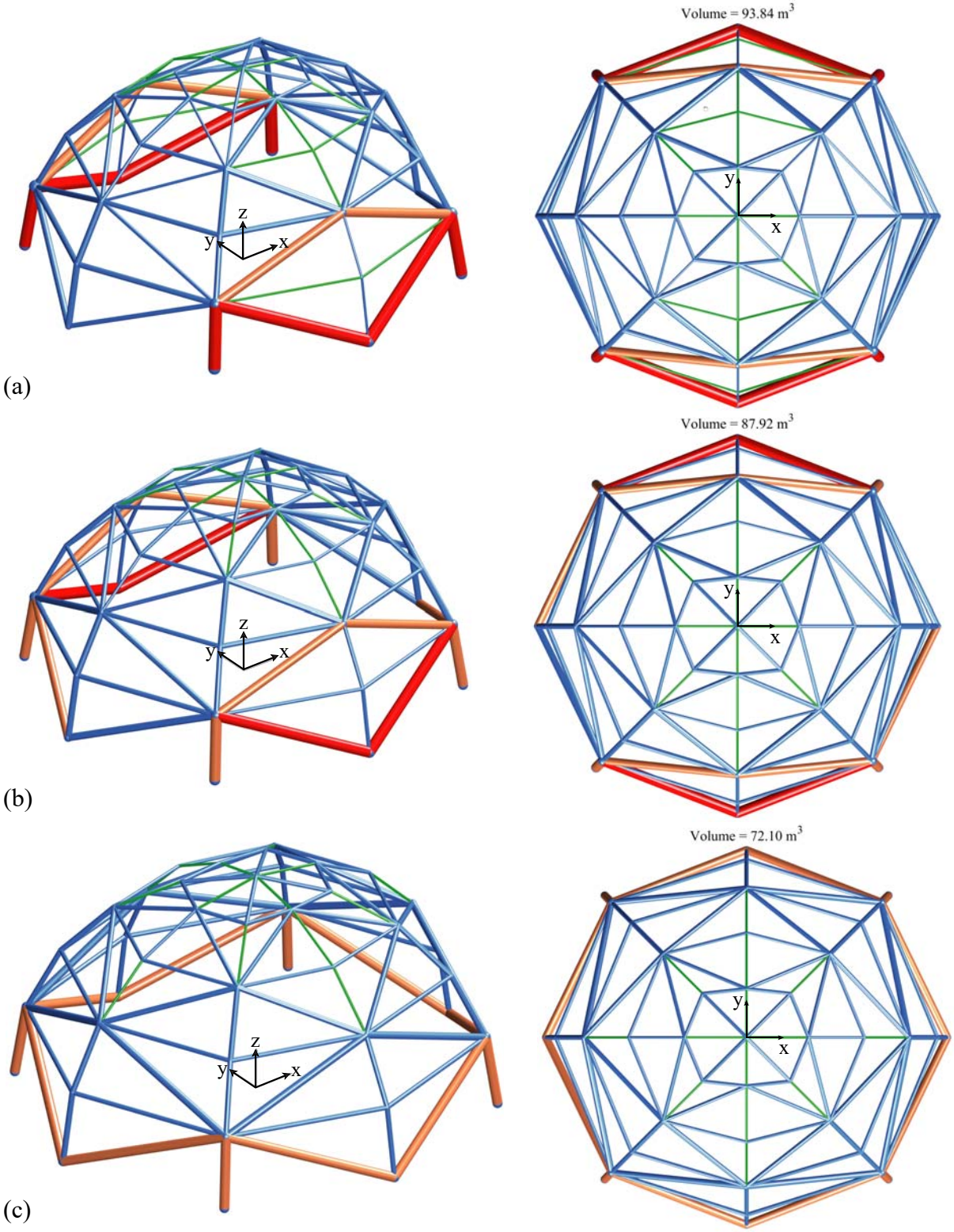

Figure 5.18: Optimized space truss dome corresponding to different angles of ground accelerations: (a) $\theta_{g1} = 0°$, $\theta_{g2} = 30°$, (b) $\theta_{g1} = 0°$, $\theta_{g2} = 60°$, (c) $\theta_{g1} = 0°$, $\theta_{g2} = 90°$. (Color legends: $A_i = A_{min}$ in green, $0.02\ m^2 < A_i \leq 0.2\ m^2$ in blue, $0.2\ m^2 < A_i \leq 0.4\ m^2$ in brown, $0.4\ m^2 < A$ in red).

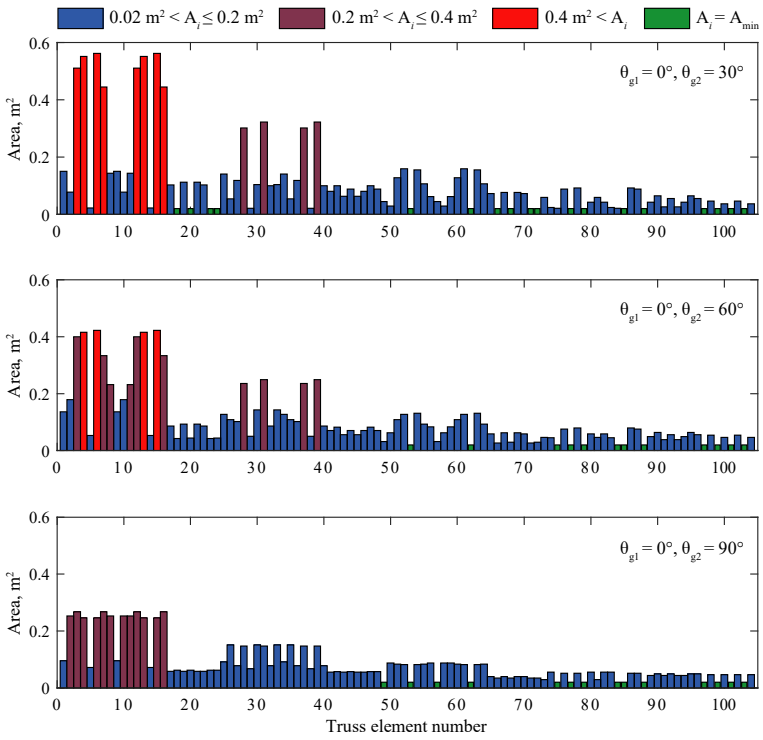

Figure 5.19: Optimized cross sectional areas of truss elements corresponding to the ground accelerations applied at different angles.

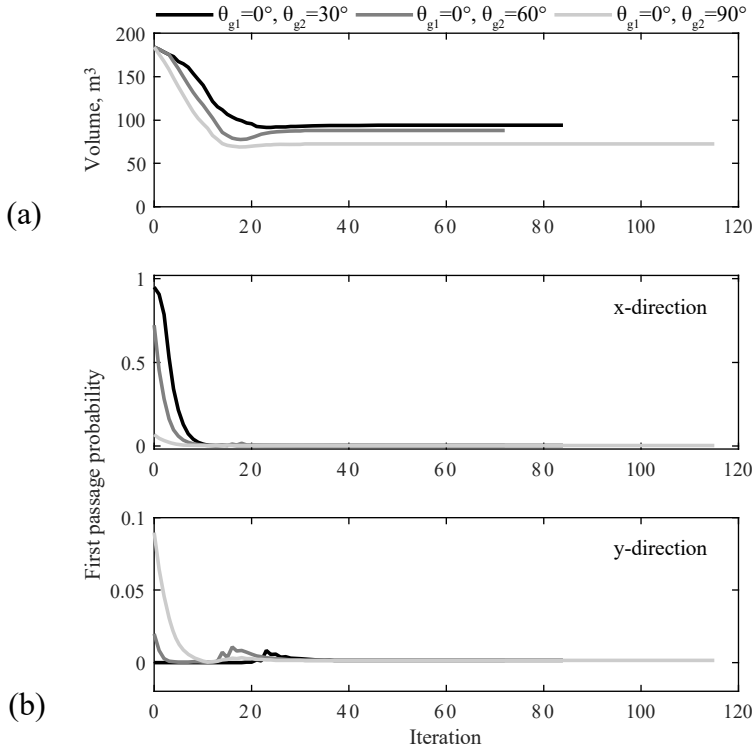

Figure 5.20: Convergence history: (a) volume, and (b) first-passage probability.

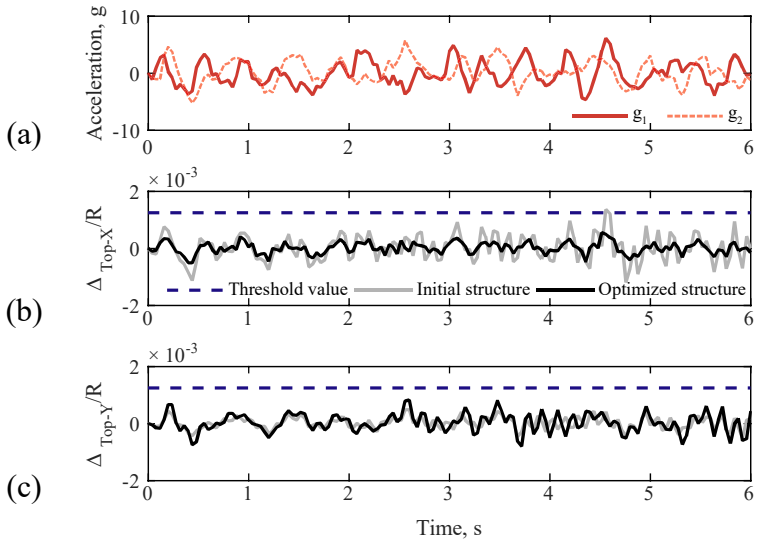

Figure 5.21: Comparison between dynamic responses by the initial structure and the optimized structures: (a) randomly generated ground accelerations ($\theta_{g1} = 0°$, $\theta_{g2} = 30°$), (b) drift ratio in the *x*-direction, and (c) drift ratio in the *y*-direction.

5.5.3. Optimization of a bracing system using topology optimization

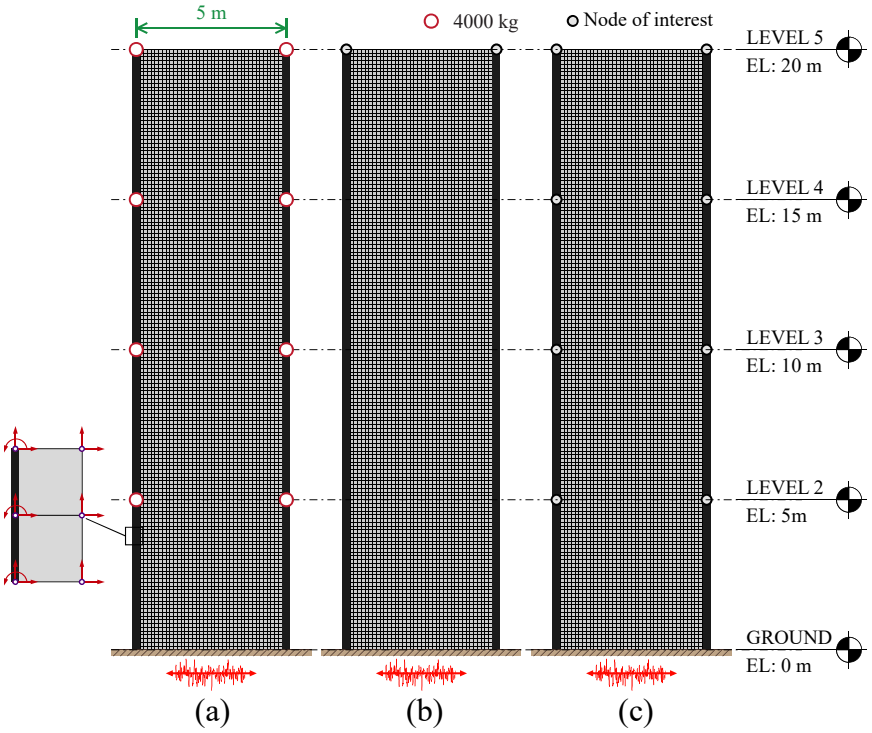

Figure 5.22: (a) Design domain and loading condition, (b) node of interest for a tip drift ratio constraint, and (c) nodes of interest for inter-story drift ratios.

The previous numerical application of the bracing system is considered as *size* optimization for a given structural layout. By contrast, *topology* optimization can identify the optimal bracing layout of a structure. To demonstrate this optimization under first-passage probability constraints, the proposed method is applied to the design domain under earthquake excitations as shown in Figure 5.22 (a). During the optimization for minimizing volume, the first-passage failures are defined in terms of inter-story drift ratios at each level and a tip drift ratio at the building height (see Figures 5.22 (b) and 5.22 (c)). The structural columns represented by two vertical lines shown in Figure 5.22 (a) are modeled by frame elements whose densities remain unchanged throughout the optimization process. Young's modulus E = 21,000 MPa and mass density ρ_m = 2,400 kg/m^3 are used as material properties for both the quadrilateral and frame elements. The additional mass of 4,000 kg is considered at each floor level as shown in Figure 5.22 (a). The damping matrix is constructed using a Rayleigh damping model with a 2 % damping ratio. Table 5.7 summarizes the

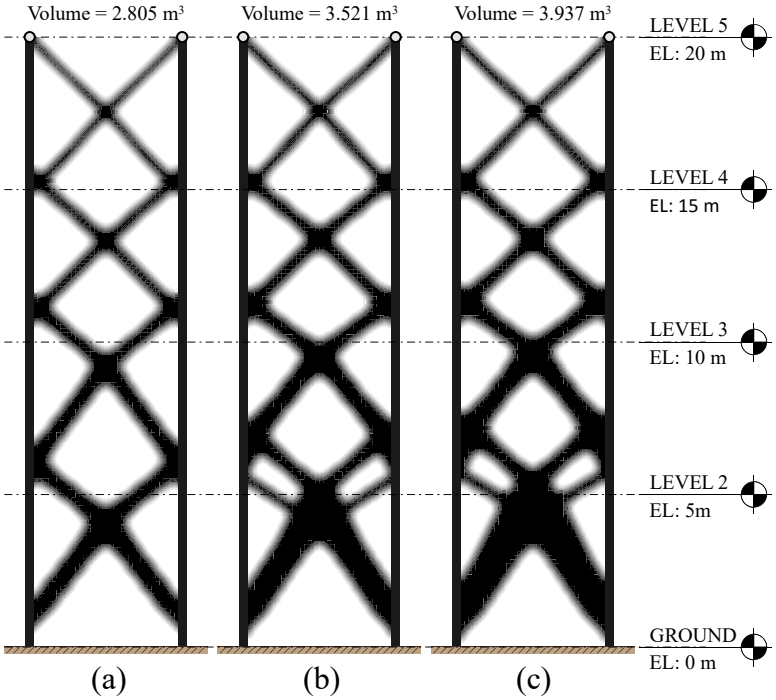

Figure 5.23: Topology optimization results from the four-story building example constrained by the first-passage probability in term of the tip drift ratio constraint: (a) $\beta^{target} = 1.5$, $P_f^{target} = 6.68$ %, (b) $\beta^{target} = 2.5$, $P_f^{target} = 0.62$ %, and (c) $\beta^{target} = 3.0$, $P_f^{target} = 0.13$ %,

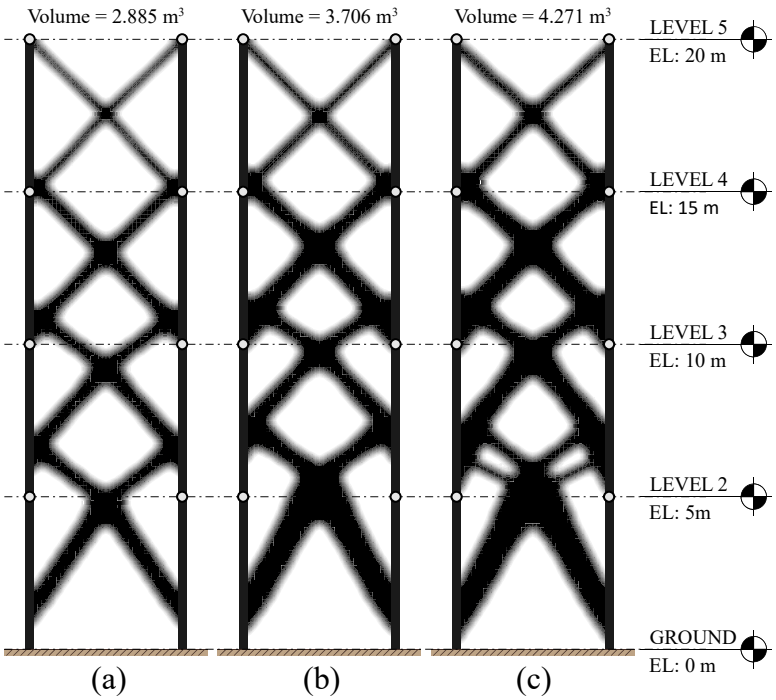

Figure 5.24: Topology optimization results from the four-story building example constrained by the first-passage probabilities in terms of inter-story drift ratio: (a) $\beta^{target} = 1.5$, $P_f^{target} = 6.68$ %, (b) $\beta^{target} = 2.5$, $P_f^{target} = 0.62$ %, and (c) $\beta^{target} = 3.0$, $P_f^{target} = 0.13$ %.

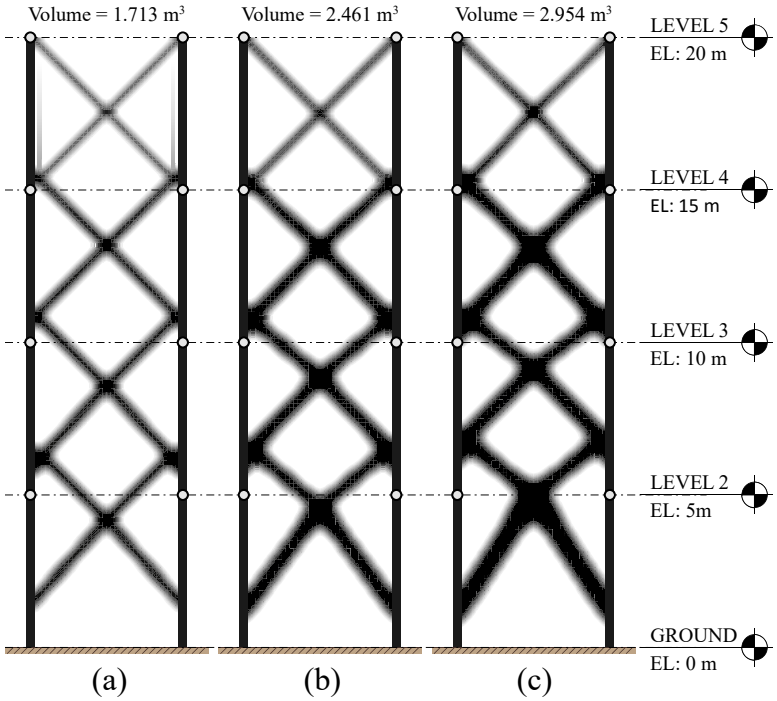

Figure 5.25: Topology optimization results from the four-story building example constrained by instantaneous failure probability in terms of inter-story drift ratio constraints: (a) $\beta^{\text{target}} = 1.5$, $P_f^{\text{target}} = 6.68$ %, (b) $\beta^{\text{target}} = 2.5$, $P_f^{\text{target}} = 0.62$ %, and (c) $\beta^{\text{target}} = 3.0$, $P_f^{\text{target}} = 0.13$ %.

Table 5.7: Parameters for ground motion filter model and constraints of topology optimization (topology optimization example).

Φ_0	ω_f	ζ_f	t (sec)	Δt (sec)	Init. density	Colum size	Thres. value
7.5	5π	0.4	6.0	0.06	0.7	0.6 m × 0.6 m	$u_{0\Delta} = 1/50$

Kanai-Tajimi filter parameters of dominant frequency ω_f and bandwidth ζ_f, column size, time interval of interest, and the threshold value u_0 of the average drift ratio at each time point. The filtering radius r is 0.25 m, and a prescribed density 0.7 is applied uniformly throughout the mesh. Topology optimization results are shown from different target failure probabilities of the inter-story drift ratios, and the tip-drift ratio constraints are shown in Figures 5.23-5.24. For the tip drift ratio constraint, the increase in the thicknesses in lower levels and additional branches of material distributions are observed as the target failure probabilities decreases, whereas bracing points and topologies remain relatively the same for all three cases under the tip drift ratio constraint in Figure 5.23. On the other hand, Figure 5.24 shows that connections of topologies to each floor level can

be checked for inter-story drift ratio constraints except the lowest level. As the target failure probability is reduced, the second lowest intersection point of bracing and column also decreases in elevation, such that in case Figure 5.24 (c), the intersection point is on the second level. Intersection points of bracings for upper two levels in both constrained optimization problems are at the midpoint of two floors so that X shapes of bracings with 90° are observed. At lower levels, the bracing intersection points become higher. In addition, there is a significant increase in material distribution in lower levels for the tip displacement constraint, whereas overall thicknesses of bracings throughout the building height are increased for the inter-story drift ratio constraint. Thus, optimization results show that reinforcing lower regions will be an efficient approach to control the tip displacement whereas adjusting each bracing module will lead to successful designs of structures fulfilling inter-story drift ratio criteria.

The instantaneous failure probability of inter-story drift ratios (Chun et al. 2016) is considered as the probabilistic constraint in Equation 5.12 (Figure 5.25) to compare with the results under constraints on the first-passage probability (Figure 5.24). Because the initial instantaneous failure probabilities (See Figures 5.26 and 5.27) are lower than the first-passage probabilities in the four story building, bracings are thinner, and the final volumes are reduced after optimization. Both constrained optimization results show that x-shape bracings in upper levels remain the same even when the target failure probability decreases. Distinct changes in the shape and the intersection point of bracings are observables in the lower floors. Optimal volume ratios for the first-passage probability constrained problem with the target failure probabilities, 0.62 % and 0.13 % to one with 6.68 % are 3.706/2.885 = 1.28 and 4.271/2.885 = 1.48. The ratios for the problem constrained by the instantaneous failure probability are 1.44 and 1.72. Thus, less sensitive changes in the failure probability of optimized bracing systems considering the first-passage probability constraint are expected under geometric uncertainties which may happen during the construction phase. Figures 5.26 and 5.27 show the convergence history of the volume and the failure probability over all

constraints. Those plot clearly demonstrate the ability of the proposed method in rapidly finding optimal material distributions which satisfy constraints.

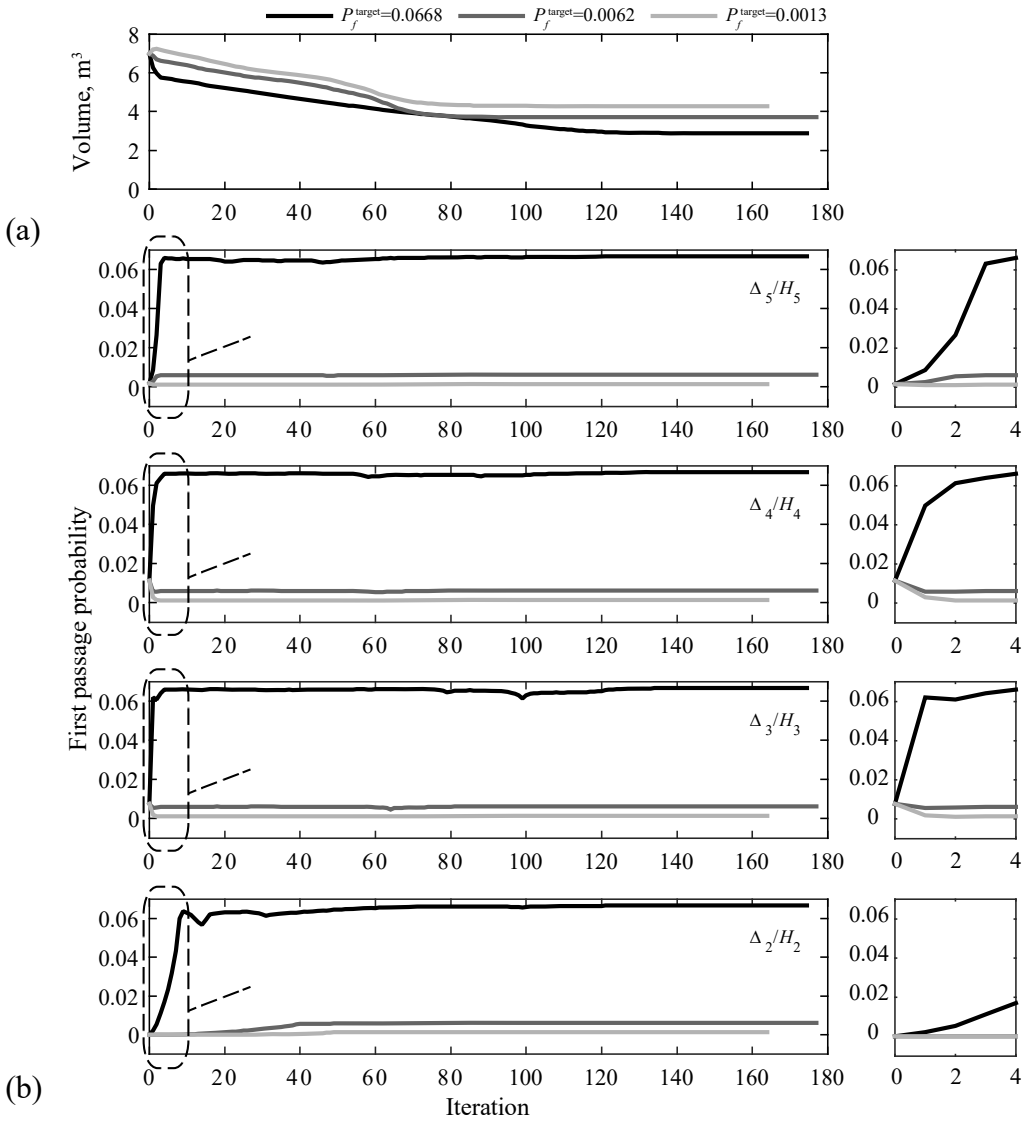

Figure 5.26: Convergence history of the four-story building (first-passage probabilities of inter-story drift ratio constraints): (a) volume, and (b) first-passage probability of each inter-story drift ratio.

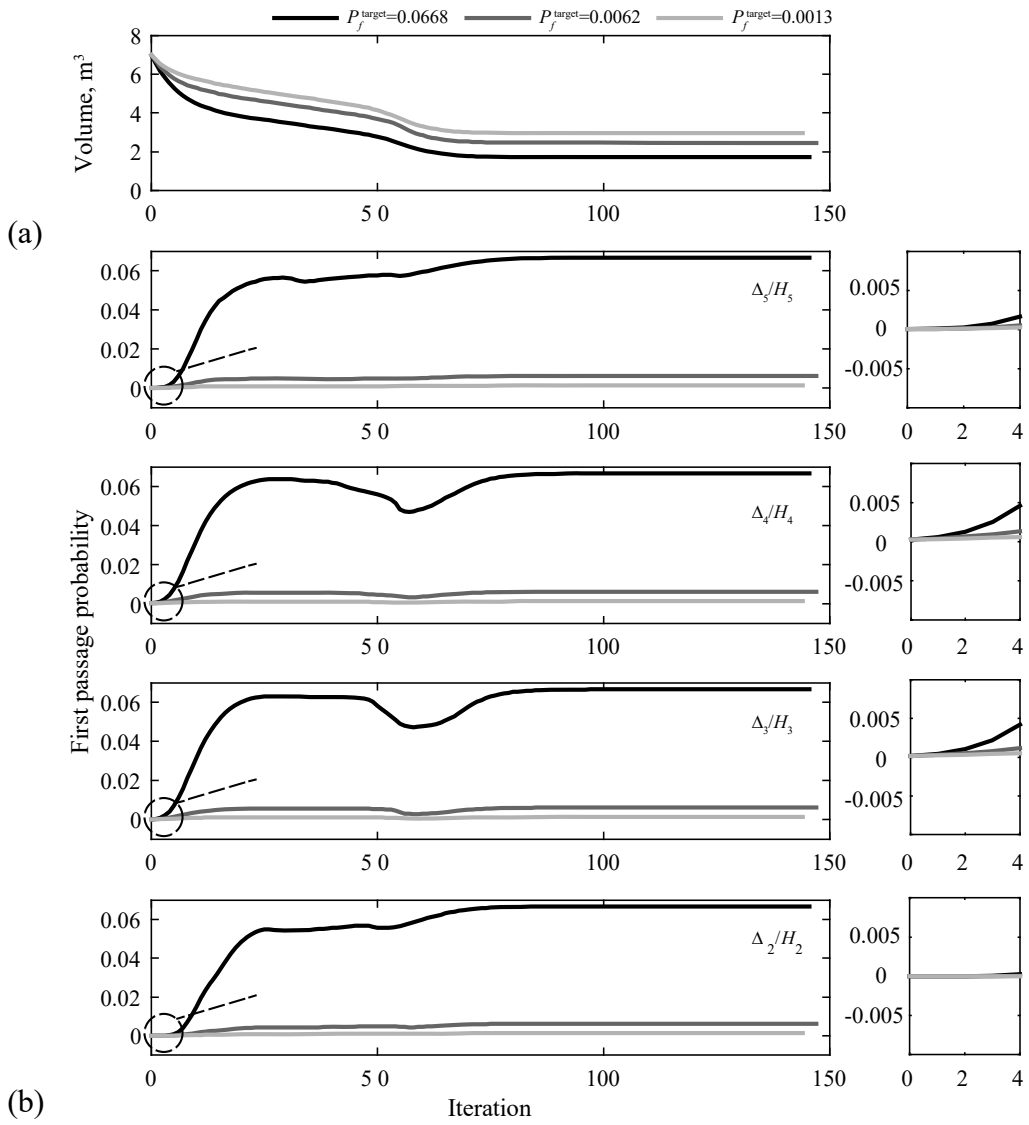

Figure 5.27: Convergence history of the four-story building (instantaneous failure probabilities of inter-story drift ratio constraints): (a) volume, and (b) failure probability of each inter-story drift ratio.

For constructability and aesthetic aspect of architecture, a pattern repetition constraint (Almeida et al. 2010; Stromberg 2011) can be implemented in the proposed framework. Therefore, the different number of patterns or the size of the primary region in optimization will result in various topologies, which can provide diverse options of solutions for the architectural and engineering schematic design process.

5.6. Concluding remarks

In this chapter, a new optimization framework is proposed to incorporate the first-passage probability into size optimization and topology optimization of structures. Using the discrete representation method and theories of structural system reliability, the first-passage probability is computed efficiently during the optimization process with a proper consideration of the statistical dependence between component failure events.

Parameter sensitivity formulation of the probabilistic constraint on the first-passage probability is also derived based on the adjoint method and sequential compounding method to facilitate the usage of efficient optimization algorithms. The developed method is successfully applied to the lateral bracing system of structures subjected to stochastic ground motions to identify optimal member sizes under engineering constraints associated with structural design criteria such as the stress, the displacement as well as the inter-story drift ratio. Through the numerical application of the space truss dome subject to simultaneous multiple earthquake ground motions, the proposed optimization framework provides reliable structural solutions for various loading scenarios.

For more practical engineering designs, load combinations in the Load and Resistance Factor Design (LRFD) specification can be implemented in optimization. Furthermore, the proposed method can further be extended to consider the first-passage probability constraint constructed by combining different types of failure events such as different time points and locations as well as multiple design criteria. The optimized system can withstand future realization of stochastic processes with a desired level of reliability. In addition, numerical examples show that the proposed topology optimization framework can provide an efficient way for structural engineers to obtain optimal design solutions that satisfy probabilistic constraints on the stochastic response in the conceptual and schematic design process.

The proposed method is based on the assumption of stationary process for the earthquake ground motions. The stochastic excitation generated by natural hazards (e.g. earthquakes, hurricanes) may be non-stationary and/or non-Gaussian. Thus, future research can be focused on

developments of optimization frameworks under non-stationary stochastic processes in time domain as well as in frequency domain.

Chapter 6

Reliability-based topology optimization by ground structure method employing a discrete filtering technique

This chapter proposes the incorporation of the discrete filtering technique into reliability-based topology optimization (RBTO) using the elastic formulation of the ground structure method. Some of the solutions identified through the conventional filtering scheme for RBTO violate the probabilistic constraints. To ensure that optimized solutions satisfy the probabilistic constraints, a different technique, the discrete filtering method is adopted, for RBTO. The discrete filtering method proposed by Ramos Jr. and Paulino (2016) allows the optimizer to achieve more physically realizable truss designs in which thin bars are eliminated while still satisfying global equilibrium. The method uses the potential energy approach with Tikhonov regularization to solve the singular system of equations that results from imposing the discrete filter. Combining this method with RBTO allows for the transformation of the reliability-based truss sizing optimization problem into a topology optimization problem accounting for uncertainties. Furthermore, a single-loop approach is adopted to enhance the computational efficiency of the proposed RBTO method. Numerical examples of two- and three-dimensional engineering designs are given to demonstrate features of the proposed method and to illustrate the influence of the discrete filter and parameter uncertainties on the optimization results. In order to verify the target failure probabilities of optimal solutions achieved by the proposed approach, the First-Order Reliability Method, and the Monte Carlo simulations are performed.

6.1. Introduction

Topology optimization is a mathematical tool which has been utilized to identify optimal solutions for various engineering problems. In particular, Topology optimization of continuum structures seeks for optimal material layouts and connectivities in a design domain (Bendsøe and Sigmund 2003). In such continuum-based topology optimization, the design domain is discretized with finite elements, each of which is assigned to void or solid material through the iterative optimization procedure (see Rozvany (2009), and Deaton and Grandhi (2014) for a state-of-the-art review of topology optimization). Particularly in the field of structural engineering, continuum-based topology optimization has been applied to design lateral-load resisting systems (Mijar et al. 1998; Stromberg et al. 2012; Bobby et al. 2014; Chun et al. 2016). On the other hand, topology optimization of discrete structures such as trusses and frames is applied to find optimal connectivity of the nodes by the structural elements. This approach commonly implements the ground structure method (Bendsøe and Sigmund 2003; Ohsaki 2010), in which the design domain is discretized with spatial nodes and highly interconnected by truss or frame elements. Topology optimization is performed on the generated ground structure to minimize an objective function while satisfying constraints, and the size of elements and connectivities are subsequently determined. Zegard and Paulino (2014, 2015) developed both two- and three-dimensional implementations of ground structure based topology optimization for trusses using the plastic formulation. The developed computer codes, GRAND and GRAND3, include an efficient algorithm for ground structure generation using restriction zones that allows for ground structure generation on arbitrary domains. Furthermore, topology optimization of truss structures considering material non-linear behavior was proposed by Ramos Jr. and Paulino (2015).

In the last decades, deterministic topology optimization (DTO) has been well developed for both the continuum and discrete topology optimization. These methods consider all design parameters such as material properties, loadings, and geometry as deterministic quantities during the optimization. However, consideration of uncertainties in loads and material properties is an

important aspect of structural engineering because they help reduce the risk of unexpected structural failures that may eventually result in catastrophic damage and/or loss of life. Therefore, optimization processes associated with the treatment of uncertainties should be utilized to obtain engineering solutions so that a satisfactory level of reliability can be achieved. This is widely referred to as a reliability-based design optimization (RBDO; Frangopol and Maute 2005; Tsompanakis et al. 2008) or reliability-based topology optimization (RBTO; Maute and Frangopol 2003; Guest and Igusa 2008; Rozvany 2008). Nguyen et al. (2010) proposed a system reliability based design optimization using the Matrix-based System Reliability (MSR) method which can consider statistical dependence and compute parametric sensitivity in an efficient way. This approach was further applied to the continuum topology optimization (Nguyen et al. 2011). Jalalpour et al. (2013) focused on the reliability-based topology optimization of truss structure to address geometric imperfections and uncertainty in the material property.

The traditional formulations in RBDO and RBTO include two nested loops of iterative computations: an optimization loop and a reliability analysis loop. The inner loop for reliability analysis is to evaluate probabilistic constraints or objective functions for the design variables updated by an outer loop for optimization. The solutions to reliability problems can be obtained by use of the first-order reliability method (FORM) or the second-order reliability method (SORM) (see Der Kiureghian 2005 for a comprehensive review). To reduce computational cost in RBDO and RBTO, a single-loop approach has been developed (Du and Chen 2004; Liang et al. 2004, 2007, 2008; Shan and Wang 2008; Nguyen et al. 2010). This method replaces the inner-loop of the reliability analysis by an approximate non-iterative solution, which eventually tends to converge to an accurate reliability estimate as the optimal design is achieved through iterations.

In topology optimization for truss structures, a lower bound of design variables is set to a very small value to avoid an ill-posed condition such as a singular matrix. As a result, the converged topology still includes the original connectivity from the generated ground structure. To define the final topology, the conventional topology optimization for truss structures implements a filtering

procedure at the end of optimization. More specifically, the conventional filtering scheme selects bars having areas greater than a small arbitrarily assigned cut-off value of the area, which subsequently become the bars defining the final optimized topology. However, the selection criteria for the lower bound and the cut-off are often ambiguous (Christensen and Klarbring 2009). Thus, the conventional filtering method may produce ill-conditioned solutions, such as a singular stiffness matrix, hanging members or many thin bars, which may be undesirable in engineering and architecture. The conventional filtering scheme in RBTO is highly likely to cause the final structure to violate the probabilistic constraints. Therefore, development of a new topology optimization framework for truss structures is needed to obtain reliable designs that satisfy global equilibrium and that are not dependent on the cut-off.

To address the aforementioned issues, a discrete filtering method proposed by Ramos Jr. and Paulino (2016) is incorporated into RBDO for truss structures so that more physically realizable truss designs, i.e. thin bars are eliminated, while still satisfying global equilibrium. As a result, a topology optimization problem accounting for uncertainties can be carried out by the reliability-based truss sizing optimization problem. The computational efficiency of the proposed method is further improved by utilizing a single-loop approach (Liang et al. 2004, 2007, 2008; Nguyen et al. 2010).

6.2. Single-loop reliability-based topology optimization formulation

In this section, mathematical formulations of RBTO are first presented. Then, as a method to enhance computational efficiency in RBTO, single-loop RBTO approach is reviewed.

6.2.1. Reliability-based topology optimization

A general mathematical formulation of reliability-based topology optimization can be written as

$$\begin{aligned} &\min_{\mathbf{d},\boldsymbol{\mu}_\mathbf{X}} \; f(\mathbf{d},\boldsymbol{\mu}_\mathbf{X}) \\ &s.t \quad P_f\left[g(\mathbf{d},\mathbf{X})\le 0\right] \le P_f^{\text{target}} \\ &\qquad \mathbf{d}^{\text{lower}} \le \mathbf{d} \le \mathbf{d}^{\text{upper}} \\ &\text{with } \mathbf{K}(\mathbf{d})\mathbf{u}(\mathbf{d},\mathbf{X}) = \mathbf{f}(\mathbf{X}) \end{aligned} \tag{6.1}$$

where $f(\cdot)$ denotes the objective function, $\mathbf{d}$ represents the vector of design variables, and $\boldsymbol{\mu}_\mathbf{X}$ is the vector of the means of random variables in $\mathbf{X}$. $g(\cdot)$ is the limit-state function whose negative value indicates violating the given constraint. $\mathbf{X}$ denotes the vector of random variables and $P_f[\cdot]$ is the failure probability of the limit-state function. $\mathbf{K}$, $\mathbf{u}$, $\mathbf{f}$ are the global stiffness matrix, the global displacement vector, and the global force vector, respectively. The probability of the failure event defined in terms of $g(\cdot)$ can be computed by integrating the joint probability density function (PDF) of $\mathbf{X}$ in the failure domain, i.e.

$$P_f = \int_{g(\mathbf{X})\le 0} f(\mathbf{x})d\mathbf{x} \tag{6.2}$$

By transforming the random variables to the space of uncorrelated standard normal random variables, i.e. $\mathbf{U}=\mathbf{T}(\mathbf{X})$, the failure probability is given by

$$P_f = \int_{G(\mathbf{u})\le 0} \varphi_n(\mathbf{u};\mathbf{I})d\mathbf{u} \tag{6.3}$$

where $\mathbf{U}$ represents the vector of uncorrelated standard normal variables transformed from $\mathbf{X}$. $G(\cdot)$ denotes the limit-state function given in terms of $\mathbf{U}$, $\varphi_n(\cdot)$ is the joint PDF of the n standard normal random variables. The correlation coefficient matrix of the joint PDF is given as the identity matrix $\mathbf{I}$ so that the random variables are uncorrelated.

In general, RBTO consists of an outer loop for optimization and an inner loop for the reliability analysis. The reliability analysis forms a loop because reliability analysis methods such as the FORM or SORM (Der Kiureghian 2005) finds the "most probable failure point (MPP)", $\mathbf{U}^*$ by performing optimization, i.e.

$$\mathbf{U}^* = \arg\min_{\mathbf{u}} \; \left\{\|\mathbf{U}\| \mid G(\mathbf{d},\mathbf{U})=0\right\} \tag{6.4}$$

In the FORM, for example, the "reliability index" β, i.e. the shortest distance from the origin to the limit-state function linearized at **U*** in the standard normal space is obtained as

$$\beta = -\frac{\nabla G(\mathbf{U}^*)}{\left\|\nabla G(\mathbf{U}^*)\right\|} \cdot \mathbf{U}^* \tag{6.5}$$

The failure probability in Equation 6.3 is approximately evaluated by use of the reliability index β as

$$P_f \cong \Phi\left[-\beta\right] \tag{6.6}$$

where Φ is the cumulative distribution function (CDF) of the standard normal distribution. Thus, the RBTO problem can be written using the so-called reliability index approach (RIA) (Enevoldsen and Sorensen 1994) as follows:

$$\begin{aligned} &\min_{\mathbf{d},\boldsymbol{\mu}_\mathbf{X}} \; f(\mathbf{d},\boldsymbol{\mu}_\mathbf{X}) \\ &s.t \quad g^{\text{RIA}}(\mathbf{d},\mathbf{U}) \equiv \beta \geq \beta^{\text{target}} \left(= -\Phi^{-1}\left[P_f^{\text{target}}\right]\right) \\ &\qquad \mathbf{d}^{\text{lower}} \leq \mathbf{d} \leq \mathbf{d}^{\text{upper}} \\ &\text{with } \mathbf{K}(\mathbf{d})\mathbf{u}(\mathbf{d},\mathbf{X}) = \mathbf{f}(\mathbf{X}) \end{aligned} \tag{6.7}$$

Alternatively, the minimum value of the limit-state function on the surface of the hypersphere with the radius β^{target} can be used to check the violation of the probabilistic constraint. This is referred to as the performance measure approach (PMA, Tu et al. 1999), which is formulated as

$$\begin{aligned} &\min_{\mathbf{d},\boldsymbol{\mu}_\mathbf{X}} \; f(\mathbf{d},\boldsymbol{\mu}_\mathbf{X}) \\ &s.t \quad g^{\text{PMA}}(\mathbf{d},\mathbf{U}) \equiv g_{P_f^{\text{target}}} \geq 0 \\ &\qquad \mathbf{d}^{\text{lower}} \leq \mathbf{d} \leq \mathbf{d}^{\text{upper}} \\ &\text{with } \mathbf{K}(\mathbf{d})\mathbf{u}(\mathbf{d},\mathbf{X}) = \mathbf{f}(\mathbf{X}) \end{aligned} \tag{6.8}$$

where $g_{P_f^{\text{target}}}$ is the P_f^{target}-quantile of the limit-state function g, alternatively obtained by

$$g^{\text{PMA}}(\mathbf{d},\mathbf{U}) = \arg\min_{G}\left\{G(\mathbf{d},\mathbf{U}) \;\middle|\; \|\mathbf{U}\| = \beta^{\text{target}} \left(= -\Phi^{-1}\left[P_f^{\text{target}}\right]\right)\right\} \tag{6.9}$$

In general, the PMA shows more efficient and robust convergence compared to the RIA, primarily because of the different way in which the probabilistic constraint is handled. The PMA minimizes

a complex objective function in Equation 6.9 while satisfying a simple constraint function, whereas the RIA solves a minimization problem of a simple objective function with a complicated constraint function in Equation 6.4.

6.2.2. Single-loop algorithm for RBTO

Efficiency in RBDO/RBTO can be improved by replacing the inner loop of the reliability analysis by a non-iterative procedure, which is often called single-loop scheme (Liang et al. 2004; Shan and Wang 2008). By enforcing the Karush-Kuhn-Tucker (KKT) optimality conditions of the probabilistic constraint in the reliability analysis, the constraint is replaced with an approximate deterministic constraint. The optimal point in Equation 6.9 should satisfy the following KKT optimality conditions:

$$\begin{aligned} &\nabla_{\mathbf{U}} G(\mathbf{d},\mathbf{U}) + \lambda \cdot \nabla_{\mathbf{U}} \left(\|\mathbf{U}\| - \beta^{\text{target}} \right) = \mathbf{0} \qquad \text{(stationarity)} \\ &\lambda \cdot \left(\|\mathbf{U}\| - \beta^{\text{target}} \right) \qquad \text{(complementary slackness)} \\ &\|\mathbf{U}\| - \beta^{\text{target}} = 0 \qquad \text{(primal feasibility)} \end{aligned} \tag{6.10}$$

From the geometric interpretation (Liang et al. 2004), the solution $\mathbf{U}$ in Equation 6.10 is derived as:

$$\mathbf{U} \equiv \mathbf{U}^{\text{t}} = \beta^{\text{target}} \left(-\frac{\nabla_{\mathbf{X}} g\left(\mathbf{d}, \mathbf{X}(\mathbf{U})\right) \mathbf{J}_{\mathbf{X},\mathbf{U}}}{\left\| \nabla_{\mathbf{X}} g\left(\mathbf{d}, \mathbf{X}(\mathbf{U})\right) \mathbf{J}_{\mathbf{X},\mathbf{U}} \right\|} \right) \tag{6.11}$$

where $\mathbf{J}_{\mathbf{X},\mathbf{U}}$ is the Jacobian of the transformation, $\mathbf{X}$ to $\mathbf{U}$ and $\mathbf{X}(\mathbf{U}) = \text{diag}(\boldsymbol{\sigma})\mathbf{U} + \boldsymbol{\mu}_{\mathbf{X}}$, where $\text{diag}(\boldsymbol{\sigma})$ is the diagonal matrix with diagonal entries σ_i. Thus, the equivalent deterministic optimization problem is formulated as

$$\begin{aligned} &\min_{\mathbf{d},\boldsymbol{\mu}_{\mathbf{X}}} \; f(\mathbf{d}, \boldsymbol{\mu}_{\mathbf{X}}) \\ &s.t \quad g^{\text{PMA}}(\mathbf{d},\mathbf{U}) \cong g^{Single}\left(\mathbf{d}, \mathbf{X}(\mathbf{U}^{\text{t}})\right) \geq 0 \\ &\qquad \mathbf{d}^{\text{lower}} \leq \mathbf{d} \leq \mathbf{d}^{\text{upper}} \\ &\text{with } \mathbf{K}(\mathbf{d}, \mathbf{X}(\mathbf{U}^{\text{t}}))\mathbf{u}(\mathbf{d}, \mathbf{X}(\mathbf{U}^{\text{t}})) = \mathbf{f}(\mathbf{X}(\mathbf{U}^{\text{t}})) \end{aligned} \tag{6.12}$$

Nguyen et al. (2010) proposed a single-loop RBDO algorithm for *system* reliability analysis using the matrix-based system reliability (MSR) method (Song and Kang 2009). Numerical examples showed that the proposed single-loop system reliability based design optimization (SRBDO) approach is efficient and accurate. This work primarily focuses on single-loop (component) reliability topology optimization. Therefore readers interested in system level constraints in optimization can refer to Nguyen et al. (2010, 2011).

6.3. Discrete filtering

A compliance minimization problem with a volume constraint in deterministic topology optimization (DTO) is formulated as

$$\begin{aligned} \min_{\mathbf{A}} \quad & \mathbf{f}^{\mathrm{T}}\mathbf{u}(\mathbf{A}) \\ s.t \quad & \sum_{i=1}^{ne} A_i L_i \le V_c \\ & \mathbf{A}^{lower} \le \mathbf{A} \le \mathbf{A}^{upper} \\ \text{with } & \mathbf{K}(\mathbf{A})\mathbf{u}(\mathbf{A}) = \mathbf{f} \end{aligned} \tag{6.13}$$

where L_i is the length of truss element i, ne is the number of truss elements, and $\mathbf{A}$ is the vector of cross sectional areas. A lower bound on each design variable is commonly assigned to avoid a singular stiffness matrix during topology optimization. Conventional topology optimization of truss structures using the ground structure approach implements a filtering process with a cut-off value, $\varepsilon_{\text{cut-off}}$ after the optimization processes is complete. Truss elements smaller than the cut-off value are eliminated, and the filtered truss structure is subsequently considered as the final topology. This end-filtering process is used to interpret the final structure from the ground structure.

DTO with the conventional filtering method is illustrated through a cantilever beam optimization problem. The rectangular cantilever beam in Figure 6.1 (a) is clamped on the left side and loaded by a vertical force F at mid-height of the right side. Using the ground structure approach, the structural domain is discretized into a finite spatial distribution of nodes that are each connected

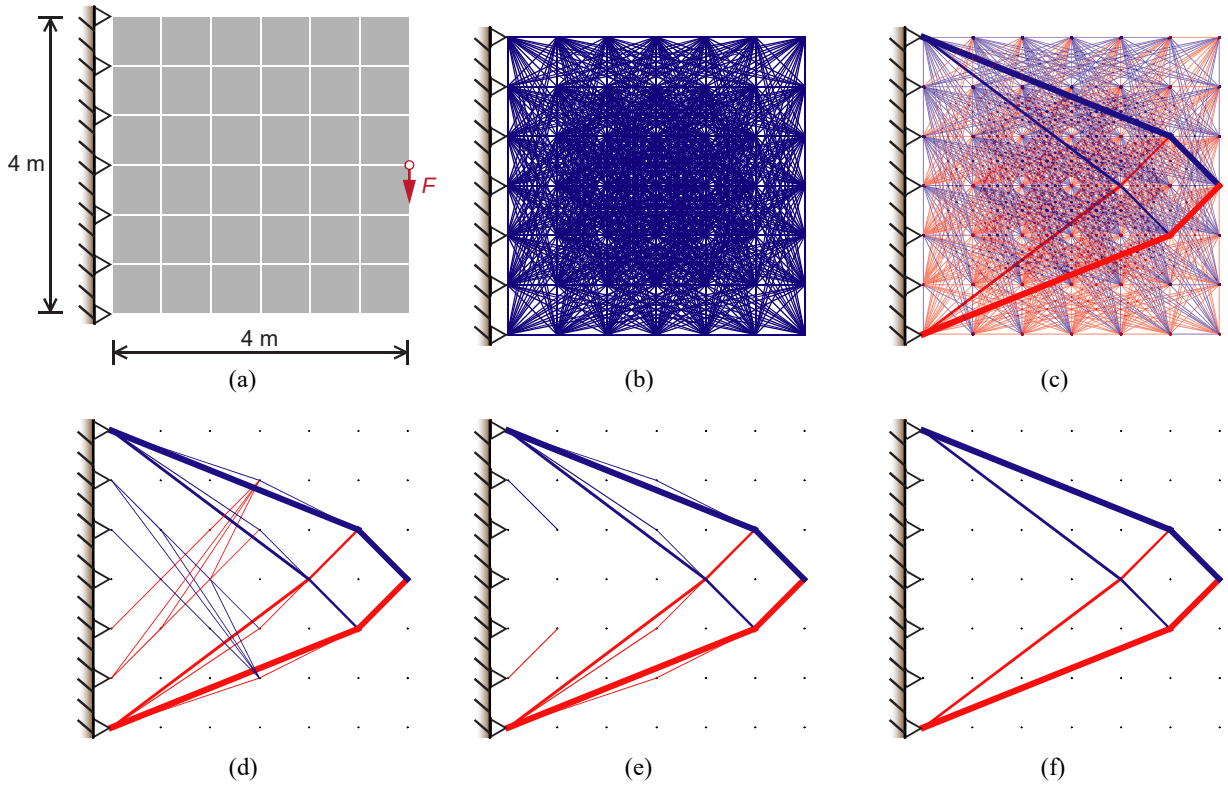

Figure 6.1: Ground structure and filtered structure for DTO employing the conventional filtering approach: (a) design domain, loading and boundary conditions, (b) ground structure, (c) filtered structure ($\varepsilon_{\text{cut-off}} = 0.00$), (d) filtered structure ($\varepsilon_{\text{cut-off}} = 0.0001$), (e) filtered structure ($\varepsilon_{\text{cut-off}} = 0.001$), and (f) filtered structure ($\varepsilon_{\text{cut-off}} = 0.1$).

to every other node with truss members as shown in Figure 6.1 (b). Figures 6.1 (c) through 6.1 (f) show final topologies after optimization according to varying cut-off values (increasing from 0 to 0.1). It should be noted that the determination of a proper cut-off value is ambiguous and is often based on a process of trial and error. For example, a small cut-off value may lead to many thin elements, which cannot be practically built, while a larger cut-off value may result in a rigid-body motion (mechanism) or hanging member shown in Figure 6.1 (e). In addition, the end-filtering process may change the final compliance.

To address these issues, Ramos Jr. and Paulino (2016) recently proposed a discrete filtering scheme that enables filtering of well-defined (e.g. satisfying the global equilibrium) structures

from ground structures. The discrete filtering process is performed with updated design variables at each optimization iteration according to:

$$Filter(\mathbf{A},\alpha_f)=\begin{cases}0 & \text{if } A_i/\max(\mathbf{A})<\alpha_f \\ A_i & \text{otherwise}\end{cases},\ 0\le\alpha_f\le 1 \tag{6.14}$$

After the discrete filtering, global equilibrium is checked to ensure that the filtered structure is well defined. If it fails to satisfy global equilibrium, the move limit in the Optimality Criteria (OC) for updating design variables is adjusted to a smaller value, and the discrete filtering technique is performed again. These steps are repeated until global equilibrium is satisfied or the number of checking processes reaches the prescribed maximum iteration. However, some structures satisfying global equilibrium may be singular due to aligned hinges and/or detached degrees of freedom. To handle the singularity of the structural system, minimization of potential energy with Tikhonov regularization is adopted. Thus, it allows for a zero bound on the design variables. The regularized compliance minimization problem in DTO can be formulated as:

$$\begin{aligned}
&\min_{\mathbf{A}} \quad \mathbf{f}^{\mathrm{T}}\mathbf{u}(\mathbf{A}) \\
&s.t \quad \sum_{i=1}^{ne} A_i L_i \le V_c \\
&\qquad \mathbf{0}\le\mathbf{A}\le\mathbf{A}^{\text{upper}} \\
&\text{with} \quad \mathbf{A}=Filter(\mathbf{A},\alpha_f) \\
&\text{and} \quad \min_{\mathbf{u}} \ \prod\left(\mathbf{u}(\mathbf{A})\right)+\frac{\lambda}{2}\mathbf{u}(\mathbf{A})^{\mathrm{T}}\mathbf{u}(\mathbf{A})
\end{aligned} \tag{6.15}$$

where λ denotes a small positive number and Π(·) represents the potential energy of the system defined as:

$$\prod\left(\mathbf{u}(\mathbf{A})\right)=\frac{1}{2}\mathbf{u}(\mathbf{A})^{\mathrm{T}}\mathbf{K}(\mathbf{A})\mathbf{u}(\mathbf{A})-\mathbf{f}^{\mathrm{T}}\mathbf{u}(\mathbf{A}) \tag{6.16}$$

The particular solution of displacements of the linear system is obtained by minimizing the potential energy with Tikhonov regularization as follows:

$$\left(\mathbf{K}(\mathbf{A})+\lambda\mathbf{I}\right)\mathbf{u}(\mathbf{A})=\mathbf{f} \tag{6.17}$$

The structure is considered in global equilibrium if the following inequality holds:

$$\left\|\mathbf{K}(\mathbf{A})\mathbf{u}(\mathbf{A})-\mathbf{f}\right\| \le \gamma\left\|\mathbf{f}\right\| \tag{6.18}$$

where γ is a prescribed tolerance (e.g. $\gamma = 10^{-4}$).

Incorporating the discrete filtering scheme into RBTO framework, one can obtain an optimal topology of a structure under uncertainties using a ground structure model as follows:

$$\begin{aligned}
&\min_{\mathbf{A},\boldsymbol{\mu}_\mathbf{X}} \quad f(\mathbf{A},\boldsymbol{\mu}_\mathbf{X}) \\
&s.t \quad g^{Single}\left(\mathbf{A},\mathbf{X}(\mathbf{U}^{\mathrm{t}})\right)\ge 0 \\
&\qquad \mathbf{0}\le\mathbf{A}\le\mathbf{A}^{\mathrm{upper}} \\
&\text{with} \quad \mathbf{A}=Filter(\mathbf{A},\alpha_f) \\
&\text{and} \quad \min_{\mathbf{u}} \quad \prod(\mathbf{A}(\mathbf{d},\mathbf{X}(\mathbf{U}^{\mathrm{t}})))+\frac{\lambda}{2}\mathbf{u}(\mathbf{A},\mathbf{X}(\mathbf{U}^{\mathrm{t}}))^{\mathrm{T}}\mathbf{u}(\mathbf{A},\mathbf{X}(\mathbf{U}^{\mathrm{t}}))
\end{aligned} \tag{6.19}$$

The proposed optimization algorithm is illustrated by a flowchart as shown in Figure 6.2. This work implements Ramos Jr. and Paulino's (2016) method into single-loop RBTO so that it can solve the singularity of the structural system after the discrete filter is carried out, and identify the structure in global equilibrium while satisfying the target failure probability.

6.4. Numerical applications

RBTO using ground structure method with the discrete filtering approach is demonstrated by numerical examples where the design variables are cross sectional areas, and the objective function of the optimal design is the minimization of the volume. The probabilistic constraint is defined in terms of the compliance with the upper limit, C_{max} such as $P_f(g: C_{max} - C) \le P_f^{\mathrm{target}}$. Applied forces, force direction, and Young's modulus are considered as random variables assumed to follow a normal distribution. It should be noted that the application of the proposed method is not limited

to normal distributions. Different combinations of random variables and statistical dependency are considered in RBTO that will be stated for each problem.

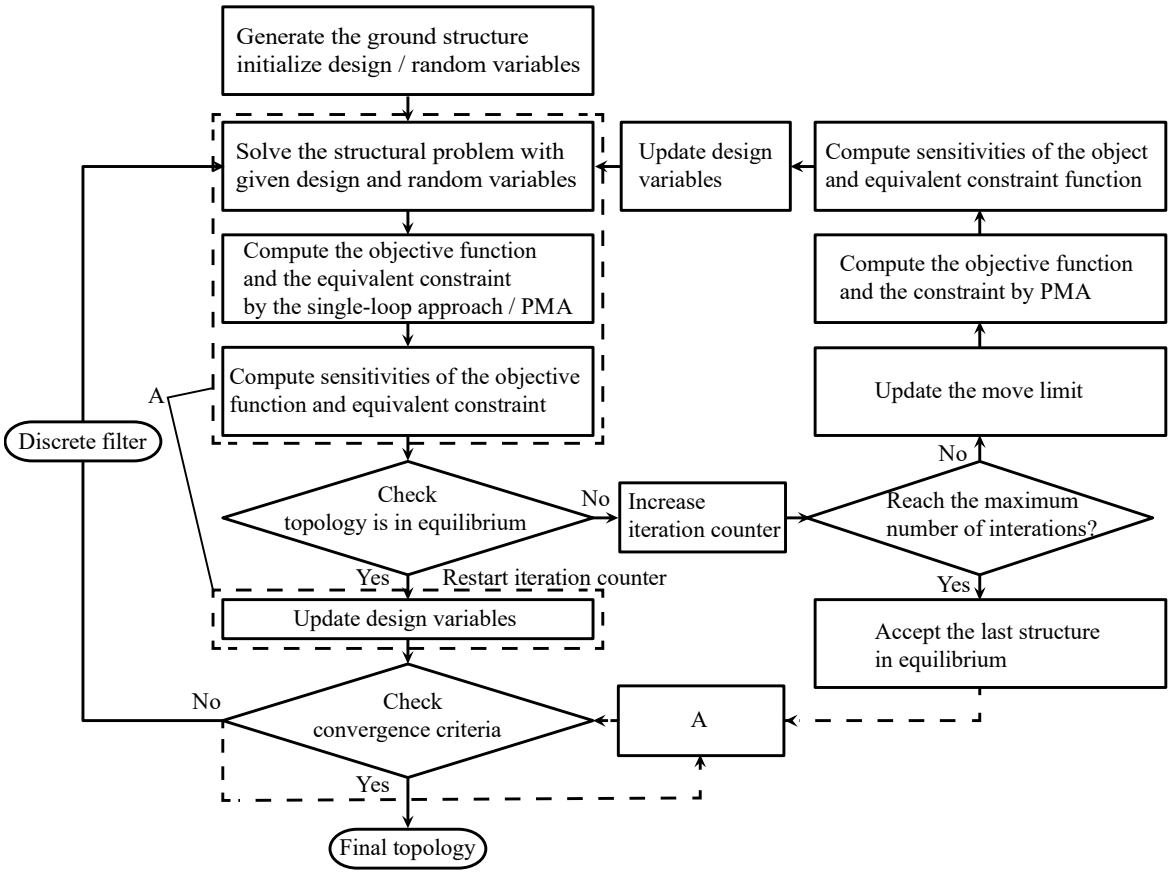

Figure 6.2: Flowchart of the proposed optimization algorithm.

The optimality criteria (OC) (Bendsøe and Sigmund 2003; Groenwold and Etman 2008; Ramos and Paulino 2015) is utilized as the update scheme. After the optimization is complete using the single-loop algorithm, the FORM and the Monte Carlo Simulation (MCS) are performed to ensure that a filtered structure satisfies the target failure probability. It should be noted that minimization of potential energy with Tikhonov regularization is also used to solve the singular system in the FORM and the MCS.

6.4.1. Comparison of conventional filtering approach and discrete filtering approach in RBTO

Here, the conventional and discrete filters are imposed on a cantilever beam optimal design to demonstrate the effects of varying filter input parameters $\varepsilon_{\text{cut-off}}$ and α_f on the final topologies. The cantilever design domain clamped on the left and loaded on the right by a vertical force at two thirds-height is discretized with 12 × 6 elements (Figure 6.3 (a)). A full connectivity level ground structure is generated as shown in Figure 6.3 (b). To incorporate uncertainties in material properties and the load, Young's modulus E and the force F are modeled as random variables following the normal distributions with means (μ_{mE} = 10,000 N/m^2, μ_{mF} = 100 N) and standard deviations (σ_{sE} = 750 N/m^2, σ_{sF} = 20 N), respectively. The objective function is the minimization of volume, and the probabilistic constraint is defined as $P_f(g{:}5 - C) \leq 0.005$. Initial cross-sectional areas are set to 0.5 m^2. The optimization results from Equation 6.12 according to varying cut-off values $\varepsilon_{\text{cut-off}}$ of the conventional filter are illustrated in Figures 6.3 (c) through 6.3 (f). Figure 6.3 (f) shows that the structural elements contributing to global equilibrium can be removed and the sequentially structural system can be in internal mechanisms as a result of the conventional filtering process. Also, using a certain cut-off value can lead to a final topology including hanging members not connected to the structure. The influence of the cut-off values on actual failure probabilities of the optimal topology is checked by use of the FORM and the MCS (Table 6.1). As the selected $\varepsilon_{\text{cut-off}}$ increases for the filtering process, a failure probability higher than the target probability is observed. That is, the conventional filtering approach may lead to the violation of the prescribed target failure probability.

Next, the same optimization problem is solved using the proposed method with varying discrete filtering values α_f. Figure 6.4 shows filtered structures which are in global equilibrium. In all plots, tension members are shown in blue and compression members in red. The thicknesses of the lines indicate the normalized area of truss elements to the maximum member area. The filtering parameter α_f affects details of the final topology as shown in Figure 6.4. Unlike the conventional

approach, the proposed method is able to find feasible solutions that satisfy the target failure probability as shown in Table 6.1. Figure 6.5 shows the convergence history of the volumes and failure probabilities of the conventional and discrete filtering approaches in RBTO for 100 iterations. The non-smooth zig-zag pattern observed in the convergence plot within the first fifty iterations is primarily due to the discrete filtering, which actively eliminates bars with areas smaller than the prescribed filtering value, α_f.

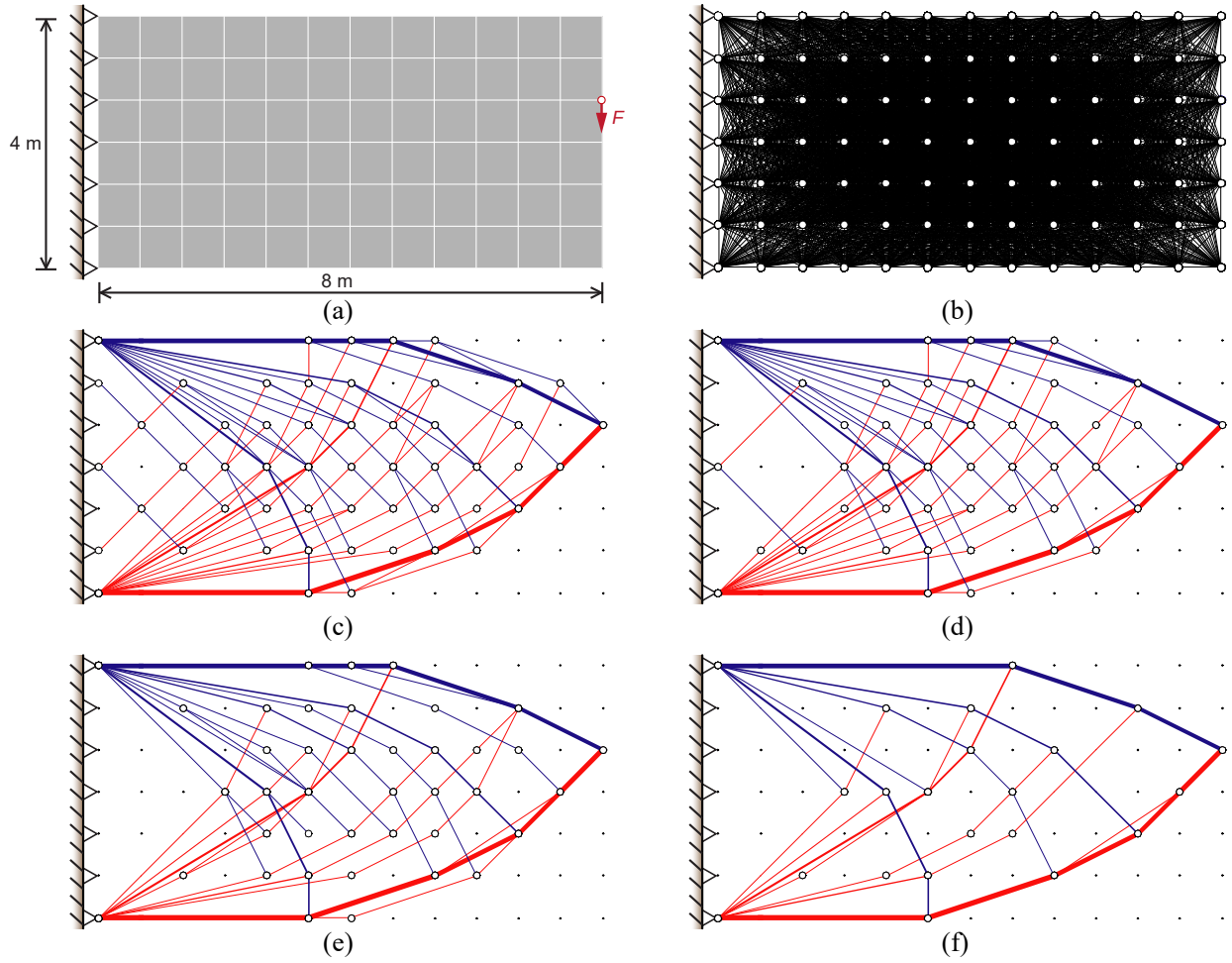

Figure 6.3: Ground structure and filtered structures with varying $\varepsilon_{\text{cut-off}}$ for RBTO using the conventional filtering approach: (a) design domain, loading and boundary conditions, (b) full connectivity ground structure, (c) $\varepsilon_{\text{cut-off}} = 0.0001$, (d) $\varepsilon_{\text{cut-off}} = 0.001$, (e) $\varepsilon_{\text{cut-off}} = 0.01$, and (f) $\varepsilon_{\text{cut-off}} = 0.05$.

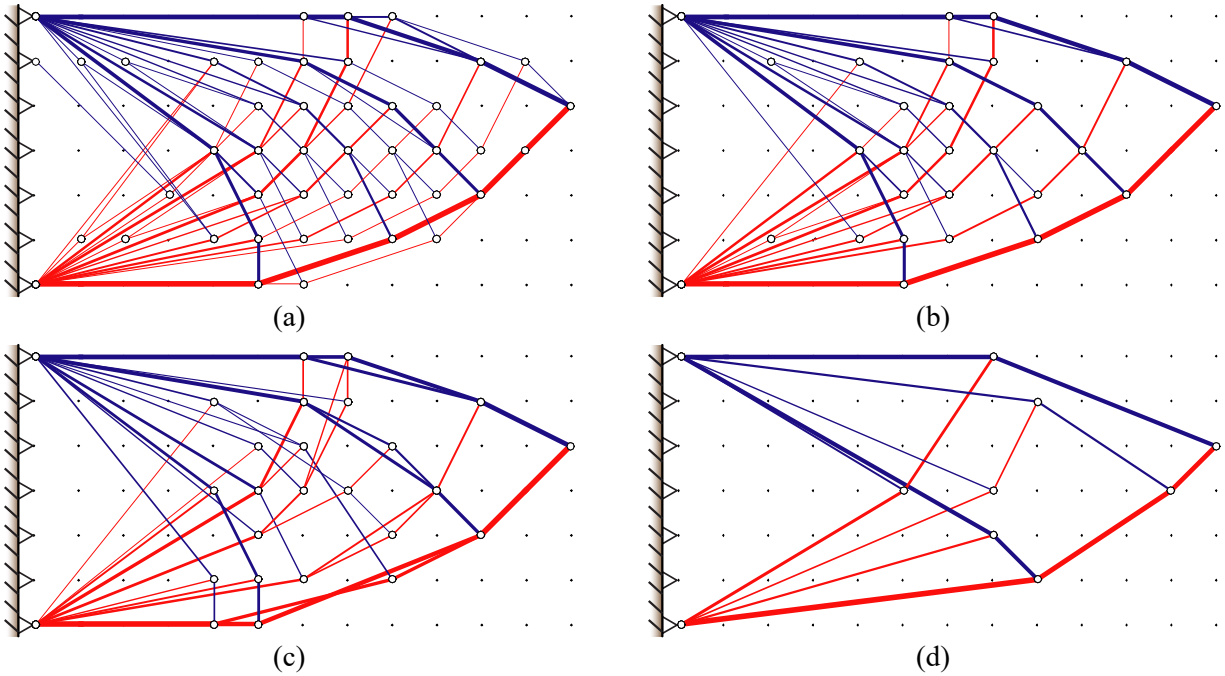

Figure 6.4: Filtered structures by RBTO with varying discrete filter values: (a) $\alpha_f = 0.0001$, (b) $\alpha_f = 0.001$, (c) $\alpha_f = 0.01$, and (d) $\alpha_f = 0.05$.

Table 6.1: Influence of filtering method on actual probabilities of the optimal topology for the cantilever beam problem.

	Conventional filtering method			
	$\varepsilon_{\text{cut-off}}$			
	0.05	0.01	0.001	0.0001
Volume	369.76	383.95	386.41	386.48
P_f FORM	1.00	8.02×10^{-3}	5.03×10^{-3}	5.01×10^{-3}
P_f MCS	1.00	8.12×10^{-3}	5.09×10^{-3}	5.08×10^{-3}
	Discrete filtering method			
	α_f			
	0.05	0.01	0.001	0.0001
Volume	407.39	391.49	387.94	387.93
$\|\|\mathbf{Ku-f}\|\|/\|\|\mathbf{f}\|\|$	4.42×10^{-7}	3.96×10^{-7}	3.97×10^{-7}	3.65×10^{-7}
P_f FORM	5.00×10^{-3}	5.00×10^{-3}	5.00×10^{-3}	5.00×10^{-3}
P_f MCS	5.05×10^{-3}	5.06×10^{-3}	5.07×10^{-3}	5.05×10^{-3}

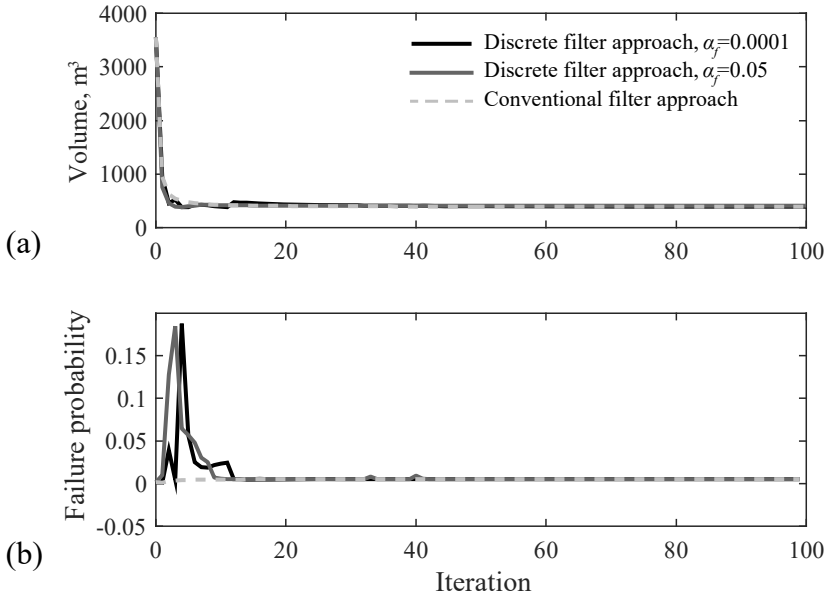

Figure 6.5: Convergence history of the cantilever problem: (a) volume, and (b) failure probability.

6.4.2. Comparison between deterministic design optimization and reliability-based design optimization

In this example of clamped beam (Figure 6.6), the results by DTO and RBTO are compared to investigate the influence of the uncertainties on the topologies. Note that, for DTO, the random variables in RBTO are replaced by deterministic parameters whose values are the same as the mean values. Five statistically independent random variables are used to describe forces (F_1, F_2, F_3), force angle (θ) and material property represented by Young's Modulus (E). All random variables are assumed to follow the normal distributions. Figure 6.6 (a) shows the design domain fixed on both left and right sides. Three parallel forces with a random angle θ are applied at the center region of the top edge of the design domain. The design domain is discretized with 40 polygonal elements after 100 Lloyd's iterations (Talischi et al. 2012a) shown in Figure 6.6 (a). On the other hand, the ground structure with a level 4 connectivity (1858 design variables) is illustrated in Figure 6.6 (b).

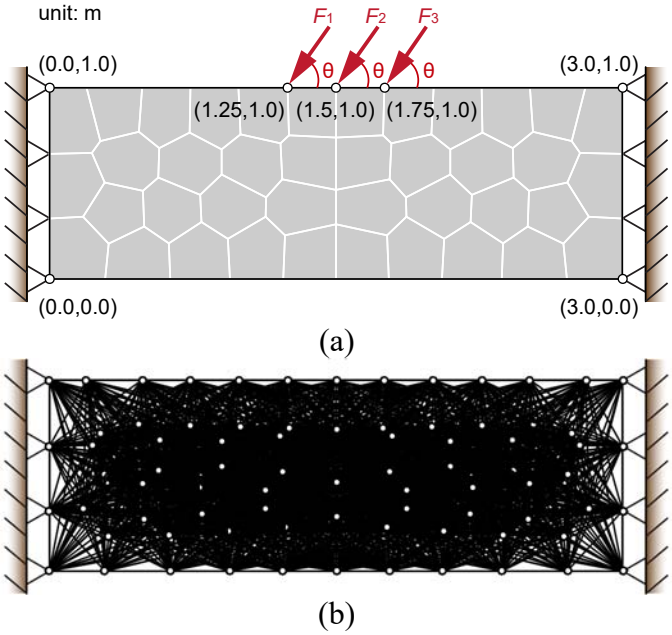

Figure 6.6: Clamped beam problem: (a) loadings and boundary conditions, and (b) level 4 connectivity ground structure.

Table 6.2 lists the mean value μ_m and standard deviation σ_s for each random variable. The target failure probability of the compliance limit-state function $Pf^{target} = 0.005$, the upper bound of design variable $A^{upper} = 1.0$ m^2, and the discrete filter coefficient $\alpha_f = 0.01$, and $C_{max} = 8$ are used in optimization.

To see the effect of the random variable θ on the final topology, two cases are considered for RBTO: (Case I) four random variables of F_1, F_2, F_3, E and deterministic force angle θ, and (Case II) five random variables of F_1, F_2, F_3, E, and θ. Figure 6.7 shows the optimal configuration of bar connectivities and sizes from DTO and RBTO. Due to the risk caused by the uncertainties, increased bar areas and additional connectivities are observed in RBTO compared to those from DTO. In addition, dominant directions of bar connectivities are between the forces and supports as shown in Figures 6.7 (a) and 6.7 (b). Additional consideration of the random variable θ (Case II) results in the creation of arch-shape connectivities towards the center on the bottom in Figure 6.7 (c), primarily due to the possibility of forces with $\theta > 45°$ that cause the further increase in compliance. Therefore, the compliance will be reduced by providing the arch-shape connectivities.

The convergence history in Figure 6.7 (d) illustrates that the proposed method is able to find the optimal solution quickly and efficiently.

Table 6.2: Parameter values of random variables used for the clamped beam problem.

E (N/m^2)		F_1 (N)		F_2 (N)		F_3 (N)		θ (N)	
μ_{mE}	σ_{sE}	μ_{mF1}	σ_{sF1}	μ_{mF2}	σ_{sF2}	μ_{mF3}	σ_{sF3}	$\mu_{m\theta}$	$\sigma_{s\theta}$
100000	7500	600	150	900	90	700	140	45	6.82

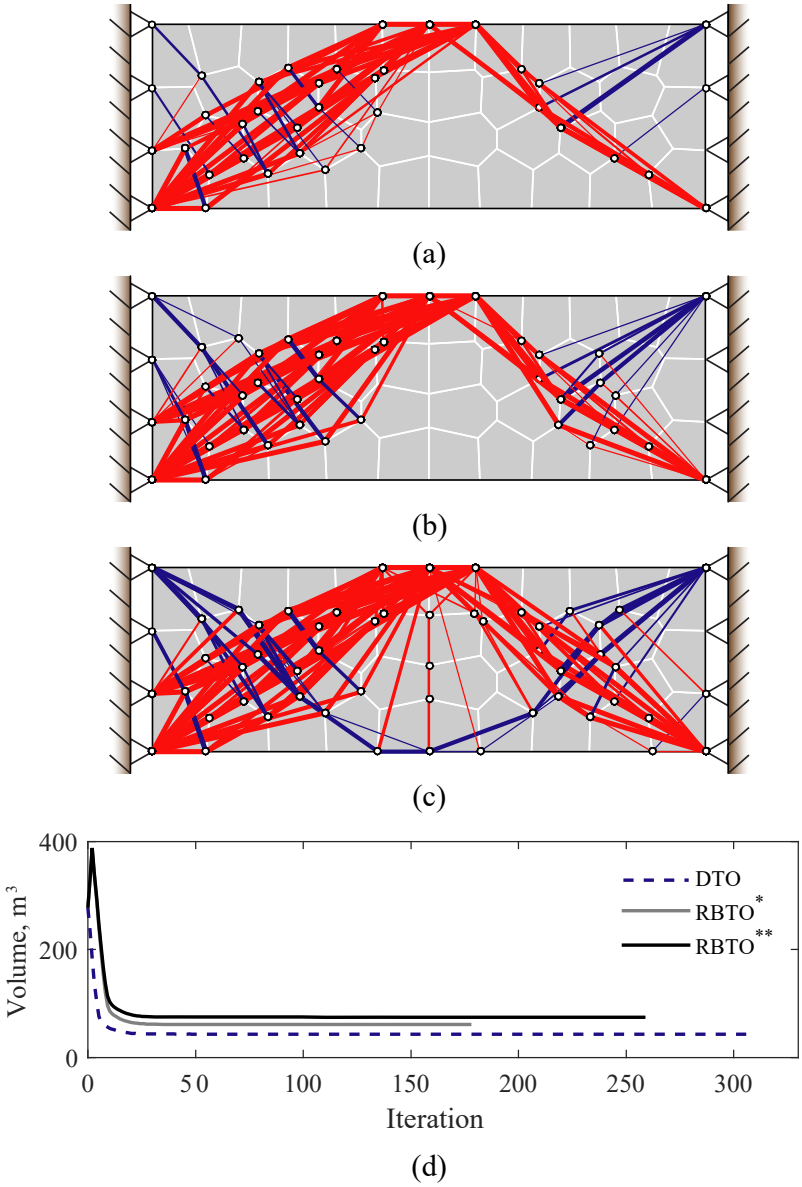

Figure 6.7: Topology optimization results by discrete filter (α_f= 0.01): (a) DTO (volume = 43.06 m^3), (b) RBTO − Case I (volume = 60.82 m^3), (c) RBTO − Case II (volume = 74.67 m^3), and (d) convergence history.

6.4.3. Curved cantilever structure optimization

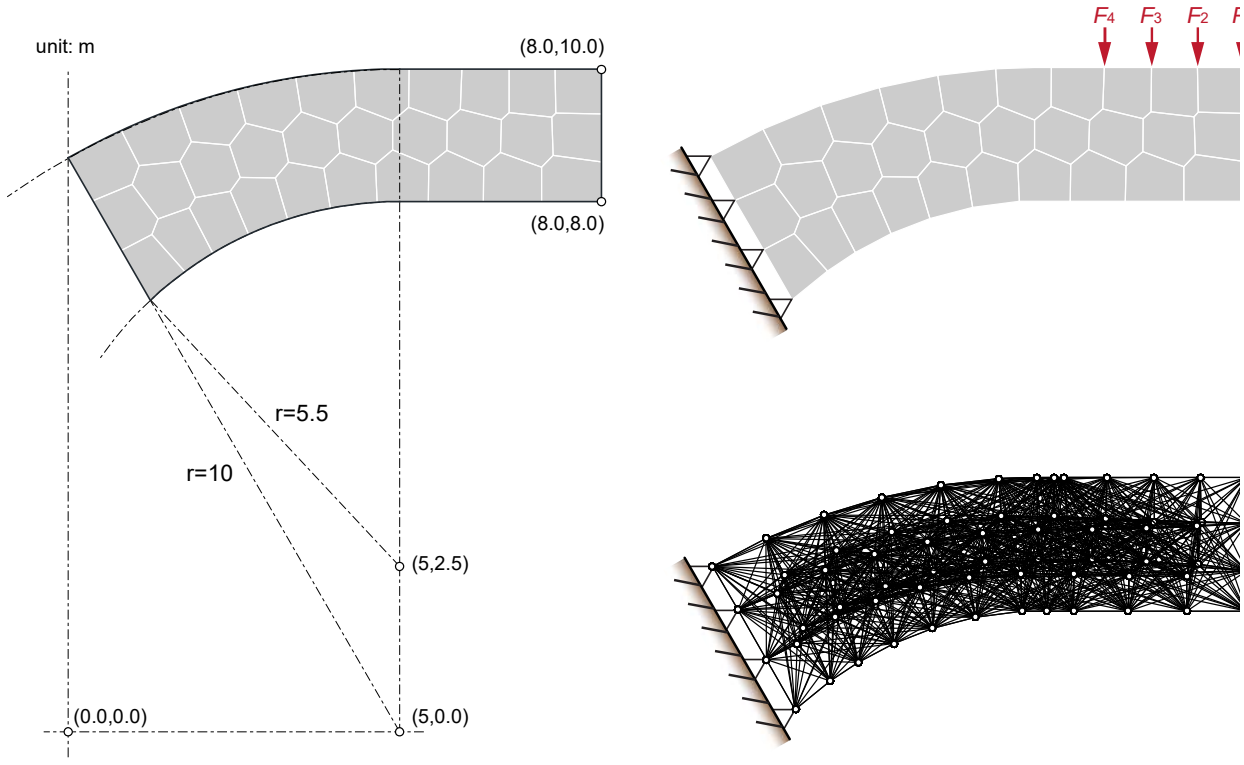

Figure 6.8: Curved beam problem: (a) design domain, and (b) loadings and boundary conditions, and level 3 connectivity ground structure.

The proposed method is also applied to design a curved cantilever truss clamped on the left side to demonstrate how the correlation affects the spatial distribution of structural members. The design domain discretized with 30 polygonal elements after 100 Lloyd's iterations is shown in Figure 6.8 (a). The ground structure for a level 3 connectivity is then generated using "GRAND" (Zegard and Paulino 2014), which generates a ground structure with a total of 981 truss members. The limit-state function is defined on the compliance computed with multiple loads, i.e. $g(8 - C(\mathbf{A},\mathbf{X}))$. Young's Modulus E and forces F_i, $i = 1,\ldots, 4$ are assumed to be normal random variables. The mean and the standard deviation of each random variable are shown in Table 6.3. The target failure probability, the upper bound of design variables, and the discrete filter coefficient are set to $P_f^{\text{target}} = 0.00075$, $A^{\text{upper}} = 1.5$ m^2, $\alpha_f = 0.01$, respectively. The correlation coefficient $\rho_{ij,}\, i \neq j,\, i,$

j = 1,…, 4 between random forces is varied from 0.0 to 0.75 to investigate the effect of the correlations between the uncertain loadings on the final topology.

Table 6.3: Parameter values of the probabilistic constraint and random variables filter used for the curved cantilever structure problem.

E (N/m^2)		F_1 (N)		F_2 (N)		F_3 (N)		F_4 (N)	
μ_{mE}	σ_{sE}	μ_{mF1}	σ_{sF1}	μ_{mF2}	σ_{sF2}	μ_{mF3}	σ_{sF3}	μ_{mF4}	σ_{sF4}
100000	7500	50	10	80	12	45	6.75	35	5.25

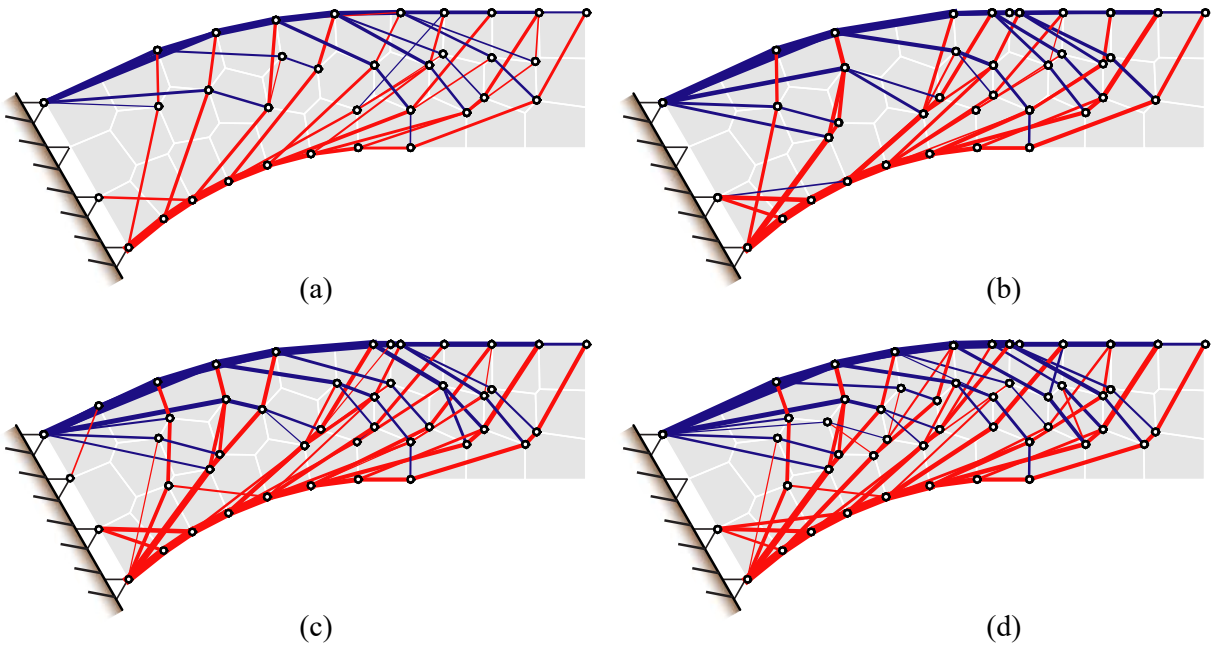

Figure 6.9: Topology optimization results by a discrete filter (α_f = 0.01): (a) DTO (volume = 54.73 m^3), (b) RBTO, ρ_{ij} = 0.0 (volume = 90.79 m^3), (c) RBTO, ρ_{ij} = 0.5 (volume = 105.39 m^3), and (d) RBTO, ρ_{ij} = 0.75 (volume = 113.91 m^3).

The optimization results from DTO and RBTO are shown in Figure 6.9. The line thicknesses in the plots are normalized to the upper bound of the cross sectional area which is 1.5 m^2. Compared to the results from DTO, overall cross sectional areas on top and bottom chords are increased in RBTO. Furthermore, additional connectivities of truss elements are clearly observed

in the RBTO results. Those connectivities in RBTO increase the stiffness of the truss structure so that the compliance decreases to satisfy the target failure probability. Furthermore, optimization results from RBTO show that the increase in the correlation coefficient results in the higher optimized volume, primarily because the positive correlation between forces increases the chance of violating the limit-state function by a raised compliance. The convergence histories of the objective function and the failure probability over iterations are plotted in Figure 6.10.

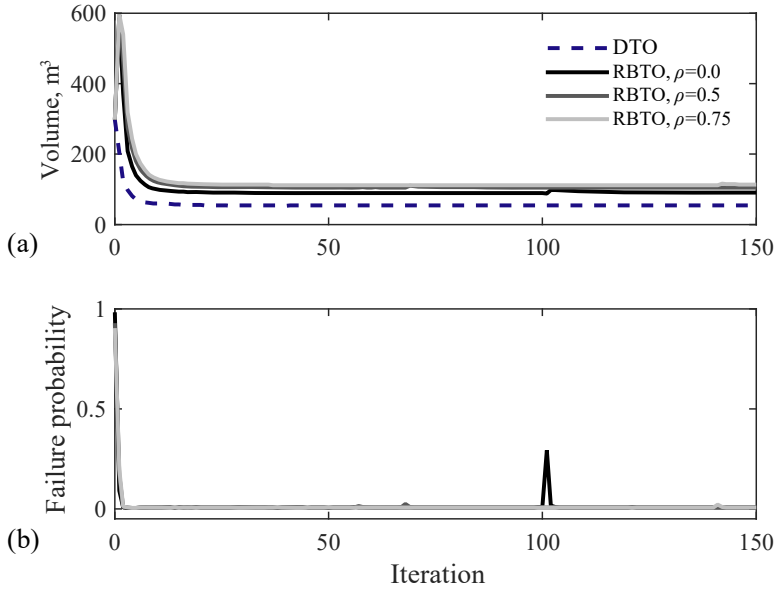

Figure 6.10: Convergence history of the curved beam problem: (a) volume, and (b) failure probability.

6.4.4. Roof structure optimization

The proposed method is applied to a large space structure fixed on ground level to identify the optimal topology while achieving the desired reliability. The problem domain is discretized with solid elements as shown in Figure 6.11(a). Figures 6.11 (b) and 6.11 (c) provide top and side views, respectively. Based on the discretized domain, the ground structure analysis and design in 3D (GRAND3, Zegard and Paulino 2015) were adopted to generate a ground structure using restriction zones (Figures 6.12 (a) and 6.12 (b)).

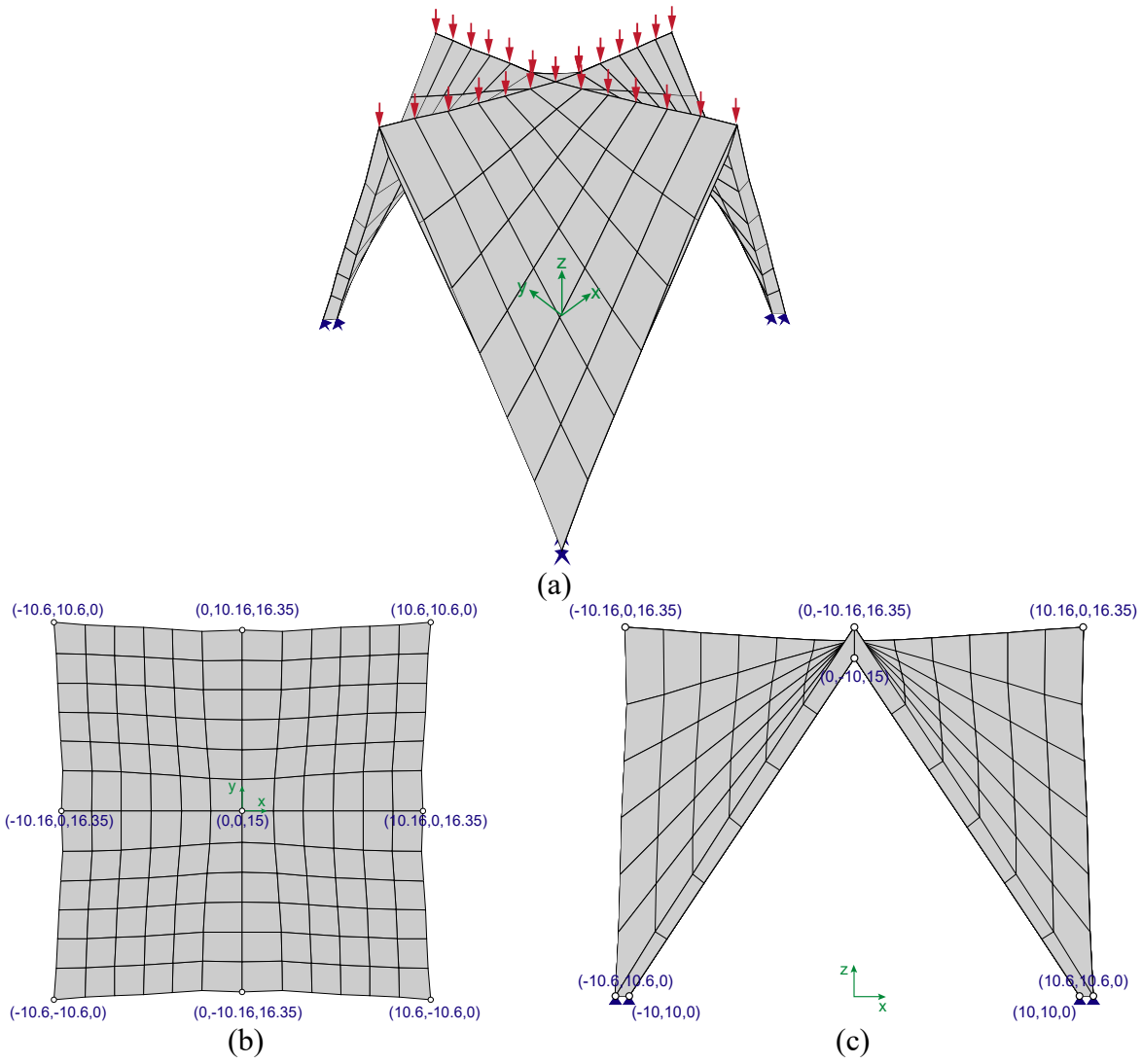

Figure 6.11: Roof structure optimization example: (a) roof structure domain, loadings and boundary conditions, (b) top view, and (c) side view.

The restriction zones prevent truss members in the ground structure from passing through the restricted region. Two connectivity levels of the ground structure shown in Figures 6.12 (c) and 6.12 (d) are generated and used for optimization with initial design variables set to 0.25 m^2. Young's modulus and applied forces (Figure 6.11 (a)) are considered as random variables following the normal distribution. The compliance under multiple loads is computed as

$$C(\mathbf{A},\mathbf{X}) = \sum_{i=1}^{nf} \mathbf{f}_i^{\mathrm{T}}(\mathbf{X})\mathbf{u}_i(\mathbf{A},\mathbf{X}) \tag{6.20}$$

where *nf* denotes the number of forces. Parameters of the probabilistic constraint on the compliance and random variables and the discrete filter are given in Table 6.4.

Figures 6.13 and 6.14 show a comparison of the optimized results for level 1 and 4 connectivity levels, respectively by DTO and RBTO. The connectivity level leads to the different topologies such as different connectivity of members in optimized solutions. Differences in optimal solutions between the deterministic and the probabilistic constraints can be clearly observed from the optimized results. To achieve the target failure probability, the overall member sizes are increased, and more connectivities between bars remain. Figure 6.15 shows optimal topologies based on varying filter sizes. It should be noted that those solutions in global equilibrium satisfy the target failure probability. Figure 6.16 shows the convergence history of the volume in optimization. The resulting volume of high connectivity level is slightly reduced for both DTO and RBTO, as expected since a higher number of design variables (connectivities) typically leads to a reduced objective. Table 6.5 presents results associated with the roof structure optimization problem.

Table 6.4: Parameter values of the probabilistic constraint and random variables, and the discrete filter used for the roof structure problem.

E (GPa)		F (kN)		$C_{\max}$	P_f^{target}	α_f	A^{upper} (m^2)
μ_{mE}	σ_{sE}	μ_{mF}	σ_{sF}				
200	40	100	20	10	0.0025	0.01	1.5

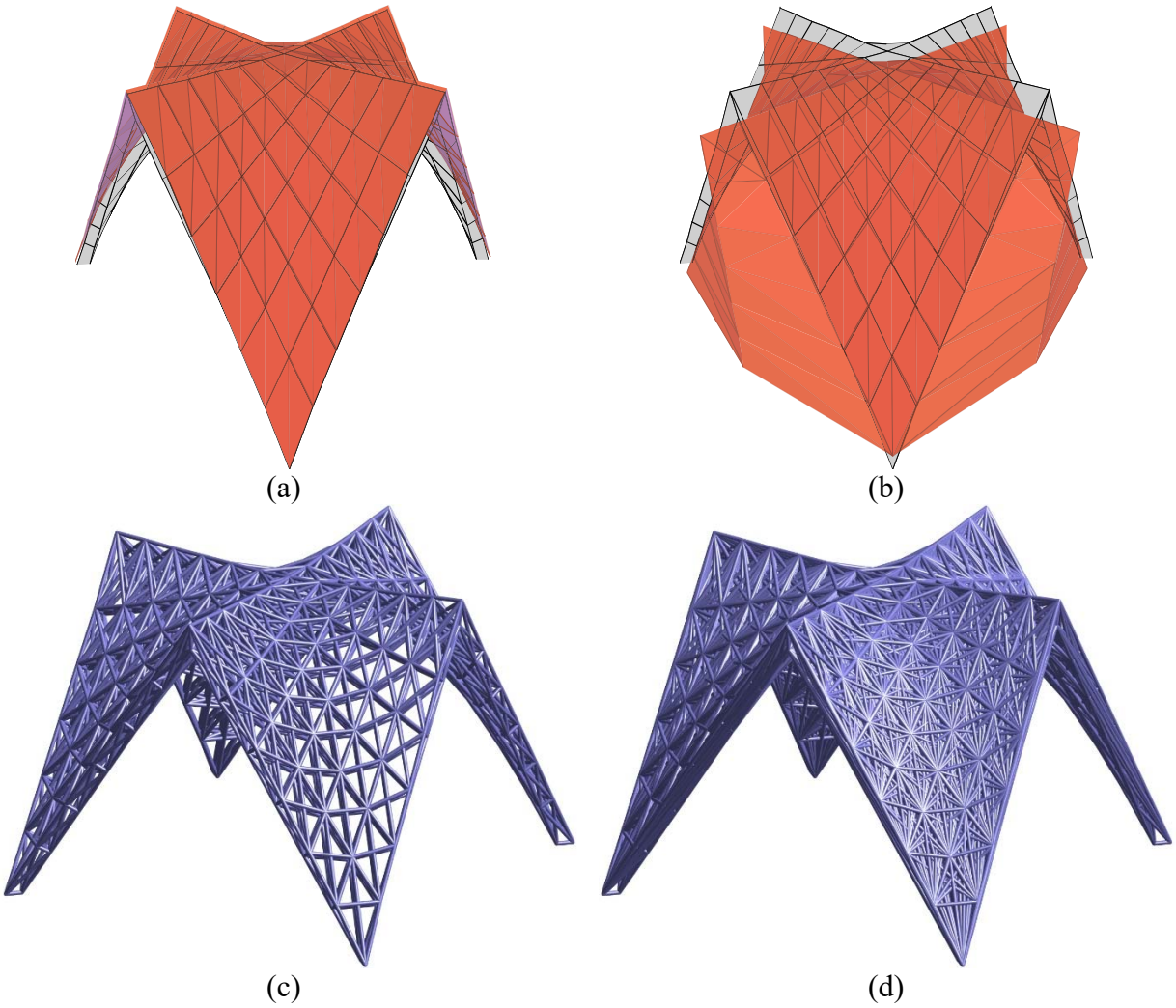

Figure 6.12: Ground structure: (a) upper restriction surface, (b) lower restriction surface. (c) level 1 connectivity (2,569 design variables), and (d) level 4 connectivity (7,995 design variables).

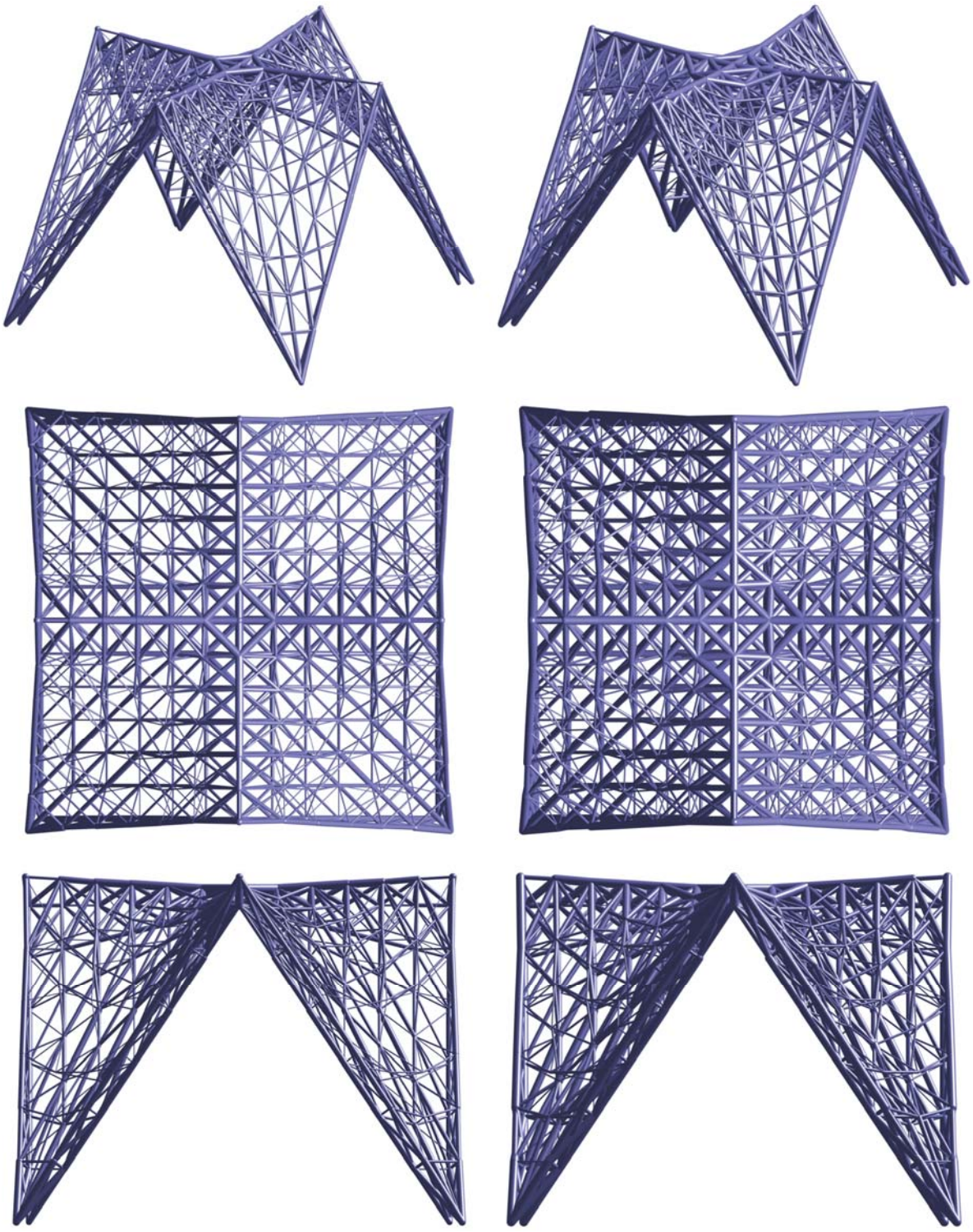

(a) (b)

Figure 6.13: Final topology by discrete filter (α_f = 0.01, level 1 connectivity): (a) DTO, and (b) RBTO (P_f^{target} = 0.0025).

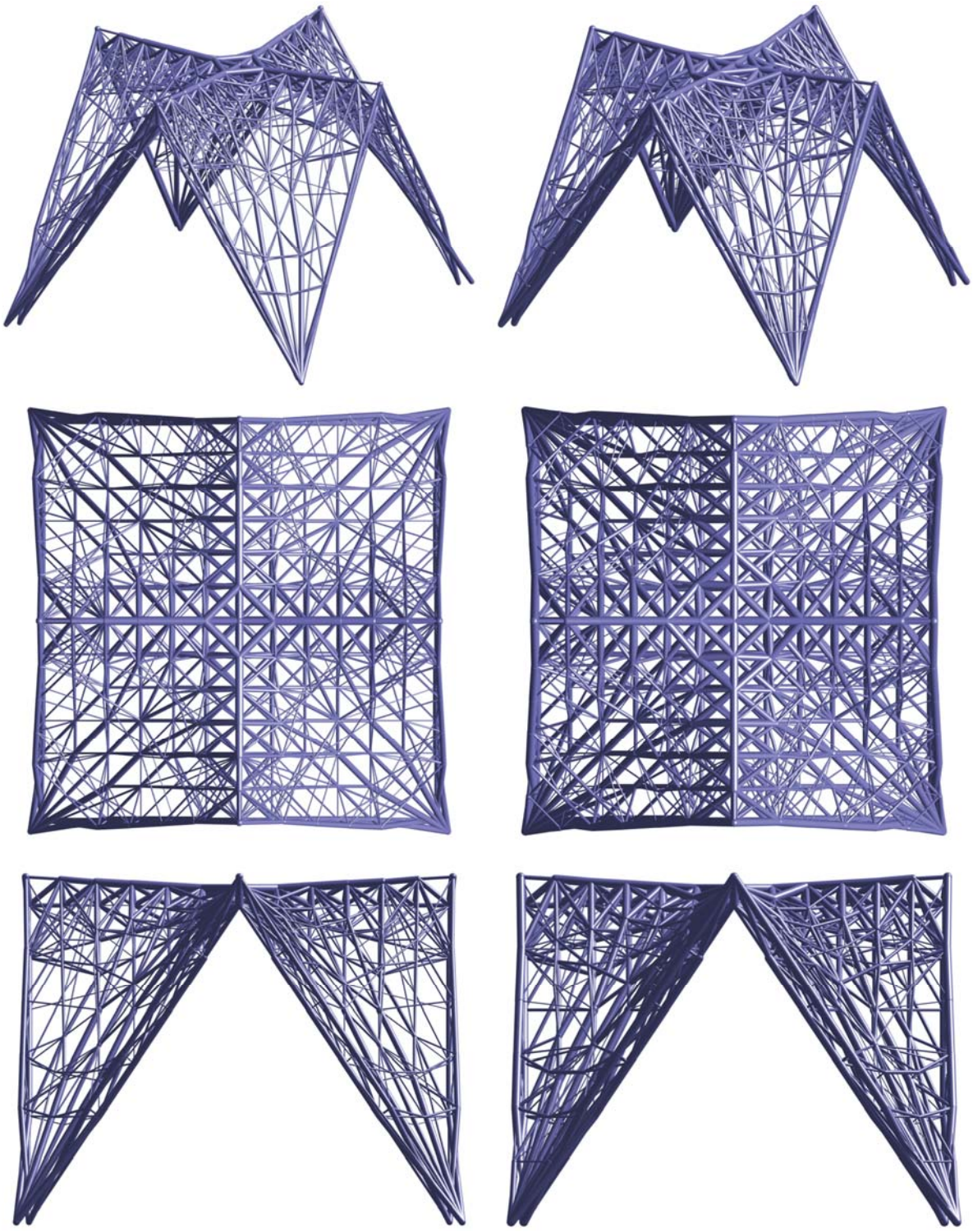

(a) (b)

Figure 6.14: Final topology by discrete filter (α_f = 0.01, level 4 connectivity): (a) DTO, and (b) RBTO (P_f^{target} = 0.0025).

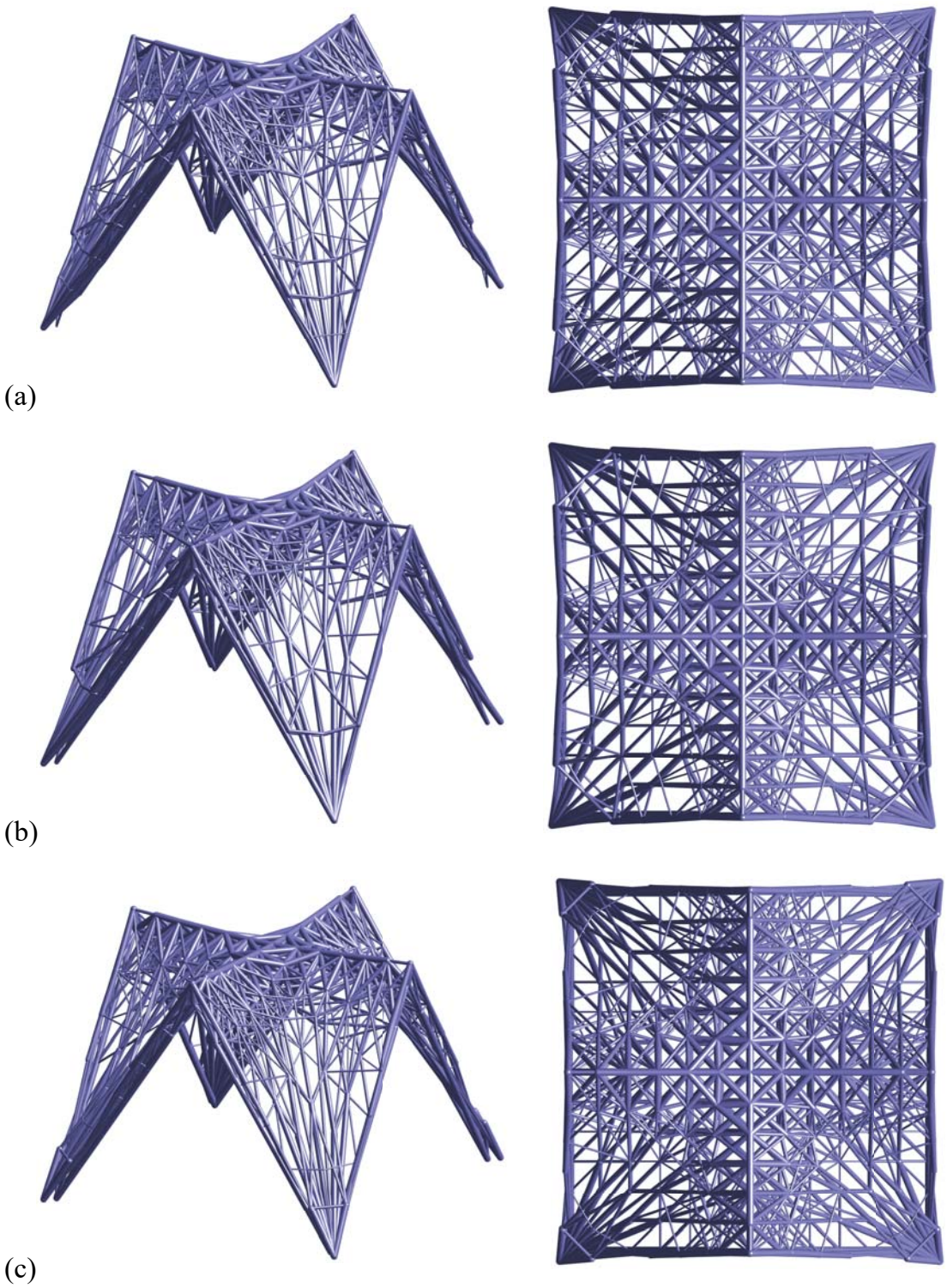

Figure 6.15: Final topology by discrete filter (level 4 connectivity, $P_f^{\text{target}} = 0.0025$): (a) $\alpha_f = 0.02$, (b) $\alpha_f = 0.03$, and (c) $\alpha_f = 0.04$.

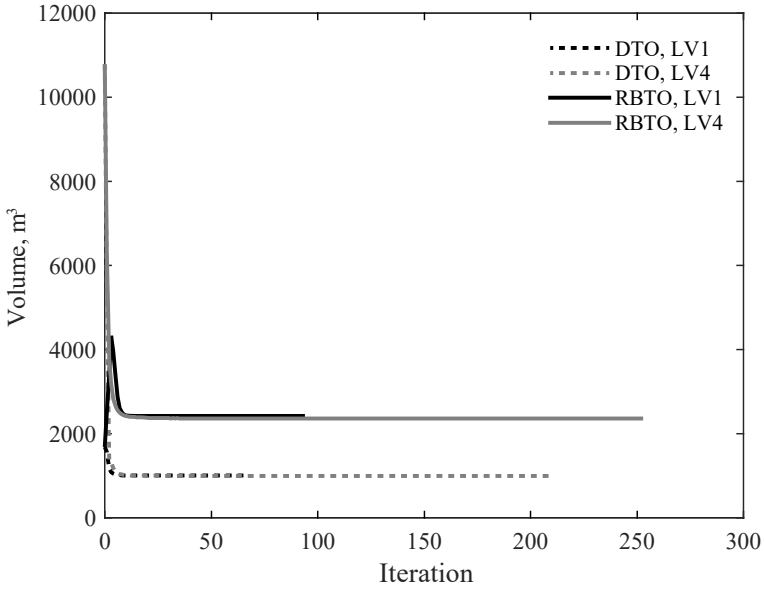

Figure 6.16: Convergence history of roof structure optimization.

Table 6.5: Representative parameters for optimal solutions of the roof structure problem.

	Level 1 connectivity	Level 4 connectivity			
		Filter size, α_f			
	0.01	0.01	0.02	0.03	0.04
Volume	2419.73	2361.73	2376.27	2433.11	2531.09
$\|\|\mathbf{Ku}-\mathbf{f}\|\|/\|\|\mathbf{f}\|\|$	3.10×10^{-6}	2.57×10^{-6}	2.69×10^{-6}	3.40×10^{-5}	2.69×10^{-5}
P_f FORM	0.0025	0.0025	0.0025	0.0025	0.0025

6.4.5. Dam structure optimization

The optimization problem is focused on a dam structure clamped at a bottom level and at the both left and right sides. The design domain is discretized using 216 solid elements and its plan views and a section view are as shown in Figure 6.17. The structure is subjected to distributed loads at each node in y-direction shown in Figure 6.18. The applied forces and Young's modulus are assumed to follow the normal distribution. All random variables are assumed to be statistically independent each other. The ground structure is generated for the level 3 connectivity as shown in Figure 6.19 (a).

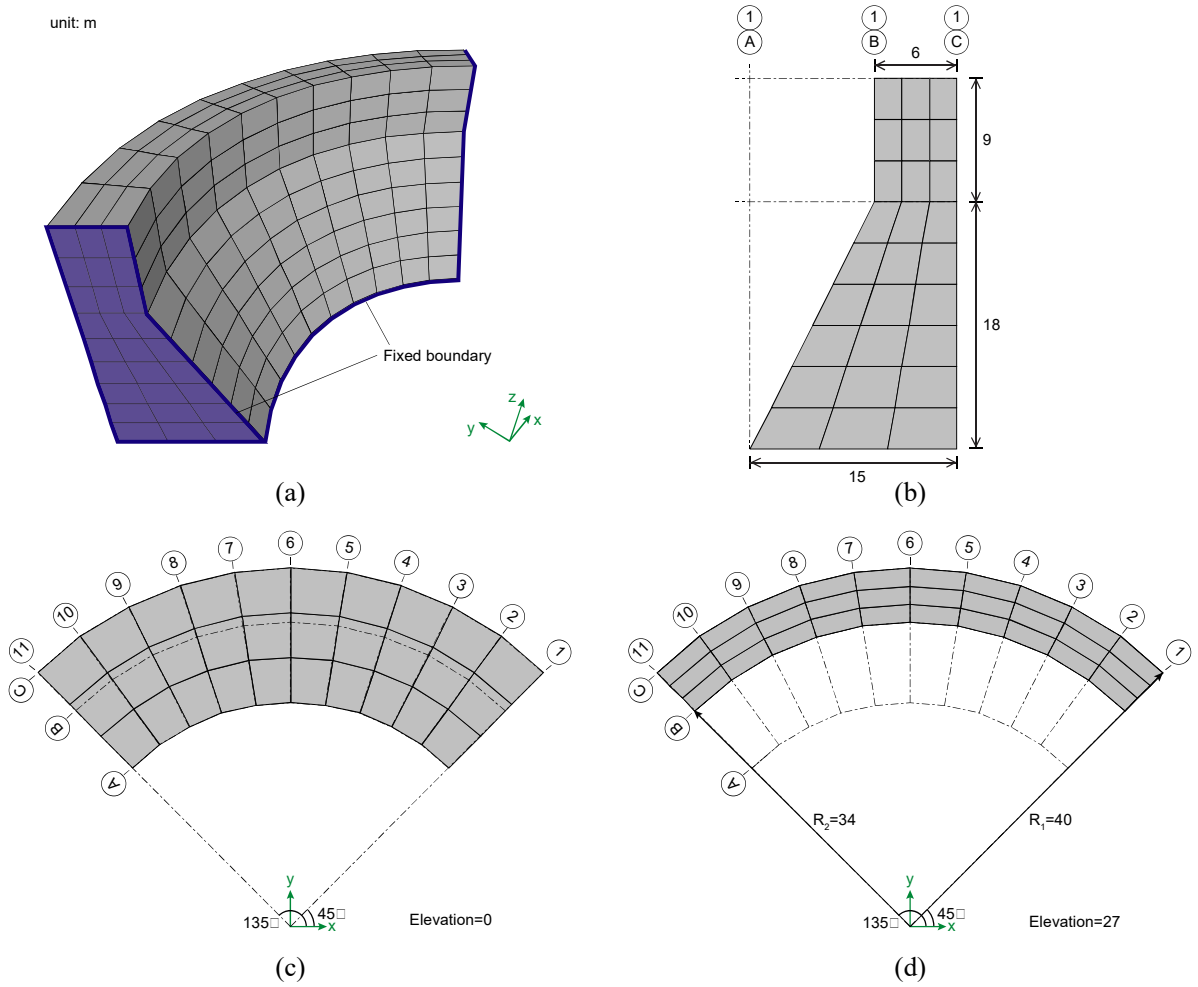

Figure 6.17: Dam structure problem: (a) problem domain definition, boundary conditions, (b) section view, (c) plan view at elevation 0 m, and (d) plan view at elevation 27 m.

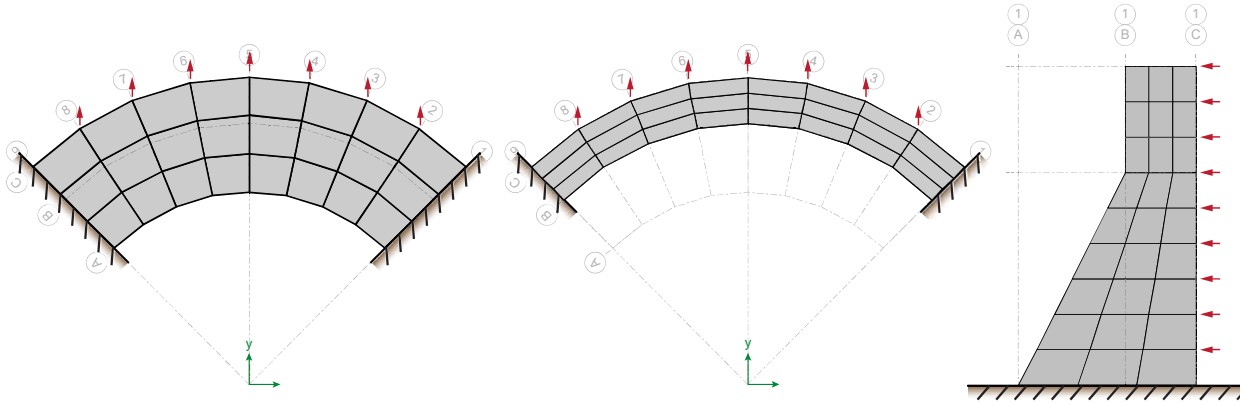

Figure 6.18: Supports and loadings configurations.

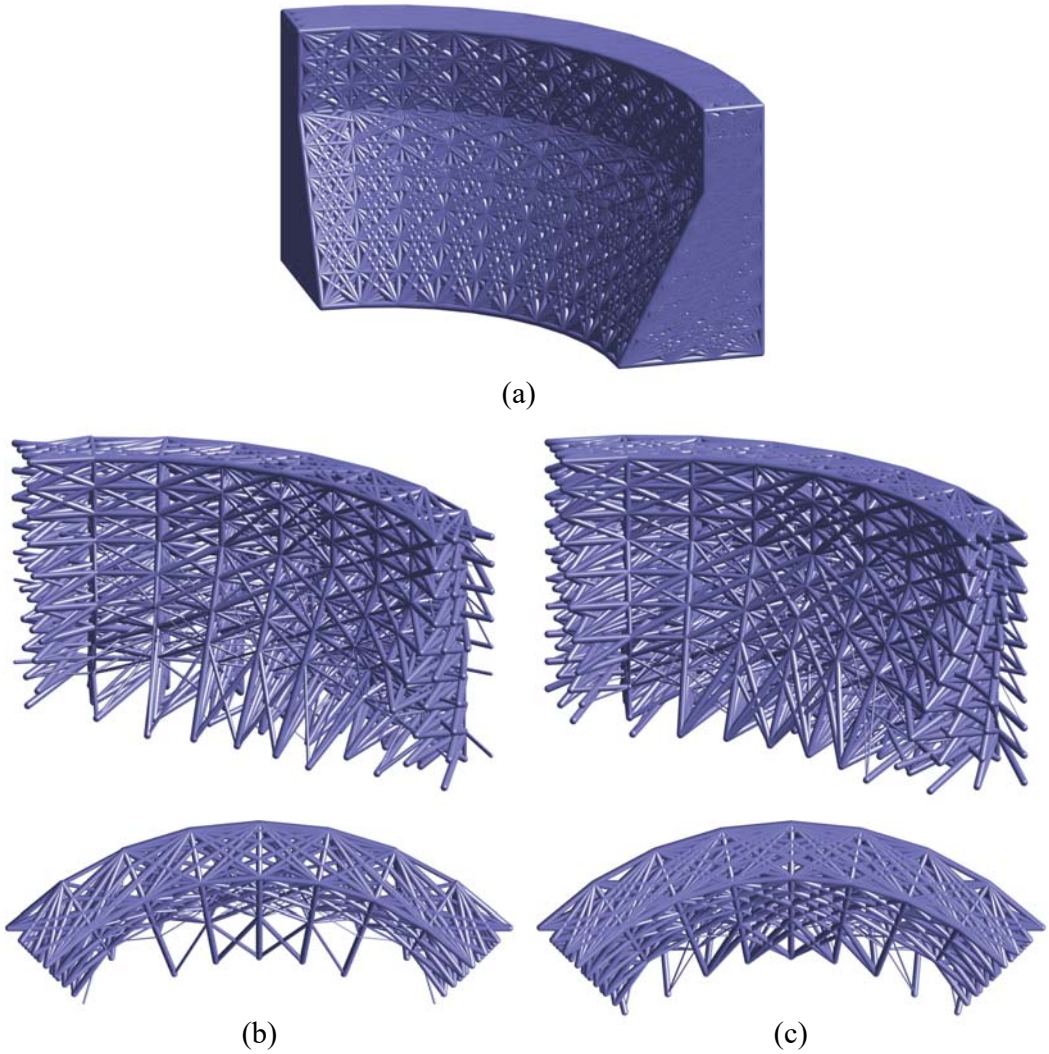

(a)

(b) (c)

Figure 6.19: Ground structure and optimized results: (a) level 3 connectivity ground structure, (b) DTO, and (c) RBTO, $P_f^{\text{target}} = 0.01$.

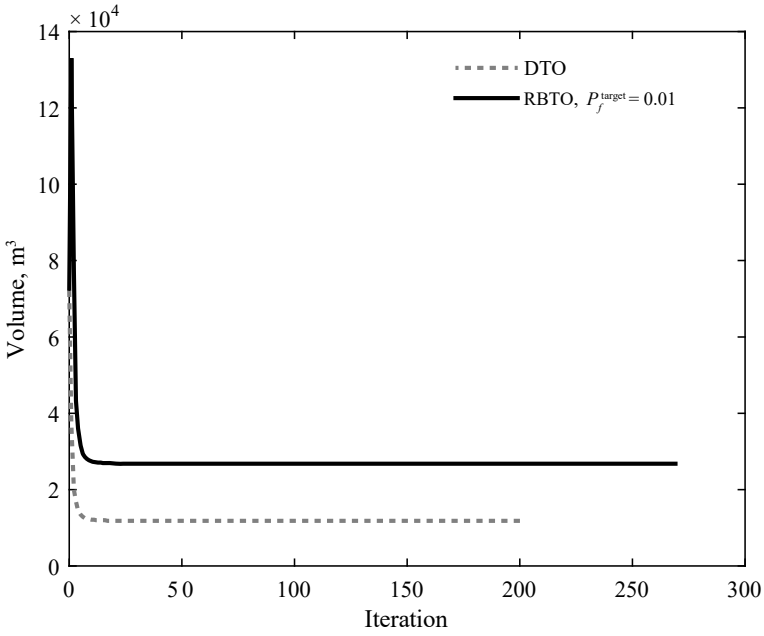

Figure 6.20: Convergence history of the dam structure.

Optimization results from DTO and RBTO with $P_f^{\text{target}} = 0.01$ are plotted in Figures 6.19 (b) and (c). Convergence of the objective function is illustrated in Figure 6.20.

6.5. Concluding remarks

This chapter presents a framework of single-loop reliability-based topology optimization that incorporates the discrete filtering scheme proposed by Ramos Jr. and Paulino (2016). Reliability-based topology optimization using the ground structure method with the conventional filtering scheme (cut-off) often leads to solutions that violate the prescribed failure probability after the post processing. The proposed method successfully finds topology optimization solutions that satisfy the target failure probability and that are in the global equilibrium. Numerical verifications by the first-order reliability method and Monte Carlo simulations confirm that the optimal topologies obtained by the proposed approach satisfy the given probabilistic constraints unlike those by a conventional filtering scheme.

The effects of uncertainties in loads and material property on optimal topologies are clearly observed and investigated through comparison with the results of deterministic optimization. Using the different discrete filter parameter and the connectivity level of the ground structure result in the various topologies with different optimized sizes while satisfying the desired failure probability. The variety of optimal solutions offers with the proposed method can allow engineers to develop multiple structural design schemes.

In the present study, a single probabilistic constraint on the compliance is considered. In reality, different types of constraints such as displacement constraints and stress constraints under uncertainties are also of great interest in structural engineering. Most of the truss structures are indeterminate so that single failure (or a component) may not result in failure of the entire structural system. Therefore, the aforementioned different failure events and various failure sequences need to be considered for more realistic applications of engineering designs. Also, a system failure event with statistical dependence between component failure events needs to be addressed in RBTO. Those remain as potential future research topics.

Chapter 7

Conclusions and future work

In this thesis, theoretical and computational frameworks are investigated and developed in reliability-based design and topology optimization of structures subject to static, dynamic forces as well as stochastic excitations. First, concepts of structural topology optimization considering fundamental dynamic excitations is tailored and then the numerical scheme to obtain high-resolution topologies while achieving computational efficiency is developed. Second, efficient sensitivity analysis methods of system failure probability are developed so that they allow the identification of significant factors in reliable engineering designs, and the use of the gradient-based optimization algorithms for reliability-based design and topology optimization. Third, the inherent stochastic excitations caused by natural or man-made hazards are explored through intricate random vibration analysis in optimization. Theoretical and numerical frameworks of topology optimization are developed for building structures under stochastic excitations considering practical engineering problems. In this chapter, a brief summary and suggested future work are presented.

7.1. Concluding remarks

One of the challenging issues related to optimization in dynamics is the expensive computational costs of the finite element analysis (FEA) in optimization procedures. The resolution of optimal topologies (optimal material distributions) is proportionally linked to the mesh size used in the FEA in conventional topology optimization. By using two different types of meshes such as a coarse finite element mesh to perform the FEA and a fine design variable mesh for optimization,

the overall computational cost can be reduced while maintaining high resolution designs. This optimization framework is especially beneficial for structural dynamics problems such as forced vibration optimization or eigenfrequency optimization, which require intensive computational cost compared to static optimization problems. In addition, irregular polygonal meshes based on the concept of Voronoi diagrams help overcome difficulties in discretizing complicated geometries of design domains. In order to address aforementioned issues, *Polygonal multiresolution topology optimization* (*PolyMTOP*) was developed. The method is four times (or more) faster than the current conventional approach for structural dynamics problems.

The system failure probability consists of many component failure events in engineering constraints, and its estimation commonly involves solving of a multi-fold integral. The lack of closed form solution of the integral makes the estimation more challenging because the numerical integration is impractical for such large number of random variables and events that need to be considered. To overcome these issues, the efficient algorithm of parameter sensitivity analysis of system reliability, *CSP* (*Chun-Song-Paulino*) method was developed. The CSP method is designed for large-scale system failure problems defined in implicit high-dimensions and time domain. It performs sensitivity analysis after simplifying the integral spaces of the system failure probability from high-dimensions to the equivalent two dimensions. The developed method was successfully applied to computing sensitivities of stochastic responses, such as the first-passage probability in time domain. This method allows for the incorporation of gradient-based algorithms into optimization frameworks in order to efficiently identify optimal solutions for problems with a large number of design variables. The CSP method was further developed to derive a new adjoint variable method for sensitivity analysis of probabilistic constraints under stochastic processes defined in time domain.

In order to incorporate random processes and structural reliability analysis into optimization, the novel *stochastic topology optimization* framework was developed. Through this framework, random excitations such as earthquake ground motions can be considered in the finite element

setting and topology optimization. During the development of this new framework, the CSP method was adopted to compute gradients of probabilistic engineering constraints associated with the stochastic responses, e.g., drift ratios. The stochastic topology optimization framework was successfully applied to a conceptual design of lateral-load resisting systems with a desirable level of reliability subject to stochastic ground motions. Moreover, the framework was further extended to stochastic reliability-based design optimization of truss structures, so that the structure subject to ground excitations can be optimized under probabilistic constraints on stresses in elements or maximum drifts.

Finally, the optimization scheme employing the discrete filter was proposed to ensure that optimized solutions satisfy the probabilistic constraints, and incorporating single-loop approach to enhance the computational efficiency of the proposed RBTO method. The effects of uncertainties in loads and material property on optimal topologies were observed and investigated through comparison with the results of deterministic optimization. Optimal solutions satisfying the desired failure probability and global equilibrium were obtained from the proposed method. Furthermore, the variety of optimal solutions can be delivered with the proposed method for applications in engineering.

7.2. Suggestions for future work

This section discusses some global ideas that may become direct or indirect extensions of this work.

7.2.1. Stochastic topology optimization in frequency domain

Research efforts have been focused on developing stochastic topology optimization framework using the discrete representation method. The discrete representation method handles the stochastic processes and derives probabilistic characteristics in time domain. The discretized time

points are considered as random variables in this method. The realization of the component failure events, therefore, need to be evaluated for the probabilistic constraint defined within a given time interval. Although it is a robust and accurate method, it requires greater computational cost and leads to time consuming processes, such as repeated evaluation of the probabilistic constraints. In order to overcome these issues, an alternative approach to characterize the stochastic input and output process in the frequency domain can be developed. The findings in this thesis can be extended and further applied to the interesting stochastic problems related to frequency-based concepts, such as power spectral density functions and spectral moments. Various failure analysis, such as probability distribution of peaks, crossing rates by using the power spectral density, stochastic fatigue analysis, and prediction of the accumulated damage can be performed in frequency domain. The applications of the topology optimization in the frequency domain in terms of the topics aforementioned still remain unexplored.

7.2.2. Extension of stochastic optimization framework for multi-hazards

Recent earthquake and tsunami events have demonstrated the limitations of current structural and geotechnical design practices that satisfy only one type of hazard at a time, leaving the structural system vulnerable to other hazards occurring concurrently. Therefore, a comprehensive design that satisfies more than one hazards will strengthen and enhance the robustness and safety of building structures. An effective tool to achieve this improved design is structural optimization. Thus, continuation of research in various aspects of natural hazards such as wind loads and ocean waves, and derivation of efficient numerical models for analysis and applications need to be explored. Algorithms and frameworks presented in this thesis can be implemented and modified to adopt the new environmental and structural challenges. Furthermore, the impact of the structural frame and connection behavior on optimal topology, and effective schemes for optimal building structure design under stochastic excitations need to be also considered.

7.2.3. Connection between architecture and engineering through visualized analysis, design and optimization tools

The objective of the extension is to develop a structural design optimization tool for engineers and architects so that professional conflicts regarding aesthetics, stability and safety of building projects can be considered and addressed. A real-time visualization program for structural analysis and design optimization with integrated visual and architectural programming languages such as Grasshopper 3D can be developed. Thus, changes in parameters and forms by architects will be reflected in structural optimization results considering engineering constraints in a real-time. Conversely, various structural options for a design project can be provided to architects, so that the functionalities of structural components embedded in architectural views can be visualized and analyzed. The final optimized result will be interpreted and transferred to computer-aided design (CAD) drawings. This integrated visualization platform will enable professionals to communicate and collaborate effectively with each other to successfully complete proposed projects.

7.2.4. Integration of additive manufacturing into structural design, material design and optimization

This research aims to incorporate emerging efficiencies to transform the proposed and existing structural design and topology optimization framework. To that end, 3D printing technology will be utilized. Additive manufacturing enables a two-way approach in the framework, in which optimal solutions can be physically reproduced through 3D printing and verified through laboratory testing. In addition, the three dimensional models can be used to accurately portray design concepts and changes. This integration process can also be applied to optimize the performance of desirable structures, reducing the gap between optimization and application of building structures, extending applications to mechanical, aerospace engineering and materials.

7.2.5. Catastrophic hazard and damage modeling for risk-informed management

Finding structural engineering solutions begins with the identification of structural demands and challenges. This fundamental yet significant process of risk assessment and management of structures are critical in decision making. Structures are constantly exposed to natural and man-made hazards, creating inherent uncertainties in the performance. This research is targeted at deriving mathematical models to represent various aspects of possible failure events that structures must withstand during the operation period. Accurate estimation of predicted damage and the model's robustness under uncertain hazards will be studied so that reliable engineering design solutions can be proposed. As a long-term research plan, further extension of catastrophic hazards modeling for probabilistic estimation of damages to support risk-informed decision-making process using machine learning theory can be considered.

7.2.6. Development of new computer-based simulation and interdisciplinary computing program

In order to increase the research efficiency, a universal computational tool needs to be developed to focus directly on developing, validating and disseminating innovative design technologies for structures. This tool can be open source and freely available to both research communities and the industry so that researchers and practicing professionals can integrate versatile and robust engineering computational tools according to specifications of the project. This tool can be used as a platform to satisfy safety measures and target costs as well as assessing post-disaster functionality. Also, the research involves more computational performance on the multiscale framework from emerging high performance computational resources. This project can be approached from two different directions to incorporate: (a) general-purpose parallel processors to increase capabilities for civil engineering design and applications; (b) massively parallel supercomputing for large scale problems such as risk assessment of multiple hazards.

Appendix A

Derivation of Equation 3.11

To derive Equation 3.11 with a uniform time step, the convolution integral in Equation 3.9 is carried out for discrete time intervals. An entry of the vector $\mathbf{a}(t_j)$ can be written as follows:

$$a_i(t_j) = \int_0^{t_j} s_i(\tau) h_s(t_j - \tau) d\tau \tag{A.1}$$

where

$$t_i = i\Delta t,\ t_j = j\Delta t \tag{A.2}$$

Then, one can consider the following three cases:

1. $i=j$

$$\begin{aligned} a_i(t_i) &= \int_0^{t_i} \sqrt{2\pi\Phi_0\Delta t}\cdot h_f(\tau - t_i) h_s(t_i - \tau) d\tau \\ &= \sqrt{2\pi\Phi_0\Delta t}\cdot\left(\int h_f(\tau - t_i) h_s(t_i - \tau) d\tau\right)\Big|_{\tau=t_i} \quad (\because\ h_f(\tau - t_i) = 0 \text{ for } 0 \le \tau < t_i) \end{aligned} \tag{A.3}$$

2. $i>j$

$$\begin{aligned} a_i(t_j) &= \int_0^{t_j} s_i(\tau) h_s(t_j - \tau) d\tau = \int_0^{t_j} \sqrt{2\pi\Phi_0\Delta t}\cdot h_f(\tau - t_i) h_s(t_j - \tau) d\tau \\ &= 0\ (\because\ h_f(\tau - t_i) = 0 \text{ for } 0 \le \tau < t_i) \end{aligned} \tag{A.4}$$

3. $i<j$

$$\begin{aligned} a_i(t_j) &= \int_0^{t_j} s_i(\tau) h_s(t_j - \tau) d\tau = \int_0^{t_j} \sqrt{2\pi\Phi_0\Delta t}\cdot h_f(\tau - t_i) h_s(t_j - \tau) d\tau \\ &= \int_{t_i}^{t_j} \sqrt{2\pi\Phi_0\Delta t}\cdot h_f(\tau - t_i) h_s(t_j - \tau) d\tau\ (\because h_f(\tau - t_i) = 0 \text{ for } 0 \le \tau < t_i) \\ &= \int_0^{t_j - t_i} \sqrt{2\pi\Phi_0\Delta t}\cdot h_f(\tilde{\tau}) h_s(t_j - t_i - \tilde{\tau}) d\tilde{\tau} \\ &= \int_0^{c\Delta t} \sqrt{2\pi\Phi_0\Delta t}\cdot h_f(\tilde{\tau}) h_s(c\Delta t - \tilde{\tau}) d\tilde{\tau},\ c = j - i \end{aligned} \tag{A.5}$$

Thus,

$$a_i(t_j) = a_i(j\Delta t) = \begin{cases} a_n(t_n) & i = j \\ 0 & i > j \\ a_{n-c}(t_n) & i < j,\ c = j - i \end{cases} \tag{A.6}$$

Therefore, the uniform step size (t_n-t_{n-1} = Δt, t_n = t_0) in the convolution integral leads to the following expression:

$$a_i(t_j) = a_i(j\Delta t) = a_{n+i-j}(t_0),\ \ i = 1, 2, ..., n,\quad j = i, ..., n \tag{A.7}$$

Appendix B

Flowchart of implementation for RBTO of structures constrained by first-passage probability

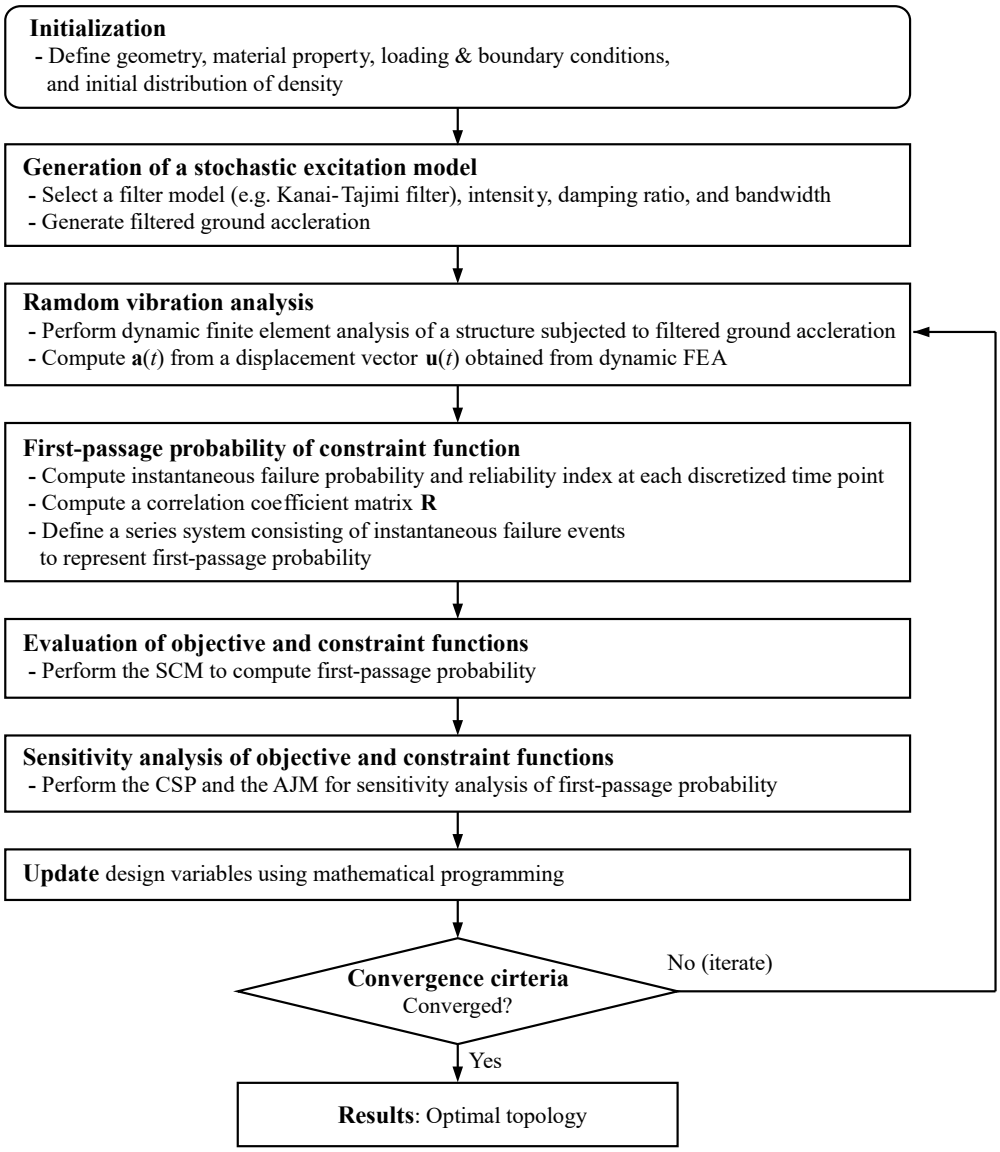

Figure B.1: Flowchart for topology optimization of a structure constrained by first-passage probability.

References

Allen, M., Raulli, M., Maute, K., and Frangopol, D.M. (2004). Reliability-based analysis and design optimization of electrostatically actuated MEMS. *Computer & Structures*, 82(13–14):1007–1020.

Almeida, S.R.M., Paulino, G.H., and Silva, E.C.N. (2009). A simple and effective inverse projection scheme for void distribution control in topology optimization. *Structural and Multidisciplinary Optimization*, 39(4):359−371.

Almeida, S.R.M., Paulino, G.H., and Silva, E.C.N. (2010). Material gradation and layout in topology optimization of functionally graded structures: a global–local approach. *Structural and Multidisciplinary Optimization* 42(6):855–868.

Asadpoure, A., Tootkaboni, M., and Guest, J. (2011). Robust topology optimization of structures with uncertainties in stiffness—application to truss structures, *Computer & Structures*, 89 (11–12):1131–1141.

ASCE. (2010). Minimum design loads for buildings and other structures. ASCE 7-10, Reston, VA.

Bendsøe, M.P. (1989). Optimal shape design as a material distribution problem. *Structural and Multidisciplinary Optimization*, 1(4):193–202.

Bendsøe, M.P. and Kikuchi, N. (1988). Generating optimal topologies in structural design using a homogenization method. *Computer Methods in Applied Mechanics and Engineering*, 71:197–224.

Bendsøe, M.P. and Sigmund, O. (1999). Material interpolation schemes in topology optimization. *Archive of Applied Mechanics*, 69 (9):635–654.

Bendsøe, M.P. and Sigmund, O. (2003). *Topology optimization – theory, methods and applications*. Engineering Online Library. Springer, Berlin, Germany, 2nd edition.

Ben-Tal, A. and Nemirovski, A. (2000). Robust solutions of linear programming problems contaminated with uncertain data. *Mathematical Programming*, 88:411–421.

Bjerager, P. and Krenk, S. (1989). Parametric sensitivity in first order reliability theory. *Journal of Engineering Mechanics*, 115(7):1577–1582.

Bobby, S., Spence, S.M., Bernardini, E., and Kareem, A. (2014). Performance based topology optimization for wind-excited tall buildings: A framework. *Engineering Structure*, 74: 242–255.

Bourdin, B. (2001). Filters in topology optimization. *International Journal for Numerical Methods in Engineering*, 50(9):2143–2158.

Chan, S.P., Cox, H.L., and Benfield, W.A. (1962). Transient analysis of forced vibrations of complex structural mechanical systems. *Journal of Royal Aeronautical Society*. 66:457–460.

Chen, L. and Letchford, C.W. (2005). Proper orthogonal decomposition of two vertical profiles of full-scale nonstationary downburst wind speeds[lzcl]. *Journal of Wind Engineering and Industrial Aerodynamics*, 93(3):187–216.

Chen, S., Chen, W., and Lee, S. (2010). Level set based robust shape and topology optimization under random field uncertainties. *Structural and Multidisciplinary Optimization*, 41(4):507–524.

Chen, X. and Kareem, A. (2005). POD-based modeling, analysis, and simulation of dynamic wind load effects on structures. *Journal of Engineering Mechanics*, 131(4):325–339.

Choi, K. and Kim, N. (2005). *Structural sensitivity analysis and optimization 1*. Springer.

Christensen, P.W. and Klarbring, A. (2009). *An introduction to structural optimization*. Springer, Linköping.

Chun J., Song J., and Paulino, G.H. (2015). Parameter sensitivity of system reliability using sequential compounding method. *Structural Safety* 55:26–36.

Chun, J., Song, J., and Paulino, G.H. (2013). System reliability based topology optimization of structures under stochastic excitations. *11th International Conference on Structural Safety & Reliability*, New York, NY.

Chun, J., Song, J., and Paulino, G.H. (2016). Structural topology optimization under constraints on instantaneous failure probability. *Structural and Multidisciplinary Optimization*, 53(4):773–799.

Clough, R. and Penzien, J. (1993). *Dynamics of structures*. New York: McGraw Hill.

Cook, R., Malkus, D., Plesha, M., and Witt, R. (2007). *Concepts and applications of finite element analysis*. 4th edition, Wiley.

Dahl J., Jensen J.S., and Sigmund, O. (2007). Topology optimization for transient wave propagation problems in one dimension. *Structural and Multidisciplinary Optimization*, 36(6):585–595

Deaton, J. and Grandhi, R. (2014). A survey of structural and multidisciplinary continuum topology optimization: post 2000. *Structural and Multidisciplinary Optimization*, 49(1):1–38.

Deodatis, G. and Shinozuka, M. (1988). Autoregressive model for nonstationary stochastic processes. *Journal of Engineering Mechanics*, 114(11):1995–2012.

Der Kiureghian, A. (2000). The geometry of random vibrations and solutions by FORM and SORM. *Probabilistic Engineering Mechanics*, 15(1):81–90.

Der Kiureghian, A. (2005). First- and second-order reliability methods. Chapter 14 in *Engineering design reliability handbook*, E. Nikolaidis, D. M. Ghiocel and S. Singhal, Edts., CRC Press, Boca Raton, FL.

Der Kiureghian, A., Ditlevsen, O., and Song, J. (2007). Availability, reliability and downtime of systems with repairable components. *Reliability Engineering and System Safety*, 92(2):231–242.

Diaz, A.R. and Kikuchi, N. (1992). Solutions to shape and topology eigenvalue optimization problems using a homogenization method. *International Journal for Numerical Methods in Engineering*, 35(7): 1487–1502.

Diaz, A.R. and Sigmund, O. (1995). Checkerboard patterns in layout optimization. *Structural and Multidisciplinary Optimization*, 10(1):40–45.

Du, J. and Olhoff, N. (2007). Topological design of freely vibrating continuum structures for maximum values of simple and multiple eigenfrequencies and frequency gaps. *Structural and Multidisciplinary Optimization*, 34(2):91–110.

Du, X.P. and Chen, W. (2004). Sequential optimization and reliability assessment method for efficient probabilistic design. *Journal of Mechanical Design*, 126(2):225–233.

Enevoldsen, I. and Sorensen, J.D. (1994). Reliability-Based Optimization in Structural Engineering. *Structural Safety*, 15(3):169–196.

Filipov, E.T., Chun, J, Paulino, G.H., Song, J. (2016). Polygonal multiresolution topology optimization (PolyMTOP) for structural dynamics. *Structural and Multidisciplinary Optimization*, 53(4):673–694.

Frangopol, D.M. and Maute, K. (2005). Reliability-Based Optimization of Civil and Aerospace Structural Systems. *Engineering Design Reliability Handbook*, CRC, Boca Raton, FL, Chap. 24.

Fujimura, K and Der Kiureghian, A. (2007). Tail-equivalent linearization method for nonlinear random vibration. *Probabilistic Engineering Mechanics*, 22(1):63–76.

Genz, A. (2004). Numerical computation of rectangular bivariate and trivariate normal and t-probabilities. *Statistics and Computing*, 14(3):251–60.

Gersch, W. and Yonemoto, J. (1977). Synthesis of multivariate random vibration systems: A two-stage least squares AR-MA model approach. *Journal of Sound and Vibration*, 52(4):553–565.

Ghosh, S. (2011). Micromechanical analysis and multi-scale modeling using the Voronoi cell finite element method (computational mechanics and applied analysis). CRC Press.

Grigoriu, M. (1993). On the spectral representation method in simulation. *Probabilistic Engineering Mechanics*, 8(2):75–90.

Grigoriu, M. (2003). Algorithm for generating sampling of homogeneous Gaussian fields. *Journal of Engineering Mechanics*, 129(1):43–49.

Groenwold, A.A. and Etman, L.F.P. (2008). On the equivalence of optimality criterion and sequential approximate optimization methods in the classical topology layout problem. *International Journal for Numerical Methods in Engineering*, 73(3):297–316.

Guest, J.K. (2009). Imposing maximum length scale in topology optimization. *Structural and Multidisciplinary Optimization*, 37(5):463–473.

Guest, J.K. and Igusa, T. (2008). Structural optimization under uncertain loads and nodal locations. *Computer Methods in Applied Mechanics and Engineering*, 198(1):116–124.

Guest, J.K., Prevost, J.H., and Belytschko, T. (2004). Achieving minimum length scale in topology optimization using nodal design variables and projection functions. *International Journal for Numerical Methods in Engineering*, 61(2):238−254.

Guo, X., Zhang, W., and Zhang, L. Zhang. (2013). Robust structural topology optimization considering boundary uncertainties. *Computer Methods in Applied Mechanics and Engineering*, 253:356–368.

Haftka, R.T. and Adelman, H.M. (1989). Recent developments in structural sensitivity analysis. *Structural and Multidisciplinary Optimization*, 1(3):137–151.

Haftka, R.T. and Gürdal, Z. (1992). *Elements of structural optimization*. 3rd edition, Springer

Haug, E. and Arora, S. (1978). Design sensitivity analysis of elastic mechanical systems. *Computer Methods in Applied Mechanics and Engineering*, 15(1):35–62.

Haug, J., Choi, K., and Komkov, V. (1986). Design sensitivity analysis of structural systems. *Academic press*, Orlando, FL.

Hohenbichler, M. and Rackwitz, R. (1986). Sensitivity and importance measures in structural reliability. *Civil Engineering Systems*, 3(4):203–209.

Houbolt, J.C. (1950). A recurrence matrix solution for the dynamic response of elastic aircraft. *Journal of the Aeronautical Sciences*, 17(9):540–550.

Huang, X., Zuo, Z., and Xie, Y. (2010). Evolutionary topological optimization of vibrating continuum structures for natural frequencies. *Computer & Structure*, 88(5–6):357–364.

Hulbert, G.M. and Chung, J. (1996). Explicit time integration algorithms for structural dynamics with optimal numerical dissipation. *Computer Methods in Applied Mechanics and Engineering*, 137(2):175–188.

Jalalpour, M., Guest, J.K., and Igusa, T. (2013). Reliability-based topology optimization of trusses with stochastic stiffness. *Structural Safety*, 43:41–49.

Jansen, M., Lombaert, G., and Schevenels, M. (2015). Robust topology optimization of structures with imperfect geometry based on geometric nonlinear analysis. *Computer Methods in Applied Mechanics and Engineering*, 285:452–467.

Jensen, J.S. (2007). Topology optimization of dynamics problems with Padé approximants. *International Journal for Numerical Methods in Engineering*, 72(13):1605–1630.

Jensen, J.S. and Pedersen, N.L. (2006). On maximal eigenfrequency separation in two-material structures: the 1D and 2D scalar cases. *Journal of Sound and Vibration*, 289(4–5):967–986.

Jog, C.S. (2002). Topology design of structures subjected to periodic loading. *Journal of Sound and Vibration*, 253(3):687–709.

Jog, C.S. and Haber, R.B. (1996). Stability of finite element models for distributed-parameter optimization and topology design. *Computer Methods in Applied Mechanics and Engineering*, 130(3–4):203–226.

Kang, J., Kim, C., and Wang, S. (2004). Reliability-based topology optimization for electromagnetic systems. COMPEL: *The International Journal for Computation and Mathematics in Electrical and Electronic Engineering*, 23(3):715–723.

Kang, W.H. and Song, J. (2010). Evaluation of multivariate normal integrals for general systems by sequential compounding. *Structural Safety*, 32(1):35−41.

Kang, W.H., Lee, Y.J., Song, J., and Gencturk, B. (2012). Further development of matrix-based system reliability method and applications to structural systems. *Structure and Infrastructure Engineering: Maintenance, Management, Life-cycle Design and Performance*, 8(5):441–457.

Kang, W.H., Song, J., and Gardoni, P. (2008). Matrix-based system reliability method and applications to bridge networks. *Reliability Engineering & System Safety*, 93(11):1584–1593.

Kaveh, A., Farzam, M., and Kalateh, M. (2012). Time-history analysis based optimal design of space trusses: the CMA evolution strategy approach using GRNN and WA. *Structural Engineering and Mechanics*, 44(3):379–403.

Kharmanda, G., Olhoff, N., Mohamed, A., and Lemaire, M. (2004). Reliability-based topology optimization. *Structural and Multidisciplinary Optimization*, 26(5):295–307.

Kim, C., Wang, S., Rae, K., Moon, H., and Choi, K.K. (2006). Reliability-based topology optimization with uncertainties. *Journal of Mechanical Science and Technology*, 20(4):494–504.

Kim, Y.Y. and Yoon, G.H. (2000). Multi-resolution multi-scale topology optimization–a new paradigm. *International Journal of Solids and Structures*, 37(39):5529–5559.

Kitagawa, G. (1996). Monte Carlo filter and smoother for non-Gaussian nonlinear state space models. *Journal of Computational and Graphical Statistics*, 5(1):1–25.

Kohn, R.V. and Strang, G. (1986). Optimal design and relaxation of variational problems. *Communications on Pure and Applied Mathematics*. 39:113–137, 139–182, 353–377.

Konakli, K. and Der Kiureghian, A. (2012). Simulation of spatially varying ground motions including incoherence, wave-passage and differential site-response effects. *Earthquake Engineering & Structural Dynamics*, 41(3):495–513.

Larsen, A.A., Laksafoss, B., Jensen, J.S., and Sigmund, O. (2008). Topological material layout in plates for vibration suppression and wave propagation control. *Structural and Multidisciplinary Optimization*, 37(6):585–594.

Li, C.C. and Der Kiureghian, A. (1993). Optimal discretization of random fields. *Journal of Engineering Mechanics*, 119(6):1136–1154.

Liang, J., Mourelatos, Z., and Tu, J. (2004). A Single-Loop Method for Reliability-Based Design Optimization. *Proceedings of the ASME Design Engineering Technical Conferences*.

Liang, J., Mourelatos, Z.P., and Nikolaidis, E. (2007). A single-loop approach for system reliability-based design optimization. *Journal of Mechanical Design*, 129(12):1215–1224.

Liang, J., Mourelatos, Z.P., and Tu, J. (2008). A single-loop method for reliability-based design optimisation. *International Journal of Product Development*, 5(1–2):76– 92.

Liu, J., and Chen, R. (1998). Sequential Monte Carlo methods for dynamic systems. *Journal of the American Statistical Association*, 93(443):1032–1044.

Lógó, J., Ghaemi, M., and Rad, M.M. (2009). Optimal topologies in case of probabilistic loading: the influence of load correlation. *Mechanics Based Design of Structures and Machines*, 37(3):327–348.

Luo, Y., Kang, Z., Luo, Z., and Li, A. (2009). Continuum topology optimization with non-probabilistic reliability constraints based on multi-ellipsoid convex model. *Structural and Multidisciplinary Optimization*, 39(3):297–310.

Lutes, L.D., Sarkani, S. (2003). *Random vibrations: analysis of structural and mechanical systems*. Elsevier Butterworth-Heinemann, Burlington MA.

Ma, Z.D., Cheng, H.C., Kikuchi, N. (1994). Structural design for obtaining desired eigenfrequencies by using the topology and shape optimization method. *Computing Systems in Engineering*, 5(1):77–89.

Ma, Z.D., Kikuchi, N., and Cheng, H.C. (1995). Topological design for vibrating structures. *Computer Methods in Applied Mechanics and Engineering*, 121(1–4):259–280.

Maeda, Y., Nishiwaki, S., Izui, K., Yoshimura, M., Matsui, K., and Terada, K. (2006). Structural topology optimization of vibrating structures with specified eigenfrequencies and eigenmode shapes. *International Journal for Numerical Methods in Engineering*, 67(5):597–628.

Martins, J.R.R.A., Sturdza, P., and Alonso, J.J. (2003). The Complex-Step Derivative Approximation, *ACM Transactions on Mathematical Software*, 29(3):245–262.

Matsui, K. and Terada, K. (2004). Continuous approximation of material distribution for topology optimization. *International Journal for Numerical Methods in Engineering*, 59(14):1925–1944.

Maute, K. and Allen, M. (2004). Conceptual design of aeroelastic structures by topology optimization. *Structural and Multidisciplinary Optimization*, 27(1–2):27– 42.

Maute, K. and Frangopol, D.M. (2003). Reliability-based design of MEMS mechanisms by topology optimization. *Computer & Structures*, 81(8–11):813–824.

Mignolet, M.P. and Spanos, P.D. (1987). Recursive simulation of stationary multivariate random processes-Part I. *Journal of Applied Mechanics*, 54(3):674–680.

Mijar, A.R., Swan, C.C., Arora, J.S., and Kosaka, I. (1998). Continuum topology optimization for concept design of frame bracing systems. *Journal of Structural Engineering*, 124:541–550.

Min, S., Kikuchi, N., Park, Y.C., Kim, S., and Chang, S. (1999). Optimal topology design of structures under dynamic loads. *Structural and Multidisciplinary Optimization*, 17(2–3):208–218.

Mousavi, S.E., Xiao, H., and Sukumar, N. (2009). Generalized Gaussian quadrature rules on arbitrary polygons. *International Journal for Numerical Methods in Engineering*, 82(1):99–113.

Natarajan, S., Bordas, S., and Roy Mahapatra, D. (2009). Numerical integration over arbitrary polygonal domains based on Schwarz-Christoffel conformal mapping. *International Journal for Numerical Methods in Engineering*. 80(1):103–134.

NEHRP. (2009). *Recommended seismic provisions for new buildings and other structures* (FEMA P-750). Federal Emergency Management Agency, Washington, D. C.

Newmark, N.M. (1959). A method of computation for structural dynamics. *Journal of Engineering Mechanics*, 85(3):67–94.

Nguyen, T (2010). *System Reliability-Based Design and Multiresolution Topology Optimization*. Ph.D. thesis. Urbana-Champaign: University of Illinois.

Nguyen, T.H., Le, C.H., and Hajjar, J.F. (2013). High-order finite elements for topology optimization. *In: 10th World congress on structural and multidisciplinary optimization*. Orlando.

Nguyen, T.H., Paulino, G.H., Song J, and Le, C.H. (2009). A computational paradigm for multiresolution topology optimization (MTOP). *Structural and Multidisciplinary Optimization*, 41(4):525–539.

Nguyen, T.H., Paulino, G.H., Song, J, and Le, C.H. (2012). Improving multiresolution topology optimization via multiple discretizations. *International Journal for Numerical Methods in Engineering*, 92(6):507–530.

Nguyen, T.H., Song, J., and Paulino, G.H. (2010). Single-loop system reliability-based design optimization using matrix-based system reliability method: theory and applications. *Journal of Mechanical Design*, 132(1):011005–1–11.

Nguyen, T.H., Song, J., and Paulino, G.H. (2011). Single-loop system reliability-based topology optimization considering statistical dependence between limit-states. *Structural and Multidisciplinary Optimization*, 44(5): 593–611.

Novak, D., Stoyanoff, S., and Herda, H. (1995). Error assessment for wind histories generated by autoregressive method. *Structural Safety*, 17(2): 79–90.

Ohsaki, M. (2010). *Optimization of finite dimensional structures*. CRC Press.

Olhoff, N. (1976). Optimization of vibrating beams with respect to higher order natural frequencies. *Journal of Structure and Mechanics*, 4(1):87–122.

Olhoff, N., Niu, B., and Cheng, G. (2012). Optimum design of band-gap beam structures. *International Journal of Solids and Structures*, 49(22):3158–3169.

Parvizian, J., Düster, A., and Rank, E. (2011). Topology optimization using the finite cell method. *Optimization and Engineering*, 13(1):57–78.

Paulino, G.H. and Le, C.H. (2008). A modified Q4/Q4 element for topology optimization. *International Journal for Numerical Methods in Engineering*, 37(3):255–264.

Pedersen, N.L. (2000). Maximization of eigenvalues using topology optimization. *Structural and Multidisciplinary Optimization*, 20(1):2–11.

Petersson, J. and Sigmund, O. (1998). Slope constrained topology optimization. *International Journal for Numerical Methods in Engineering*, 41(8):1417–1434.

Poulsen, A. (2002). Topology optimization in wavelet space. *International Journal for Numerical Methods in Engineering*, 53:567–582.

Rahmatalla, S. and Swan, C. (2004). A Q4/Q4 continuum structural topology optimization implementation. *Structural and Multidisciplinary Optimization*, 27(1–2):130–135.

Ramos Jr., A. and Paulino, G.H. (2015). Convex topology optimization for hyperelastic trusses based on the ground-structure approach. *Structural and Multidisciplinary Optimization*, 51(2):287–304.

Ramos Jr., A. and Paulino, G.H. (2016). Filtering structures out of ground structures - a discrete filtering tool for structural design optimization. *Structural and Multidisciplinary Optimization.* Available Online. DOI 10.1007/s00158–015–1390–1.

Rezaeian, S. and Der Kiureghian, A. (2008). A stochastic ground motion model with separable temporal and spectral nonstationarities. *Earthquake Engineering & Structural Dynamics*, 37(13):1565–1584.

Rezaeian, S. and Der Kiureghian, A. (2010). Simulation of synthetic ground motions for specified earthquake and site characteristics. *Earthquake Engineering & Structural Dynamics*, 39(10): 1155–1180.

Rezaeian, S. and Der Kiureghian, A. (2012). Simulation of orthogonal horizontal ground motion components for specified earthquake and site characteristics. *Earthquake Engineering & Structural Dynamics*, 41(2):335–353.

Rozvany, G.I.N. (2008). Exact analytical solutions for benchmark problems in probabilistic topology optimization. *EngOpt 2008–International Conference on Engineering Optimization*, Rio de Janeiro.

Rozvany, G.I.N. (2009). A critical review of established methods of structural topology optimization. *Structural and Multidisciplinary Optimization*, 37(3):217–237.

Rozvany, G.I.N., Zhou, M., and Birker, T. (1992). Generalized shape optimization without homogenization. *Structural and Multidisciplinary Optimization*, 4(3):250–252.

Rubio, W.M., Paulino, G.H., and Silva, E.C.N. (2011). Tailoring vibration mode shapes using topology optimization and functionally graded material concepts. *Smart Materials and Structures*, 20(2):025009.

Salajegheh, E., Heidari, A. (2005). Optimum design of structures against earthquake by wavelet neutral network and filter banks. *Earthquake engineering and structural dynamics*. 34(1):67–82.

Schevenels, M., Lazarov, B.S., and Sigmund, O.(2011). Robust topology optimization accounting for spatially varying manufacturing errors. *Computer Methods in Applied Mechanics and Engineering*, 200(49–52):3613–3627.

Shan, S. and Wang, G.G. (2008). Reliable Design Space and Complete Single-Loop Reliability-Based Design Optimization. *Reliability Engineering & System Safety*, 93(8):1218–1230.

Shinozuka, M. (1972). Monte Carlo solution of structural dynamics. *Computer and Structures*, 2(5–6):855–874.

Shinozuka, M. and Deodatis, G. (1991). Simulation of the stochastic process by spectral representation. *Applied Mechanics Reviews*, 44(4):191 –204.

Shinozuka, M. and Deodatis, G. (1996). Simulation of multi-dimensional Gaussian stochastic fields by spectral representation. *Applied Mechanics Reviews*, 49(1):29–53.

Shinozuka, M. and Jan, C.M. (1972). Digital simulation of random processes and its applications. *Journal of Sound and Vibration*, 25(1):111–128.

Sigmund, O. (2007). Morphology-based black and white filters for topology optimization. *Structural and Multidisciplinary Optimization*, 33(4):401–424.

Sigmund, O. (2009). Manufacturing tolerant topology optimization, *Acta Mechanica Sinica*, 25 (2):227–239.

Sigmund, O. and Petersson, J. (1998). Numerical instabilities in topology optimization: a survey on procedures dealing with checkerboards, mesh-dependencies and local minima. *Structural Optimization*, 16(1):68–75.

Sleesongsom, S. and Bureerat, S. (2013). New conceptual design of aeroelastic wing structures by multi-objective optimization. *Engineering Optimization*, 45(1):107–122.

Song, J. and Der Kiureghian, A. (2003). Bounds on system reliability by linear programming. *Journal of Engineering Mechanics*, 129(6):627–636.

Song, J. and Der Kiureghian, A. (2005). Component importance measures by linear programming bounds on system reliability. *In: Proceedings of the Ninth International Conference on Structural Safety and Reliability (ICOSSAR9)*, Rome, Italy.

Song, J. and Der Kiureghian, A. (2006). Joint first-passage probability and reliability of systems under stochastic excitation. *Journal of Engineering Mechanics* 132(1):65−77.

Song, J. and Kang, W.H. (2009). System reliability and sensitivity under statistical dependence by matrix-based system reliability method. *Structural Safety*, 31(2):148–156.

Soong, T.T. and Grigoriu, M. (1993). *Random vibration of mechanical and structural systems*. Prentice Hall, Englewood Cliffs, N.J.

Spanos, P.D and Mignolet, M.P. (1990). Simulation of Stationary Random Processes: Two-Stage MA to ARMA Approach. *Journal of Engineering Mechanics*, 116(3):620–641.

Spanos, P.D. and Ghanem, R. (1989). Stochastic finite element expansion for random media. *Journal of Engineering Mechanics*, 115(5):1035–1053.

Spanos, P.D. and Mignolet, M.P. (1987) Recursive simulation of stationary multivariate random processes–Part II. *Journal of Applied Mechanics*, 54(3):681–687.

Stolpe, M. and Svanberg, K. (2001). An alternative interpolation scheme for minimum compliance topology optimization. *Structural and Multidisciplinary Optimization*, 22(2):116–124.

Stromberg, L.L., Beghini, A., Baker, W.F., and Paulino, G.H. (2011). Application of layout and topology optimization using pattern gradation for the conceptual design of buildings. *Structural and Multidisciplinary Optimization*, 43(2):165–80.

Stromberg, L.L., Beghini, A., Baker, W.F., and Paulino, G.H. (2012). Topology optimization for braced frames: Combining continuum and beam/column elements. *Engineering Structure*, 37: 106–124.

Sues, R.H., Cesare, M. (2005). System reliability and sensitivity factors via the MPPSS method. *Probabilistic Engineering Mechanics*, 20(2):148–157.

Sukumar, N. (2004). Construction of polygonal interpolants: a maximum entropy approach. *International Journal for Numerical Methods in Engineering*, 61(12):2159–2181.

Sukumar, N. and Malsch, E.A. (2006). Recent advances in the construction of polygonal finite element interpolants. *Archives of Computational Methods Engineering*, 13(1):129–163.

Sukumar, N. and Tabarraei, A. (2004). Conforming polygonal finite elements. *International Journal for Numerical Methods in Engineering*, 61:2045–2066.

Sutradhar, A., Paulino, G.H., Miller, M.J., and Nguyen, T.H. (2010). Topological optimization for designing patient-specific large craniofacial segmental bone replacements. *Proceedings of the National Academy of Sciences of the United States of America*, 107(30):13222–13227.

Svanberg, K. (1987). The method of moving asymptotes - a new method for structural optimization. *International Journal for Numerical Methods in Engineering*, 24(2):359–373.

Talischi, C., Paulino, G.H., and Le, C.H. (2009a). Honeycomb Wachspress finite elements for structural topology optimization. *Structural and Multidisciplinary Optimization*, 37(6):569–583.

Talischi, C., Paulino, G.H., Pereira, A., and Menezes, I.F.M. (2009b). Polygonal finite elements for topology optimization: a unifying paradigm. *Structural and Multidisciplinary Optimization*, 82(6):671–698.

Talischi, C., Paulino, G.H., Pereira, A., and Menezes, I.F.M. (2012a). PolyMesher: a general-purpose mesh generator for polygonal elements written in MATLAB. *Structural and Multidisciplinary Optimization*, 45(3):309–328

Talischi, C., Paulino, G.H., Pereira, A., and Menezes, I.F.M. (2012b). PolyTop: a MATLAB implementation of a general topology optimization framework using unstructured polygonal finite element meshes. *Structural and Multidisciplinary Optimization*, 45(3):329–357.

Tcherniak, D. (2002). Topology optimization of resonating structures using SIMP method. *International Journal for Numerical Methods in Engineering*, 54(11):1605–1622.

Tsai, T.D. and Cheng, C.C. (2013). Structural design for desired eigenfrequencies and mode shapes using topology optimization. *Structural and Multidisciplinary Optimization*, 47(5):673–686.

Tsompanakis, Y., Lagaros, N.D., and Papadrakakis, M. (2008). *Structural Design Optimization Considering Uncertainties*, Taylor & Francis, London, UK.

Tu, J. and Choi, K.K, and Park, Y.H. (1999). A New Study on Reliability Based Design Optimization. *Journal of Mechanical Design*, 121(4):557–564.

Vanmarcke, E.H. (1975). On the distribution of the first-passage time for normal stationary random processes. *Journal of Applied Mechanics*, 42(1):215−220.

Wang, F., Lazarov, B., and Sigmund, O. (2011). On projection methods, convergence and robust formulations in topology optimization. *Structural and Multidisciplinary Optimization*, 43(6):767–784.

Yang, R.J. and Chahande, A.I. (1995). Automotive applications of topology optimization. *Structural and Multidisciplinary Optimization*, 9(3–4):245–249.

Yoon, G.H. (2010a). Maximizing the fundamental eigenfrequency of geometrically nonlinear structures by topology optimization based on element connectivity parameterization. *Computer & Structure*, 88 (1–2):120–133.

Yoon, G.H. (2010b). Structural topology optimization for frequency response problem using model reduction schemes. *Computer Methods in Applied Mechanics and Engineering*, 199(25–28):1744–1763.

Zegard, T. and Paulino, G.H. (2014). GRAND — Ground structure based topology optimization for arbitrary 2D domains using MATLAB. *Structural and Multidisciplinary Optimization*, 50 (5):861–882.

Zegard, T. and Paulino, G.H. (2015). GRAND3 — Ground structure based topology optimization for arbitrary 3D domains using MATLAB. *Structural and Multidisciplinary Optimization,* 52 (6):1161–1184.

Zhang, J. and Ellingwood, B. (1994). Orthogonal series expansions of random fields in reliability analysis. *Journal of Engineering Mechanics*, 120(12):2660–2677

Zhou, K. (2013). Topology optimization of truss-like continuum structures for natural frequencies. *Structural and Multidisciplinary Optimization*, 47(4):613–619.

Zienkiewicz, O.C. (1977). A new look at the newmark, houbolt and other time stepping formulas. A weighted residual approach. *Earthquake Engineering & Structural Dynamics*, 5(4):413–418.